

**CONTROL OF A MICROGRID THROUGH ENERGY
STORAGE DEVICES USING EVOLUTIONARY AND
NEURO-FUZZY METHODS**

BY

MOHAMMED ASHRAF ALI

A Thesis Presented to the
DEANSHIP OF GRADUATE STUDIES

KING FAHD UNIVERSITY OF PETROLEUM & MINERALS

DHAHRAN, SAUDI ARABIA

In Partial Fulfillment of the
Requirements for the Degree of

MASTER OF SCIENCE

In

ELECTRICAL ENGINEERING

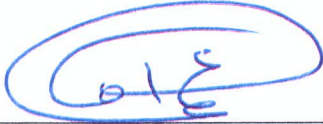
MAY 2013

KING FAHD UNIVERSITY OF PETROLEUM & MINERALS

DHAHRAN- 31261, SAUDI ARABIA

DEANSHIP OF GRADUATE STUDIES

This thesis, written by **MOHAMMED ASHRAF ALI** under the direction of his thesis advisor and approved by his thesis committee, has been presented to and accepted by the Dean of Graduate Studies, in partial fulfillment of the requirements for the degree of **MASTER OF SCIENCE IN ELECTRICAL ENGINEERING.**



Dr. Ali A. Al-Shaikhi
Department Chairman



Dr. Salam A. Zummo
Dean of Graduate Studies



28/5/13

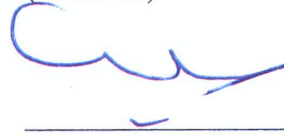
Date



Dr. A.H. Abdur-Rahim
(Advisor)



Dr. Ibrahim O. Habiballah
(Member)



Dr. Samir A. Al-Baiyat
(Member)

© Mohammed Ashraf Ali

2013

Dedicated to
My Beloved Parents,
My Brother and
My Sisters

ACKNOWLEDGMENTS

All praises and worship are for ALLAH SWT alone; we seek His help and ask for His forgiveness, we thank Him for providing us with knowledge and we always strive to achieve His reward. I feel privileged to glorify His name in the sincerest way through this small accomplishment. Peace and blessings be upon the greatest human being that ever walked on this earth, the last and the final Prophet, Muhammad (peace be upon him), upon his family, his companions, and all those who follow him until the day of judgement.

I would like to thank my parents, Mr. and Mrs. Mohammed Ali, from the bottom of my heart for their immense patience and the motivation they had given me and also for teaching me the true meaning of hard work through their lives. My brother Mohammed Ayyub Ali and sisters, too share the same acknowledgements for their support. It would not be wrong to say that they have worked more than me, in making me what I am today. I ask Allah to reward all of them the best in this world and the hereafter, aameen.

I would like to pay a high tribute to my thesis advisor Dr. Abu Hamed Abdur-Rahim for his invaluable guidance and helpful ideas throughout this research. His appreciation and words of motivation gave a new life to my efforts in hard times. I am also indebted to him for his valuable time, efforts, his continuous support and inspiration. I always admired his knowledge, intuition and vision. I feel very great to say, he has successfully instilled in me a passion for scientific research, which will continue to guide me for many more years to come.

I owe a deep appreciation to my committee members, Dr. Samir Al-Baiyat and Dr. Ibrahim O. Habiballah, who have spared their valuable times and given their thoughtful suggestions and also they have been a source of constant help and encouragement. I thank all the other teachers who taught me in the university.

I acknowledge King Fahd University of Petroleum & Minerals for supporting my M.S. studies. I am thankful to Dr. Ali Ahmed Al-Shaikhi, Chairman Electrical Engineering Department, for providing an excellent environment of learning and research in the department.

Many thanks and appreciation is for my seniors Abdur-Rahman Aravind, Mohammed Khaleel Ahmed and Mohammed Touseef Hussain and also my colleagues Mohammed Fahham, Amer bin Ziyad and Mohammed Asrar-ur-Rahman, who have been a great source of moral support. They were very supportive during this work and helped me lot in one way or the other. I thank them all.

Last but not the least; I thank the Indian community brothers of KFUPM who have been extremely supportive in all the aspects of life during my stay in Saudi Arabia.

جزاكم الله خيرا

TABLE OF CONTENTS

ACKNOWLEDGMENTS	VI
TABLE OF CONTENTS	VIII
LIST OF TABLES	XII
LIST OF FIGURES	XIII
LIST OF SYMBOLS	XXI
ABSTRACT	XXIV
CHAPTER 1 INTRODUCTION	1
1.1 Evolution of Distributed Generation	1
1.1.1 Microgrids	2
1.1.2 Microgrid Controls	4
1.1.3 Intelligent Controls	7
1.2 Thesis Motivation	9
1.3 Thesis Objectives	10
1.4 Thesis Contributions	11
1.5 Thesis Organization	12
CHAPTER 2 LITERATURE SURVEY	14
2.1 Introduction	14
2.2 Microgrid Components	15
2.2.1 Photovoltaic system	15
2.2.2 Fuel cell system	20

2.2.3	Wind energy system	22
2.3	Microgrid Architecture	26
2.4	Issues Reported in Microgrids	27
2.5	Dynamic Performance Enhancement	29
2.5.1	Conventional methods	29
2.5.2	Bulk energy storage systems (ESS).....	30
2.6	Bio-geography based Optimization	33
2.6.1	Overview	33
2.6.2	Elitism of species	35
2.6.3	Migration of species	35
2.6.4	Mutation of species.....	38
CHAPTER 3 MICROGRID SYSTEM MODELING		40
3.1	Introduction.....	40
3.2	The Microgrid Architecture	40
3.3	Small-Scale Conventional Micro Generation	43
3.3.1	Microgenerator connected to grid.....	44
3.4	The Photovoltaic System.....	46
3.4.1	The power electronic interface for PV system	49
3.5	The Wind Energy System.....	58
3.5.1	The wind turbine model	59
3.5.2	The variable speed PMSG model	61
3.5.3	The wind system converter model.....	63
3.5.4	The DC link capacitor model	65
3.5.5	The LC filter and coupling transmission line model.....	66
3.6	The Fuel-Cell System	68

3.6.1	The fuel cell stack connected to PCC.....	70
3.7	The Small-Signal Model of the Microgrid Components	71
3.7.1	The small-signal model of microgenerator	72
3.7.2	The small-signal model of photovoltaic system	73
3.7.3	The small-signal model of fuel cell system.....	76
3.7.4	The small-signal model of wind system	77
3.8	The Composite Microgrid Model.....	81
3.8.1	Microgrid system model.....	81
CHAPTER 4 EVALUATION OF MICROGRID PERFORMANCE		86
4.1	Small-Signal Analysis.....	86
4.2	Non-linear Time Domain Analysis	94
CHAPTER 5 ENERGY STORAGE CONTROLLER		100
5.1	Introduction.....	100
5.2	Battery Energy Storage System (BESS)	101
5.2.1	The voltage source converter model	103
5.2.2	Dynamical model of BESS	104
5.2.3	Decoupled P-Q control	105
5.3	Supercapacitor Energy Storage System (SCESS).....	108
5.3.1	Dynamic model of SCESS	109
5.3.2	Supercapacitor DC-DC converter control circuit.....	110
5.3.3	P-Q decoupled control system.....	112
5.4	The Composite System Model with Central Storage Controller	112
5.5	Controller Design	113
5.5.1	Biogeography based optimization (BBO) procedure	115

5.5.2	Design of adaptive neuro-fuzzy control system	119
5.5.3	Generation of training data using BBO	120
5.5.4	Adaptive neuro-fuzzy method	120
5.5.5	ANFIS training algorithm	124
 CHAPTER 6 TESTING THE ADAPTIVE NEURO-FUZZY ENERGY STORAGE CONTROLLER		128
6.1	Generation of Adaptive Controller Parameters	129
6.2	BESS Energy Storage Controller	136
6.2.1	Torque pulse disturbance	137
6.2.2	Torque step disturbance	147
6.3	Supercapacitor (SCESS) Energy Storage Controller	155
6.3.1	Torque pulse disturbance	155
6.3.2	Torque step disturbance	162
6.4	Comparison of Adaptive BESS and SCESS Controllers	170
 CHAPTER 7 CONCLUSIONS AND FUTURE WORK		174
7.1	Conclusions	174
7.2	Future Work	176
 REFERENCES		177
VITAE		190

LIST OF TABLES

Table 2.1: Summary of short-term energy storage system characteristics	32
Table 4.1: Eigen values of the composite microgrid model	87
Table 4.2: Critical Eigen values associated with composite microgrid	88
Table 5.1: ANFIS hybrid learning rule	125
Table 6.1: The BBO algorithm parameters	129
Table 6.2: Range of decoupled control parameters	130
Table 6.3: Optimum P-Q decoupled controller parameters for BESS when 0.15 pu torque pulse is applied at the microgenerator for 300 msec.....	131

LIST OF FIGURES

Figure 2.1: Emigration and Immigration rate model in BBO.....	36
Figure 3.1: Single line diagram of microgrid.....	41
Figure 3.2: Detailed layout of microgrid under investigation.....	42
Figure 3.3: Synchronous generator connected to grid	44
Figure 3.4: Electrical equivalent of a PV cell.....	47
Figure 3.5: Approximate PV circuit model.....	48
Figure 3.6: Interconnection of PV module to PCC.....	50
Figure 3.7: Circuit representation of DC-boost converter	51
Figure 3.8: DC-link capacitor model	52
Figure 3.9: Inverter circuit description	54
Figure 3.10: LC filter and coupling inductance circuit.....	56
Figure 3.11: Schematic of variable speed WT-PMSG connected to grid.....	58
Figure 3.12: Two mass model of drive train.....	61
Figure 3.13: Electrical equivalent circuit of PMSG.....	62
Figure 3.14: Converter configuration for variable speed PMSG wind system.....	64
Figure 3.15: Simplified PEM fuel cell stack model.....	69
Figure 3.16: Fuel cell stack connected to PCC.....	70
Figure 3.17: Composite microgrid model.....	82
Figure 4.1: Plot of dominant eigenvalues of microgenerator for varying wind penetration	89
Figure 4.2: Plot of dominant eigenvalues of microgrid for varying PV power output.....	90

Figure 4.3: Plot of dominant eigenvalues of microgrid for varying fuel cell power penetration.....	91
Figure 4.4: Plot of dominant eigenvalues of PV system for various wind participation ..	92
Figure 4.5: Plot of dominant eigenvalues of fuel cell system for various wind participation	93
Figure 4.6: Plot of dominant eigenvalues of microgrid for varying load requirement	94
Figure 4.7: Response of the microgrid voltage following a disturbance of 15% torque pulse for 0.3 sec a) wind generation at 0.9 pu b) wind generation at 0.1pu	95
Figure 4.8: Response of the microgenerator speed deviations following a disturbance of 15% torque pulse for 0.3 sec a) wind generation at 0.9 pu b) wind generation at 0.1pu..	96
Figure 4.9: Response of the PV DC-link voltage following a disturbance of 15% torque pulse for 0.3 sec a) wind generation at 0.9 pu b) wind generation at 0.1pu	97
Figure 4.10: Response of the wind DC-link voltage following a disturbance of 15% torque pulse for 0.3 sec a) wind generation at 0.9 pu b) wind generation at 0.1pu	97
Figure 4.11: Response of the VSC DC-link voltage following a disturbance of 15% torque pulse for 0.3 sec a) wind generation at 0.9 pu b) wind generation at 0.1pu	98
Figure 4.12: Response of the VSC current following a disturbance of 15% torque pulse for 0.3 sec a) wind generation at 0.9 pu b) wind generation at 0.1pu.....	99
Figure 5.1: Composite microgrid system equipped with battery energy storage	102
Figure 5.2: Circuit model of battery	103
Figure 5.3: Block diagram representation of decoupled P-Q control strategy	106
Figure 5.4: Composite microgrid system equipped with supercapacitor based energy storage.....	108

Figure 5.5: Supercapacitor circuit representation	109
Figure 5.6: Circuit description of supercapacitor DC-DC converter control scheme.....	110
Figure 5.7: Flow chart of the proposed BBO based optimal control design.....	118
Figure 5.8: Model of adaptive control strategy.....	119
Figure 5.9: Typical equivalent ANFIS architecture.....	122
Figure 5.10: Flow chart of ANFIS network to be employed for P-Q decoupled controller	127
Figure 6.1: Variation of cost function against iterations for 0.15 pu input torque pulse applied at microgenerator for 300 msec.....	131
Figure 6.2: Convergence of Kp1 against iterations for optimization when 0.15 pu input torque pulse is applied at microgenerator for 300 msec	132
Figure 6.3: Convergence of Kp2 against iterations for optimization when 0.15 pu input torque pulse is applied at microgenerator for 300 msec	132
Figure 6.4: Convergence of Kp3 against iterations for optimization when 0.15 pu input torque pulse is applied at microgenerator for 300 msec	133
Figure 6.5: Convergence of Kp4 against iterations for optimization when 0.15 pu input torque pulse is applied at microgenerator for 300 msec	133
Figure 6.6: Convergence of Ki1 against iterations for optimization when 0.15 pu input torque pulse is applied at microgenerator for 300 msec	134
Figure 6.7: Convergence of Ki2 against iterations for optimization when 0.15 pu input torque pulse is applied at microgenerator for 300 msec	134
Figure 6.8: Convergence of Ki3 against iterations for optimization when 0.15 pu input torque pulse is applied at microgenerator for 300 msec	135

Figure 6.9: Convergence of K_{i4} against iterations for optimization when 0.15 pu input torque pulse is applied at microgenerator for 300 msec	135
Figure 6.10: Microgenerator rotor speed deviation when a 15% torque pulse is applied for 300 msec, (a) Without BESS (b) With adaptive BESS control	138
Figure 6.11: Microgenerator terminal voltage variation when a 15% torque pulse is applied for 300 msec, (a) Without BESS (b) With adaptive BESS control.....	138
Figure 6.12: PV array current variation when a 15% torque pulse is applied for 300 msec, (a) Without BESS (b) With adaptive BESS control	139
Figure 6.13: PV filter capacitor voltage variation when a 15% torque pulse is applied for 300 msec, (a) Without BESS (b) With adaptive BESS control	140
Figure 6.14: PMSG rotor speed variation when a 15% torque pulse is applied for 300 msec, (a) Without BESS (b) With adaptive BESS control	141
Figure 6.15: PMSG terminal voltage variation when a 15% torque pulse is applied for 300 msec, (a) Without BESS (b) With adaptive BESS control	141
Figure 6.16: PMSG stator current variation when a 15% torque pulse is applied for 300 msec, (a) Without BESS (b) With adaptive BESS control	142
Figure 6.17: VSC DC-link voltage variation when a 15% torque pulse is applied for 300 msec, (a) Without BESS (b) With adaptive BESS control	143
Figure 6.18: VSC current variation when a 15% torque pulse is applied for 300 msec, (a) Without BESS (b) With adaptive BESS control.....	143
Figure 6.19: Microgrid bus voltage variation when a 15% torque pulse is applied for 300 msec, (a) Without BESS (b) With adaptive BESS control	144

Figure 6.20: Microgrid delivered power to the grid variation when a 15% torque pulse is applied for 300 msec, (a) Without BESS (b) With adaptive BESS control.....	144
Figure 6.21: Injected real power by the BESS controller following a torque pulse of 15% for 300 msec duration	145
Figure 6.22: Injected reactive power by the BESS controller following a torque pulse of 15% for 300 msec duration.....	146
Figure 6.23: Microgenerator load angle variation following a 10% change in input torque, (a) Without BESS (b) With adaptive BESS control	147
Figure 6.24: Microgenerator terminal voltage variation following a 10% change in input torque, (a) Without BESS (b) With adaptive BESS control.....	148
Figure 6.25: PV array output current variation following a 10% change in input torque, with (a) Without BESS (b) With adaptive BESS control	149
Figure 6.26: Fuel cell DC-link voltage variation following a 10% change in input torque, with (a) Without BESS (b) With adaptive BESS control	149
Figure 6.27: PMSG rotor speed variation following a 10% change in input torque, with (a) Without BESS (b) With adaptive BESS control	150
Figure 6.28: PMSG stator current variation following a 10% change in input torque, with (a) Without BESS (b) With adaptive BESS control	151
Figure 6.29: VSC DC-link voltage variation following a 10% change in input torque, with (a) Without BESS (b) With adaptive BESS control	151
Figure 6.30: Microgrid voltage variation following a 10% change in input torque, with (a) Without BESS (b) With adaptive BESS control.....	152

Figure 6.31: Real power delivered to the grid variation following a 10% change in input torque, with (a) Without BESS (b) With adaptive BESS control	152
Figure 6.32: Injected real power by the BESS controller following a 10% change in input torque	153
Figure 6.33: Injected reactive power by the BESS controller following a 10% change in input torque	154
Figure 6.34: Microgenerator speed variation when a 15% torque pulse is applied for 300 msec, (a) Without SCESS (b) With adaptive SCESS control.....	156
Figure 6.35: Microgenerator terminal voltage variation when a 15% torque pulse is applied for 300 msec, (a) Without SCESS (b) With adaptive SCESS control	156
Figure 6.36: PV array current variation when a 15% torque pulse is applied for 300 msec, (a) Without SCESS (b) With adaptive SCESS control.....	157
Figure 6.37: PV DC-link voltage variation when a 15% torque pulse is applied for 300 msec, (a) Without SCESS (b) With adaptive SCESS control.....	158
Figure 6.38: PMSG stator current variation when a 15% torque pulse is applied for 300 msec, (a) Without SCESS (b) With adaptive SCESS control.....	158
Figure 6.39: PMSG terminal voltage variation when a 15% torque pulse is applied for 300 msec, (a) Without SCESS (b) With adaptive SCESS control.....	159
Figure 6.40: Microgrid bus voltage variation when a 15% torque pulse is applied for 300 msec, (a) Without SCESS (b) With adaptive SCESS control.....	160
Figure 6.41: Real power delivered to the grid variation when a 15% torque pulse is applied for 300 msec, (a) Without SCESS (b) With adaptive SCESS control	160

Figure 6.42: Injected real power by the SCESS controller following a 15% torque pulse for 300 msec.....	161
Figure 6.43: Injected reactive power by the SCESS controller following a 15% torque pulse for 300 msec	161
Figure 6.44: Microgenerator rotor angle variation following a 10% change in input torque, (a) Without SCESS (b) With adaptive SCESS control.....	162
Figure 6.45: Microgenerator terminal voltage variation following a 10% change in input torque, (a) Without SCESS (b) With adaptive SCESS control.....	163
Figure 6.46: Fuel cell stack current variation following a 10% change in input torque, (a) Without SCESS (b) With adaptive SCESS control	164
Figure 6.47: Fuel cell DC-link voltage variation following a 10% change in input torque, (a) Without SCESS (b) With adaptive SCESS control.....	164
Figure 6.48: PMSG stator current variation following a 10% change in input torque, (a) Without SCESS (b) With adaptive SCESS control	165
Figure 6.49: Wind system terminal voltage variation following a 10% change in input torque, (a) Without SCESS (b) With adaptive SCESS control.....	166
Figure 6.50: VSC DC-link voltage variation following a 10% change in input torque, (a) Without SCESS (b) With adaptive SCESS control	166
Figure 6.51: VSC current variation following a 10% change in input torque, (a) Without SCESS (b) With adaptive SCESS control	167
Figure 6.52: Microgrid voltage variation following a 10% change in input torque, (a) Without SCESS (b) With adaptive SCESS control	168

Figure 6.53: Real power delivered to the grid variation following a 10% change in input torque, (a) Without SCESS (b) With adaptive SCESS control.....	168
Figure 6.54: Real power injected by adaptive SCESS controller following a 10% change in input torque.....	169
Figure 6.55: Reactive power injected by adaptive SCESS controller following a 10% change in input torque.....	169
Figure 6.56: Microgenerator load angle variation when a three-phase grid fault is applied for 400 msec, (a) With BESS control (b) With SCESS control	171
Figure 6.57: Microgenerator rotor speed deviation when a three-phase grid fault is applied for 400 msec, (a) With BESS control (b) With SCESS control.....	171
Figure 6.58: Microgrid voltage variation when a three-phase grid fault is applied for 400 msec, (a) With BESS control (b) With SCESS control	172
Figure 6.59: Injected real power variation when a three-phase grid fault is applied for 400 msec, (a) With BESS control (b) With SCESS control	173
Figure 6.60: Injected reactive power variation when a three-phase grid fault is applied for 400 msec, (a) With BESS control (b) With SCESS control	173

LIST OF SYMBOLS

DG	:	Distributed generation
VSC	:	Voltage source converter
PV	:	Photovoltaic system
WT	:	Wind turbine
PMSG	:	Permanent magnet synchronous generator
PCC	:	Point of common coupling
ESS	:	Energy storage system
BESS	:	Battery energy storage system
SCESS	:	Supercapacitor energy storage system
ESR	:	Equivalent series resistance
SMES	:	Superconducting magnetic energy storage
ω_0	:	Synchronous speed
P_m, P_e	:	Mechanical input and electrical output of the microalternator
M, H	:	Machine inertia coefficient and inertia constant
E_{fd}	:	D-axis field voltage of microalternator

V_g	:	Terminal voltage of the microalternator
V_{gref}	:	Reference terminal voltage of the microalternator
x_d	:	D-axis synchronous reactance
x_d'	:	D-axis transient reactance
T_{do}'	:	Open circuit field constant
K_A, T_A	:	Gain and time constant of the exciter
E_g	:	Energy gap
P_{mw}, P_{ew}	:	Mechanical input and electrical output of the wind system
H_g	:	Inertia constant of the wind generator
x_{dw}, x_{qw}	:	d and q axes PMSG reactance
E_{fdw}	:	D-axis field voltage of PMSG
K_s	:	Stiffness constant
$R_{pff}, L_{pff}, C_{pff}$:	Resistance, inductance and capacitance of the PV output filter
R_p, L_p	:	Resistance and inductance of the PV output coupling line.
$R_{wff}, L_{wff}, C_{wff}$:	Resistance, inductance and capacitance of the wind output filter
R_w, L_w	:	Resistance and inductance of the wind output coupling line.

R_s, L_s	:	Resistance and inductance of the VSC transmission line.
r_g, x_g	:	Resistance and reactance of line between microalternator and microgrid
r_b, x_b	:	Resistance and reactance of line between microgrid and main grid
g, b	:	Conductance and susceptance of the load
V_s, θ	:	Voltage magnitude and phase angle of microgrid
i_{gwd}, i_{gwq}	:	D-q axes PMSG currents
m_{pv}, ψ_{pv}	:	Modulation index and phase angle of the PV inverter
m_{wr}	:	Modulation index of the wind generator side converter
m_{wi}, ψ_{wi}	:	Modulation index and phase angle of the wind inverter

ABSTRACT

Full Name : [Mohammed Ashraf Ali]
Thesis Title : [Control of a Microgrid through Energy Storage devices using Evolutionary and Neuro-Fuzzy methods]
Major Field : [Electrical Engineering]
Date of Degree : [May,2013]

Widespread use of renewable energy sources and their integration at local distribution levels have contributed to the development of microgrids. Optimum operation of distributed generators (DG) in a microgrid is a subject of intensive research. This thesis proposes an intelligent control of energy storage system in a microgrid comprising of conventional micro generation along with photovoltaic, fuel cell and wind energy units. Detailed nonlinear and small-signal dynamic models of the microgrid are developed. The optimum generation mix from various DG sources is evaluated through eigenvalue analysis of the system. The small-signal analysis reveals that large participation of PV, fuel cell, and wind can drive the microgrid to the brink of unstable region without adequate control. Validity of the results obtained from linearized analysis has been established through nonlinear system simulations. A central energy storage based controller is proposed to supervise and enhance the microgrid operation. The energy storage devices considered are battery and supercapacitor. A voltage source inverter interfaces the storage devices to the microgrid AC bus. A decoupled control strategy has been implemented for both storage controllers facilitating real and reactive power control of the microgrid system. The optimum parameters of the decoupled P-Q controller are determined through an evolutionary bio-geography based optimization

technique. An adaptive neuro-fuzzy technique has been employed to update the controller parameters for randomly changing renewable inputs as well as to take care of arbitrary operation of the microgrid.

The adaptive neuro-fuzzy control of the storage system has been tested through a number of simulation studies. Input torque steps representing sudden changes in DG inputs show that the stability of the system may be affected depending on level of loading of the units. However, the storage units can provide the necessary space for the DG's to redistribute the power. The DG units have shown significant withstanding capabilities under low voltage condition when backed by appropriate storage control. Both battery and supercapacitor storages were observed to enhance the system transient performance. However, the supercapacitor based storage control is found to be superior to the battery system in terms of quick damping of transients with negligible rotor speed deviations, constant terminal voltage, and smooth power delivery to the grid.

ملخص الرسالة

الاسم الكامل: علي أشرف محمد

عنوان الرسالة: التحكم في الشبكات الصغيرة من خلال أجهزة تخزين الطاقة باستخدام طريقة ضوابط عصبية ذكية مطورة

التخصص: الهندسة الكهربائية

تاريخ الدرجة العلمية: نيسان , 2013

أدى انتشار استخدام مصادر الطاقة المتجددة و اندماجها في مستويات توزيع الطاقة الكهربائية الى تطور شبكات الكهرباء المصغرة، و يعتبر التشغيل الامثل للمولدات الموزعة في شبكات الكهرباء المصغرة مادة لبحث علمي مكثف، تطرح هذه الرسالة نظام تحكم ذكي في نظام تخزين الطاقة لشبكة كهرباء مصغرة تتكون من جزء توليد كهرباء تقليدي و جزء غير تقليدي يتمثل في استخدام وحدات طاقة شمسية و خلايا طاقة و وحدات لانتاج الطاقة من الرياح. تم تطوير نظم تفصيلية لا خطية للنظام الكهربائي المصغر و لديناميكية الاشارات الصغيرة في النظام. و تم تقييم نظام التوليد الكهربائي الامثل المتكون من مجموع المصادر الكهربائية المتوفرة باستخدام تحليل اقيمة الذاتية للنظام. كشف تحليل ديناميكية الاشارات الصغيرة ان الاشتراك الكبير لالواح توليد الطاقة الشمسية و خلايا الطاقة و وحدات انتاج الطاقة من الرياح قد يؤدي بالنظام الكهربائي المصغر الى عدم الاستقرار عندما لا يتم اسخدام تقنية تحكم مناسبة. و قد تم التحقق من صحة هذه النتائج باستخدام تحليل لنظام خطي تم تطويره من خلال محاكاة للنظام اللاخطي. تطرح هذه الرسالة ايضا نظام تحكم مركزي لوحدات تخزين الطاقة لتطوير و تحسين اداء اداء الشبكة الكهربائية المصغرة. و فيما يتعلق بنظام تخزين الطاقة، تم اخذ نوعين في الاعتبار هما البطاريات و المواسعات الفائقة حيث يقوم جهاز عاكس للفولتية بالتوصيل بين وحدات تخزين الطاقة التي تعمل على التيار الثابت و الشبكات الكهربائية التي تعمل على التيار المتردد. و تم تطوير و تطبيق استراتيجية مستقلة للتحكم في وحدات تخزين الطاقة التي توفر الطاقة الفعالة و المتفاعلة للنظام المصغر. و المعايير الامثل لنظام التحكم تم الحصول عليها من خلال طريقة جديدة للبحث عن افضل الحلول. تم استخدام طريقة عصبية-ضبابية متكيفة لتحديث معايير نظام التحكم حتى

تواكب التغييرات العشوائية في كميات الطاقة الصادرة عن الاجهزة المعتمدة على الطاقة المتجددة اثناء عمل النظام الكهربائي المصغر.

تم اختبار هذه الطريقة العصبية-الضبابية المتكيفة من خلال تطبيق عدة دراسات للمحاكاة. و بين استخدام التغييرات في العزم لمحاكاة التغييرات المفاجئة في الطاقة المنتجة عن مولدات الطاقة المعتمدة على الطاقة المتجددة ان استقرار النظام قد يتأثر اعتمادا على نسبة الاحمال في النظام. و مع ذلك فان وحدات تخزين الطاقة تستطيع توفير العجز في الطاقة التي يحتاجها النظام. كما أن وحدات انتاج الطاقة اللامركزية ابدت قدرات عالية على مقاومة حصول عدم استقرار في النظام في حالة انخفاض الفولتية عند استخدام وحدات تخزين طاقة مناسبة. و لوحظ ان البطاريات و المواسعات الفائقة تعمل على تحسين استقرار النظام و لكن تجدر الاشارة ان اداء المواسعات الفائقة كان افضل من اداء البطاريات من ناحية سرعة التعامل و تحييد الظروف الفجائية في النظام بدون اي فروقات تذكر في سرعة دوارات المولدات و من ناحية ثبات الفولتية المتولدة من المولدات و توصيل الطاقة السلس الى الشبكة .

ماجستير في العلوم الهندسية

جامعة الملك فهد للبترول والمعادن

الظهران, المملكة العربية السعودية

2013

CHAPTER 1

INTRODUCTION

1.1 Evolution of Distributed Generation

Traditional power generation occurs in centralized power plants, which comprise of large power stations producing the bulk amount of power utilizing fossil fuels. Electrical power generation through these traditional means pose a few limitations. Usage of conventional fossil fuels has adverse effects on the environment in terms of carbon dioxide emissions and nuclear waste problems. Transmissions networks have their associated problems of real power losses and reactive power consumption. Also, the traditional generation is vulnerable to stability issues, sometimes giving rise to energy security issues.

Owing to the rapid increase in global energy consumption and decline of fossil fuels, the development of renewable energy sources, and the interest in their local connection at the distribution level has increased [1]. Restructuring of electrical power systems is observed due to increased use of renewables in the generation of electricity. Other important factors such as environmental, economic benefits and technological developments in the distribution systems have motivated the increased use of renewable systems. In a deregulated system, the power generation, besides taking place at the power stations in large quantities, also takes place at the distribution level, with emphasis being placed on renewable energy resources like wind, fuel cells and photovoltaic (PV)

systems. These small scale generators are integrated with the utility to facilitate power transfer and supply local loads under grid contingencies. The power system involving generation at the distribution level is called Distributed Generation (DG) system [2].

Internal combustion engines, gas turbines, micro turbines, fuel cells, photovoltaic systems and wind power are the different forms of DG. Depending on the type of connection with the utility, DGs can be broadly classified into two categories. The first category of DGs includes inertial machines such as internal combustion engines and micro turbines, which use the rotating machinery. The other category of DG units requires power electronic devices, voltage source inverter (VSI) for their connection to grid [3–8]. The DGs that fall under this category include fuel cells, photovoltaic systems and wind systems etc. [9]. The use of inverters to interface the renewable energy sources are meant for flexibility in operation and control. Uncertain nature of power obtainable from inverter interfaced DGs present various problems such as the limited overload capability, absence of physical inertia, wide-band of dynamics, sensitivity to parameter variations and switching harmonics [10].

1.1.1 Microgrids

The widespread use of DG penetration and the presence of multiple DG units at distribution level have brought about the concept of the microgrid [11]. A microgrid can be defined as a portion of an electrical network, which views generation and associated loads as a subsystem [2]. In general, a microgrid can operate as a grid connected system or in an ‘island’ mode [12]. In the grid connected or non-autonomous mode, the DG unit is controlled to feed certain power into the network at an established voltage [12]. In this mode, the microgrid behaves as a controllable source or loads by either providing or

absorbing power from the main grid, depending on the generation, load mix and market policies [6]. In the islanded or autonomous mode, a group of DG units is formed to maintain the reliability of critical loads, mainly when the utility supply is not available [13]. It is also called standalone mode.

The difficulties that arise in an electrical microgrid containing renewable energy sources such as uncertain nature of power , inefficient power sharing, voltage and frequency control can be overcome by employing a central controller, which will supervise power flow among various DG units. The designed central controller must be robust to different contingencies that arise in a power system during normal or abnormal operating conditions. Energy storage device, in combination with a voltage source converter (VSC), can act as a central controller. The storage device can act a dispatchable DG source and can swiftly exchange power with the utility grid [14] . In the literature, various energy storage technologies have been proposed, that can be included in the DC side of VSC. Some of these are batteries, super capacitors, flywheels, super conducting magnetic energy storage systems (SMES) etc. Energy capacitors offer various advantages compared to other devices as they are very robust, need low maintenance, have high power density, very fast response time, and can be operational through decades [15].

The various components of a microgrid can be interfaced to the power system in either of the two ways: direct connection or connection through power electronic devices. Small micro alternators have synchronous machines operating at synchronous speed when connected with the utility. They are used mostly with reciprocating engines and gas turbines. The power electronics technology allows extracting power from renewable sources and converting electric power to fixed frequency ac power. The flexibility and

adaptability of the system has increased due to the advent of power electronics. Most renewable sources generate either in the form of DC, or other forms, which requires some power electronics devices for their interconnection with the grid.

Microgrids have the capability of benefiting the environment by reduced emissions and increased local controls, thus, enhancing the system overall operational flexibility. It is worthwhile to note the advantages of microgrids in improving the technical performance of local distribution grid as described below:

- Low capital investments and shorter construction times.
- Increased reliability of power supply during contingencies in the main grid via partial or complete islanding process.
- Intelligent scheduling of selective nearby DG units to relieve peak loading and decreasing the cost of electrical energy through active participation of renewable sources of generation.
- Local control of active and reactive power dispatch so as to have a control on voltage variations and energy security.
- Diminished line power flow causing decline in energy loss.
- Market deregulation, allowing individual players to participate in generation, and hence, creating employment opportunities.

1.1.2 Microgrid Controls

In grid autonomous or independent mode, the microgrid has no connection with utility; it has to feed total active and reactive power requirements of the load. Also the frequency and voltage magnitude are controlled by the DG units [16]. Independent operation of a

microgrid enhances the reliability of a supply system in the event of failure of the utility grid. The issues related to a microgrid operating under the autonomous mode include voltage management, frequency management, and balance between supply and demand, power quality, and communication among microgrid components [17]. With multiple DG sources in a microgrid, the design of efficient control strategy is difficult and tedious task [18].

In grid connected mode, a microgrid is interconnected with utility grid; here the utility dictates the microgrid voltage and frequency. The DG units embedded into a microgrid supply either total load or a part of it. The issues concerned with a microgrid operating in this mode include energy security, quality, reactive power support and power flow management [19]. In this mode, the microgrid performs as a controllable load, or source, by either absorbing or injecting power to the utility grid, depending on the net power difference.

When a microgrid containing multiple DG sources operate under the autonomous mode, it is difficult to design a control strategy which can facilitate efficient power sharing among the DGs [18]. However, with an interconnection to the utility grid, the frequency/voltage variation, can be reduced by balancing the power supply and demand during normal and emergency conditions.

The integration of renewable energy sources such as photovoltaic, fuel cells and wind generation systems, with the utility distribution systems, require power electronics devices. This introduces a number of challenges which needs extensive research and thorough understanding of the various concepts. Absence of physical inertia, limited real

and reactive power support, operational issues are few of the problems that have been addressed in this thesis. The main theme of this research is to enhance the transient performance of a microgrid during contingencies through appropriate real and reactive power support, so as to have efficient power sharing among various components of microgrid.

Controls in a power system generally fall into two main categories. They are mechanical based techniques, employing control equipment towards the mechanical side adjusting the torque input. In a micro turbine, the mechanical power control includes the use of sophisticated turbine governing system, which regulates the flow of input fuel. The inherent problem with the mechanical control systems is the time lag being taken to respond for a contingency. Due to the use of moving parts, the response time is larger, and hence, mechanical controls are not suitable in transient stability studies.

Photovoltaic systems and fuel cells stacks do not have any rotating machinery, and hence, no mechanical control is needed. On the other hand, in wind energy generation systems, the mechanical control includes the blade pitch control [20] and the tip speed ratio control applied at the wind turbine [21]. The aerodynamic power produced by a wind turbine can be regulated easily either through blade pitch control, or tip speed ratio. Most of the variable speed wind turbines employ pitch angle control, thus, making control through pitch an important technique in wind systems [20]. The maximum power delivered by a wind turbine to a generator can be altered by carefully controlling the pitch angle [22].

The electrical controls for wind turbines include the application of various control algorithms either at the power converters or at the load side [23]. Owing to the flexibility in the control system design, most of the research is concentrated on the electrical control of wind systems [24], [25]. More advanced and sophisticated control systems can be easily developed which can improve the system performance under disturbances and are also robust to system parameter variations.

One of the objectives of control in a microgrid is to maintain the system stability in case of contingencies. The disturbances that can normally occur in a microgrid include sudden load and generation changes leading to transients, loss of a generation source or load, faults occurring on the PCC bus. It is the duty of a control unit to restore the system back to normal operating region after the contingency. The control system developed must be robust enough to work under any abnormal operating condition.

This thesis proposes the use of intelligently controlled energy storage devices as a means of providing the additional real power support needed for a microgrid to overcome unstable regions of operation. The reactive power support can be obtained through a voltage source converter (VSC) connected at the common bus. The storage devices provide the appropriate real power backup to the microgrid under contingencies. Optimal controller parameters to provide satisfactory dynamic performance under all sorts of disturbances need to be determined.

1.1.3 Intelligent Controls

The purpose of intelligent control algorithms in modern power systems is to imitate the human abilities of learning, adapting and handling large volumes of data in order to

effectively control a complex process. The uncertain nature of power from renewable energy sources such as the photovoltaic and wind systems in a microgrid justifies the use of intelligent control techniques. On-line based and Off-line based control algorithms are the two main classifications involved in intelligent techniques. The off-line based techniques, also called search algorithms or evolutionary algorithms, work with system being disconnected from line. These algorithms are mostly population based stochastic search techniques, providing the user with optimal control settings while minimizing or maximizing a certain performance index called objective function. Simplicity, flexibility of control, robustness, and ability to provide global optimal parameters are some of the advantages while computation time, limitation to single operating condition are the demerits inherent with search techniques.

On-line based intelligent control techniques have been developed to overcome the drawbacks obtained with search algorithms, and introduce the capability of learning and adaptability for wide range of operating scenarios. Neural network, Fuzzy logic control and Neuro-Fuzzy control belong to this class. Unexpected variations in renewable energy sources such as wind speeds facilitate the use of control algorithms employing neural network [26], [27]. Neural networks emulate the human brain working process, wherein it has many interconnected components called neurons capable of processing information when activated through an activation function. Such networks are highly complex, model free systems, and have adaptive learning ability. The only disadvantage with these networks is the non-inclusion of transients in the model.

Fuzzy-logic control on the other hand offers the flexibility of introducing uncertainty with the variables but require a huge knowledge base derived either from

experience of an operator [28], [29]. Fuzzy logic control includes the use of linguistic variables instead of numbers, and membership functions governed through a set of linguistic rules in order to derive an output [30].

Adaptive Neuro-Fuzzy inference systems (ANFIS) combine the advantages of both neural networks and fuzzy logic [31], [32]. ANFIS derives the adaptive learning capability under wide range of operating conditions from the neural network and the uncertainty involved in the control variables from the fuzzy systems. Also there is no requirement of knowledge base as opposed to fuzzy logic control. Heuristic techniques like genetic algorithm, particle swarm optimization, differential evolution etc., [33], [34] are often used to obtain the training data required for ANFIS systems. Learning from the trained data and applying it to actual scenarios are the functions described for ANFIS systems. The membership functions inherent in the fuzzy system are normally determined from a huge amount of data presented to the ANFIS network. Application of the ANFIS network to physical systems online requires adaptation of the membership functions depending on the data presented.

1.2 Thesis Motivation

In an electrical microgrid, the DG sources requiring the use of power electronic converters pose many operational and stability problems. Since the microgrid contain synchronous sources, maintenance of rotor angle stability and voltage stability are very important. It is required to keep the voltage at the point of common coupling (PCC) within acceptable limits during normal conditions as well as during contingencies. Large penetration of power from renewable sources may affect the voltage at PCC as well as

the rotor angle stability. Other problems that arise due to integration of renewables include generation of switching harmonics, voltage and frequency variations in the microgrid which may deteriorate the stable operation.

External real and reactive power support is needed for a microgrid in order to mitigate these voltage and rotor angle instability problems. Thus, there is a need to search for devices which could provide an appropriate power backup during transients. Energy storage devices such as battery and super capacitor connected through a voltage source converter (VSC) can function as central managerial controller to coordinate power flow among various DG units. Design of a control system for these devices is generally a complicated task, as separate control over real and reactive power extraction is desirable. Decoupled control strategy could be well suited for such an application. P-Q decoupled controller parameters are to be found using an adaptive intelligent control for satisfactory system operation assuring efficient power sharing among DG sources under different contingencies. Online tuning of the controller parameters through adaptive based control algorithms is required to take into account the uncertain nature of renewable power and for arbitrary operation of the microgrid. In this work, the controller parameters are obtained through adaptive neuro-fuzzy based method.

1.3 Thesis Objectives

This thesis proposes to study the influence of incorporation of the energy storage devices in performance enhancement of a microgrid. The energy storage devices proposed to be considered are battery and super capacitors, which are interfaced through voltage source converter.

Main objectives of the thesis are as follows:

1. To develop a non-linear and small-signal dynamic model of a microgrid containing conventional micro generation along with renewable sources that include photovoltaic, wind generation and fuel cell systems.
2. To identify the penetration limits of power obtainable from renewables so as to have satisfactory steady state and transient operation of the microgrid.
3. To study the behavior of VSC operated battery storage device and VSC operated super capacitor device as a central controller for a grid connected microgrid.
4. To design a non-linear P-Q decoupled controller for the above storage devices by utilizing current and power controllers.
5. Determining the optimal controller settings using an intelligent Bio-geography Based Optimization (BBO) search technique.
6. Implementation of an adaptive neuro-fuzzy network for the P-Q decoupled battery storage and P-Q decoupled supercapacitor storage.
7. To evaluate the controller performance through simulation studies incorporating various contingencies.

1.4 Thesis Contributions

The main contributions of the thesis are as follows:

- Derivation of mathematical description of an electrical microgrid with renewable energy sources such as photovoltaic, wind energy system and fuel cell system.
- Studying the impact of integration of renewables to the electrical grid through linearized system models.

- Incorporation of electrical energy storage devices such as batteries and super-capacitors for real power support along with a voltage source converter for reactive power support.
- Design of nonlinear P-Q decoupled control algorithm which would provide swift exchange of real and reactive power with the microgrid.
- Optimization of decoupled control parameters through intelligent BBO search method and implementation of adaptive neuro-fuzzy network for the controller.
- Performance evaluation of intelligent battery and supercapacitor based decoupled controllers in enhancing transient stability boundaries.

1.5 Thesis Organization

The thesis is organized in a total of 7 chapters. The contents of each of these chapters are illustrated below:

- Chapter 1 introduces the thesis work, and gives a brief description of various important terminologies. The thesis motivation and research objectives are stated.
- Chapter 2 presents a detailed literature review. Descriptions of various components of a microgrid configuration are explained in detail and the related issues are also presented. It also includes recent literature review of hybrid microgrid models, the various problems encountered along with their solutions. It also gives a detailed description of various processes involved in the bio-geography based search technique.

- Chapter 3 develops the detailed modeling of various system components in a microgrid system. Dynamic nonlinear and small-signal linearized model of photovoltaic systems, fuel cell systems, and wind energy systems in addition to microgenerator are derived. The models of various power electronic devices that are to be used for integration of renewables have also been established.
- Chapter 4 presents the performance evaluation of the composite microgrid model developed in chapter 3 through small-signals and non-linear analysis in order to identify the suitable generation mix from various distributed sources for reliable and satisfactory steady operation of microgrid.
- Dynamic models of the battery and supercapacitor storage central controllers are developed in chapter 5. The P-Q decoupled control strategy is established for the storage devices with an emphasis being laid on intelligent tuning of controller settings.
- The evaluation of proposed neuro-fuzzy based central decoupled control system for battery and supercapacitor based storage under various contingencies is presented in chapter 6. Also comparison among the two controllers is established for a low voltage criterion at the grid bus.
- Chapter 7 concludes the salient findings of the work and also highlights the scope for further research.

CHAPTER 2

LITERATURE SURVEY

2.1 Introduction

This chapter summarizes some of the salient studies performed on the analysis of electrical microgrid systems employed in modern power industry. The studies involve the dynamic performance enhancement and power system stabilization with microgrids. Different aspects of modeling a microgrid system and type of simulations as reported in literature have been reviewed. In general, the literature survey has been decomposed into three sections.

The first section deals with the recent studies performed on the individual components of a microgrid system such as photovoltaic system, fuel cell system and the hybrid microgrid model. The various issues involved in a microgrid architecture right from modeling till the operation and control are discussed in the second section. This section is mostly concerned with the evaluation of dynamic performance and the solution techniques proposed in literature. The last section focuses on the several control algorithms and approaches that can be employed in enhancing the transient stability of a microgrid. It reviews the several control techniques that have been reported in improving the performance of a microgrid. Towards the end of the chapter an intelligent search technique called biogeography based optimization is discussed in detail.

2.2 Microgrid Components

An electrical microgrid can be viewed as a subsystem with its associated loads and generation units operating either autonomously or in connection with main utility grid. It has several DG units producing electrical power operating in synchronism with each other in order to supply local load or deliver power over the tie line. They are treated as small distribution systems that connect multiple customers to multiple distributed sources of generation and storage interfacing through power electronic converters [35].

A microgrid in general, has two main types of DG units, inertial or rotating type DG units and stationary or inverter type DG units which require power electronic converters for their connection to the main grid [36]. Under the category of inertial DG units, the most commonly used are micro alternator, gas turbines, internal combustion engines etc. The photovoltaic systems, fuel cell systems and wind generation systems require power electronic devices for integration and hence they fall under the category of inverter type DGs. In this work we review the most commonly used technologies for DGs i.e., the wind generation, fuel cell and photovoltaic systems. The small scale power production units employed in electrical microgrids are usually in the range of 4kW-10MW [37].

2.2.1 Photovoltaic system

The method of extracting energy from the Sun dates back to hundreds of centuries. Mankind has learnt to make use of solar radiations in a variety of applications. Based on the photoelectric effect, incident radiation of solar energy can be directly converted into electricity by a method called photovoltaic. Electrical charges are produced in a solar cell

when the incident photon energy is sufficient enough to break the covalent bond of the semiconductor material [38]. Owing to the generation of charges an internal electric field is observed which results in separation of oppositely charged carriers. Photocurrent flows due to the motion of these charge carriers. Several solar cells connected in various configurations such as series-parallel arrangement constitute a solar array or a solar module. The obtainable power output from a PV module usually depends upon the number of cells and their arrangement.

A PV cell essentially exhibits non-linear characteristics, as it can be imagined as a combination of a current source in parallel with an ideal diode [38]. A practical PV cell is the one that incorporates series and parallel resistances to account for voltage drop in the device and shunt current loss. Determination of various parameters of a solar cell is an important task in order to understand the behavior of the device and also to model the system with high accuracy [39].

In literature, several PV electrical models have been proposed by researchers considering the simple idealized model or detailed cell model replicating the actual physics behind the solar cell. Some of these models are inefficient and some of them are complex for simple power system applications such as load flow, transient stability studies, economic operations etc. [40]. The PV cell circuit descriptions reported can be classified into four categories. The first category of modeling requires the temperature coefficient of maximum power and it is able to predict the power at only one point [41]. The other category of PV model is obtained through bilinear interpolation of I-V curves [42] provided by the manufacturer, which will be useful in determining the characteristics of the device at any operating condition. This method requires four I-V curves at varying

irradiance and for two difference temperatures which are not usually possible. The experimental method of obtaining the PV model has also been proposed by few researchers [43] but such a method requires extensive experiments to be done to determine the characteristics at five discrete operating points. Owing to their complexity, such types of models are seldom used. The electrical circuit model of a PV cell [44] [37], obtained through the data sheets provided by manufacturer has gained popularity due to its simplicity and ease of obtaining characteristics at any operating region. In this work the PV cell circuit components are determined from the data sheets provided. BPSX-150 solar module manufactured by the BP Solar Corporation is considered [45].

The comprehensive PV model designed using power electronic components has been the center of focus, received more attention from many researchers and hence many studies report the application of such type of model [46–49]. Detailed dynamic model of a PV system explains the behavior and associated control circuitry very well but they are seldom employed for microgrid studies due to their computational complexity. Description of a PV module either as constant real power generation [50] or constant negative real power loads [51] has also been noticed. Such simplifications of PV model are not applicable for transient stability studies and are mostly employed in steady-state analysis.

T. Yun in [52] designed a PV transient model in order to conform with the practical data obtained from a specified PV module having a voltage source converter controlled through a modulation technique. The control action was obtained through derivation of mathematical relations which showed the independency of model equations upon the actual PV system. A simplified model of PV system was developed by National

Renewable Energy Laboratory (NREL), where the PV system has been modeled as controlled current source [53] considering the current magnitude and phase angle into account. Neglecting the transients in the PV module, the control algorithms were established at the DC side. A controlled voltage source model has been proposed for a simplified PV system in [46] was found to be more accurate than the current controlled model. Representation of PV system as a voltage source preserves system signals and hence it is easier to employ control techniques. There are no studies which demonstrate the use of voltage source model of PV system in microgrid dynamic stability.

Reference [54] proposes the development of a PV based stabilizer system in order to enhance the dynamic stability of a distribution network. No control loops were noticed in the model. Detailed and simplified dynamic model of PV generation system has been published in [55] which are then integrated with the power system network. The transient stability studies were established considering the model as a non-dispatchable source rendering its use in microgrid.

The problems encountered due to extensive integration of PV systems into local power grids include generation of unwanted voltage and current harmonics, voltage variations in distribution feeders, flickers and stresses on distribution transformer. On a sunny day, due to huge power penetration from the PV system, it has noticed that the voltage at the common bus rise leading to further problems. Thus it is necessary to study the effects of PV power penetration and discuss the solutions that would mitigate such problems.

The summary of the various technical problems incurred with the interconnection of PV systems was mentioned in [56]. It has been shown by the author that the transient stability of a power system worsens with the amplified power penetration from DG units. Oscillatory stability of the power system is observed to be affected with the integration of DGs. A comprehensive study on the benefits and interconnection issues of PV systems was found in [57]. The authors provided solutions to the mentioned problems by making reference to the “IEEE Std. 929, Recommended Practice for Utility Interface of Photovoltaic Systems.”

It is observed that the harmonic content varies proportionally with the power penetration from photovoltaic system. The increased reactive power requirements, voltage flicker, over current and anti-islanding were some of the technical issues reported due to large participation of renewable sources. Power electronic inverter circuitry employed for interfacing PV systems pose many operational and power quality problems as reported in [58]. The authors have studied the effect of inverters upon the power quality issues by considering different inverter circuit topologies and different network configurations. It is also seen that various control strategies were developed in order to minimize the power distortions. Simulation results were then validated through experimental recordings.

The power harmonic problems being analyzed through a new technique called impedance based harmonic analysis is observed in [59] . The authors have reported that the quasi-resonance problem that arise due to the effective inverter impedance and grid impedance can be overcome by employing a dual loop control action possible with proportional integral (PI) and proportional resonant (PR) controllers.

Practical case studies demonstrating the impact of 100kW PV system on a power system network in Austria has been noticed in [60]. In this study the various power quality terminologies such as voltage swell, flicker and harmonic content were measured and compared with the EN50160 standard.

Power system protective devices are also affected with the participation of power from PV units. In reference [61] the effect of PV power penetration upon the system protection equipment was discussed. Various protective coordination concepts such as fuse to fuse relay to relay and relay to circuit breaker were mentioned. The underutilization of protective margin of various devices was also shown.

The electrical losses that occur in a power system network due to voltage rise at PCC were noted in [62]. Various factors found to be responsible for grid voltage rise such as light loads; increased PV penetration and harmonic content were pointed out. The authors also proposed a control strategy based on inverter switching in order to mimic the rise in voltage at the grid.

2.2.2 Fuel cell system

Electrochemical devices which convert the chemical energy of a fuel directly into electricity are called fuel cells. They are characterized by high energy efficiency, low pollutant emissions, and has an unlimited supply of fuel [63], [64]. Efficiency and environmental benefits that are need of this current global energy industry can be easily met with fuel cells and also now they are into the process of commercialization [65]. The development in fuel cells was mostly due to advancements in the automotive industry,

because fuel cells can replace fossil fuels and provide environmentally propulsion forces [66].

Models found in literature for fuel cells are mostly steady state type and are typically used for component sizing, cumulative fuel consumption or hybridization studies. The various components such as compressor, heat exchanger and fuel cell stack voltage as a static performance or efficiency map are represented by these models [67]. When fuel cells are used for power generation they are basically low voltage, high current electrical generators and hence power electronic devices must be used in order to convert the low voltage to a considerable level. This will introduce step currents and other dynamics in the output of a fuel cell, which cannot modeled by the steady state models reported in [68–70].

Transient models of generic fuel cells have been described in [69] wherein they take into account temperature changes. These models have limitations or requiring extensive temperature measurements. Recently owing to development of high performance computing and advanced numerical algorithms helped researchers to develop PEM fuel cell systems as individual components with higher accuracy. A complete mathematical model of PEM fuel cell systems has been described in [71] where the model explains the physical complex phenomena of the system.

In reference [72] a new approach of fuel cell modeling has been reported, wherein the fuel cell model is obtained from data from fuel cells datasheets which are provided by stack manufacturers and are publicly available. The model described is a generic model combining the properties of electrical and chemical models. Two different models have

been proposed detailed model and the simplified model. The second type models a fuel cell stack by a controlled voltage source in series with a constant resistance. It can be used to depict fuel cell stacks operating at nominal temperature and pressure. The detailed model describes behavior of a particular fuel cell stack when the parameters such as pressures, temperature, compositions and flow rates of fuel and air vary. These variations will affect the performance of a fuel cell system. In this case the model is similar to the simplified model except the parameters are updated based on the input pressures and flow rates.

2.2.3 Wind energy system

Since 1990 there has been rapid growth and technological development seen in the wind power conversion technology. Owing to abundance availability of winds all over the globe, the wind power generation market has developed into a highly competitive environment. Wind machines generally fall into two categories the fixed speed type and the variable speed turbines. Fixed speed machines are usually composed of self-excited induction generators with either two pole pairs or rotor resistance controlled type. They operate at a constant speed irrespective of variations in wind energy. On the other hand, the variable speed wind systems include grid connected wind turbines and generator coupled through modern power electronic circuitry extracting maximum output from wind. They can be either wound rotor machines or permanent magnet synchronous generator or externally magnetized synchronous generator [73].

The Fixed speed wind turbine concept

Most of the wind turbines operating during 1990's were found to be fixed rotor speed with no influence from wind speed variations [74]. Induction generators of wound rotor type operating in the asynchronous mode have very little variation in rotor speed and hence can be considered fixed speed machines. Wind generators connected to power grids operate at a speed defined by the nominal frequency of the utility grid. For varying wind speeds, constant rotor speed operation is established through gear ratio and special design of the generator [75]. The squirrel cage induction generator driven through a wind turbine is generally used as constant speed wind generation system, where in an external capacitor bank reduces the reactive power demand and compensates for no-load current of the generator. Robustness, ease of operation, lesser maintenance and relatively lower cost promotes the use of squirrel cage machines. But the demerits of such machines appears in the form of electromagnetic torque oscillations for wind speed variations, causing mechanical stresses and fatigue on the system.

Modeling and short circuit analysis of a fixed speed wind turbine operating in grid connected mode is observed in [76] [77]. The fault is applied at the proximity to wind turbine generator and the effect of operating electrical and mechanical parameters upon the critical clearing time are recorded. The wind speed, the power output, the short-circuit capacity of PCC bus, the reactive power compensation , the hub-generator resonant frequency, the rotor inertia and the fault location are some of the parameters mentioned by the authors in [77].

Reference [78] proposes dynamic models of fixed speed wind farms developed by a new concept involving equivalent wind turbine obtained through cumulative accumulation. Here in this work the researchers have designed two different configurations of equivalent model. The first model operates for identical winds while the other model can operate with variable incoming winds.

Reduced third order equivalent model and comprehensive dynamic model of wind systems driven through fixed speed wind turbines are presented in [79]. Transient stability and fault ride through capability were examined in the article.

Stability enhancement of a fixed speed induction generator by employing STATCOM is noticed in [80]. The effect of fault location and varying fault durations upon the system dynamic stability is investigated and by the application of shunt facts controller the stability boundaries were improved.

The Variable speed wind turbine concept

Optimal tip-speed ratio or blade pitch angle control defines the operation strategy of a variable speed wind turbine, which make it to run at a certain speed relative to the current wind speed, to extract maximum power from wind energy [74]. Adaptive control of wind turbine parameters such as blade angle or gear ratio control, the energy captured can be increased corresponding to the wind speed [20].

Use of variable speed turbines in wind energy generation systems has inherent benefits such as reduced mechanical stresses, diminished torque oscillations, efficient operation and highest aerodynamic efficiency. Direct AC to AC conversion accomplished through cyclo-converters or voltage source inverters (AC-DC-AC) are the two well-

known concepts utilized by modern wind generators employing variable speed machines. Elimination of gear box, advancement in power electronics technology, higher efficiency and effective speed control are some of the factors that motivates the use of direct driven permanent magnet synchronous generator (PMSG) with a full scale converter. The converter operating near the generator controls the electromagnetic torque while the grid side converter regulates the dc bus voltage and the power fed into the grid. Well-designed control strategy will guarantee safer and reliable operation of wind turbine generating system (WTGS) even during grid contingencies.

Reference [81] develops a dynamic model of a variable speed wind turbine running a PMSG machine with pitch angle and stability control strategies. The drive train system is depicted through a single mass model to demonstrate the generator mechanical characteristics. Pitch angle control for wind turbine and speed control block for PMSG were the two significant achievements reported in the work.

The authors in [82] have developed a comprehensive model and optimum control strategies of a variable speed wind generator system. Comparisons are made between the various models in terms of gain in energy obtained and also a new technique is established to extract the maximum energy from the system. Dynamic stability studies of a power system network involving wind farms with optimal tuning of rotor side converter controller parameters for DFIG system is noticed in [83]. The authors considered both the stator and rotor side dynamics in the design of controller.

2.3 Microgrid Architecture

Due to availability of renewable sources at local levels, the presence of small scale generation units and their connection with distribution networks has been on the rise since few years. The extensive use of distributed generation enhances the reliability of a power system network while benefiting the utilities economically. These reasons have led a path for the development of electrical microgrids. An electrical microgrid appears either as a single source or load depending on the net generation at common bus. The authors in [84], [85] have demonstrated that an electrical microgrid working in parallel with the main utility grid affects the system voltage, line current, power quality, protection and network reliability. The effect is dependent on the location and capacity of PCC bus and load characteristics of microgrid.

Calculation of optimal sizing of a PV array in a PV/wind hybrid microgrid system is established in [86] to extract power from renewable sources more efficiently and economically. The use of energy storage systems in order to compensate for power variations from renewable sources under changing conditions for an islanded microgrid formed with PV/wind system is reported in [87]. The limitation of this study is that the capacity of storage system is very low and limited to 240 W.

T. Tadokoro [88] presented an autonomous microgrid system with generations from PV-diesel system for a small island. The hybrid system is considered to be composed of 300kW diesel power and 750kW PV power feeding private houses in the island located far away from the utility grid. The work appears to be feasible with limitations that the control strategies and MPPT techniques are not considered.

A 500W hybrid generation system composed of PV and fuel cell connecting the main grid is observed in [89]. The authors successfully designed a controller based on the uninterrupted power generation concept. MPPT controllers for both PV and wind energy systems were noticed in a small scale hybrid PV/wind system proposed in [90]. The environmental conditions like irradiance and wind speed were not taken into account while designing the controller and also the concept of energy storage and transient stability are not addressed.

A microgrid system with generation from inertial machine (a synchronous generator with exciter and governor systems) and electronically coupled DG sources is seen in [91]. Inclusion of sub synchronous range into the dynamic model is an achievement made by the author by incorporating the transients of transmission lines and filters. Many configurations of microgrids are found in the literature viz., AC microgrids, DC microgrids and AC/DC microgrids. The loads can be directly fed from DC generation units without the need of any converter system in a DC microgrid whereas AC microgrids require extensive use of power electronic converters to obtain AC output. The authors in [92] published hybrid AC/DC microgrid in order to minimize the energy losses that are noted in AC-DC-AC conversion process.

2.4 Issues Reported in Microgrids

Several factors are responsible for abnormalities in the operation of microgrids under both the autonomous and grid connected mode. Disturbances, overloading of DGs, generation of switching harmonics, power quality issues, are some of the problems encountered in microgrids due to the presence of electronically coupled DG sources.

Owing to these issues the safe operation and meeting the load demand under off grid mode is extremely challenging task requiring extensive control system to be incorporated. Unlike conventional power generation systems, no frequency response is seen in microgrids as a result of load changes or generation change due to absence of rotational parts. But the frequency response or droop characteristics can be obtained by controlling the interfacing inverter to emulate the synchronous alternator. In this manner, the power sharing mechanism can be established in microgrids with generations from electronically coupled sources [93].

Power electronic switches present in the inverter circuits of microgrids work on modulation techniques require switching frequencies for their operation. These presences of these frequencies and voltage distortions in main grid constitute for poor power quality. Incorporation of well-designed filter can minimize the power quality problems but require supplementary control loops. In [94], the authors reported a filter circuit for a three phase inverter, incorporating an isolation transformer and supplementary controllers to achieve good power quality while rejecting grid side disturbances.

Multiple distributed power inverters pertaining to various sources in a microgrid system, operating in a distribution network introduce critical power quality issues and grid stability problems. In [95], the simulations and practical experiments investigate the harmonic interactions with various inverter circuit topologies and control techniques. The authors have reported that the series and parallel resonance between the network and inverters constitute the power quality problems.

Eigen value based stability analysis for a small-signal microgrid model is noticed in [96]. The authors have considered constant power loads and carried out sensitivity analysis in order to enhance the dynamic stability by regulating the voltage and current controller parameters. Small signal stability analysis of a microgrid through two-point estimate based method incorporating various uncertainties is reported in [97].

2.5 Dynamic Performance Enhancement

In an electrical microgrid involving renewable sources as generation units, the power output is very uncertain and extremely capricious. As the power participation from renewables is increased there arise several problems which disturb the system stability and give rise to critical issues. Also it is noticed during a short-circuit fault on a micro source, the mechanical input torque remains the same whereas the output electrical power and electromechanical torque are reduced due to diminishing terminal voltage. Owing to excess mechanical input, the turbine and generator accelerate and absorb more reactive power from the system, thus hindering the terminal voltage recovery. To enhance the dynamic performance under such phenomena several techniques have been proposed in literature focusing on voltage recovery and speed control.

2.5.1 Conventional methods

As mentioned earlier, during contingencies the micro sources require additional reactive power support in order to overcome the voltage collapse and maintain stability. In the literature, various FACTS devices were seen to provide reactive power support needed during faults [98–100]. Most of the research points out that SVC and STATCOM [101] as the potential candidates that would supply reactive power during contingencies.

Additional controllers designed using various techniques such as genetic algorithms [102], PI control [103] [104], fuzzy-logic based control [105] and minimum susceptance control [106] were noticed to be operating along with STATCOM.

Mechanical control methods such as changing the gear ratio of wind generation systems in a microgrid to spill part of extracted mechanical power and consequently improving system stability has been proposed in [107] . Active power during fault controlled through a braking resistor in order to ride fault is observed in [108] . Both electrical and mechanical control techniques operating in co-ordination in order to overcome transients for a wind generation system is seen in [109].

For a wind generator modeled through an induction generator the method of rotor resistance control is found to be an effective means of enhancing dynamic stability. During transients the control of rotor resistance will present a higher electromagnetic torque thus reduces the system acceleration and aids in system voltage recovery. Dynamic slip control and pitch control are the other methods reported in literature to achieve the same objective [110].

2.5.2 Bulk energy storage systems (ESS)

Energy storage devices employed along with STATCOM have the capability of providing both real and reactive power support and have emerged as most promising devices for power system applications [111]. These devices can act as central controllers for a microgrid with uncertain generation sources providing the necessary real and reactive power provision when needed.

In literature we find various types of energy storage devices being reported. Of all the storage technologies four are most commonly used, which are: battery technology, flywheel, superconducting magnetic storage systems (SMES) and super capacitors. These devices perform the same task, differing in the manner in which energy is stored, consequently their modeling and control techniques differ significantly. When choosing a particular storage technology or device there are various factors which are need to be considered such as size, rating, speed of energy exchange and cost. The characteristics of different storage technologies are being reported in reference [112].

Table 2.1 shows these devices along with their properties. From the table, it is evitable that for short-term storage requirement applications such as for dynamic performance enhancements, the most promising technologies are flywheels and super capacitors. They both offer similar characteristics and are both suitable for transient applications. But the flywheels are physically large and involve numerous safety and maintenance issues. Hence, very few publications have been reported on flywheels. The other storage technologies based on chemical storage includes battery systems [113] have considerable large response time and hence they are not preferred for short storage applications. These devices can be used along with PV systems for storing electrical energy during excess and then discharging when there is less generation. Such techniques have been extensively reported in literature along with photovoltaic systems.

Reference [114] demonstrates the use of STATCOM with battery energy storage system (BESS) for wind power applications where in the storage device is used to level the power fluctuations by charging and discharging operation. It is also being reported that during voltage sag or fault the BESS unit has the capability of boosting the stability

margin by absorbing active power from the wind farm. Reference [115] suggests the use of braking resistor along with BESS for enhancing the transient stability margin. Energy capacitor storage method for restoring voltage stability of a power system is observed in [116].

The various principles of super capacitor based energy storage system along with their structure, characteristics and performance is studied in [117] for microgrid applications. Dynamic support system through super capacitor for hybrid microgrids in order to facilitate transition between the operating modes (grid connected/ islanded mode) is depicted in [118]. The hardware components of the microgrid system were also developed.

Table 2.1: Summary of short-term energy storage system characteristics

Technology	Energy Equations	Energy Cost (\$/kWh/year)	Power Cost (\$/kW/year)	Storage Time	Round Trip Efficiency
Lead Acid Battery	$E(t) = E_0 + \int v(t)i(t)dt$	69	91	60-300 min	63 %
Super Capacitors	$E(t) = \frac{1}{2} C V_{sc}^2$	711	6	0.006-6 min	86 %
SMES	$E(t) = \frac{1}{2} L_{smes} I_{smes}^2$	370,000	59	0.006-6 min	21 %
Flywheel	$E(t) = \frac{1}{2} J\omega^2$	96	1.2	0.006-6 min	89 %

In references [15], [119], [120] the applications of super capacitor based energy storage for transient stability enhancement is very well established. Battery super capacitor hybrid storage systems for microgrid application are demonstrated in [121]. The storage unit is included with batteries (124V, 10 batteries) and super capacitor module (20F, 324V), buck-boost DC-DC converter and a voltage source inverter. The authors successfully designed control strategies in order to mitigate transient powers from renewable sources while achieving optimized storage.

2.6 Bio-geography based Optimization

2.6.1 Overview

Learning from the nature has motivated the developments of algorithms which simulates the natural processes and effectively utilize them to engineering optimization problems related to any field. Genetic algorithm, particle swarm optimization, differential evolution, simulated annealing, tabu search, bio-geography based optimization, evolutionary programming etc., are some of the heuristic techniques that constitute intelligent control. These algorithms are simple search procedures, guided through a fitness function, which can be either maximized or minimized to yield optimal results. The simplicity, robustness, lower computational burden, efficient utilization of memory, faster convergence and lower computational effort are some of the features desirable for an optimization algorithm. The bio-geography based optimization provides many advantages such as simple operating procedure, efficient performance, capability of providing global solutions, faster convergence rate, no premature convergence, applicability to non-linear and non-differentiable optimization problems, and, robustness

to parameter variations. The merits offered by BBO makes it competitive with other population based optimization techniques.

The BBO is an inhabitants based stochastic operated evolutionary search algorithm for multimodal global optimization developed by Dan Simon [122], simulating the biogeography of nearby habitats and how they interact with each other. Robert MacArthur and Edward Wilson in their publication, “The Theory of Island Biogeography”, [123] proposed the mathematical models of biogeography in terms of species count and their topographical distribution. The fundamental principles of island biogeography govern the operating processes of BBO[122]. Richness of isolated natural communities in terms of species distribution underlines the field of biogeography. As stated in reference [124], various ecological and geographical factors such as rainfall, vegetation diversity, diversity of topographical features, land area, temperature etc., affect the species distribution in a habitat. An island or habitat denotes, “the ecological area that is inhabited by particular plant or animal species and geographically isolated from other habitats”. Each habitat represents a candidate solution to the optimization problem. The richness of a habitat is determined by a factor called Habitat Suitability Index (HSI). In BBO, the island or habitat are denoted through Suitability Index Variables (SIV), denoting solution features being represented through real numbers. The problem dimension decides the number of SIV decision variables as shown below.

$$\text{Habitat } H = [SIV_1 \quad SIV_2 \quad SIV_3 \quad \dots \quad SIV_{nd}] \quad (2.1)$$

The fitness measure of habitats is evaluated in terms of HSI which is given by.

$$HSI = f(\text{Habitat}) = f(SIV_1 \quad SIV_2 \quad SIV_3 \quad \dots \quad SIV_{nd}) \quad (2.2)$$

The mutation, migration and elitism among various habitats or islands constitute the numerous processes encountered in the field of biogeography. The probabilistic control operations on the various habitats through migration and mutation processes underline the main idea of searching. Each of these processes is discussed in the subsequent sections.

2.6.2 Elitism of species

Similar to other evolutionary population based algorithms, a pre specified p number of habitats that have high suitability indices are passed through next generations without perturbing through migration or mutation processes.

2.6.3 Migration of species

In the field of biogeography, the species distribution among habitats or islands is not fixed and is dependent on the habitat suitability to host several species. Large species count are found in habitats with high HSI index values, while small species count are found with those habitats having low HSI. Thus, the species distribution is not uniform and hence there is a possibility of species population traversing across the habitats. Migration process defines the movement of species across various habitats in a population. Emigration and Immigration are the two basic sub processes that are found to occur frequently in a group of habitats.

Emigration process is defined as the tendency of species to relocate from highly dense islands to less populated habitats, while the immigration process corresponds to import of species to a habitat. The habitats rich in species count have high emigration rate μ , thus allowing species to migrate to other nearby islands. Thus in other words, such

habitats are found to densely populate with large number of species and have very low immigration rate λ . On the other side, the habitats sparse in species have low HSI indices which would characterize them by high immigration rate λ and low emigration rate μ . Dynamic behavior is noticed in the islands that have low HSI indices in their distribution of species than for high HSI habitats [122]. Assumption of linear relationships among islands HSI, its emigration and immigration rate would simplify the search procedure. The rates of immigration and emigration are assumed to be constant for all the islands in a population and are found to be function of species count in the habitats.

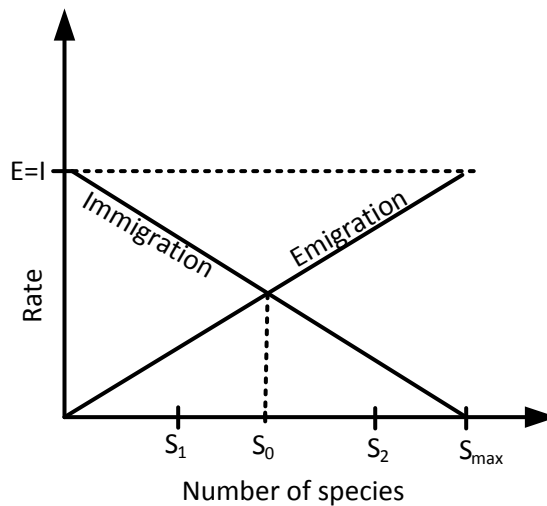


Figure 2.1: Emigration and Immigration rate model in BBO

The relationship between various migration factors like habitat fitness (species count), emigration rate μ and immigration rate λ is shown in Figure 2.1. The maximum possible emigration and immigration rates are denoted by E and I respectively. The species count in terms of number of species present in a habitat is denoted by S measured in terms of fitness criterion HSI. Equal immigration and emigration rates are observed at the equilibrium point S_0 while S_{max} denotes the maximum species count a habitat can

support. Excellent habitat performance in terms of high emigration rate and low immigration rate can be noticed at S_2 , while poor performance is seen at S_1 , due to low emigration rate and high immigration rate.

The emigration rate λ_i and immigration rate μ_i for each of the habitats is determined after evaluation of the fitness or suitability index through the following relations:

$$\lambda_i = I \left(\frac{1-n_i}{m} \right) \text{ and } \mu_i = E \left(\frac{n_i}{m} \right) \quad (2.3)$$

Here n_i denotes the number of species in i^{th} habitat determined in terms of suitability indices and m corresponds to the maximum m number of species or the population size. Larger values of n_i determines the quality of habitats, as higher suitability indices tend to generate large values for n_i .

Sharing of attributes among various habitats utilizing the immigration and emigration rates of each population member is generally accomplished through a probabilistic model. The probability of a habitat that contains exactly S species at time t is denoted by P_S . Defining a probability of species modification P_{mod} , the decision to perturb a given solution is taken based on other members. After selection of a habitat in a population, the decision to modify the solution utilizing the migration process is taken probabilistically based on the immigration and emigration rates. For a given habitat, if immigration operation is required to be performed, then the immigrating island is selected probabilistically based on the normalized immigration rate.

The probability of species containing exactly S species is computed using the relation:

$$\frac{dP_S}{dt} = \begin{cases} -(\lambda_i + \mu_i)P_S + \mu_{i+1}P_{S+1} & S = 0 \\ -(\lambda_i + \mu_i)P_S + \mu_{i+1}P_{S+1} + \lambda_{i-1}P_{S-1} & 1 \leq S \leq S_{max} - 1 \\ -(\lambda_i + \mu_i)P_S + \lambda_{i-1}P_{S-1} & S = S_{max} \end{cases} \quad (2.4)$$

The migration process in BBO simulates the recombination approach involved in genetic algorithms, where in offspring are obtained through combination of many parent solutions. In genetic algorithms such processes would produce new solutions, while the BBO migration modifies the existing solutions without generating new ones.

The pseudo code for the migration procedure is described as under [122],

Select a habitat H_i with probability $\propto \lambda_i$

If H_i is selected

For $j=1$ to n

Select a habitat H_j with probability $\propto \mu_i$

If H_j is selected

Randomly select an SIV σ from H_j

Replace a random SIV in H_i with σ

End

End

End

2.6.4 Mutation of species

The suitability indices of habitats can change abruptly due to various cataclysmic events such as natural catastrophes, disease etc. To incorporate such events in the simulation process of BBO, the mutation operation is defined, which enhances the biological diversity among the population. The probabilities of species count of islands determine

the mutation rates of various habitats [125]. Improved solutions in the later stage of search process are obtained through mutation among solution members having low values of species count probabilities with habitats of higher suitability indices, thus enriching the ecological diversity while avoiding the dominance.

The rate of mutation mt expressed in terms of the solution species count probability P_i as given by:

$$mt = m_{max} * \left(\frac{1 - P_i}{P_{max}} \right) \quad (2.5)$$

Here m_{max} is a user defined parameter while P_{max} denotes the maximum species count probability.

The pseudo code for the mutation process is described as under [122] ,

For j=1 to m

Probability P_i calculated from λ_i and μ_i

Select SIV $H_i(j)$ with probability $\propto P_i$

If $H_i(j)$ is selected

Replace $H_i(j)$ with a randomly generated SIV

End

End

CHAPTER 3

MICROGRID SYSTEM MODELING

3.1 Introduction

This chapter describes the dynamic model of an electrical microgrid, showing detailed mathematical description of each of its DG component. The presence of associated power electronic circuitry for integration of renewable DG units is also considered. Small scale micro-turbine along with synchronous generator, a photovoltaic system, a fuel cell system and a PMSG wind system are considered as various DG components of the microgrid under investigation. Energy storage devices such as battery and super capacitor connected through a voltage source converter (VSC) is modeled as a central managerial controller to coordinate power flow among various DG units. A small-signal linearized model is derived to study the penetration limits of renewable sources.

3.2 The Microgrid Architecture

Figure 3.1 shows a schematic diagram of the microgrid under investigation. The microgrid has four DG units connected to the main grid along with integrated load at (point of common coupling) PCC bus. In order to make provision for sub-synchronous frequency ranges, the transient models of filters and connecting transmission links have also been incorporated. DG1 represents small scale conventional generation system

which may portray a gas-turbine or micro generation system and it is considered to be equipped with an excitation control. A VSC along with associated power electronic filter and coupling line inductance connects photovoltaic system (DG2) and fuel cell (DG3) system to the main grid. DG4 represents a variable speed permanent magnet synchronous generator (PMSG) wind system driven by an horizontal axis wind turbine and is assumed to be interfaced through appropriate converters with an additional filter circuit at the grid side of the converter. Energy storage device interfaced through a VSC functions as a central controller administering the system operation.

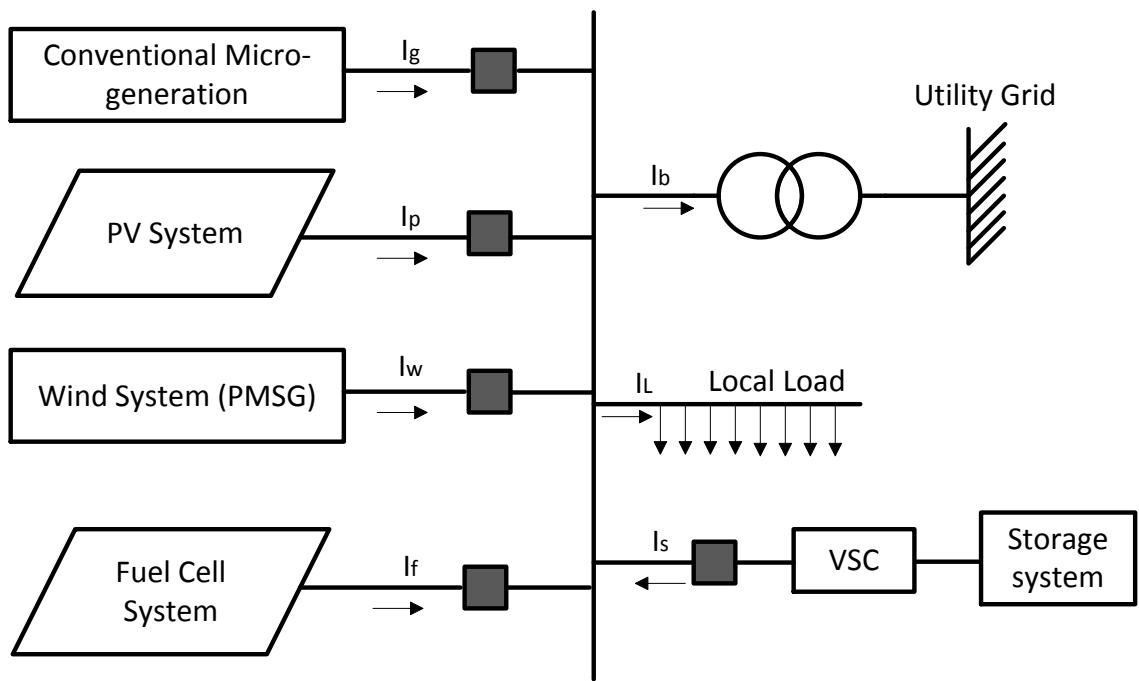


Figure 3.1: Single line diagram of microgrid

The dynamic model of the system includes the transient models for each of the component DGs along with the interconnecting power electronic converters and the central controller. A detailed layout of the microgrid architecture under study is shown in Figure 3.2. The various power electronic converters along with interconnecting coupling lines and filter circuits are also displayed. The storage device is considered to be provided with a P-Q decoupled control strategy.

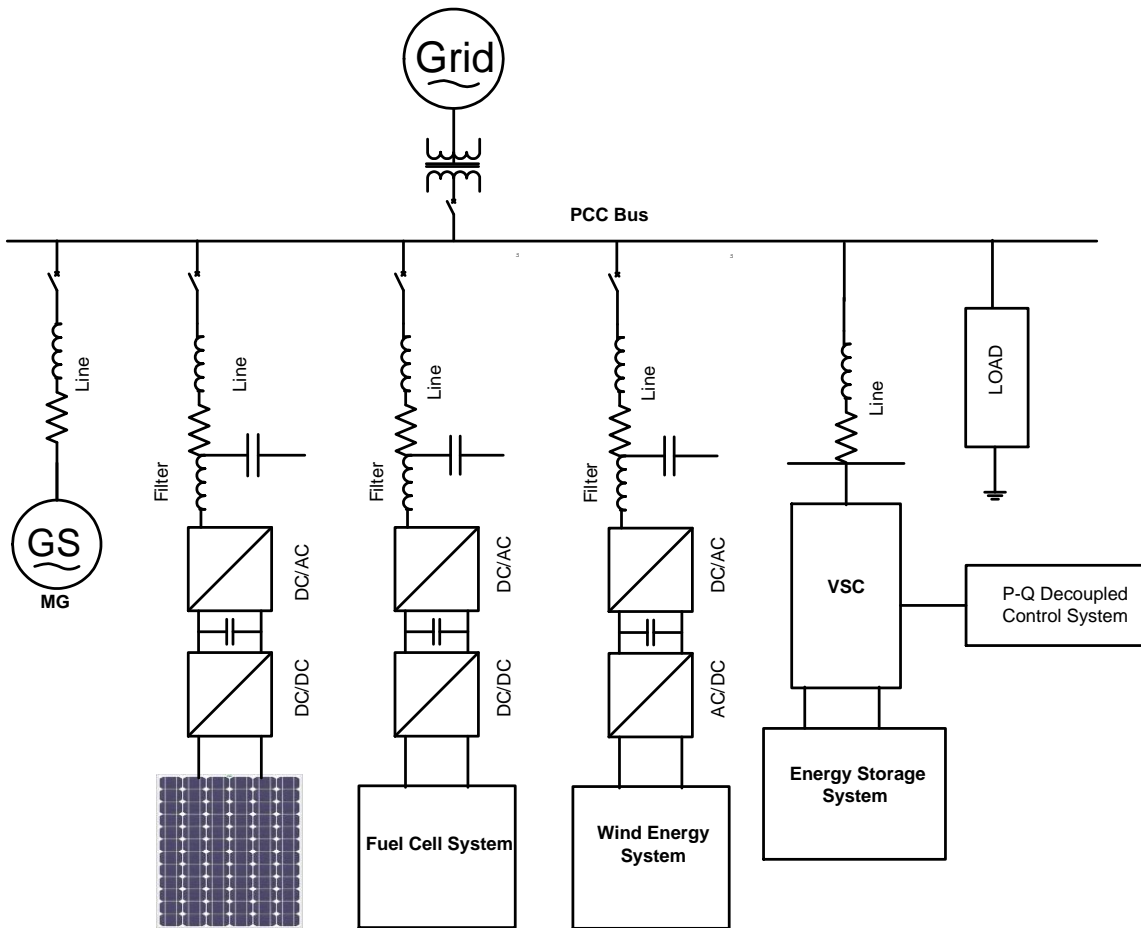


Figure 3.2: Detailed layout of microgrid under investigation

The detailed non-linear mathematical description of each of the microgrid components is given in the following sections.

3.3 Small-Scale Conventional Micro Generation

The conventional generation system can be modeled as a synchronous alternator driven by a gas-turbine or a diesel engine, and there by generating electrical power of fundamental frequency which makes possible for direct connection to the utility grid. A 3rd order model consisting of the swing equation and internal voltage equation of an alternator is being used as a dynamic model for synchronous generator [126].

The rotor mass of a synchronous alternator can be modeled by a 2nd order differential equation, known as the swing equation, relating the rotational inertia and the powers as:

$$\frac{2H}{\omega_b} \frac{d^2\delta}{dt^2} = P_m - P_e - D(\omega - \omega_b) \quad (3.1)$$

Decomposing the swing equation into two first order non-linear differential equation as:

$$\frac{d\delta}{dt} = \omega_b(\omega - 1) \quad (3.2)$$

$$\frac{d\omega}{dt} = \frac{1}{2H} [P_m - P_e - D(\omega - \omega_b)] \quad (3.3)$$

The load angle, rotor speed, mechanical power input, electrical power output of the generator and damping are denoted by δ , ω , P_m , P_e and D respectively in the equations (3.1), (3.2) and (3.3).

Due to excitation applied on the dc windings of the synchronous alternator, there develops an EMF which drives a current through the terminals and also develops a terminal voltage. The micro generator has a voltage obtained along q-axis. The internal voltage e_q' is given by the following equation:

$$\frac{de_q'}{dt} = \frac{1}{T_{d0}'} [E_{fd} - e_q' - (X_d - X_d')i_{gd}] \quad (3.4)$$

In (3.4), x_d , x_d' and T_{d0}' are the d-axis synchronous reactance, transient reactance and open circuit field constants respectively.

The synchronous generator is considered to be equipped with a voltage regulator and using IEEE ST-1A exciter in the field, the governing relation can be written as:

$$\frac{dE_{fd}}{dt} = \frac{1}{T_A} \{K_A \langle V_{gref} - V_g \rangle - \langle E_{fd} - E_{fd0} \rangle\} \quad (3.5)$$

In (3.5), the field voltage along d-axis is E_{fd} , the gain and time constants of the exciter are K_A and T_A respectively.

The electrical output from synchronous alternator is alternating in nature, and hence, it can be directly coupled to the main utility grid with no requirement of any power conversion device. The state variables chosen for the micro generator system are

$$X_{MG} = [\delta, \omega, e_q', E_{fd}] \quad (3.6)$$

3.3.1 Microgenerator connected to grid

This section develops the modeling equations pertaining to a microgenerator when connected to utility grid.

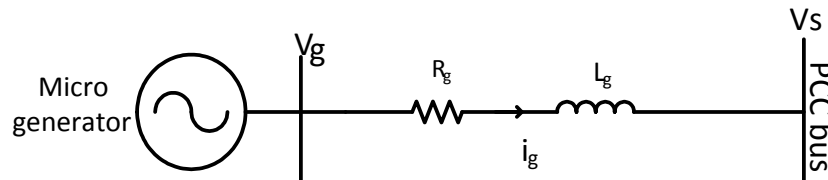


Figure 3.3: Synchronous generator connected to grid

Figure 3.3 show the interconnection of conventional micro generator to PCC bus through a transmission line with resistance R_g and inductance L_g .

The interconnection relationships can be derived by applying Kirchhoff's voltage law (KVL) in Figure 3.3, the terminal voltage can be expressed as:

$$V_g = V_s + (R_g + jX_g)i_g \quad (3.7)$$

The terminal voltage equation can be decomposed into d-q terms as

$$V_{gd} + jV_{gq} = V_{sd} + jV_{sq} + (R_g + jX_g)(i_{gd} + ji_{gq})$$

$$X_q i_{gq} + j(e_q' - X_d' i_{gd}) = (V_{sd} + R_g i_{gd} - X_g i_{gq}) + j(V_{sq} + R_g i_{gq} + X_g i_{gd})$$

Now separating the real and imaginary parts; considering $X_1 = (X_d' + X_g)$ and $X_2 = (X_q + X_g)$ we get,

$$i_{gd} = \frac{-R_g V_{sd} + (e_q' - V_{sq})X_2}{R_g^2 + X_1 X_2} \quad (3.8)$$

$$i_{gq} = \frac{V_{sd} X_1 X_2 + R_g (e_q' - V_{sq}) X_2}{X_2 (R_g^2 + X_1 X_2)} \quad (3.9)$$

Here, the terminal voltage can be related with the above mentioned currents by:

$$V_g = \sqrt{V_{gd}^2 + V_{gq}^2} = \sqrt{(X_q i_{gq})^2 + (e_q' - X_d' i_{gd})^2} \quad (3.10)$$

Also the electrical power output of the generator can be expressed as:

$$P_e = V_{gd} i_{gd} + V_{gq} i_{gq} = e_q' i_{gq} + (X_q - X_d') i_{gd} i_{gq} \quad (3.11)$$

Thus, utilizing the equations (3.8), (3.9) in (3.10) and (3.11), the terminal voltage and power output of the micro-generator can be expressed in terms of the microgrid voltage components V_{sd} and V_{sq} .

3.4 The Photovoltaic System

In a photovoltaic system, the fundamental block is a solar cell, which is a semiconductor device behaving as a current source when solar radiation is incident on it. It assumes the characteristic of an ideal diode when there is no illumination. The incident solar irradiation, array short circuit current, array open circuit voltage, cell temperature and load connected to the array determines the operation characteristics of a solar array [127]. The irradiance applied to a photovoltaic unit dictates the output current and power. There exists a nonlinear I-V and P-V characteristics for a solar array which has dependency of cell temperature and radiation intensity. The relationship between PV output current and temperature is very weak. The temperature has very little effect on PV current, but increased temperatures cause the PV cell to conduct at a low voltage, thus diminishing the power output [128].

In this study, the PV cell has been modeled through a general electrical equivalent circuit consisting of a photo diode, a normal p-n junction diode, leakage current being represented through a shunt resistor, and a series resistance corresponding internal resistance being offered to the current flow [129]. The general exact equivalent model is shown in Figure 3.4 wherein the PV cell is represented by four important components.

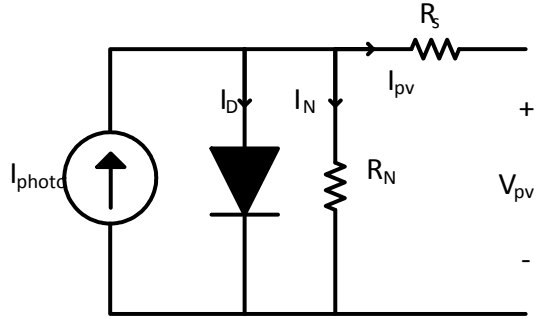


Figure 3.4: Electrical equivalent of a PV cell

The incident solar radiation produces a photo current, which then passes through the array into the load. By Kirchhoff's Current Law (KCL) the net output current from the cell is given by:

$$i_{pv} = I_{photo} - I_D - \frac{(V_{pv} + i_{pv}R_s)}{R_N} \quad (3.12)$$

From the above equation (3.12), the p-n junction diode current can be expressed as:

$$I_D = I_{RSC} \left(e^{\frac{(V_{pv} + R_s i_{pv})}{nv_T}} - 1 \right) \quad (3.13)$$

The reverse saturation current I_{RSC} , the PV cell current i_{pv} and voltage V_{pv} , the diode ideality factor η , and the thermal voltage v_T determines the terms associated with the PV module.

The current generated by the photo diode, being a function of PV cell working temperature and incident solar irradiation, is given as:

$$I_{photo} = [I_{SC} + a(T - T_{ref})]G \quad (3.14)$$

From(3.14), I_{SC} is the PV cell short current at a temperature of 25°C and irradiance of $1\text{kW}/\text{m}^2$, 'a' being the temperature coefficient of I_{SC} , the reference temperature and irradiation being represented by T_{ref} and G respectively.

Temperature dependency of the reverse saturation current can be obtained from:

$$I_{RSC} = I_{RSCref} \left(\frac{T}{T_{ref}} \right)^{\frac{3}{n}} e^{\frac{-qE_g}{nk} \left(\frac{1}{T} - \frac{1}{T_{ref}} \right)} \quad (3.15)$$

I_{RSCref} and E_g are the PV cell reverse saturation current at a reference temperature, and energy band-gap of the semiconductor material used for the cell respectively.

Approximate electrical equivalent circuit model of a PV cell can be obtained from the exact circuit description in Figure 3.4, by ignoring the shunt resistance R_N giving the circuit as shown in Figure 3.5.

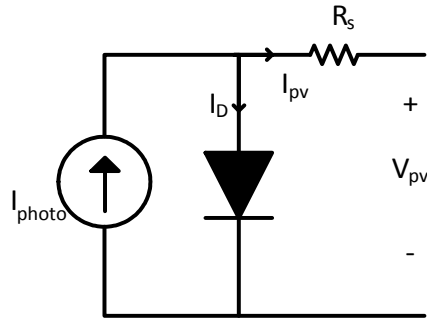


Figure 3.5: Approximate PV circuit model

The cell output current obtained from approximate model in Figure 3.5 can be written as:

$$i_{pv} = I_{SC} - I_{RSC} \left[e^{q \left(\frac{V_{pv} + i_{pv} R_s}{n v_T} \right)} - 1 \right] \quad (3.16)$$

Due to low power generation capacity of a solar cell, several cells are connected in series and parallel combinations, in order to obtain reasonable power output. For a solar array consisting of N_s series modules and N_{prll} parallel modules, the characteristic current equation can be carved as:

$$i_{pv} = N_{prll}I_{photo} - N_{prll}I_{RSC} \left[e^{\left(\frac{V_{pv} + i_{pv}R_s}{N_s + N_{prll}}\right)/nv_T} - 1 \right] \quad (3.17)$$

Nonlinear relationship between the cell current and voltage demonstrated from (3.17) can be solved by employing a numerical iterative technique called Newton-Raphson algorithm [130]. The voltage of the module is expressed in terms of the module current by the relation (3.18):

$$V_{pv} = N_s \left[\ln \left(\frac{N_{prll}I_{photo} - i_{pv}}{N_{prll}I_s} + 1 \right) nv_T - \frac{i_{pv}R_s}{N_{prll}} \right] \quad (3.18)$$

Specifying the module current with an initial guess, the module voltage can be obtained by nonlinear numerical solution of (3.18).

3.4.1 The power electronic interface for PV system

The interconnection of photovoltaic system to utility grid requires the use of various power electronics devices. The fundamental electronic circuitry essential for a PV system is called a power conditioning unit. The DC/DC converter, DC link capacitor, DC/AC inverter and filter circuit constitutes the major components of a power conditioning unit. Since the power output of the solar array is DC type of low magnitude, a DC/DC converter is necessary in order to transform the output power from lower level to higher voltage level. Interfacing of DC power producing PV device to main utility grid requires a DC/AC inverter. The occurrence of harmonics and power quality problems due to the

inclusion of power electronic devices can be smoothed by employing a LC filter at the output terminals of inverter. In order to mitigate the sub synchronous resonance the resistance R_{pdr} is applied in series with the filter capacitor.

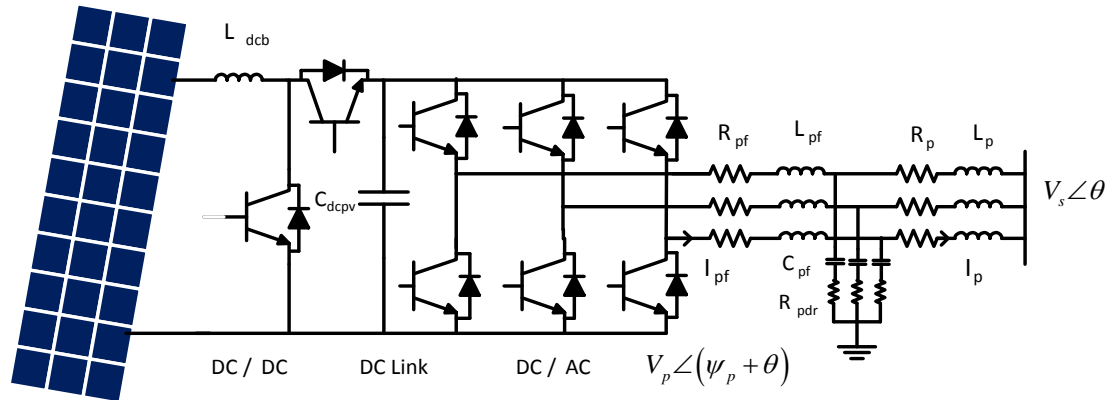


Figure 3.6: Interconnection of PV module to PCC

Figure 3.6 depicts the use of power electronic circuitry for interfacing a PV module to the utility grid. In the following section, the various components involved in the power conditioning unit are sketched.

DC/DC Boost Converter

Thyristor and IGBT representing power electronic switches and variety of storage elements such as an inductors or capacitors forms the basis circuitry of a DC converter. With controlled switching of various powers electronic devices, the transient power flowing from input towards the output can be affected. The requirements of storage devices to be employed in a converter is to provide a low output voltage ripple, and hence, such a state can be obtained only through formation of low pass filter [131].

The choice of boost converter is justified due to the low voltage output of a PV module. The voltage obtained from the PV array is stepped up to a reasonable value before being applied for inversion. The output DC voltage of boost converter is decided by the converter duty cycle, which is defined as the ratio of ON period to the switching period. Continuous current conduction (CCM) mode of operation for the DC boost converter is the need, as the PV module has to feed power grid into the grid with high reliability.

The circuit model of DC boost converter used in the work is depicted in Figure 3.7. An energy storing inductor, a power electronic switch obtained through IGBT, and a forward acting diode completes the circuit for boost converter. Sometimes the use of capacitor at the output terminals is justified to smoothen out the raised output voltage.

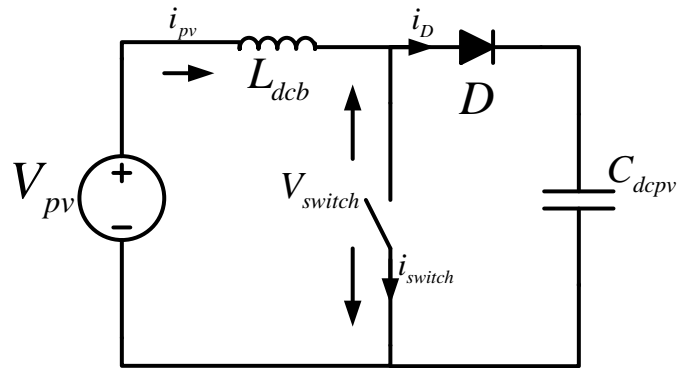


Figure 3.7: Circuit representation of DC-boost converter

Application of KVL to the boost converter circuit in Figure 3.7 yields the dynamical relations involved in the converter model. The current flowing through energy storing inductor can be taken as a state variable. The differential equation describing the DC boost converter model is obtained as:

$$V_{pv} = L_{dcb} \frac{di_{pv}}{dt} + V_{switch} \quad (3.19)$$

The voltage obtained across the switch can be written in terms of the converter duty ratio dr_{pv} and output capacitor voltage V_{dcpv} as:

$$V_{switch} = (1 - dr_{pv})V_{dcpv} \quad (3.20)$$

Incorporation of (3.20) into (3.19), the transient equation pertaining to DC boost converter can be expressed as:

$$\frac{di_{pv}}{dt} = \frac{1}{L_{dcb}} [V_{pv} - V_{switch}] = V_{pv} - (1 - dr_{pv})V_{dcpv} \quad (3.21)$$

The DC-Link Capacitor Model

Filtering the DC output voltage obtained from the DC boost converter, and to act as an energy storing device, thereby maintaining a constant voltage at the input terminals of power electronic inverter are the main functions of a DC link capacitor. Regulation of voltage at dc link capacitor is usually achieved by the DC boost converter so that the inverter is able to feed the grid with proper current. De-activation of the dc link capacitor occurs when the converter output currents and inverter input current are made equal [132].

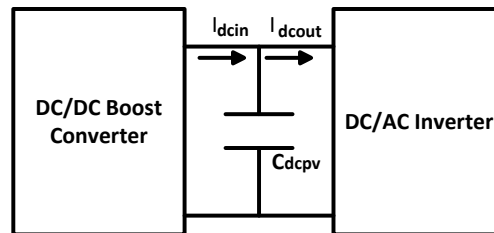


Figure 3.8: DC-link capacitor model

The DC-link capacitor acts as a connecting link between the DC boost converter and DC/AC inverter, as shown in Figure 3.8. Selecting a large value of capacitor will diminish the voltage ripples induced in the DC-link due to periodic switching of power electronic converter, while a small capacitor enables faster control of DC-link voltage. Therefore, the size of DC-link capacitor requires a trade-off between the voltage ripples and fast changes in DC voltage.

The use of KCL at the link node connecting the DC boost converter with the DC/AC inverter would yield the dynamic relation as:

$$I_{dcin} - I_{dcout} = C_{dcpv} \frac{dV_{dcpv}}{dt} \quad (3.22)$$

The output current of converter is $I_{dcin} = (1 - dr_{pv})i_{pv}$, while the inverter input current I_{dcout} could be written in terms of inverter output current. Voltage V_{dcpv} across the DC-link capacitor depicts its dynamics and is taken as a state variable.

The DC/AC Inverter Model

The purpose of DC/AC inverter in the power conditioning unit of photovoltaic system is to provide an output AC voltage of proper magnitude and frequency in order to be able to integrate with the grid. The voltage source inverter (VSI) being modeled through a voltage gain model is used in this work.

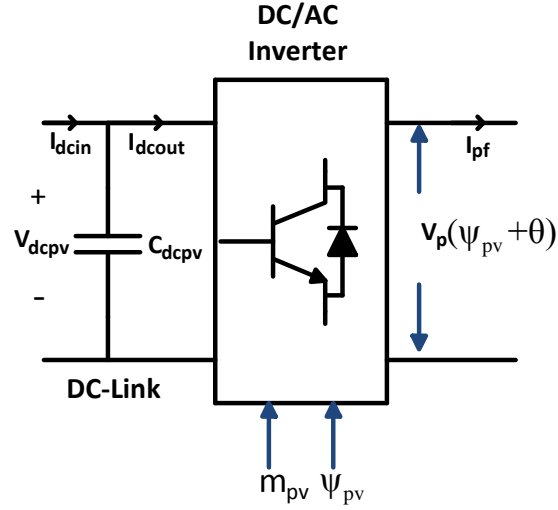


Figure 3.9: Inverter circuit description

It can be seen from the Figure 3.9 that the DC power through the capacitor is:

$$P_{DC} = V_{dcpv} I_{dcout} \quad (3.23)$$

Towards the AC side of the inverter, the instantaneous power output can be expressed as:

$$P_{AC} = \text{Re}[V_p I_{pf}^*] \quad (3.24)$$

Decomposing the inverter output voltage and currents into d-q components, the AC power output is written as,

$$P_{AC} = V_{pd} i_{pfd} + V_{pq} i_{pfq} \quad (3.25)$$

Assuming the inverter to be lossless, the DC and AC powers can be equated as:

$$P_{DC} = P_{AC} \quad (3.26)$$

$$V_{dcpv} I_{dcout} = V_{pd} i_{pfd} + V_{pq} i_{pfq}$$

Considering the inverter to be operated in the PWM mode, with a modulation index m_{pv} and phase angle of the inverter ψ_{pv} , an expression can be derived for the inverter output voltage in terms of the DC-link voltage as,

$$V_p = m_{pv} * V_{dcpv} \angle \psi_{pv} \quad (3.27)$$

The d-q components of the inverter output voltage from (3.27) are given by:

$$V_{pd} = m_{pv} * V_{dcpv} * \cos(\psi_{pv} + \theta) \quad (3.28)$$

$$V_{pq} = m_{pv} * V_{dcpv} * \sin(\psi_{pv} + \theta)$$

Introducing (3.28) into (3.26) will yield the following expression:

$$I_{dcout} = (i_{pfd} m_{pv} \cos(\psi_{pv} + \theta) + i_{pq} m_{pv} \sin(\psi_{pv} + \theta)) \quad (3.29)$$

Thus, using the above equation (3.29), the state equation pertaining to dynamics of DC-link capacitor can be expressed in terms of d-q components of inverter output current.

The Output LC Filter and Coupling Line Model

Application of a low pass filter formed with passive circuit components will attenuate the ripples found in inverter output voltage. Incorporation of capacitor and inductor as energy storing devices working in reactive modes will respond to the frequency changes in inverter output. Passage of low frequency harmonics through inductor, and high frequency components through the capacitor will guarantee diminished ripples in the system [133].

In this study, the use of coupling line with an inductance and a resistance is being proposed to connect the PV circuit with the grid system. The resonance problem that

might arise due to filter capacitor and coupling inductor is avoided through the use of a damping resistor in the filter circuit. Figure 3.10 shows the model of a coupling circuit along with the filtering circuit employed to obtain high quality power from PV system.

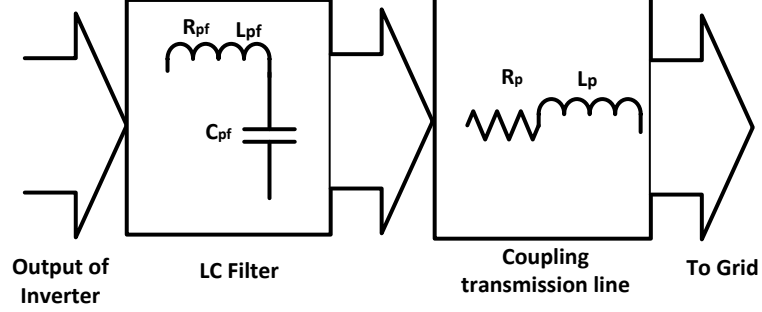


Figure 3.10: LC filter and coupling inductance circuit

The dynamics involved with the LC filter and coupling circuit components can be easily derived by applying KVL around the loop formed by the PV inverter and the filter capacitor, which will give a differential equation as:

$$V_p = i_{pf}R_{pf} + L_{pf} \frac{di_{pf}}{dt} + V_{cp} + (i_{pf} - i_p)R_{pdr} \quad (3.30)$$

In equation (3.30), R_{pf} Corresponds to filter resistance, L_{pf} depicts the filter inductance, V_{cp} is the filter capacitor voltage, and R_{pdr} is the damping resistor.

Decomposition of equation (3.30) into d-q components will yield the following nonlinear ordinary differential relations:

$$\begin{aligned} \frac{di_{pfd}}{dt} = & \frac{-\omega_0 R_{pf}}{L_{pf}} i_{pfd} + \omega_0 \omega i_{pfdq} + \frac{\omega_0 m_{pv} V_{dcpv} \cos(\psi_{pv} + \theta)}{L_{pf}} \\ & - \frac{\omega_0 V_{cpd}}{L_{pf}} - \omega_0 R_{pdr} (i_{pfd} - i_{pd}) \end{aligned} \quad (3.31)$$

$$\begin{aligned} \frac{di_{pfq}}{dt} = & \frac{-\omega_0 R_{pf}}{L_{pf}} i_{pfq} - \omega_0 \omega i_{pfd} + \frac{\omega_0 m_{pv} V_{dcpv} \sin(\psi_{Pv} + \theta)}{L_{pf}} \\ & - \frac{\omega_0 V_{cpq}}{L_{pf}} - \omega_0 R_{Pdr} (i_{pfq} - i_{pq}) \end{aligned} \quad (3.32)$$

Writing KVL in the loop formed around the filter capacitor, coupling transmission line, and microgrid bus will produce the dynamic relations pertaining to coupling inductance as:

$$V_{cp} = i_p R_p + L_p \frac{di_p}{dt} + V_s - (i_{pf} - i_p) R_{Pdr} \quad (3.33)$$

In d-q components the above equation can be expressed as,

$$\begin{aligned} \frac{di_{pd}}{dt} = & \frac{-\omega_0 R_p}{L_p} i_{pd} + \omega_0 \omega i_{pq} + \frac{\omega_0}{L_p} (V_{cpd} - V_{sd}) \\ & + \omega_0 R_{Pdr} (i_{pfd} - i_{pd}) \end{aligned} \quad (3.34)$$

$$\begin{aligned} \frac{di_{pq}}{dt} = & \frac{-\omega_0 R_p}{L_p} i_{pq} - \omega_0 \omega i_{pd} + \frac{\omega_0}{L_p} (V_{cpq} - V_{sq}) \\ & + \omega_0 R_{Pdr} (i_{pfq} - i_{pq}) \end{aligned} \quad (3.35)$$

Now for the filter capacitor the use of KCL produces,

$$C_{pf} \frac{dV_{cp}}{dt} = (i_{pf} - i_p) \quad (3.36)$$

Expressing the above equation into d-q reference frame, gives two nonlinear ordinary differential equations explaining the dynamics involved with the filter capacitor as,

$$\frac{dV_{cpd}}{dt} = \frac{1}{C_{pf}} (i_{pfd} - i_{pd}) + \omega_0 \omega V_{cpq} \quad (3.37)$$

$$\frac{dV_{cpq}}{dt} = \frac{1}{C_{pf}} (i_{pfq} - i_{pq}) + \omega_0 \omega V_{cpd} \quad (3.38)$$

Thus, the interconnection of photovoltaic system with the utility grid requiring the use of power electronic converters and associated filter circuitry can be represented with eight nonlinear ordinary differential equations, each equation denoting a state variable used in the process.

The state variables selected for the PV system when interfaced to the utility grid are,

$$X_{PV} = [i_{pv}, V_{dcpv}, i_{pfd}, i_{pfq}, i_{pd}, i_{pq}, V_{cpd}, V_{cpq}] \quad (3.39)$$

3.5 The Wind Energy System

In the last few decades, there has been extensive research reported in the domain of wind systems. The behavior of wind turbines along with the corresponding power generation devices is very well understood by researchers and comprehensive models have been developed which depict the performance of wind systems to a larger extent. This section describes the mathematical representation of a permanent magnet synchronous generator (PMSG) driven by a wind turbine along with the associated power electronic converter circuits.

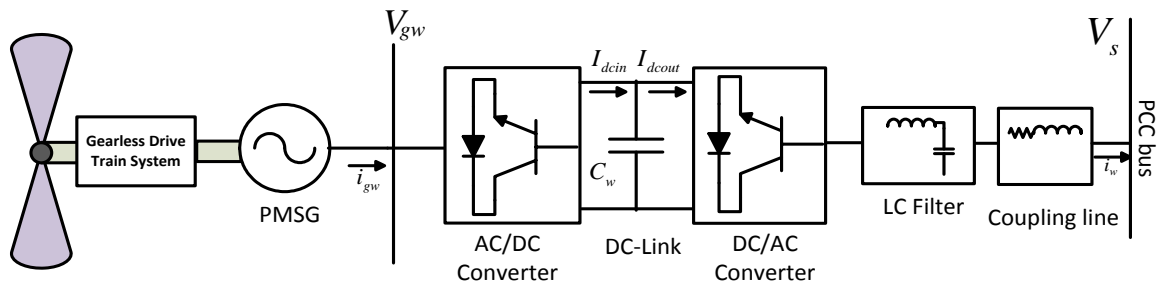


Figure 3.11: Schematic of variable speed WT-PMSG connected to grid

As shown in Figure 3.11, a horizontal axis wind turbine drives the rotor of a permanent magnet synchronous generator through a gearless drive train. Field excitation to the generator is obtained through permanent magnets mounted on the generator rotor. Power electronic converters connected between the stator of PMSG and the grid provides an AC voltage of constant grid frequency to be able to feed the grid.

The wind turbine, the gearless drive train, the PMSG, the converter circuits and transmission line connected at grid side constitute the dynamic model of the wind generation system. The IGBT switch, controlled through PWM a method, forming an important component of power electronic converter system, connects directly with the stator of PMSG system and receives an AC power at variable frequency. Two voltage source converters (VSC) connected as a back-to-back converter system through a DC-link constitutes the power electronic circuitry. Generator side converter acts as a rectifier, while the grid side converter acting as an inverter maximizes the power injected into the DC-link. The dynamic model of each of the component involved with the generation system is dealt in the following section.

3.5.1 The wind turbine model

Extraction of energy from wind and conversion into mechanical power is the main function of a wind turbine employed in a wind generation system. There are various configurations of wind turbine being around the globe and the choice of a particular wind turbine depends on several factors. Wind speed, the turbine rotor size, and the blade area affect the power output of a wind turbine. Cubic relation between the wind speed and the mechanical power output is exciting, as a small increase in speed will amount to greater increase in the wind power. Owing to economic and technical challenges, there has been

a limitation on the size of the wind turbine blades. The amount of power P_m extracted from the wind turbine is related to the wind speed V_w by [134].

$$P_m = \frac{1}{2} \rho \pi R^2 V_w^3 C_p(\beta, \lambda) \quad (3.40)$$

Here, R is the radius of the rotor blades and C_p is a power coefficient, which is a function of the tip speed ratio λ and the blade pitch angle β . The parameter λ may be defined as the ratio of linear speed at the tip of the blades to the speed of wind, given as:

$$\lambda = \frac{\omega_t R}{V_w} \quad (3.41)$$

The power coefficient C_p being a nonlinear function of the tip speed ratio and blade pitch angle is usually written as [135],

$$C_p(\beta, \lambda) = 0.5176 \left[\frac{116}{\lambda_i} - 0.4\beta - 5 \right] e^{\frac{-21}{\lambda_i}} + 0.0068\lambda \quad (3.42)$$

$$\frac{1}{\lambda_i} = \frac{1}{\lambda + 0.08\beta} - \frac{0.035}{\beta^3 + 1}$$

The drive train system of wind energy conversion system to be used in this study includes a two mass model as shown in Figure 3.12. The wind turbine constituting a greater mass having inertia of H_t connects the PMSG rotor with inertia of H_g . A mechanical shaft with a stiffness coefficient of K_s is used to couple the two masses. The damping coefficients for the turbine and generator are taken as D_t and D_g respectively.

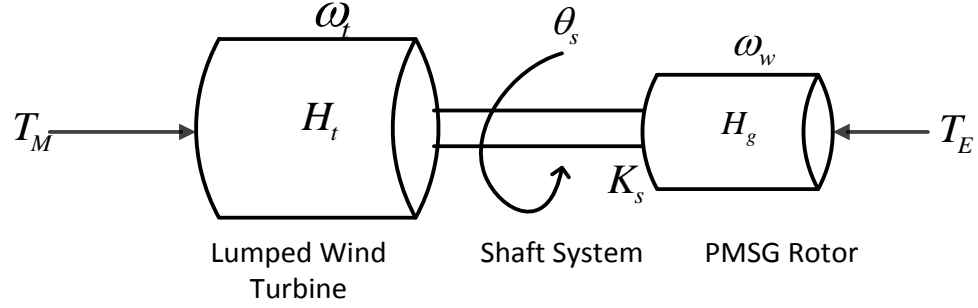


Figure 3.12: Two mass model of drive train

Four first order nonlinear ordinary differential equations describe the electromechanical dynamics of the drive train system in terms of the torsional angle θ_s , the turbine speed ω_t , the PMSG rotor angle δ_w and the PMSG rotor speed ω_w as [136],

$$\frac{d\theta_s}{dt} = \omega_0(\omega_t - \omega_w) \quad (3.43)$$

$$\frac{d\omega_t}{dt} = \frac{1}{2H_t}(P_{mw} - K_s\theta_s - D_t(\omega_t - 1)) \quad (3.44)$$

$$\frac{d\delta_w}{dt} = \omega_0(\omega_w - 1) \quad (3.45)$$

$$\frac{d\omega_w}{dt} = \frac{1}{2H_g}(K_s\theta_s - P_{ew} - D_g(\omega_w - 1)) \quad (3.46)$$

3.5.2 The variable speed PMSG model

The nonlinear transient model of a variable speed permanent magnet synchronous generator (PMSG) will be developed in this section. The voltage-current-flux relationships for a PMSG system can be expressed as,

$$\begin{aligned} \psi_d &= -X_{dw}i_{gwd} + X_{afd}i_{fd} \\ \psi_q &= -X_{qw}i_{gwd} \end{aligned} \quad (3.47)$$

$$\begin{aligned}\psi_{fdw} &= -X_{afdwi}i_{gwd} + X_{ffdwi}i_{fdw} \\ V_{gwd} &= -R_a i_{gwd} - \omega_w \psi_q + \frac{1}{\omega_0} \frac{d\psi_d}{dt} \\ V_{gwd} &= -R_a i_{gwd} + \omega_w \psi_d + \frac{1}{\omega_0} \frac{d\psi_q}{dt}\end{aligned}\tag{3.48}$$

Due to the use of permanent magnets in the field circuit of the PMSG machine, the field flux pertaining to the term $X_{afdwi}i_{fdw}=\psi_0$ is assumed to be constant. The PMSG system can be assumed as a source of Emf e_{gw} driving current to the circuit through its own resistance and reactance. Considering sinusoidal flux distribution, the equivalent circuit for a PMSG can be shown as in Figure 3.13,

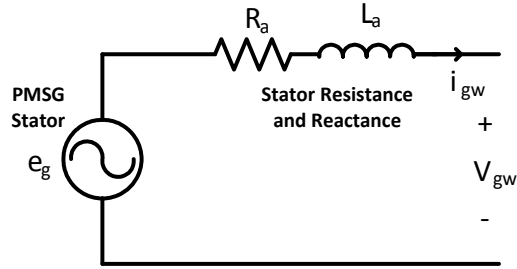


Figure 3.13: Electrical equivalent circuit of PMSG

From the equations (3.47) and (3.48), considering the flux produced by the permanent magnets in the field circuit of PMSG to be constant, we can write the voltage relations as,

$$V_{gwd} = -R_a i_{gwd} + \omega_w X_{qwi} i_{gwq} - \frac{X_{dwi}}{\omega_0} \frac{di_{gwd}}{dt}\tag{3.49}$$

$$V_{gwq} = -R_a i_{gwq} - \omega_w X_{dwi} i_{gwd} + \omega_w \psi_0 - \frac{X_{qwi}}{\omega_0} \frac{di_{gwq}}{dt}\tag{3.50}$$

Hence, the dynamical relations for the PMSG system can be finally written as,

$$\frac{di_{gwd}}{dt} = \frac{\omega_0}{x_{dw}} [-R_a i_{gwd} + \omega_w X_{qw} i_{gwg} - V_{gwd}] \quad (3.51)$$

$$\frac{di_{gwg}}{dt} = \frac{\omega_0}{x_{qw}} [-R_a i_{gwg} - \omega_w X_{dw} i_{gwd} + \omega E_{fdw} - V_{gwg}] \quad (3.52)$$

Here, i_{gwd} and i_{gwg} are the d-q axes PMSG currents, X_{dw} and X_{qw} are the stator reactance along d-q axes, E_{fdw} is the field voltage along d-axis, ω_w is the generator rotor speed.

The relation governing the electromechanical torque produced by the PMSG is,

$$T_{ew} = E_{fdw} * i_{gwg} + (X_{qw} - X_{dw}) * i_{gwd} * i_{gwg} \quad (3.53)$$

Hence, the electrical power output obtained from the PMSG is written as,

$$P_{ew} = \omega_w * T_{ew} \quad (3.54)$$

3.5.3 The wind system converter model

In order to feed, the electrical power obtained from the permanent magnet synchronous generator driven by a wind turbine to the utility grid, two back-to-back converters, one on the grid side and the other at the stator side coupled through a common DC-link are necessary. Due to the use of DC-link capacitor there exists a decoupling between the two converters and hence separate control algorithms could be employed.

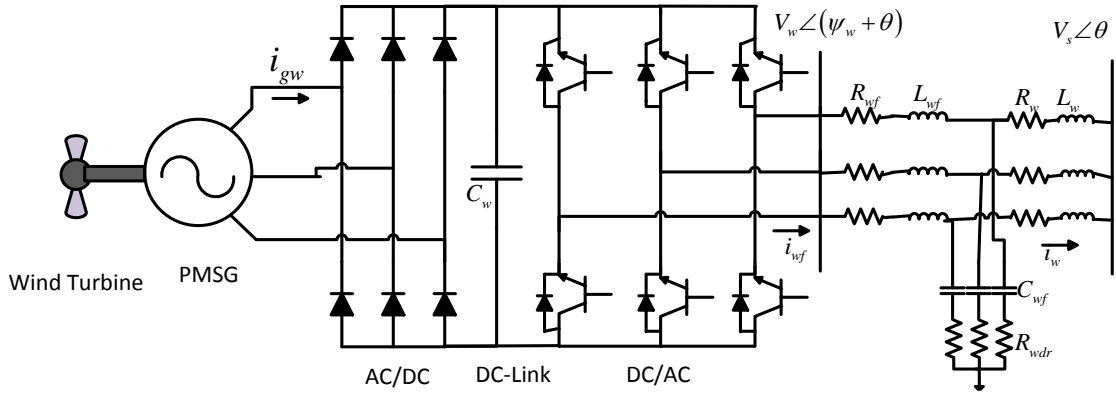


Figure 3.14: Converter configuration for variable speed PMSG wind system

As shown in Figure 3.14, the rectification operation is obtained through the converter working near the PMSG side while the other converter performs the inversion operation converting the DC voltage obtainable from the output of rectifier into fixed frequency AC voltage. The use of DC-link capacitor provides an intermediate storage, isolating the generator side synchronous system and grid side synchronous system. Keeping the voltage across the DC-link capacitor as constant, the transfer of real power from the generator into the grid can be achieved.

As shown in Figure 3.14, the stator of PMSG directly feeds power into the rectifier, there exists a relation between the terminal voltage of PMSG and the rectifier output voltage as indicated,

$$V_{gw} = m_{wr} V_{dcw} \cos \alpha_1 \quad (3.55)$$

Here, m_{wr} is the modulation index of the PMSG side converter system, V_{dcw} is the DC-link capacitor voltage and α_1 is the firing angle. Replacing the firing angle with the generator rotor angle using relation $\alpha_1 = 90 - \delta_w$ and decomposing into d-q components will give,

$$\begin{aligned}
V_{gwd} &= m_{wr} V_{dcw} \sin \delta_w \\
V_{gwq} &= m_{wr} V_{dcw} \cos \delta_w
\end{aligned}
\tag{3.56}$$

The power output from the PMSG system, which is same as, the power on the AC side of the rectifier is given by,

$$P_{gw} = V_{gwd} i_{gwd} + V_{gwq} i_{gwq} \tag{3.57}$$

Now referring to the grid-side converter system, the modulation index m_{wi} and its phase angle ψ_{wi} dictates the output voltage given as,

$$\begin{aligned}
V_w &= m_{wi} V_{dcw} \angle (\psi_{wi} + \theta) \\
V_{wd} &= m_{wi} V_{dcw} \cos(\psi_{wi} + \theta) \\
V_{wq} &= m_{wi} V_{dcw} \sin(\psi_{wi} + \theta)
\end{aligned}
\tag{3.58}$$

The d-q components of inverter output voltage are V_{wd} and V_{wq} respectively and θ is the phase angle of the microgrid voltage V_s .

The voltage V_w drives a current i_{wf} towards the grid, hence the power output of the inverter can be written as,

$$P_w = V_{wd} i_{wfd} + V_{wq} i_{wfq} \tag{3.59}$$

3.5.4 The DC link capacitor model

Application of KCL at the DC-link node will produce the dynamic relation describing the behavior of the DC-link capacitor. It can be seen that the dc power through the capacitor is given as,

$$P_{DC} = V_{dcw} * C_w * \frac{dV_{dcw}}{dt} \quad (3.60)$$

Assuming the capacitor to be lossless the net power change will be $P_g - P_w$, hence

$$V_{dcw} C_w \frac{dV_{dcw}}{dt} = P_g - P_w \quad (3.61)$$

Finally the transient of the DC-link voltage can be written as,

$$\begin{aligned} \frac{dV_{dcw}}{dt} = \frac{1}{C_w} [& m_{wr} \sin \delta_w i_{gwd} + \cos \delta_w i_{gwq} \\ & - m_{wi} \cos(\psi_{wi} + \theta) i_{wd} - m_{wi} \sin(\psi_{wi} + \theta) i_{wq}] \end{aligned} \quad (3.62)$$

3.5.5 The LC filter and coupling transmission line model

The purpose of filtering circuit in the PMSG system is to attenuate the harmonics encountered in the output current of the inverter before being fed to the utility grid. A LC filter is employed in order to achieve the smoothening of output current. The dynamic relations would be derived by applying KVL and KCL to the filter section shown in Figure 3.14. Consider the filter circuit to be included with a resistance of R_{wf} , an inductance of L_{wf} and a damping rheostat R_{wdr} , the voltage equation can be written as,

$$V_w = i_{wf} R_{wf} + L_{wf} \frac{di_{wf}}{dt} + V_{cw} + (i_{wf} - i_w) R_{wdr} \quad (3.63)$$

Similar to the dynamical equations obtained for PV system, the splitting of above equation will produce two nonlinear differential equations describing the dynamics of the filter inductance as given by,

$$\begin{aligned} \frac{di_{wfd}}{dt} = & \frac{-\omega_0 R_{wf}}{L_{pf}} i_{wfd} - \frac{\omega_0 V_{0wd}}{L_{wf}} - \omega_0 R_{wdr} (i_{wfd} - i_{wd}) \\ & + \omega_0 \omega i_{wfq} + \frac{\omega_0 m_{wi} V_{dcw} \cos(\psi_{wi} + \theta)}{L_{wf}} \end{aligned} \quad (3.64)$$

$$\begin{aligned} \frac{di_{wfq}}{dt} = & \frac{-\omega_0 R_{wf}}{L_{pf}} i_{wfq} - \frac{\omega_0 V_{0wq}}{L_{wf}} - \omega_0 R_{wdr} (i_{wfq} - i_{wq}) \\ & - \omega_0 \omega i_{wfd} + \frac{\omega_0 m_{wi} V_{dcw} \sin(\psi_{wi} + \theta)}{L_{wf}} \end{aligned} \quad (3.65)$$

Now applying KVL to the loop formed by the filter capacitor and the coupling line will produce the following equations,

$$V_{cw} = i_w R_w + L_w \frac{di_w}{dt} + V_s - (i_{wf} - i_w) R_{wdr} \quad (3.66)$$

Thus the d-q components of the coupling line current can be expressed by nonlinear differential equations of the first order as,

$$\begin{aligned} \frac{di_{wd}}{dt} = & \frac{-\omega_0 R_w}{L_w} i_{wd} + \omega_0 \omega i_{wq} + \frac{\omega_0}{L_w} (V_{owd} - V_{sd}) \\ & + \omega_0 R_{wdr} (i_{wfd} - i_{wd}) \end{aligned} \quad (3.67)$$

$$\begin{aligned} \frac{di_{wq}}{dt} = & \frac{-\omega_0 R_w}{L_w} i_{wq} - \omega_0 \omega i_{wd} + \frac{\omega_0}{L_w} (V_{owq} - V_{sq}) \\ & + \omega_0 R_{wdr} (i_{wfq} - i_{wq}) \end{aligned} \quad (3.68)$$

To obtain the dynamics of the filter capacitor C_{wf} we write KCL at the node producing the following,

$$C_{wf} \frac{dV_{cw}}{dt} = (i_{wf} - i_w)$$

$$\frac{dV_{c wd}}{dt} = \frac{1}{C_{wf}} (i_{wfd} - i_{wd}) + \omega_0 \omega V_{cwq} \quad (3.69)$$

$$\frac{dV_{cwq}}{dt} = \frac{1}{C_{wf}} (i_{wfq} - i_{wq}) - \omega_0 \omega V_{c wd}$$

Thus the integration of variable speed WT-PMSG wind system with the microgrid will result in thirteen dynamical relations describing the behavior of each of the components. The state variables chosen for the wind system are expressed as,

$$\begin{aligned} X_{wind} \\ = [\theta_s, \omega_t, \delta_w, \omega_w, i_{gwd}, i_{gwq}, V_{dcw}, i_{wfd}, i_{wfq}, i_{wd}, i_{wq}, V_{c wd}, V_{cwq}] \end{aligned} \quad (3.70)$$

3.6 The Fuel-Cell System

Electrochemical devices working on the principle of electrolytic chemical reaction converting the chemical energy of a fuel directly into electricity are called Fuel cells. Only water and heat are rejected to the surroundings making the fuel cell energy ecofriendly and environmentally useful. High efficiency, low pollutant emissions, high reliability and little maintenance are some of the characteristics of fuel cell power systems [72]. To drive the load connected at the terminals of a fuel cell system, power electronic interface is needed as the obtained power from fuel cells is an unregulated dc voltage. Fuel cells being, low voltage high current devices, require the use of DC boost converter and other associated power electronic circuitry in order to be integrated with the utility grid.

In order to achieve design, control and simulation of modern fuel cell power systems, an accurate model is necessary depicting the dynamic and steady state performances of such systems to a larger extent. Fuel cells of variety of configurations requiring variant fuel combinations have been reported in the literature, but the most

commonly used is the proton exchange membrane fuel cell (PEM-FC). Chemical, Experimental and Electrical are the three important model types being reported for fuel cells. Each of this model type has certain limitations due to which they are not suitable for the simulation of modern fuel cell power systems. The generic model, combining the features of chemical and electrical models proposed in [72], is a new approach requiring only a few parameters provided in the manufacturers datasheet, is employed in this work. Such a model is capable of reflecting the effect of operating parameters on the fuel cell and can be easily simulated in the simulation programs.

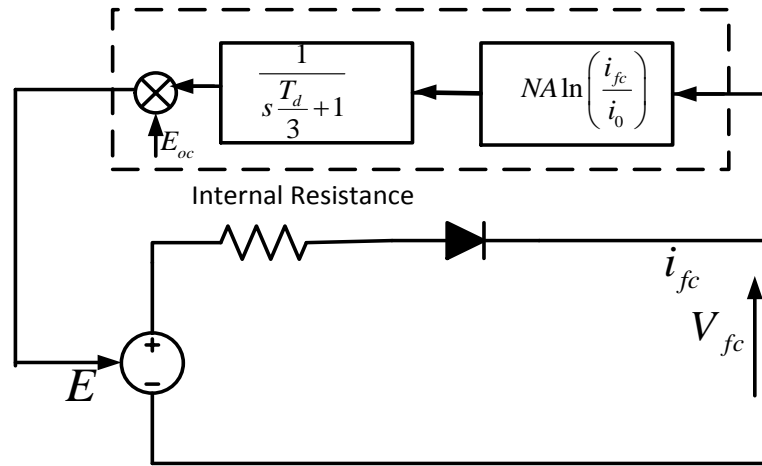


Figure 3.15: Simplified PEM fuel cell stack model

The amount of power produced by a fuel cell is very low (in the range of watts) and also the voltage level is very small, hence several fuel cells are connected in series in order to form a fuel cell stack there by obtaining electrical energy at a considerable voltage.

The simplified generic model of a PEM fuel cell stack is shown in Figure 3.15, where the fuel cell stack is denoted by a controlled voltage source in series with a

constant resistance. Such a model depicts the transient performance of a fuel cell system with a considerable accuracy and is also relatively very simple. Operation of fuel cell stacks at normal condition of temperature and pressure is easily observed using this model.

The magnitude of controlled voltage source being employed in the simplified model is given by the expression,

$$E = E_{oc} - NA \ln \left(\frac{i_{fc}}{i_0} \right) \frac{1}{s \frac{T_d}{3} + 1} \quad (3.71)$$

$$v_{fc} = E - R_{ohm} i_{fc} \quad (3.72)$$

Here the open circuit voltage is E_{oc} , N denotes the number of series connected cells, A is the Tafel slope, i_0 is the exchange current, R_{ohm} the internal resistance, T_d the response time (at 95% of the final value) and the fuel cell stack current and voltage denoted by i_{fc} and v_{fc} respectively. The response time indicates the delay involved due to the slowness of the chemical reactions at electrode surfaces.

3.6.1 The fuel cell stack connected to PCC

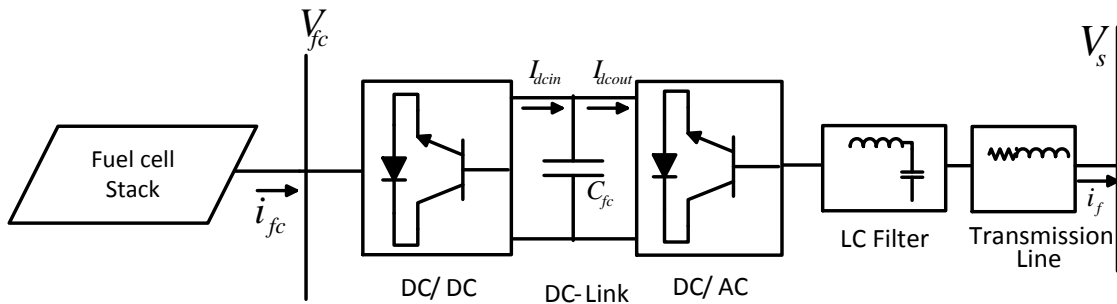


Figure 3.16: Fuel cell stack connected to PCC

The PEM-FC being a source of DC voltage requires the use of power electronic converters for interconnection with the utility grid. The DC boost converter connected at the output of fuel cell stack will enhance the voltage level before being applied to DC/AC inverter as shown in Figure 3.16. The use of an LC filter along with coupling transmission line will serve the purpose of feeding the grid from the power obtained through fuel cell stacks.

Similar to the photovoltaic system described before, the dynamic model of the PEM-FC stack connected to the utility grid can be obtained by considering state variables across the various energy storing devices. The transient model will make use of the following state quantities,

$$X_{FC} = [i_{fc}, V_{dcfc}, i_{ffd}, i_{ffq}, i_{fd}, i_{fq}, V_{cfd}, V_{cq}] \quad (3.73)$$

3.7 The Small-Signal Model of the Microgrid Components

The non-linear equations obtained in the previous section for each of the microgrid components are linearized around an operating point to produce the small-signal models. This section is consecrated with the linear models of the various microgrid components under study. The small-signal models are necessary to carry out the Eigen value analysis in order to identify the threshold limit of generation mix from various DGs without hampering the stability. Small-signal state space model of micro generator, photovoltaic system, fuel cell system and wind generation system will constitute the small-signal model of the microgrid.

3.7.1 The small-signal model of microgenerator

The non-linear set of equations pertaining to the synchronous generator driven through a micro-turbine described in section 3.3 are perturbed around an operating point to yield the linearized state space model as indicated below:

$$\frac{d\Delta\delta}{dt} = \omega_0\Delta\omega \quad (3.74)$$

$$\frac{d\Delta\omega}{dt} = \frac{1}{2H}\{-\Delta P_e - D\Delta\omega\} \quad (3.75)$$

$$\frac{d\Delta e'_q}{dt} = \frac{1}{T'_{do}}[\Delta E_{fd} - \Delta e'_q - (X_d - X'_d)\Delta i_{gd}] \quad (3.76)$$

$$\frac{d\Delta E_{fd}}{dt} = \frac{K_A}{T_A}\Delta V_g - \frac{1}{T_E}\Delta E_{fd} \quad (3.77)$$

The non-state quantities involved in the linearized equations of the micro generator need to be expressed in terms of the state variables as shown below,

Electrical current output of the generator is obtained as,

$$\Delta i_g = \Delta i_{gd} + j\Delta i_{gq} \quad (3.78)$$

The current output of the generator along d-axis as given in (3.8) is perturbed to give,

$$\Delta i_{gd} = \frac{-R_t}{R_t^2 + X_1 X_2} \Delta V_{sd} + \frac{X_2}{R_t^2 + X_1 X_2} (\Delta e_{q'} - \Delta V_{sq}) \quad (3.79)$$

In a similar fashion the current output along q-axis as given in (3.9) is perturbed to produce,

$$\Delta i_{gq} = \frac{\Delta V_{sd}}{X_1} + \frac{R_t}{X'_d + X_t} (\Delta e_{q'} - \Delta V_{sq}) \quad (3.80)$$

Next the terminal voltage of the generator is expressed in terms of the perturbed currents as,

$$V_g^2 = V_{gd}^2 + V_{gq}^2$$

$$\Delta V_g = \frac{V_{gd0}}{V_{g0}} (X_q \Delta i_{gq}) + \frac{V_{gq0}}{V_{g0}} (\Delta e_q' - X_d' \Delta i_{gd}) \quad (3.81)$$

The perturbed electrical power output of the micro generator can be written as,

$$P_e = (e_q' i_{gq}) + (X_q - X_d') i_{gd} i_{gq}$$

$$\Delta P_e = e_{q0}' \Delta i_{gq} + i_{gq0} \Delta e_q' + (X_q - X_d') [i_{gd0} \Delta i_{gq} + i_{gq0} \Delta i_{gd}] \quad (3.82)$$

Using the perturbed relations for the current output from (3.79) (3.80), the terminal voltage in (3.81) and the electrical power output in (3.82), the linearized state space model is obtained for the micro generator in terms of the linearized microgrid voltage components ΔV_{sd} and ΔV_{sq} .

3.7.2 The small-signal model of photovoltaic system

The small-signal model of the characteristic voltage equation of the PV module and the small signal model of the power conditioning unit will constitute the linearized model of the photovoltaic system.

The perturbed relation of the PV output voltage showing the dependency of PV voltage upon the PV output current as in (3.18) can be written as,

$$\frac{d\Delta v_{pv}}{dt} = -N_s \left[\frac{nv_T}{N_{prll} I_{photo} - i_{pv0} + N_{prll} I_s} + \frac{R_s}{N_{prll}} \right] \Delta i_{pv} \quad (3.83)$$

Considering the equation in the form,

$$\frac{d\Delta v_{pv}}{dt} = K_{pv}\Delta i_{pv} \quad (3.84)$$

Where the constant of proportionality is given as,

$$K_{pv} = -N_s \left[\frac{nv_T}{N_{prll}I_{photo} - i_{pv0} + N_{prll}I_s} + \frac{R_s}{N_{prll}} \right] \quad (3.85)$$

Each of the components involved in the power conditioning unit of the PV system such as the DC-boost converter, the DC-link capacitor, the DC/AC inverter, the LC output filter and coupling transmission line when linearized around an operating point will give the complete small-signal model.

For the DC-boost converter relation in (3.21), the perturbed relation is given as,

$$\frac{d\Delta i_{pv}}{dt} = \frac{1}{L_{dc}} [\Delta V_{pv} - (1 - d_{rpv})\Delta V_{dcpv}] \quad (3.86)$$

For the DC-link capacitor dynamic voltage equation described in (3.22), perturbation would give the following,

$$\begin{aligned} \frac{d\Delta V_{dcpv}}{dt} = \frac{-1}{C_{dcpv}} & [-i_{pfd0}m_{pv} \sin(\psi_{pv} + \theta)\Delta\psi_{pv} + m_{pv}\cos(\psi_{pv} + \\ & \theta)\Delta i_{pfd} + i_{pfd0} \cos(\psi_{pv} + \theta)\Delta m_{pv} + i_{pfd0}m_{pv} \cos(\psi_{pv} + \theta)\Delta\psi_{pv} + \\ & m_{pv}\sin(\psi_{pv} + \theta)\Delta i_{pfd} + i_{pfd0} \sin(\psi_{pv} + \theta)\Delta m_{pv} - (1 - d_{rpv})\Delta i_{pv}] \end{aligned} \quad (3.87)$$

The set of linear equations concerned with the LC filter output current along d-q frame are obtained from perturbations of (3.31) and (3.32) respectively.

$$\begin{aligned}
\frac{di_{pfd}}{dt} &= \frac{-\omega_0 R_{pf}}{L_{pf}} \Delta i_{pfd} + \omega_0 (\Delta i_{pfd} + i_{pfd0} \Delta \omega) - \frac{\omega_0 \Delta V_{cpd}}{L_{pf}} + \frac{\omega_0}{L_{pf}} [m_{pv} \cos(\psi_{pv} + \theta) \Delta V_{dcpv} \\
&- m_{pv} V_{dcpv0} \sin(\psi_{pv} + \theta) \Delta \psi_{pv} + V_{dcp0} \cos(\psi_{pv} + \theta) \Delta m_{pv}] - \frac{\omega_0 R_{pdr}}{L_{pf}} (\Delta i_{pfd} - \Delta i_{pq})
\end{aligned} \tag{3.88}$$

$$\begin{aligned}
\frac{di_{pq}}{dt} &= \frac{-\omega_0 R_{pf}}{L_{pf}} \Delta i_{pq} - \omega_0 (\Delta i_{pq} + i_{pq0} \Delta \omega) - \frac{\omega_0 \Delta V_{cpq}}{L_{pf}} + \frac{\omega_0}{L_{pf}} [m_{pv} \sin(\psi_{pv} + \theta) \Delta V_{dcpv} \\
&+ m_{pv} V_{dcpv0} \cos(\psi_{pv} + \theta) \Delta \psi_{pv} + V_{dcp0} \sin(\psi_{pv} + \theta) \Delta m_{pv}] - \frac{\omega_0 R_{pdr}}{L_{pf}} (\Delta i_{pq} - \Delta i_{pfd})
\end{aligned} \tag{3.89}$$

The d-q components of the linearized current output through the coupling inductance is obtained by perturbing the equations (3.34) and (3.35) as,

$$\begin{aligned}
\frac{di_{pd}}{dt} &= \frac{-\omega_0 R_p}{L_p} \Delta i_{pd} + \omega_0 (\Delta i_{pd} + i_{pd0} \Delta \omega) + \frac{\omega_0}{L_p} (\Delta V_{cpd} - \Delta V_{sd}) \\
&+ \frac{\omega_0 R_{pdr}}{L_p} (\Delta i_{pfd} - \Delta i_{pd})
\end{aligned} \tag{3.90}$$

$$\begin{aligned}
\frac{di_{pq}}{dt} &= \frac{-\omega_0 R_p}{L_p} \Delta i_{pq} + \omega_0 (\Delta i_{pq} + i_{pq0} \Delta \omega) + \frac{\omega_0}{L_p} (\Delta V_{cpq} - \Delta V_{sq}) \\
&+ \frac{\omega_0 R_{pdr}}{L_p} (\Delta i_{pq} - \Delta i_{pfd})
\end{aligned} \tag{3.91}$$

Finally the dynamical relations for the filter capacitor voltage given in (3.37) and (3.38) are linearized to give,

$$\frac{dV_{cpd}}{dt} = \omega_0 (\Delta V_{cpq} + V_{cpq0} \Delta \omega) + \frac{\omega_0}{C_{pf}} (\Delta i_{pfd} - \Delta i_{pd}) \tag{3.92}$$

$$\frac{dV_{cpq}}{dt} = -\omega_0(\Delta V_{cpd} + V_{cpd0}\Delta\omega) + \frac{\omega_0}{C_{pf}}(\Delta i_{pfq} - \Delta i_{pq}) \quad (3.93)$$

Thus the linearized small-signal state space vector for the PV generation unit consists of the following,

$$\Delta X_{PV} = [\Delta i_{pv}, \Delta V_{dcpv}, \Delta i_{pfd}, \Delta i_{pfq}, \Delta i_{pd}, \Delta i_{pq}, \Delta V_{cpd}, \Delta V_{cpq}] \quad (3.94)$$

3.7.3 The small-signal model of fuel cell system

The small-signal model of the characteristic voltage equation of the fuel cell stack and the small signal model of the power conditioning unit will constitute the linearized model of the fuel cell system.

The characteristic equation of the fuel cell stack voltage when perturbed will give,

$$\frac{d\Delta v_{fc}}{dt} = -NA \frac{i_0}{i_{fc0}} \Delta i_{fc} - R_{ohm} \Delta i_{fc} \quad (3.95)$$

This equation can be written in the form as,

$$\frac{d\Delta v_{fc}}{dt} = K_{fc} \Delta i_{fc} \quad (3.96)$$

The linearized model of the power conditioning unit of the fuel cell system will include the transient small-signal models for each of the components such as the DC-boost converter, the DC-link capacitor, the DC/AC Inverter, the LC filter and coupling transmission line.

The linearized state variables selected for the fuel cell system are as follows,

$$\Delta V_{dcfc}, \Delta i_{ffd}, \Delta i_{ffq}, \Delta i_{fd}, \Delta i_{fq}, \Delta V_{cfd}, \Delta V_{cfq} \quad (3.97)$$

3.7.4 The small-signal model of wind system

Linearized model of the horizontal axis wind turbine, the permanent magnet synchronous generator, the associated power conditioning unit will constitute the small-signal model of the wind system. The electromechanical dynamic relations involved with the WT-PMSG system two mass models as described in section 3.5.1 are perturbed to yield the linearized state equations as given under,

$$\frac{d\Delta\theta_s}{dt} = \omega_0[\Delta\omega_t - \Delta\omega_w] \quad (3.98)$$

$$\frac{d\Delta\omega_t}{dt} = \frac{1}{2H_t}(-K_s\Delta\theta_s - D_t(\Delta\omega_t)) \quad (3.99)$$

$$\frac{d\Delta\delta_w}{dt} = \omega_0(\Delta\omega_w) \quad (3.100)$$

$$\frac{d\Delta\omega_w}{dt} = \frac{1}{2H_g}(K_s\Delta\theta_s - \Delta P_{ew} - D_g(\Delta\omega_w)) \quad (3.101)$$

Perturbation of the terminal voltage of PMSG system as provided in equations (3.55) and (3.56) results in linearized form of V_{gw} .

$$V_{gw} = V_{gwd} + jV_{gwq} \text{ where}$$

$$V_{gwd} = m_{wr}V_{dcw}\sin\delta_w \text{ and } V_{gwq} = m_{wr}V_{dcw}\cos\delta_w \quad (3.102)$$

$$\begin{aligned} \Delta V_{gwd} = \\ m_{wr}V_{dcw0}\cos\delta_w\Delta\delta_w + m_{wr}\sin\delta_w\Delta V_{dcw} + V_{dcw0}\sin\delta_w\Delta m_{wr} \end{aligned} \quad (3.103)$$

$$\begin{aligned} \Delta V_{gwq} = \\ -m_{wr}V_{dcw0}\sin\delta_w\Delta\delta_w + m_{wr}\cos\delta_w\Delta V_{dcw} + V_{dcw0}\cos\delta_w\Delta m_{wr} \end{aligned} \quad (3.104)$$

Equations (3.103) and (3.104) are utilized to derive the linearized equation of the electrical power output obtained from the PMSG as stated below,

$$P_{ew} = R_a(i_{gwd}^2 + i_{gwq}^2) + V_{gwd}i_{gwd} + V_{gwq}i_{gwq}$$

Perturbing the above equation around an operating point would give,

$$\begin{aligned} \Delta P_{ew} = 2R_a(i_{gwd0}\Delta i_{gwd} + i_{gwq0}\Delta i_{gwq}) + V_{gwd0}\Delta i_{gwd} + i_{gwd0}\Delta V_{gwd} + V_{gwq0}\Delta i_{gwq} \\ + i_{gwq0}\Delta V_{gwq} \end{aligned}$$

Incorporation of expressions of ΔV_{gwd} and ΔV_{gwq} into the above gives,

$$\begin{aligned} \Delta P_{ew} = P_{ew1}\Delta i_{gwd} + P_{ew2}\Delta i_{gwq} + P_{ew3}\Delta\delta_w + P_{ew4}\Delta V_{dcw} + \\ P_{ew5}\Delta m_{wr} \end{aligned} \quad (3.105)$$

Here the various terms are,

$$P_{ew1} = V_{gwd0} + 2R_a i_{gwd0} \quad P_{ew2} = V_{gwq0} + 2R_a i_{gwq0}$$

$$P_{ew3} = i_{gwd0}m_{wr}V_{dcw}\cos\delta_w - i_{gwq0}m_{wr}V_{dcw}\sin\delta_w$$

$$P_{ew4} = i_{gwd0}m_{wr}\sin\delta_w + i_{gwq0}m_{wr}\cos\delta_w$$

$$P_{ew5} = i_{gwd0}V_{dcw}\sin\delta_w + i_{gwq0}V_{dcw}\cos\delta_w$$

The PMSG stator output currents along d-q axes as mentioned in equations (3.51) and (3.52) are perturbed to yield the following,

$$\frac{d\Delta i_{gwd}}{dt} = \frac{\omega_0}{X_{dw}} [-R_a\Delta i_{gwd} + X_{qw}\Delta i_{gwq} + X_{qw}i_{gwq0}\Delta\omega - \Delta V_{gwd}] \quad (3.106)$$

$$\begin{aligned} \frac{d\Delta i_{gwq}}{dt} = \frac{\omega_0}{X_{dw}} [-R_a\Delta i_{gwq} - X_{dw}\Delta i_{gwd} - X_{dw}i_{gwd0}\Delta\omega + E_{fdo}\Delta\omega \\ - \Delta V_{gwq}] \end{aligned} \quad (3.107)$$

For the power conditioning unit employed in wind system, the small-signal model includes the linear equations for the DC-link capacitor, LC filter and coupling inductance.

The DC-link capacitor voltage as described in (3.62) can be linearized as,

$$\frac{dV_{dcw}}{dt} = \frac{1}{C_w} [m_{wr} \sin \delta_w i_{gwd} + \cos \delta_w i_{gwq} - m_{wi} \cos(\psi_{wi} + \theta) i_{wd} - m_{wi} \sin(\psi_{wi} + \theta) i_{wq}]$$

Differentiation on both sides would give,

$$\frac{d\Delta V_{dcw}}{dt} = \frac{1}{C_w} [m_{wr} \sin \delta_w \Delta i_{gwd} + m_{wr} \cos \delta_w \Delta i_{gwq} + m_{wr} (i_{gwd0} \cos \delta_w - i_{gwq0} \sin \delta_w) \Delta \delta_w$$

$$+ (\sin \delta_w i_{gwd0} + \cos \delta_w i_{gwq0}) \Delta m_{wr} - m_{wi} \cos(\theta + \psi_{wi}) \Delta i_{wd} - m_{wi} \sin(\theta + \psi_{wi}) \Delta i_{wq}$$

$$- (i_{wd0} \cos(\theta + \psi_{wi}) + i_{wq0} \sin(\theta + \psi_{wi})) \Delta m_{wi} + m_{wi} (i_{wd0} \sin(\theta + \psi_{wi})$$

$$- i_{wq0} \cos(\theta + \psi_{wi})) \Delta \psi_{wi}$$

(3.108)

The LC filter output current along d-q axes as given in (3.64) and (3.65) can be perturbed as depicted,

$$\frac{d\Delta i_{wfd}}{dt} = \frac{-\omega_0 R_{wf}}{L_{wf}} \Delta i_{wfd} + \omega_0 (\Delta i_{wfq} + i_{wfq0} \Delta \omega) + \frac{\omega_0}{L_{wf}} [m_{wi} \cos(\psi_{wi} + \theta) \Delta V_{dcw}$$

$$- m_{wi} V_{dcw0} \sin(\psi_{wi} + \theta) \Delta \psi_{wi} + V_{dcw0} \cos(\psi_{wi} + \theta) \Delta m_{wi}] - \frac{\omega_0 \Delta V_{c wd}}{L_{wf}}$$

$$- \frac{\omega_0 R_{wdr}}{L_{wf}} (\Delta i_{wfd} - \Delta i_{wq})$$

(3.109)

$$\begin{aligned}
\frac{d\Delta i_{wfq}}{dt} &= \frac{-\omega_0 R_{wf}}{L_{wf}} \Delta i_{wfq} - \omega_0 (\Delta i_{wfd} + i_{wfd0} \Delta \omega) + \frac{\omega_0}{L_{wf}} [m_{wi} \sin(\psi_{wi} + \theta) \Delta V_{dcw} \\
&+ m_{wi} V_{dcw0} \cos(\psi_{wi} + \theta) \Delta \psi_{wi} + V_{dcw0} \sin(\psi_{wi} + \theta) \Delta m_{wi}] - \frac{\omega_0 \Delta V_{cwq}}{L_{wf}} \\
&- \frac{\omega_0 R_{wdr}}{L_{wf}} (\Delta i_{wfq} - \Delta i_{wq})
\end{aligned} \tag{3.110}$$

The coupling inductor current linearized equations along d-q reference frame are given below,

$$\frac{d\Delta i_{wd}}{dt} = \frac{-R_w}{L_w} \Delta i_{wd} + \omega_0 (\Delta i_{wq} + i_{wq0} \Delta \omega) + \frac{1}{L_w} (\Delta V_{c wd} - \Delta V_{sd}) + \frac{\omega_0 R_{wdr}}{L_w} (\Delta i_{wfd} - \Delta i_{wd}) \tag{3.111}$$

$$\frac{d\Delta i_{wq}}{dt} = \frac{-R_w}{L_w} \Delta i_{wq} + \omega_0 (\Delta i_{wd} + i_{wd0} \Delta \omega) + \frac{1}{L_w} (\Delta V_{cwq} - \Delta V_{sq}) + \frac{\omega_0 R_{wdr}}{L_w} (\Delta i_{wfq} - \Delta i_{wq}) \tag{3.112}$$

The linearized state equations pertaining to the filter capacitor are given as,

$$\frac{d\Delta V_{c wd}}{dt} = \omega_0 (\Delta V_{cwq} + V_{cwq0} \Delta \omega) + \frac{1}{C_{wf}} (\Delta i_{wfd} - \Delta i_{wd}) \tag{3.113}$$

$$\frac{d\Delta V_{cwq}}{dt} = -\omega_0 (\Delta V_{c wd} + V_{c wd0} \Delta \omega) + \frac{1}{C_{wf}} (\Delta i_{wfq} - \Delta i_{wq}) \tag{3.114}$$

Thus the wind system linearized model is represented through the following state vector,

$$\Delta X_{wind} = [\Delta\theta_s, \Delta\omega_t, \Delta\delta_w, \Delta\omega_w, \Delta i_{gwd}, \Delta i_{gwdq}, \Delta V_{dcw}, \Delta i_{wfd}, \Delta i_{wfdq}, \Delta i_{wd}, \Delta i_{wdq}, \Delta V_{c wd}, \Delta V_{c wdq}] \quad (3.115)$$

3.8 The Composite Microgrid Model

In this section electrical microgrid formed with conventional micro-turbine, photovoltaic unit, fuel cell system and wind power is modeled with dynamical differential equations. The non-linear model so obtained is perturbed around an operating point in order to find small-signal linearized system description, which can be used to determine the threshold limit of power extraction from renewable sources for satisfactory operation of the microgrid. The results obtained through small-signal Eigen value analysis are verified by carrying out non-linear time domain simulations.

3.8.1 Microgrid system model

The microgrid model considered for small-signal linear analysis is shown in Figure 3.17. Exhaustive power electronic circuitry consisting of voltage source converters and LC output filters interface the renewable energy systems such as photovoltaic, fuel cell and wind generation. Incorporation of load at the common bus is also considered. An energy storage device coupled through a voltage inverter is included in the study as a central supervisory controller to take correction actions when necessary to mitigate transients.

Employing KCL to the microgrid model shown in Figure 3.17, the composite state space model can be derived. The sums of input currents at the PCC bus are equal to the outgoing currents according to KCL as depicted under:

$$i_g + i_p + i_f + i_w + i_s = i_b + i_L \quad (3.116)$$

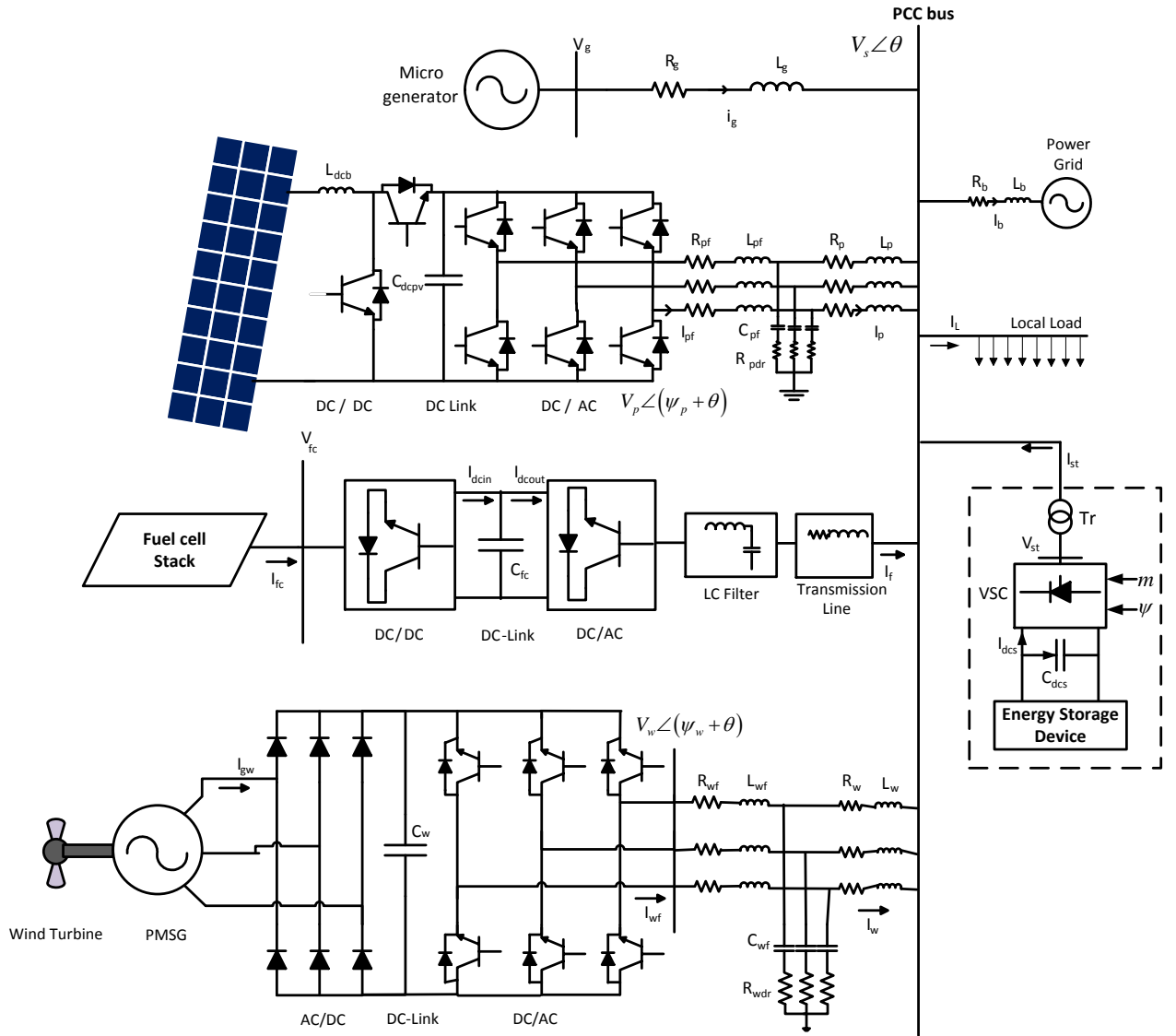


Figure 3.17: Composite microgrid model

Splitting the equation (3.116) along d-q frames gives,

$$i_{gd} + i_{pd} + i_{fd} + i_{wd} + i_{sd} = i_{bd} + i_{Ld} \quad (3.117)$$

$$i_{gq} + i_{pq} + i_{fq} + i_{wq} + i_{sq} = i_{bq} + i_{Lq} \quad (3.118)$$

The expressions for micro-generator current along d-q axes can be substituted by their respective relations as mentioned in equations (3.8) and (3.9), whereas the load current and grid current are derived as functions of microgrid voltage components V_{sd} and V_{sq} as,

Modeling the load at the PCC bus as a simple admittance with $Y = g - jb$, the load current can be expressed as $i_L = V_S Y$

$$\begin{aligned} i_{Ld} + ji_{Lq} &= (V_{sd} + jV_{sq})(g - jb) \\ i_{Ld} &= gV_{sd} + bV_{sq} \text{ and } i_{Lq} = gV_{sq} - bV_{sd} \end{aligned} \quad (3.119)$$

The current traversing to the utility grid i_b can be written as,

$$\begin{aligned} i_b &= \frac{V_s - V_b}{R_b + jX_b} \\ i_{bd} + ji_{bq} &= \frac{V_{sd} + jV_{sq} - (V_b \sin\delta + jV_b \cos\delta)}{R_b + jX_b} \end{aligned} \quad (3.120)$$

Now equating the real and imaginary parts in (3.120), the d-q current components are obtained as shown,

$$i_{bd} = \frac{(V_{sq} - V_b \sin\delta)R_b + (V_{sd} - V_b \cos\delta)X_b}{R_b^2 + X_b^2} \quad (3.121)$$

$$i_{bq} = \frac{(V_{sd} - V_b \cos\delta)R_b + (V_{sq} - V_b \sin\delta)X_b}{R_b^2 + X_b^2} \quad (3.122)$$

Thus the various current components are substituted in the equations (3.117) and (3.118), whereupon solved to yield microgrid bus voltages as,

$$i_{gd} + i_{pd} + i_{fd} + i_{wd} + i_{sd} = i_{bd} + i_{Ld}$$

$$\frac{-R_g V_{sd} + (e_q' - V_{sq})X_2}{Z_1} + i_{pd} + i_{fd} + i_{wd} + i_{sd} = \frac{(V_{sq} - V_b \sin\delta)R_b + (V_{sq} - V_b \cos\delta)X_b}{Z_b} + gV_{sd} + bV_{sq}$$

Upon simplification this will result in,

$$\begin{aligned} & [gZ_b Z_1 + Z_1 R_b + R_g Z_b] V_{sd} + [bZ_b Z_1 + X_b Z_1 + X_2 Z_b] V_{sq} \\ & = Z_b Z_1 (i_{pd} + i_{fd} + i_{wd} + i_{sd}) + Z_b e_q' X_2 + V_b \cos\delta X_b Z_1 + V_b \sin\delta Z_1 R_b \end{aligned} \quad (3.123)$$

Similarly from equation (3.118) the currents can be written as,

$$i_{gq} + i_{pq} + i_{fq} + i_{wq} + i_{sq} = i_{bq} + i_{Lq}$$

$$\begin{aligned} & \frac{V_{sd} Z_1 - R_g^2 V_{sd} + R_g (e_q' - V_{sq}) X_2}{X_2 Z_1} + i_{pq} + i_{fq} + i_{wq} + i_{sq} = \frac{(V_{sq} - V_b \cos\delta)R_b + (V_{sq} - V_b \sin\delta)X_b}{Z_b} + gV_{sq} - bV_{sd} \\ & - [X_b X_2 Z_1 + bZ_b X_2 Z_1 + Z_1 Z_b - R_g^2 Z_b] V_{sd} + X_2 [gZ_b Z_1 + Z_1 R_b + R_g Z_b] V_{sq} \\ & = Z_b X_2 Z_1 (i_{pq} + i_{fq} + i_{wq} + i_{sq}) + R_g Z_b e_q' X_2 + V_b \cos\delta R_b X_2 Z_1 - V_b \sin\delta X_b X_2 Z_1 \end{aligned} \quad (3.124)$$

Now solving equations (3.123) and (3.124) for microgrid bus voltage components to produce the following,

$$V_{sq} = D (i_{pd} + i_{fd} + i_{wd} + i_{sd}) + E e_q' + F (i_{pq} + i_{fq} + i_{wq} + i_{sq}) + G V_b \quad (3.125)$$

$$V_{sd} = \frac{1}{A} [Z_b Z_1 (i_{pd} + i_{fd} + i_{wd} + i_{sd}) + Z_b X_2 e_q' + V_b Z_1 (R_b \sin\delta + X_b \cos\delta) - B V_{sq}] \quad (3.126)$$

Here the various constants are as given below.

$$A = [gZ_b Z_1 + Z_1 r_b + r_t Z_b] \quad B = [bZ_b Z_1 + X_b Z_1 + X_2 Z_b]$$

$$C = [X_b X_2 Z_1 + bZ_b X_2 Z_1 + Z_1 Z_b - r_t^2 Z_b] \quad \text{Den} = BC + A^2 X_2$$

$$D = \frac{1}{\text{Den}} C Z_b Z_1 \quad E = \frac{1}{\text{Den}} (C Z_b X_2 + Z_b X_2 r_t A) \quad F = \frac{1}{\text{Den}} (A X_2 Z_1 Z_b)$$

$$G = \frac{1}{\text{Den}} [Z_1 C (r_b \sin\delta + X_b \cos\delta) + A X_2 Z_1 (r_b \cos\delta - X_b \sin\delta)]$$

The microgrid bus voltage components present in the differential equations of the various component models are then replaced by the equations (3.125) and (3.126) to obtain the nonlinear form as,

$$\frac{dX}{dt} = f(X, u) \quad (3.127)$$

The state vector and the corresponding control vector are given as,

$$X = [X_{Gen}, X_{Controller}, X_{PV}, X_{Wind}, X_{FC}]$$

$$X_{Gen} = [\delta, \omega, e'_q, E_{fd}]$$

$$X_{Controller} = [i_{sd}, i_{sq}, V_{dcs}]$$

$$X_{PV} = [i_{pfd}, i_{pfq}, i_{pd}, i_{pq}, V_{cpd}, V_{cpq}, i_{pv}, V_{dcpv}]$$

$$X_{Wind} = [\theta_s, \omega_t, i_{gwd}, i_{gqw}, \delta_w, \omega_w, i_{wfd}, i_{wfq}, i_{wd}, i_{wq}, V_{cwd}, V_{cwq}, V_{dcw}]$$

$$X_{FC} = [i_{ffd}, i_{ffq}, i_{fd}, i_{fq}, V_{cfd}, V_{cfq}, i_{fc}, V_{dcf}]$$

And the control vector is given as,

$$u = [u_{Controller}, u_{PV}, u_{Wind}, u_{FC}]$$

$$u_{Controller} = [m, \psi], \quad u_{PV} = [m_{pv}, \psi_{pv}], \quad u_{Wind} = [m_{wr}, m_{wi}, \psi_{wi}],$$

$$u_{FC} = [m_{fc}, \psi_{fc}]$$

CHAPTER 4

EVALUATION OF MICROGRID PERFORMANCE

The performance of the microgrid for different generation mixes of the DGs is presented in this chapter. The composite non-linear microgrid system discussed in section 3.8 is perturbed around an operating point to obtain linearized model. A small signal analysis of the system is followed by the nonlinear system modeling. Linearized system analysis determines the amount of generation mix for satisfactory operation of the microgrid while the nonlinear analysis is carried out to verify the results obtained through small-signal analysis.

4.1 Small-Signal Analysis

The microgrid system model developed in the previous chapter is represented by the state equations of the form:

$$\frac{dX}{dt} = f(X, u) \quad (4.1)$$

Linearized form of the equations can be written as:

$$\left[\frac{d\Delta X}{dt} \right] = [A_{composite}][\Delta X] + [B][\Delta U] \quad (4.2)$$

The state matrix $A_{composite}$ is given by:

$$A_{composite} = \begin{bmatrix} (A_{GG})_{4 \times 4} & (A_{GP})_{4 \times 8} & (A_{GF})_{4 \times 8} & (A_{GW})_{4 \times 13} \\ (A_{PG})_{8 \times 4} & (A_{PP})_{8 \times 8} & (A_{PF})_{8 \times 8} & (A_{PW})_{8 \times 13} \\ (A_{FG})_{8 \times 4} & (A_{FP})_{8 \times 8} & (A_{FF})_{8 \times 8} & (A_{FW})_{8 \times 13} \\ (A_{WG})_{13 \times 4} & (A_{WP})_{13 \times 8} & (A_{WF})_{13 \times 8} & (A_{WW})_{13 \times 13} \end{bmatrix}_{33 \times 33}$$

Here, the linearized system states ΔX are the variations of $X_{Gen}, X_{PV}, X_{Wind}, X_{FC}$ and the control U is a vector of u_{PV}, u_{Wind}, u_{FC} .

For a particular system operating scenario with power extraction from micro-generation=0.2 pu, the PV system=0.4 pu, the fuel cell system=0.4 pu and the wind energy=0.4 pu, the eigenvalues as obtained from linearized model are given in Table 4.1. It is assumed that the load on the microgrid is 1.4 pu operating steady state at a grid voltage of 0.985 pu. The dominant eigenvalues or the eigenvalues which can contribute to the system instability are listed in Table 4.2. These critical Eigen states as determined from their location with respect to imaginary axis

Table 4.1: Eigen values of the composite microgrid model

<i>DG Source</i>	<i>Real part</i>	<i>Imaginary Part</i>
<i>PMSG wind energy system</i>	-299.886	$\pm 3090.804i$
	-266.620	$\pm 2205.433i$
	-4.64124	$\pm 377.749i$
	-188.475	$\pm 511.625i$
	-0.52494	$\pm 34.1296i$
	-0.083664	$\pm 4.09577i$

	-1.094161	
<i>Microgenerator</i>	-98.7752	
	-0.01067	$\pm 16.8988i$
	-1.67072	
<i>Photovoltaic system</i>	-106.522	$\pm 3104.250i$
	-82.9422	$\pm 2218.914i$
	-0.31482	$\pm 3.650615i$
	-188.246	$\pm 512.5659i$
<i>Fuel cell system</i>	-106.522	$\pm 3104.250i$
	-82.9422	$\pm 2218.914i$
	-188.246	$\pm 512.5659i$
	-1.14658	$\pm 3.634041i$

Table 4.2: Critical Eigen values associated with composite microgrid

<i>System component</i>	<i>Eigen value</i>	<i>Modes</i>
<i>Wind turbine</i>	$-0.083664 \pm 4.09577i$	Electromechanical modes
<i>Microgenerator</i>	$-0.01067 \pm 16.8988i$	Electromechanical modes
<i>Photovoltaic system</i>	$-0.31482 \pm 3.650615i$	Inverter oscillatory modes
<i>PMSG machine</i>	$-0.52494 \pm 34.1296i$	Electromechanical modes

The identification of penetration limits from various renewable sources is determined by considering various operating conditions of the microgrid. The variations in real part of the dominant eigenvalues were observed for different penetration levels. Keeping the PV and fuel cell power penetration into the microgrid constant, the effect of microgenerator and wind energy on the system stability is examined. It is assumed that the PV and fuel cell powers are held constant at 0.2 pu while the micro-generator power contributed in varied from 0.1 pu to 0.7 pu and wind power output is changed in steps of 0.2 pu beginning from 0.2 pu until 1.0 pu. The stability of the microgrid is assessed through the plot of variation of real part of the dominant eigenvalue when the penetration powers of microgenerator change as shown in Figure 4.1. It can be seen that as the wind power participation is increased, the stability margin worsens. Also it is noticed that the higher microgenerator power improves the system stability boundaries.

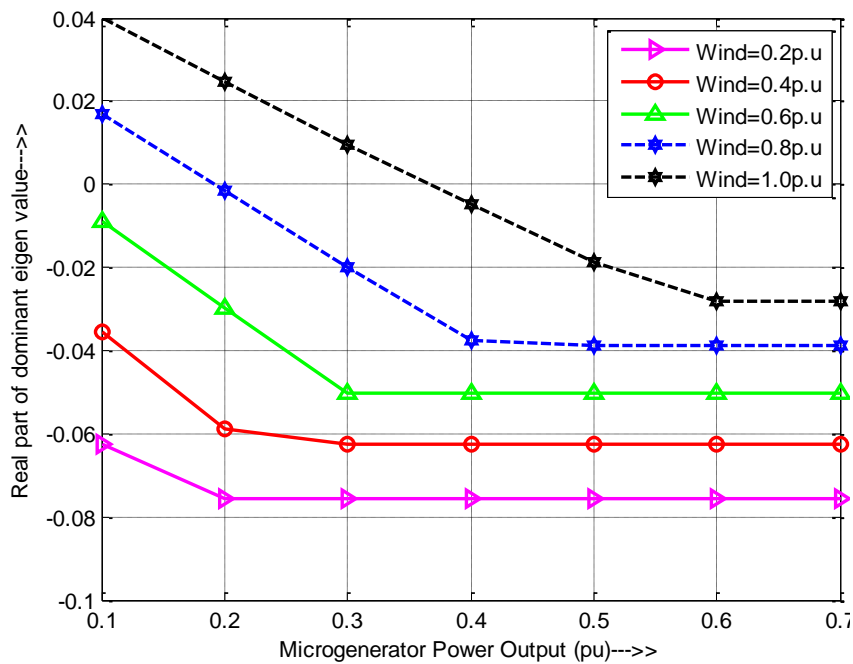


Figure 4.1: Plot of dominant eigenvalues of microgenerator for varying wind penetration

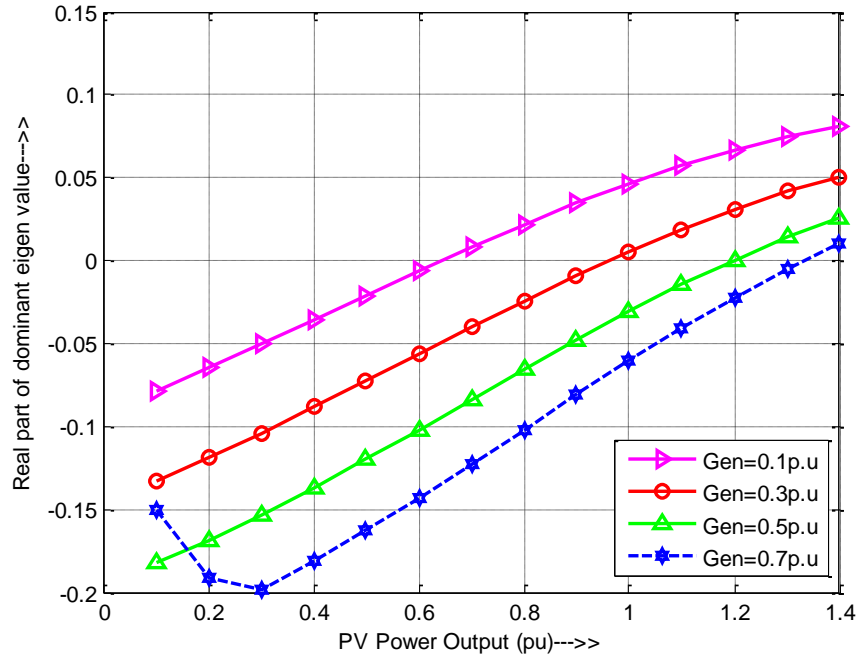


Figure 4.2: Plot of dominant eigenvalues of microgrid for varying PV power output

Figure 4.2 shows the effect of PV power participation on the microgrid stability for various values of microgenerator power output. The power extracted from wind energy and fuel cell system is kept fixed at 0.2 pu while the load is held constant at 1.0 pu. For a particular value of microgenerator power the variation real part of dominant eigenvalue is plotted against varying PV power penetration. It is considered that the PV power is varied from 0.1pu to 1.4 pu and the microgenerator power is changed in steps of 0.1pu, 0.3pu, 0.5pu and 0.7 pu respectively. From Figure 4.2, it can be noted that the stability of the microgrid system is enhanced as the participation of microgenerator is increased. On the other hand, greater integration of PV power worsens the system stability. For example it can be said that the system enters into the unstable region for PV power of 0.8pu if the micro-generation is below 0.1pu.

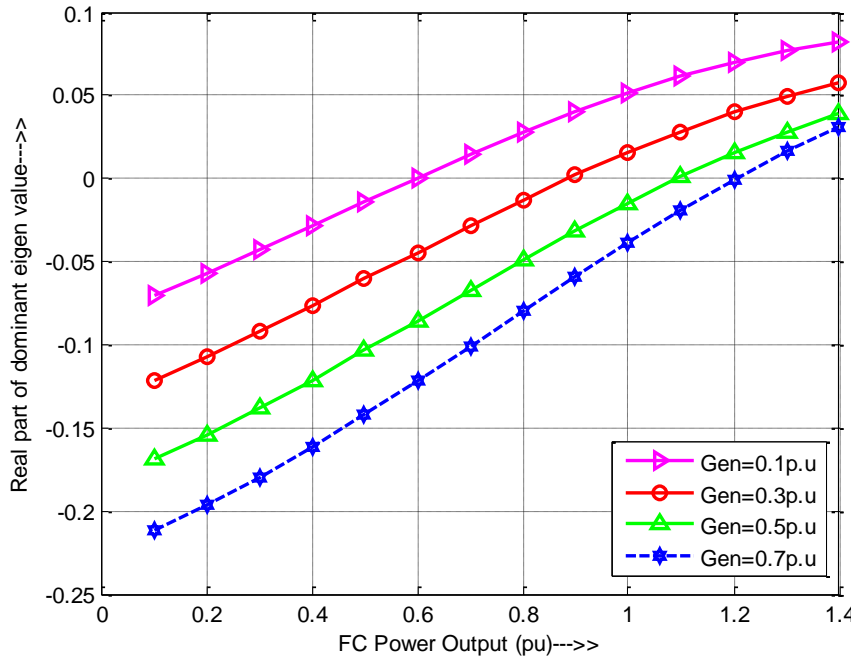


Figure 4.3: Plot of dominant eigenvalues of microgrid for varying fuel cell power penetration

The effect of fuel cell power participation towards the microgrid stability can be seen in Figure 4.3. To evaluate the fuel cell effect, the power obtainable from other sources such as wind and PV system are kept fixed at 0.2 pu. The penetration of fuel cell power is changed from 0.1 pu to 1.4 pu under step changes in micro generation. It is observed that increased participation of fuel cell distorts the system stability and there is a threshold limit for power extraction. On the other hand, it is also noticed that increased power contribution from microalternator enhance the system stability.

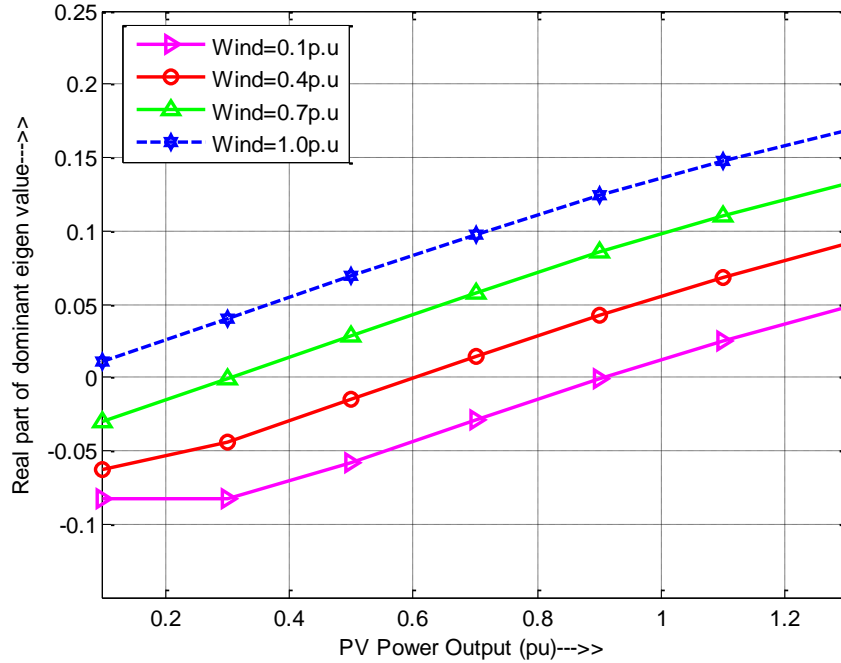


Figure 4.4: Plot of dominant eigenvalues of PV system for various wind participation

In Figure 4.4, the behavior of microgrid stability in terms of eigenvalue analysis when the power obtainable from PV and wind system is taken into account can be observed. Here, the micro generation and fuel cell powers are held fixed at 0.2pu each and the effect of varying PV penetration for various values of wind power is studied. It can be noticed that increased renewable power contribution degrades the system stability margin. A similar type of observation can be made when the fuel cell power extraction is varied against wind power for fixed powers from other sources. As shown in Figure 4.5, the increased contribution of fuel cell power worsens the microgrid transient stability. For example it can be inferred that for wind power penetration at 1.0pu the microgrid enters into unstable mode if the fuel cell power is more than 0.2pu.

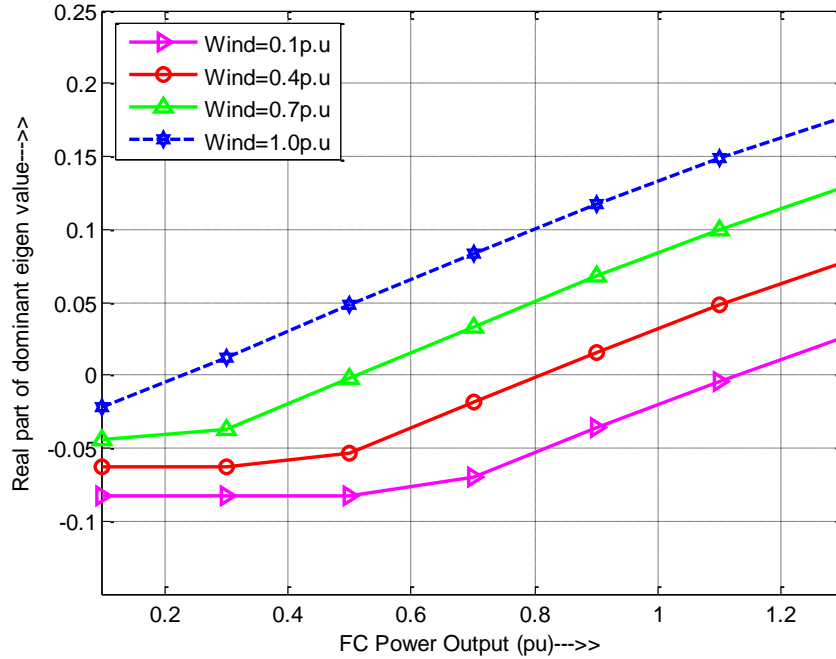


Figure 4.5: Plot of dominant eigenvalues of fuel cell system for various wind participation

The effect of variation of real and reactive components of load on the microgrid dynamic stability is shown in Figure 4.6. The variations in the real part of dominant eigenvalues are plotted against varying reactive load. It is considered that the real load varies from 0.4pu to 0.7pu while the reactive load is changed uniformly from 0.1pu to 1.1pu in steps of 0.05pu. In this case, the power taken from various sources such as the micro generation, the wind system, PV and fuel cell device are kept fixed at 0.2pu each. It is seen that increased in the reactive power demand the system loose stability and the stability margin is reduced. On the other hand, for a particular value of reactive load increase in the real load enhance the stability due to increase in the system power factor.

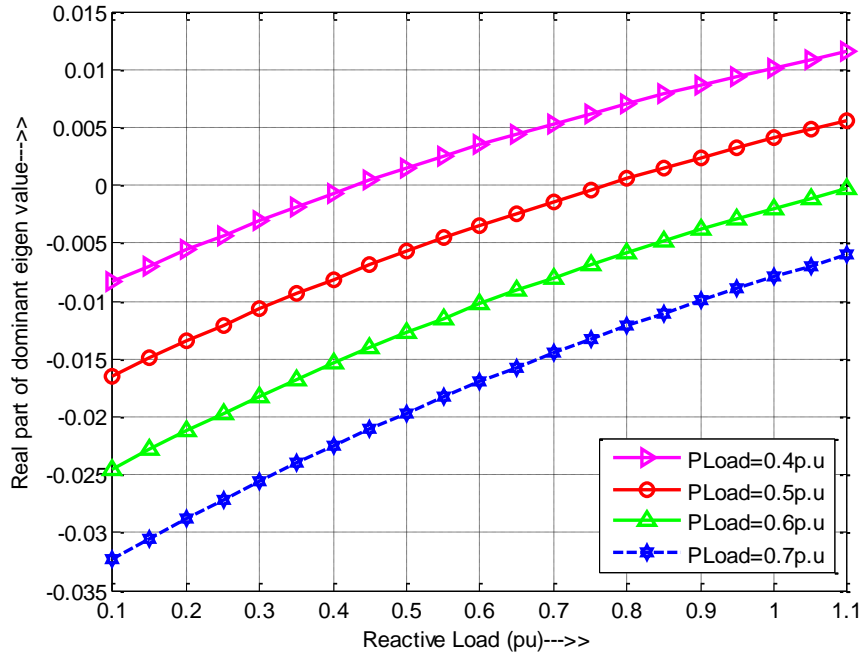


Figure 4.6: Plot of dominant eigenvalues of microgrid for varying load requirement

It can be inferred from the eigenvalue based analysis that there is a threshold limit of power extracted from renewable sources without affecting the system stability. Increase in the power penetration from renewables deteriorates the system transient performance and may lead to sustained oscillations.

4.2 Non-linear Time Domain Analysis

To verify the results obtained in the linearized small-signal analysis, nonlinear time domain simulations were carried out for the composite microgrid model. For two different operating scenarios the system stability is investigated by simulating a transient condition. A disturbance of 0.15 pu input torque pulse for duration of 0.3 sec is applied at the micro generation system. Keeping the power obtained from microgenerator, PV, fuel

cell fixed at 0.2 pu, 0.3 pu and 0.3 pu respectively, and the load kept at 1pu, the performance of the microgrid is observed for two different cases a) wind system delivers 0.9 pu and b) wind system delivers 0.1 pu. The responses for the microgrid voltage, the microgenerator speed deviations, PV DC-link voltage, wind DC-link voltage, VSC DC-link voltage and VSC current are shown in Figure 4.7-Figure 4.12. It can be seen that, the first operating condition pertaining to wind power of 0.9 pu represents unstable region while the operating point corresponding to wind power of 0.1pu shows stable operation.

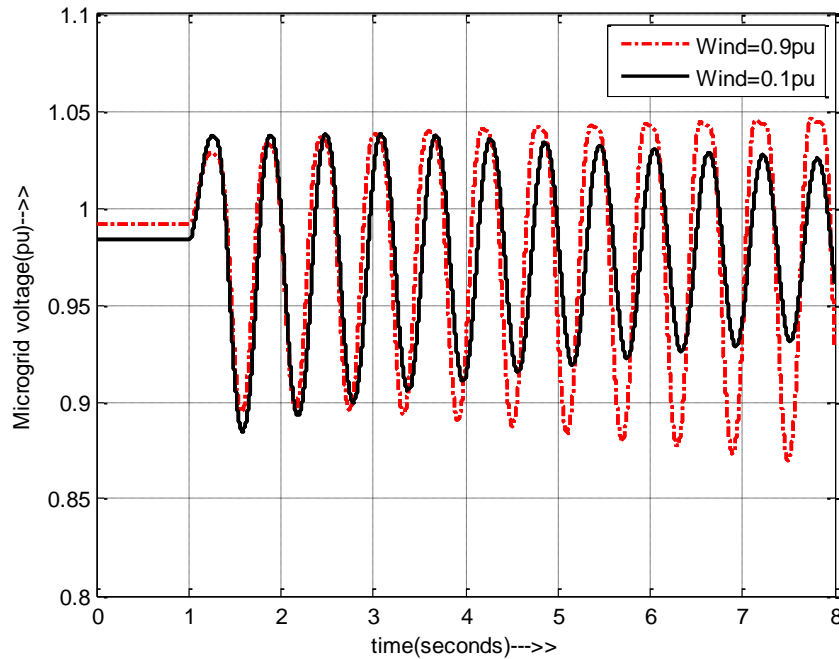


Figure 4.7: Response of the microgrid voltage following a disturbance of 15% torque pulse for 0.3 sec a) wind generation at 0.9 pu b) wind generation at 0.1pu

It can be noticed from Figure 4.7, that higher participation of renewable source in the form of wind power affects the system transient stability making it prone to undamped oscillations. For wind power at 0.9 pu a small disturbance in the system results in unstable operation while for wind power fixed at 0.1pu the system oscillations vanish and stable operating scenario is established.

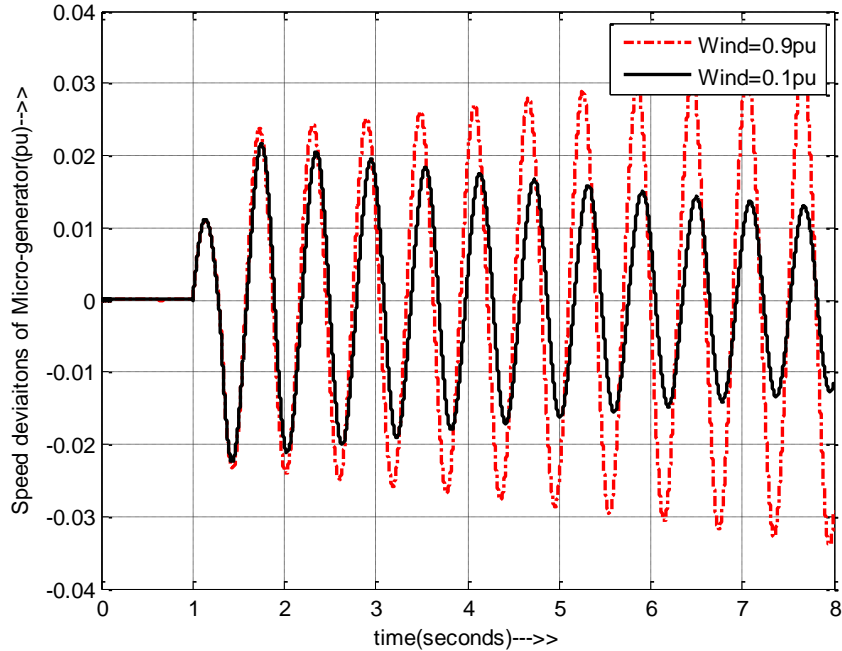


Figure 4.8: Response of the microgenerator speed deviations following a disturbance of 15% torque pulse for 0.3 sec a) wind generation at 0.9 pu b) wind generation at 0.1pu

The speed deviations in the microgenerator following a 15% torque pulse for 300 msec is shown in Figure 4.8. It is observed that for an operating condition with wind power of 0.9 pu the speed variations grow in amplitude and may reach to very large values. The transient oscillations die out for wind power of 0.1 pu thereby demonstrating stable operation of the microgrid.

The variations in PV DC-link voltage and wind system DC-link voltage are shown in Figure 4.9-Figure 4.10. Operation at wind power of 0.9 pu results in undamped oscillations of large amplitudes whereas for wind power participation of 0.1 pu damped oscillations are observed and system stability is restored.

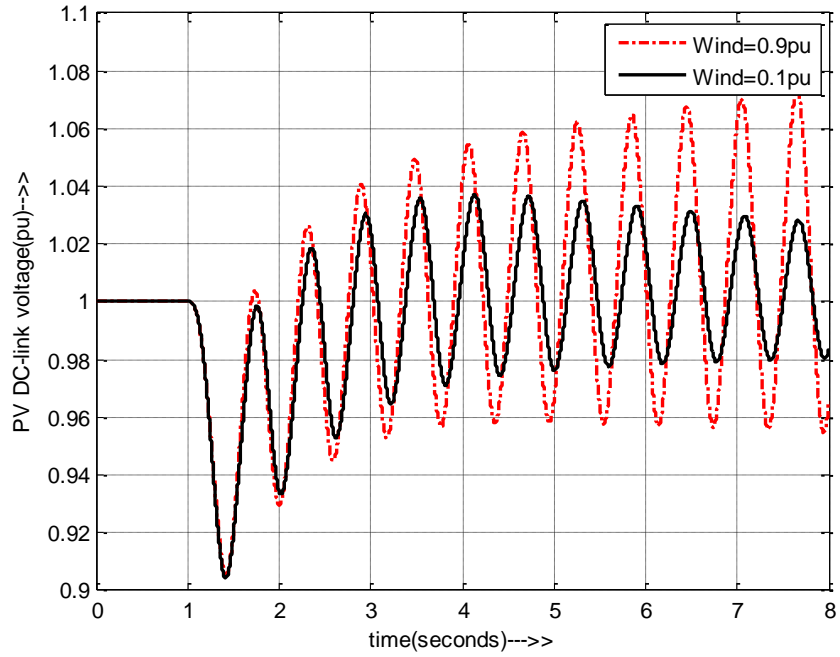


Figure 4.9: Response of the PV DC-link voltage following a disturbance of 15% torque pulse for 0.3 sec a) wind generation at 0.9 pu b) wind generation at 0.1pu

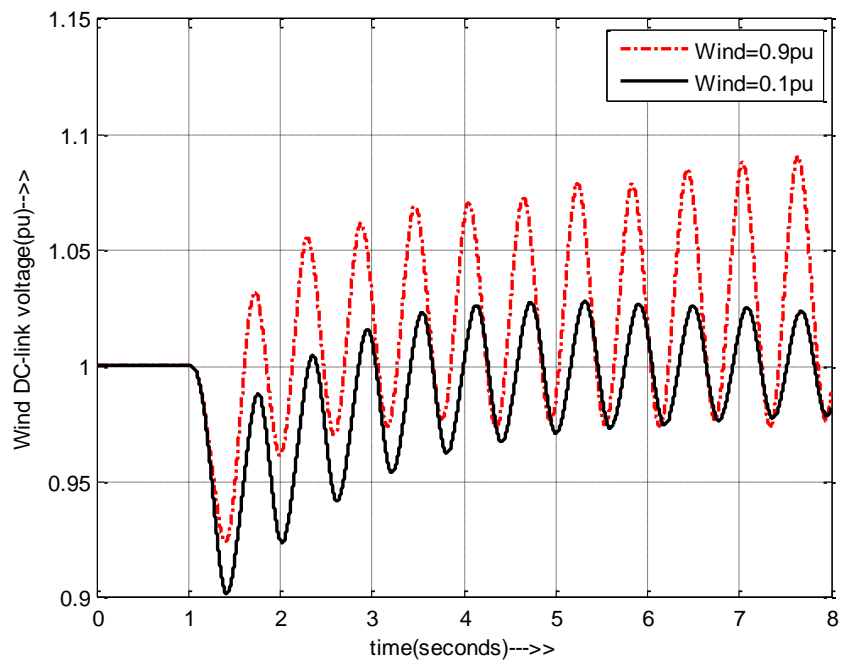


Figure 4.10: Response of the wind DC-link voltage following a disturbance of 15% torque pulse for 0.3 sec a) wind generation at 0.9 pu b) wind generation at 0.1pu

Figure 4.11-Figure 4.12 shows the variations of VSC DC-link voltage and current following a torque pulse of 0.15 pu for 300 msec. It is observed that for higher participation of wind power, the system stability is lost even for a small disturbance where as stable operation is possible for wind power penetration of 0.1 pu.

Thus the non-linear time based simulations verify that the increased penetration power from renewables affects the system stability tending the microgrid to move towards the unstable region. Hence, there is a need for control devices which could enhance the microgrid operation under large participation of renewables.

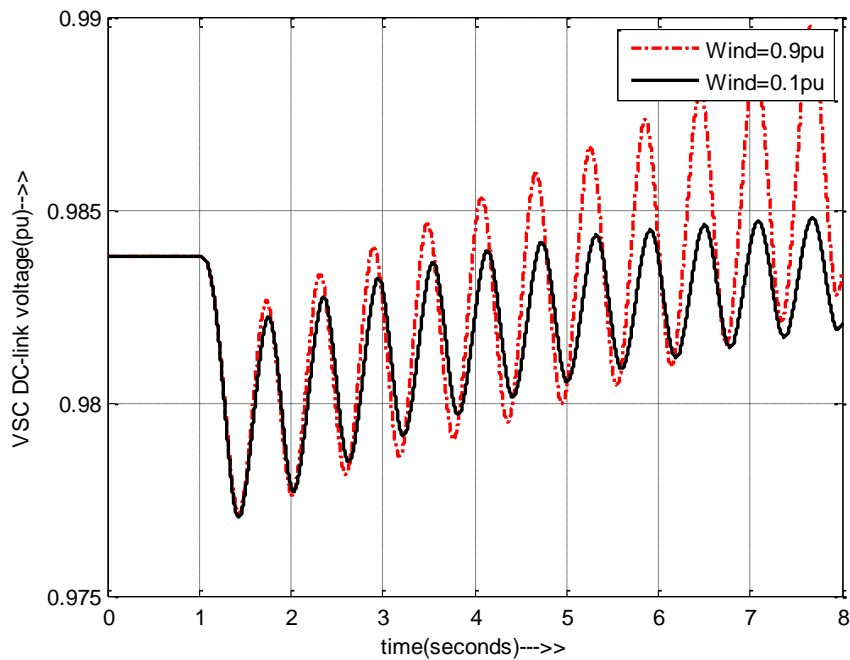


Figure 4.11: Response of the VSC DC-link voltage following a disturbance of 15% torque pulse for 0.3 sec a) wind generation at 0.9 pu b) wind generation at 0.1pu

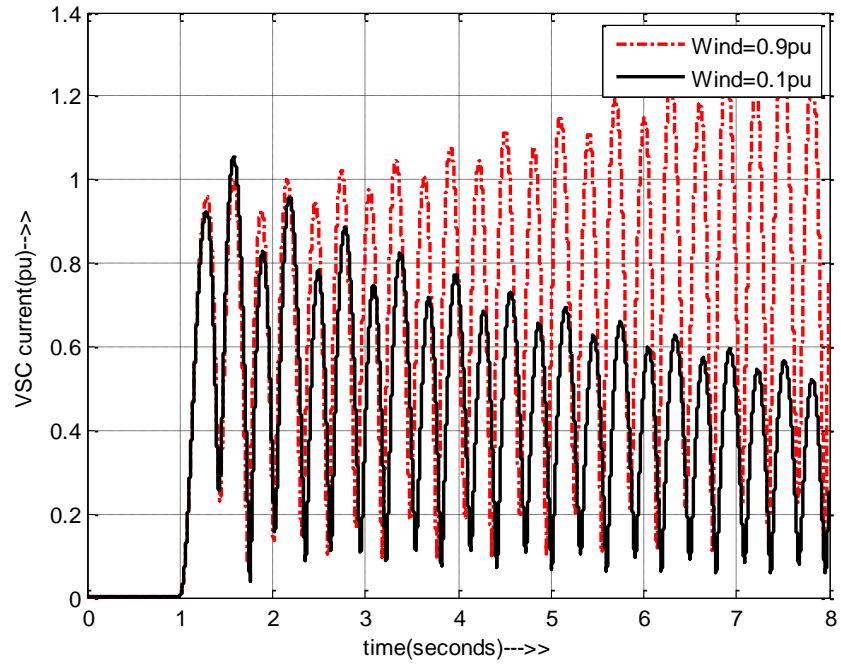


Figure 4.12: Response of the VSC current following a disturbance of 15% torque pulse for 0.3 sec a) wind generation at 0.9 pu b) wind generation at 0.1pu

CHAPTER 5

ENERGY STORAGE CONTROLLER

5.1 Introduction

The small-signal analysis of composite microgrid model consisting of PV, wind, fuel cell and microgenerator developed in chapter 3 was carried out to study its behavior for varying penetration of renewables. The simulation studies conducted in chapter 4 reveals that there exists a threshold limit of power interface from renewables above which the system performance deteriorates. The voltage and frequency control in a microgrid is very important, as changes in input and load may cause sustained oscillations leading to eventual voltage collapse or unstable operation. In order to extract maximum power from renewable sources it is essential to improve the transient under-performance through effective control strategies. Normally mechanical compensation methods such as blade pitch control, optimal torque control, turbine governor control along with voltage, current and power control on the generator side are employed. Presence of moving parts in mechanical control methods attribute to various problems such as slow response time, maintenance issues, non-robustness etc. These problems prohibit their applications for a microgrid and hence, alternatives involving electrical controls on the different DGs are explored.

This thesis proposes dynamic real and reactive power control obtained from central energy storage devices. Two relatively recent and less expensive energy storage schemes have been identified are:

- (i) Battery energy storage system (BESS)
- (ii) Supercapacitor energy storage system (SCESS)

Both these devices are interfaced to the microgrid system through controlled voltage source converters. The detailed modeling and control arrangements of the storage units are presented in the following sections.

5.2 Battery Energy Storage System (BESS)

The reactive power demand in a microgrid rises sharply following low voltages in the system. This requires for external support to restore system voltage and to reduce transients in the DG's and their converters. The real power control in a system is essential for enhancing dynamic performance through quick damping of oscillations. The reactive power control in a microgrid contributes for voltage recovery. A central interfacing voltage source converter backed up by a battery can provide additional real and reactive power support. The voltage source converter is responsible for providing appropriate reactive power whereas the battery supplies the necessary real power. This section describes a battery storage system employed to function as a central supervisory controller. The dynamic model of battery storage unit is developed.

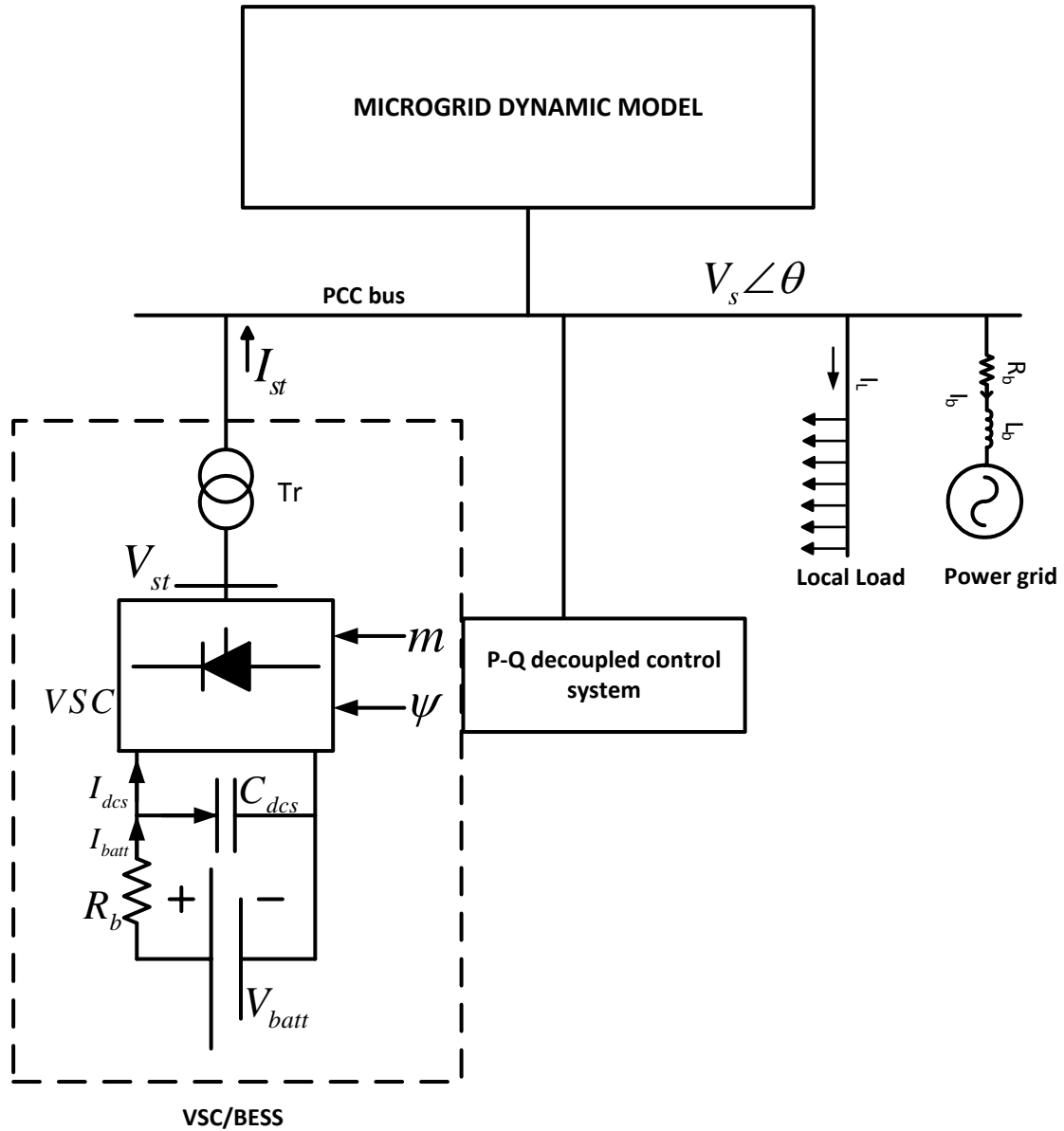


Figure 5.1: Composite microgrid system equipped with battery energy storage

The composite model of electrical microgrid under investigation when incorporated with battery storage system (VSC/BESS) is shown in Figure 5.1. A voltage source converter connects the battery with the microgrid bus through a coupling transformer Tr. In this study, as shown in Figure 5.2, the battery storage system is

modeled through an ideal DC voltage source V_{batt} along with a series resistance R_b accounting for electrical losses.

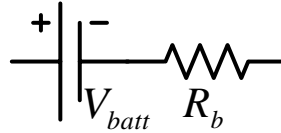


Figure 5.2: Circuit model of battery

The assumption that during short period of transients the battery would have negligible effect on its potential is valid. Modulation index m of the VSC has the role for compensating the reactive power required while the storage device provides the necessary real power supplement during transients [120].

5.2.1 The voltage source converter model

In order to interface various energy storage devices with the microgrid a voltage source converter (VSC) is employed as shown in Figure 5.1. By appropriate control algorithm, a VSC can generate a balanced set of three-phase voltages at fundamental frequency, with adjustable magnitude and phase angle. It can exchange reactive power with the system bus by injecting a current of variable amplitude and almost in quadrature with the line voltage at the point of interconnection. In this work, the VSC has been modeled as a controllable voltage source. The two control variables are the modulation index m and phase angle ψ defined by pulse width modulation technique. The necessary dynamical relations for the VSC are given in the following.

A variable AC voltage V_{st} is produced by the VSC whose amplitude is controlled by m is given as:

$$V_{st} = mV_{dcs} \angle \Psi \quad (5.1)$$

Including the converter transformer, the voltage-current dynamical relation for the VSC can be written as:

$$L_{st} \frac{dI_{st}}{dt} + R_{st} I_{st} = V_{st} - V_s \quad (5.2)$$

In the equation (5.2), R_{st} and L_{st} represents the resistance and inductance of the VSC and the converter transformer together. Decomposing the above equation into d-q reference frame and taking into per-unit system, will give two differential equations as mentioned below.

$$\begin{bmatrix} \frac{dI_{std}}{dt} \\ \frac{dI_{stq}}{dt} \end{bmatrix} = \begin{bmatrix} -\omega_0 R_{st} & \frac{\omega}{L_{st}} \\ \frac{\omega}{L_{st}} & -\omega_0 R_{st} \end{bmatrix} \begin{bmatrix} I_{std} \\ I_{stq} \end{bmatrix} + \frac{\omega_0}{L_{st}} \begin{bmatrix} mV_{dcs} \cos(\psi + \theta) - V_{sd} \\ mV_{dcs} \sin(\psi + \theta) - V_{sq} \end{bmatrix} \quad (5.3)$$

The transient relation for the DC-link voltage is given by [137],

$$\frac{dV_{dcs}}{dt} = -\frac{m}{C_{dcs}} (i_{std} \cos(\psi + \theta) + i_{stq} \sin(\psi + \theta)) \quad (5.4)$$

Thus, with the inclusion of voltage source converter into the microgrid following three state variables are added with the existing state quantities.

$$X_{VSC} = [I_{std}, I_{stq}, V_{dcs}] \quad (5.5)$$

5.2.2 Dynamical model of BESS

In the BESS central controller shown in Figure 5.1, the application of KCL at the DC side of the voltage source converter results in the following relation.

$$C_{dcs} \frac{dV_{dcs}}{dt} = -I_{dcs} + I_{batt} \quad (5.6)$$

Assuming the interfacing converter to be lossless, equating the power balance on the DC and AC sides will give dynamical relation for the DC-link capacitor.

$$\frac{dV_{dcs}}{dt} = -\frac{m}{C_{dcs}} (i_{std} \cos \psi + i_{stq} \sin \psi) + \frac{I_{batt}}{C_{dcs}} \quad (5.7)$$

The equation (5.7) could be rewritten to give the dynamical model of VSC based

BESS as given under:

$$\frac{dV_{dcs}}{dt} = -\frac{m}{C_{dcs}} (i_{std} \cos \psi + i_{stq} \sin \psi) + \frac{V_{batt} - V_{dcs}}{R_b C_{dcs}} \quad (5.8)$$

Equation (5.8) along with (5.3) constitutes the dynamical model of VSC based BESS.

5.2.3 Decoupled P-Q control

It is observed that under steady state operating region, the power electronic converter connecting energy storage system with the microgrid floats ($I_{st} = 0$), and no power flow takes place from the energy storage device. Initiation of voltage source converter action occurs whenever a deviation in steady state condition is observed through change in the microgrid voltage magnitude and angle resulting in power exchange [138]. Following a disturbance, the real and reactive powers as injected by the VSC are:

$$P_{st} = V_s I_{std} \cos \theta + V_s I_{stq} \sin \theta \quad (5.9)$$

$$Q_{st} = V_s I_{std} \sin \theta - V_s I_{stq} \cos \theta$$

Independent control over the real and reactive power flow through the VSC can

be achieved by performing a transformation to obtain a new set of VSC currents as:

$$I_{st}^{new} = I_{st} e^{-j\theta} \quad (5.10)$$

Along d-q reference frame the above relation can be expressed as,

$$I_{std}^{new} = I_{std} \cos \theta + I_{stq} \sin \theta \quad (5.11)$$

$$I_{stq}^{new} = I_{std} \sin \theta - I_{stq} \cos \theta$$

Thus using new set of VSC currents, the real and reactive power decoupled relationships can be extracted as shown:

$$P_{st} = V_s I_{std}^{new}; \text{ and } Q_{st} = -V_s I_{stq}^{new} \quad (5.12)$$

From the relation (5.12), it can be noticed that the real P_{st} and reactive power Q_{st} injections can be regulated independently by new pair of VSC currents I_{std}^{new} and I_{stq}^{new} .

Designing a decoupled control strategy for energy storage system involves exchange of real and reactive powers separately with the microgrid system under contingencies. As noticed from equation (5.12), the real power injection P_{st} is a function in terms of i_{std}^{new} , while the reactive power Q_{st} depends on i_{stq}^{new} . The respective control strategy is shown in Figure 5.3.

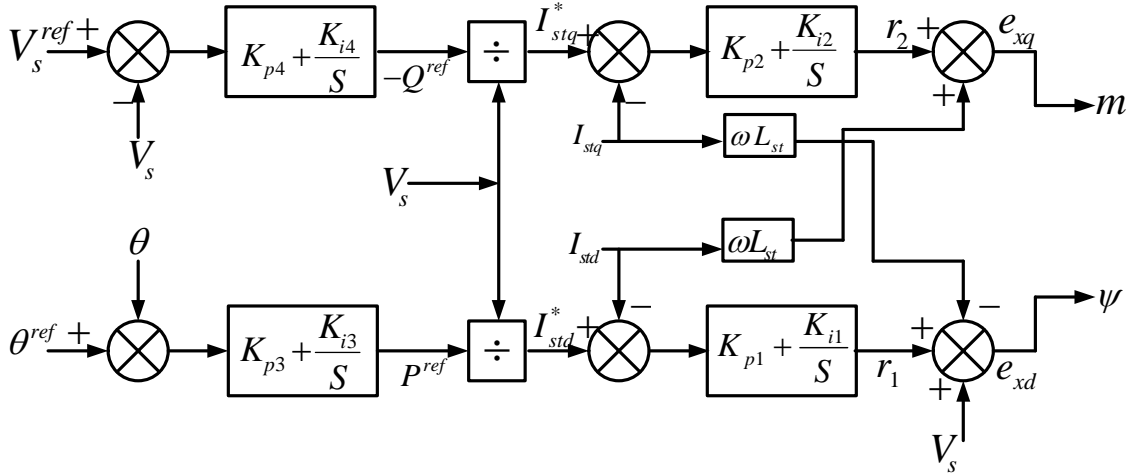


Figure 5.3: Block diagram representation of decoupled P-Q control strategy

Now for the new pair of VSC currents the dynamic relations can be written as:

$$\frac{d}{dt} \begin{bmatrix} I_{std}^{new} \\ I_{stq}^{new} \end{bmatrix} = \omega_0 \begin{bmatrix} \frac{-R_{st}}{L_{st}} & 0 \\ 0 & \frac{-R_{st}}{L_{st}} \end{bmatrix} \begin{bmatrix} I_{std}^{new} \\ I_{stq}^{new} \end{bmatrix} + \begin{bmatrix} r_1 \\ r_2 \end{bmatrix} \quad (5.13)$$

The terms r_1 and r_2 used in the decoupled controller are given by the following equation.

$$\begin{bmatrix} r_1 \\ r_2 \end{bmatrix} = \omega_0 \begin{bmatrix} \frac{\omega}{\omega_0} I_{std}^{new} + \frac{e_{xd}}{L_{st}} - \frac{V_s}{L_{st}} \\ -\frac{\omega}{\omega_0} I_{std}^{new} + \frac{e_{xq}}{L_{st}} \end{bmatrix} \quad (5.14)$$

Here the various terms are,

$$e_{xd} = mV_{dcs} \cos\psi = \frac{L_{st}}{\omega_0} (r_1 - \omega I_{std}^{new}) + V_s \quad (5.15)$$

$$e_{xq} = mV_{dcs} \sin\psi = \frac{L_{st}}{\omega_0} (r_2 + \omega I_{std}^{new}) \quad (5.16)$$

$$m = \frac{\sqrt{e_{xd}^2 + e_{xq}^2}}{V_{dcs}} \quad (5.17)$$

$$\psi = \tan^{-1} \left(\frac{e_{xd}}{e_{xq}} \right) \quad (5.18)$$

Thus the relationships (5.15) and (5.16) suggest that the new set of currents I_{std}^{new} and I_{stq}^{new} are excited by r_1 and r_2 respectively, through a first order relationship. By defining feedback loops and PI controllers as shown in Figure 5.3, the control strategy is achieved through following relations.

$$r_1 = \left(K_{p1} + \frac{K_{i1}}{s} \right) (I_{std}^* - I_{std}) \quad (5.19)$$

$$r_2 = \left(K_{p2} + \frac{K_{i2}}{s} \right) (I_{stq}^* - I_{stq}) \quad (5.20)$$

5.3 Supercapacitor Energy Storage System (SCESS)

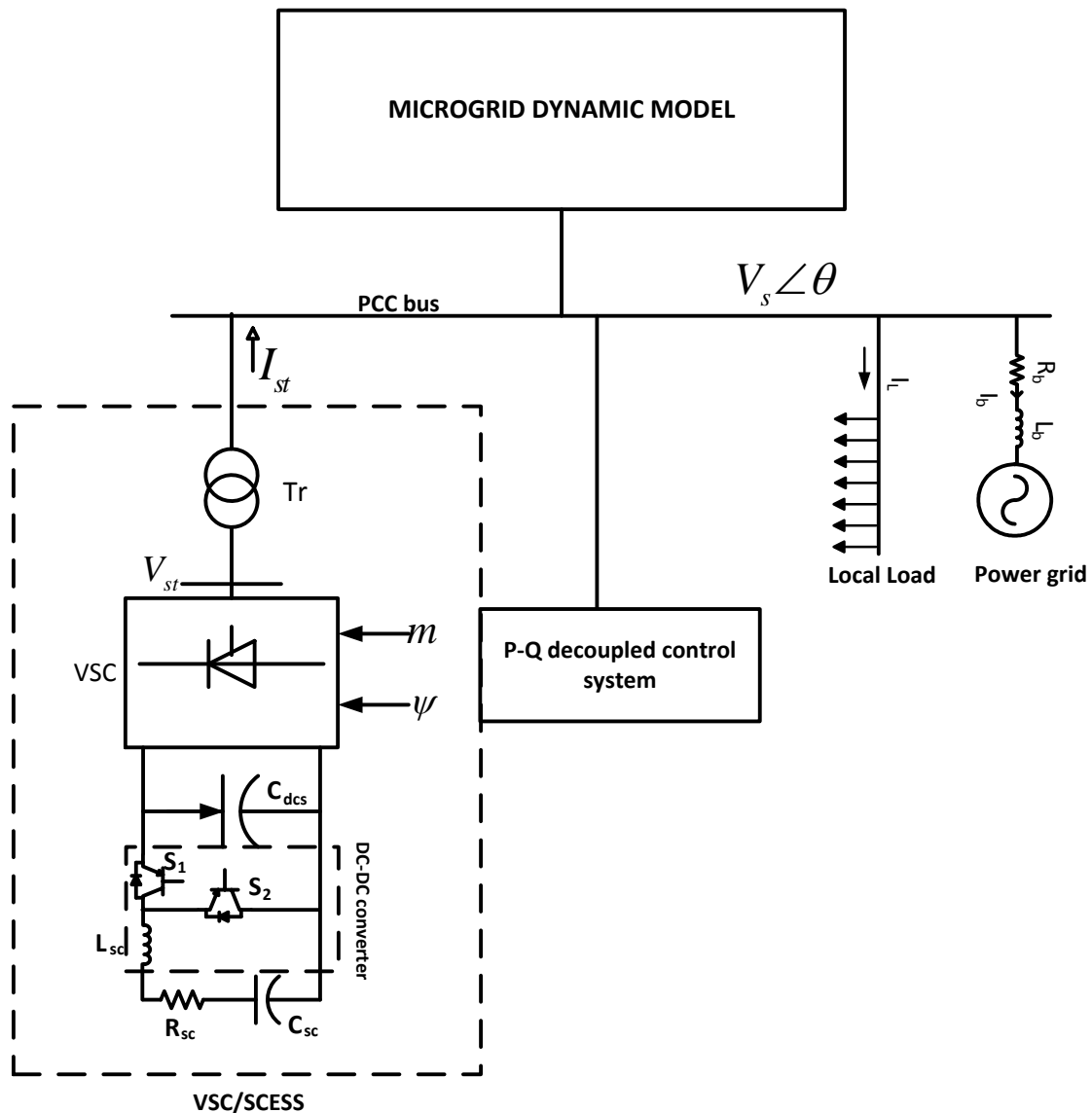


Figure 5.4: Composite microgrid system equipped with supercapacitor based energy storage

Figure 5.4 shows the composite model of the electrical microgrid under investigation when incorporated with a supercapacitor based energy storage system (VSC/SCESS). A controlled voltage source converter connects the supercapacitor module with the microgrid bus through a coupling transformer Tr . A bi-directional DC-DC converter

acting as buck-boost converter is also seen in the interfacing circuit. This converter facilitates charging and discharging of supercapacitor and provides additional control flexibility. Control of power electronic based switches S_1 and S_2 through pulse width modulation techniques resulting in variation of converter duty cycle D_r determine the operational strategy.

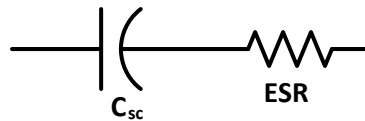


Figure 5.5: Supercapacitor circuit representation

Ignoring the internal module dynamics, the supercapacitor is represented as an ideal capacitance with an equivalent series resistance (ESR) as shown in Figure 5.5. Internal resistive losses in the module viz. dielectric, electrolytic solution and material of the plates are represented by equivalent resistance (ESR). However, within the capacitor's working region, fixed value capacitance and ESR can accurately model a real supercapacitor.

5.3.1 Dynamic model of SCESS

The d-q components of the current injected by the interfacing VSC are specified in equation (5.3). The DC-link capacitor dynamical voltage relation is modified with the inclusion of supercapacitor as described below:

Application of KCL at the DC side of the voltage source converter based SCESS shown in Figure 5.4 gives,

$$C_{dcs} \frac{dV_{dcs}}{dt} = -I_{dcs} - I_{sc} \quad (5.21)$$

Assuming the interfacing converter to be lossless, equating the power balance on the DC and AC sides will give dynamical relation for the DC-link capacitor.

$$\frac{dV_{dcs}}{dt} = -\frac{m}{C_{dcs}} (i_{std} \cos \psi + i_{stq} \sin \psi) - \frac{I_{sc}}{C_{dcs}} \quad (5.22)$$

Incorporating the DC-DC converter duty ratio D_r the above equation becomes,

$$\frac{dV_{dcs}}{dt} = -\frac{m}{C_{dcs}} (i_{std} \cos \psi + i_{stq} \sin \psi) - \frac{D_r I_{sc}}{C_{dcs}} \quad (5.23)$$

Thus, the equations (5.3) and (5.23) constitute the dynamical model of SCESS.

5.3.2 Supercapacitor DC-DC converter control circuit

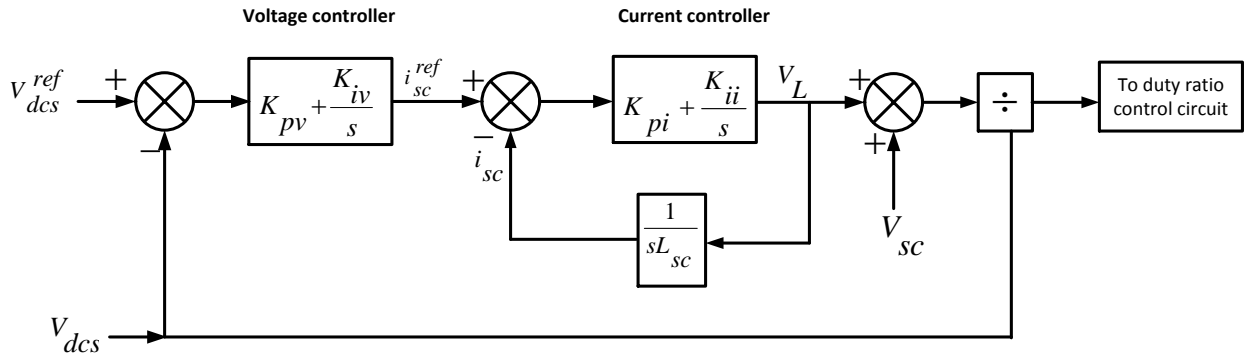


Figure 5.6: Circuit description of supercapacitor DC-DC converter control scheme

As shown in Figure 5.6, the supercapacitor based control system is connected to the voltage source converter through a bi-directional dc-dc converter formed with switches S_1 and S_2 . Control of the duty ratio (D_r) of converter through modulated switching techniques, the charging and discharging of supercapacitor storage can be regulated. The three energy storing components i.e. the supercapacitor C_{sc} , the choke L_{sc} and the DC-

link capacitor C_{dcs} constitutes the important elements of bi-directional dc-dc buck-boost converter.

The control strategy proposed for the supercapacitor dc-dc converter circuit is shown in Figure 5.6, comprising of dc-link voltage controller and supercapacitor current controller in order to achieve the following objectives: i) regulating the dc-link voltage with the energy stored in supercapacitor and ii) to maintain the supercapacitor voltage within its operating range.

The reference signal i_{SC}^{ref} for the current controller is obtained through propagation of error signal between the reference dc-link voltage V_{dcs}^{ref} and the measured voltage V_{dcs} from a PI based voltage controller. The sum of supercapacitor voltage V_{SC} and the choke reference voltage V_L^{ref} contribute towards the reference voltage for the converter V_{PWM}^{ref} . From the circuit diagram Figure 5.6, the mathematical relations governing the control strategy can be written as:

$$i_{SC}^{ref} = (V_{dcs}^{ref} - V_{dcs}) \left(K_{pv} + \frac{K_{iv}}{s} \right) \quad (5.24)$$

$$V_L^{ref} = (i_{SC}^{ref} - i_{SC}) \left(K_{pi} + \frac{K_{ii}}{s} \right) \quad (5.25)$$

$$V_{PWM}^{ref} = V_{SC} + V_L^{ref} \quad (5.26)$$

$$Duty\ ratio\ D_r = \frac{V_{SC} + V_L}{V_{dcs}} \quad (5.27)$$

5.3.3 P-Q decoupled control system

The modulation index (m) and phase angle (ψ) of the interfacing voltage source converter are the control variables for a SCESS. Design of a control strategy involves determination of these variables for an operating scenario. In order to have separate control over the real and reactive power exchange a P-Q decoupled control system is employed. The description of control strategy along with corresponding mathematical equations is mentioned in section 5.2.3. The block diagram representation of the control scheme is presented in Figure 5.3. The inverter voltage vector is controlled through m and ψ as specified by the equation (5.17) and (5.18).

For the central energy storage based decoupled control system, the generation of reference real and reactive powers is very important in order to provide appropriate power injections under transients. As shown in Figure 5.3, the reactive reference power Q^{ref} is obtained by considering the deviations in microgrid bus voltage ($V_s^{\text{ref}} - V_s$) propagated through a PI controller, while the real reference power P^{ref} for control strategy is obtained from the variations in the microgrid bus voltage angle ($\theta^{\text{ref}} - \theta$).

5.4 The Composite System Model with Central Storage Controller

This section describes the complete non-linear description of the system model after incorporating the central energy storage system. For the case of BESS and SCESS control devices, it is assumed that the voltage source converter injects current I_{st} into the line. Combining the transient relations of the energy storage device with the system equations

gives the complete nonlinear model. The closed-form state space model of composite microgrid including a VSC/BESS and VSC/SCESS is given by:

$$\dot{X} = f(X, U) \quad (5.28)$$

For BESS control system the vector of states is given as:

$$X = [X_{composite}, I_{std}, I_{stq}, V_{dcs}] \quad (5.29)$$

The state vector $X_{composite}$ is mentioned in section 3.8 while the control vector is given by:

$$U_{BESS} = [U_{composite}, m, \psi] \quad (5.30)$$

For SCESS control system the vector of states is given as:

$$X = [X_{composite}, I_{std}, I_{stq}, V_{dcs}, E_{sc}] \quad (5.31)$$

The corresponding control vector is:

$$U_{SCESS} = [U_{composite}, m, \psi, D_r] \quad (5.32)$$

5.5 Controller Design

The performance of the storage control system depends on gains of the P-Q controller given in Figure 5.3. Stability enhancement of the microgrid can be achieved only through correct settings of controller parameters. The PI gains have to be optimized for specific operating scenarios and also, they must be robust to operate satisfactorily over a range of operation. The random input change in the renewables demands adjustment of the gains

to meet varying conditions. Tuning the gains for optimum performance under variable operational regime is a challenging task.

The control designs are normally carried out in linear domain for simplicity. These designs though provide satisfactory results for specific operating conditions; they fail to act reasonably for off-nominal operation. In order to have good response during changing operating scenarios it is desirable to carry out control design in nonlinear domain. A possible approach is the use of neural network based techniques which approximates system nonlinearities quite precisely. Neural networks are normally trained to get weighting matrices which predict control for certain input condition. Adaptability of these weights for randomly varying inputs poses difficulties. Fuzzy logic techniques can provide solution to this problem but such methods require a huge knowledge base created from operator experience or intelligence. An appropriate selection of membership functions will generate an adaptive control over variable operating scenarios.

The adaptive neuro-fuzzy systems have gained popularity in recent times to predict system control under randomly varying system conditions. The neuro-fuzzy method, however, requires generation of a large optimum input-output data set for control design. These data sets have to be generated under various contingencies and for wide operating region. A nonlinear biogeography based optimization algorithm is used in this study to generate the optimum data sets. Intelligent searching procedures generally require fitness criteria for evaluation of various individuals encountered during the process.

In the subsequent sections the biogeography based optimization procedure and the adaptive neuro-fuzzy techniques employed in this thesis are presented in brief.

5.5.1 Biogeography based optimization (BBO) procedure

The BBO, being an inhabitant based algorithm, is a kind of searching procedure which requires number (NP) of candidate solutions (X_d^n) called habitats to form a generation(P^n), where in each habitat would contain certain solution features (SIV_{nd}).

The algorithm is composed of following steps:

Step-1: Initialization

The independent decision variables in BBO technique usually, called SIVs, are control parameters required to be optimized while minimizing or maximizing a fitness index. A real valued vector of SIVs constitutes a habitat or an island. The problem dimension determines the number of SIVs in a habitat. Each habitat in the population is a candidate solution for the optimization problem.

Various BBO parameters such as the maximum number of species S_{max} , the maximum emigration E and immigration I rates, the elitism parameter p and the maximum mutation rate m_{max} are selected. The problem dimension d, the range of each control element SIV, the population size NP and the number of generations n are specified.

The initial inhabitants are generated randomly within the search space for each control variable SIV based on the relation:

$$x_{k,i}^n = x_{i,min}^n + random(x_{i,max}^n - x_{i,min}^n) \quad k = 1, NP \quad i = 1, d \quad (5.33)$$

Step-2: Evaluation of fitness

After the formation of initial set of solutions, the suitability indices are calculated by evaluating the objective function. The composite nonlinear system model formed after incorporation of P-Q decoupled control based energy storage system is simulated and the fitness criterion is calculated using following equation.

$$J = \min \left\{ \int_{t=0}^{t_{sim}} t[\alpha_1 |d\omega| + \alpha_2 |dV_s| + \alpha_3 |dV_{dcs}|] dt \right\} \quad (5.34)$$

The various important factors like the species count S , the emigration rate μ and immigration rate λ are mapped with the HSI using the following relation.

$$\lambda_i = I \left(\frac{1-n_i}{m} \right) \text{ and } \mu_i = E \left(\frac{n_i}{m} \right) \quad (5.35)$$

Habitat with best fitness value is considered as the best solution and, for every generation the best solution is updated by keeping stored in an external variable.

Step-3: Elitism operation

Rank the population in terms of HSI values either in ascending or descending order. A pre specified p number of elite habitats pass through the next generation without any modification.

Step-4: Migration process

Each of the non-elite solution members is then migrated probabilistically to achieve better habitats. The selection of any SIV for migration procedure is described as under:

1. Lower immigration rate λ_{lower} and upper emigration rate μ_{upper} is selected for a given population set.
2. For each island the actual immigration rate λ and emigration rate μ is computed.
3. Then the selection of habitat and SIV are done depending on the above rates.

The migration process in BBO generates a population set which is different from the original initial set of habitats.

Step-5: Mutation process

Updating of number of species probability for each island is performed using the relation.

$$\frac{dP_S}{dt} = \begin{cases} -(\lambda_i + \mu_i)P_S + \mu_{i+1}P_{S+1} & S = 0 \\ -(\lambda_i + \mu_i)P_S + \mu_{i+1}P_{S+1} + \lambda_{i-1}P_{S-1} & 1 \leq S \leq S_{max} - 1 \\ -(\lambda_i + \mu_i)P_S + \lambda_{i-1}P_{S-1} & S = S_{max} \end{cases} \quad (5.36)$$

Then each of the non-elite habitats undergoes mutation process depending on its probability. The habitats with mutation rates, as calculated from equation (2.5) , larger than a randomly generate number are chosen for mutation. A randomly generated island set replaces the current habitat set thus providing diversity among the population. The fitness index of each new island set is calculated.

Step-6: Stopping criteria

Following conditions when satisfied terminate the iterative process.

- a) Maximum number of generations has been completed.
- b) The number of generations a solution does not change surpasses a predefined constant.
- c) An adequate solution is obtained.

The various steps constituting the optimization procedure of BBO algorithm are shown in Figure 5.7.

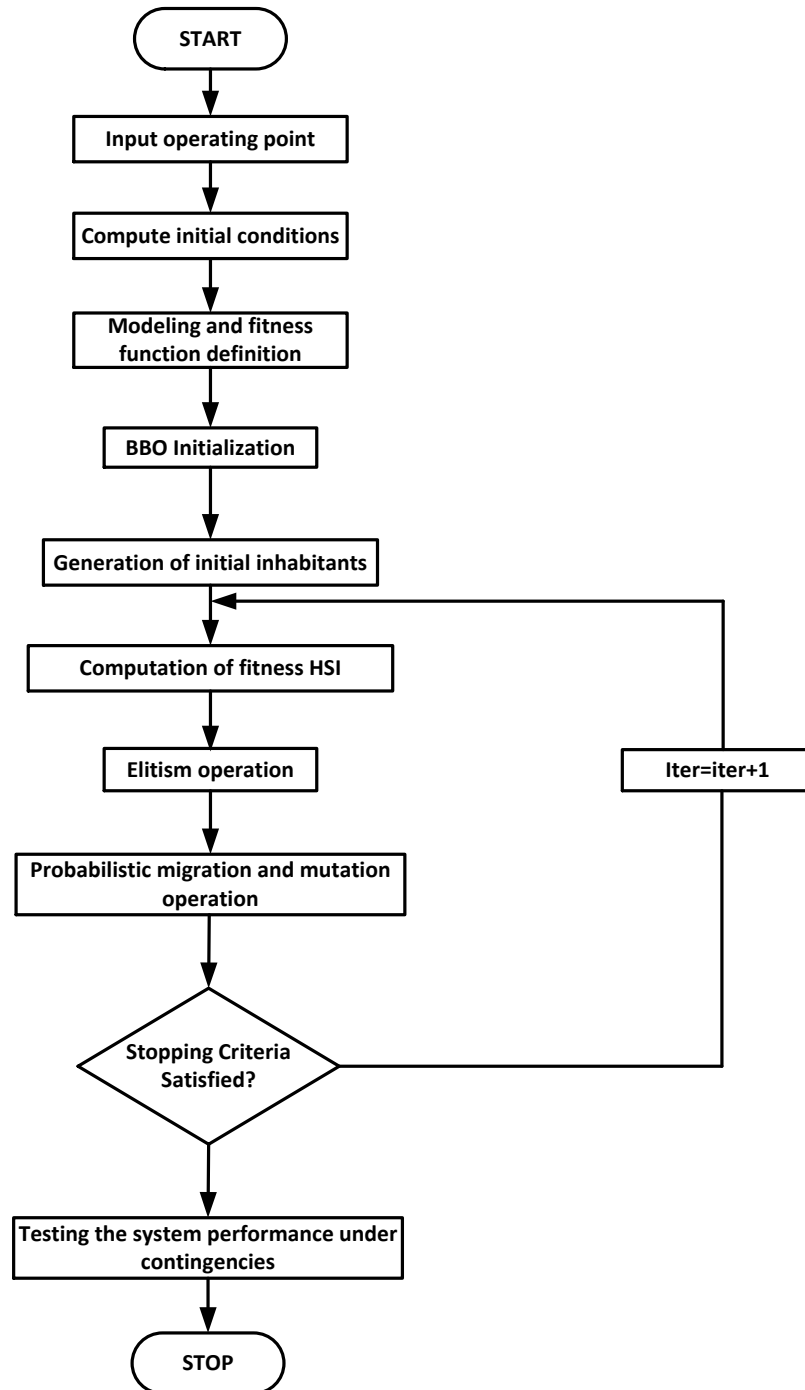


Figure 5.7: Flow chart of the proposed BBO based optimal control design

5.5.2 Design of adaptive neuro-fuzzy control system

The adaptive control system for a microgrid model involves the generation of decoupled controller gains adaptively for varying system contingencies and also for random input changes in the renewables. Various online intelligent control algorithms such as neural networks, fuzzy logic and neuro-fuzzy systems can be adopted to work with a microgrid system.

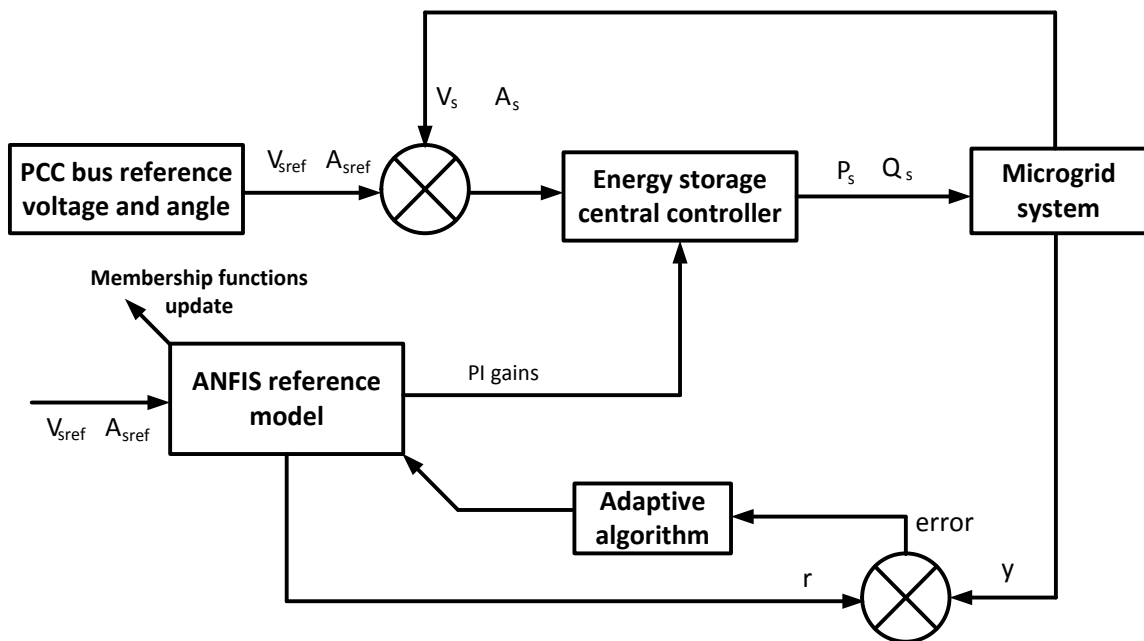


Figure 5.8: Model of adaptive control strategy

Adaptive neuro-fuzzy systems combine the advantages of both neural networks and fuzzy logic, derive the adaptive learning capability and fuzziness in the control variables, and hence can provide a smart control strategy for a microgrid. The inherent uncertain nature of power obtainable from renewables justifies the selection of neuro-fuzzy systems as a control option. Such an adaptive control scheme is shown in

Figure 5.8. The adaptive learning algorithm updates the firing strengths of the membership functions associated with each input variable.

5.5.3 Generation of training data using BBO

The training data set required to modify the membership functions present in the neuro-fuzzy system is obtained through BBO algorithm. The optimal decoupled control parameters are obtained through simulation of search technique for a wide range of operating scenarios and system contingencies. The procedure to obtain training data is described below.

1. Define a range of system operating points and randomly generate 100 set of population in terms of operating scenarios (real and reactive powers of various sources).
2. A nonlinear time domain objective function is defined to guide the search process effectively.
3. For every set of operating point the search algorithm provides a set of optimal controller parameters which are stored in an external array.
4. At the end of main loop, 100 set of input-output pairs are obtained which can be used for training of neuro-fuzzy system.

5.5.4 Adaptive neuro-fuzzy method

The fuzzy logic control usually involves four principal components: a fuzzifier, rule base, inference engine, and defuzzifier. Transformation of crisp input data into suitable linguistic values is performed by a fuzzifier. The rule base characterizes the control goals and control policy of the domain experts by means of a set of linguistic control rules. An

inference engine has the capability of simulating human decision-making based on fuzzy concepts. The final stage involves conversion of fuzzy outputs to appropriate control values. Membership functions in a fuzzy system are used to fuzzify the input variables into linguistic variables. These functions provide a gradual transition between a membership and non-membership in a given set.

In the case of fuzzy logic controllers, the mapping of human knowledge or experience into the fuzzy inference system is a cumbersome task. No standard procedures are found which could provide an efficient way of transformation. Usually, trial and error approach determines the type, size and settings of the input and output membership functions. Effective tuning methods for the input and output membership functions and reduction in the rule base to the least necessary rules have always been on the list.

The adaptive neuro-fuzzy systems are designed to mitigate the above mentioned issues while providing the combined advantages of neural networks and fuzzy systems [139]. Neuro-fuzzy systems are usually trained through a neural network learning algorithm. Thus, ANFIS systems are hybrid intelligent models which combine the adaptive learning capabilities of the neural network and the high level reasoning capability of a fuzzy inference system. The ANFIS systems works in two mutually distinct phases, neural-network phase where in system classifies data and find patterns, the other phase develops a fuzzy expert system through adaptive tuning of membership functions [140].

When an input-output data pair is presented to an ANFIS network, a fuzzy inference system (FIS) is constructed, with the membership functions being tuned by

employing either least squares method or a back propagation algorithm or a combination of both [141].

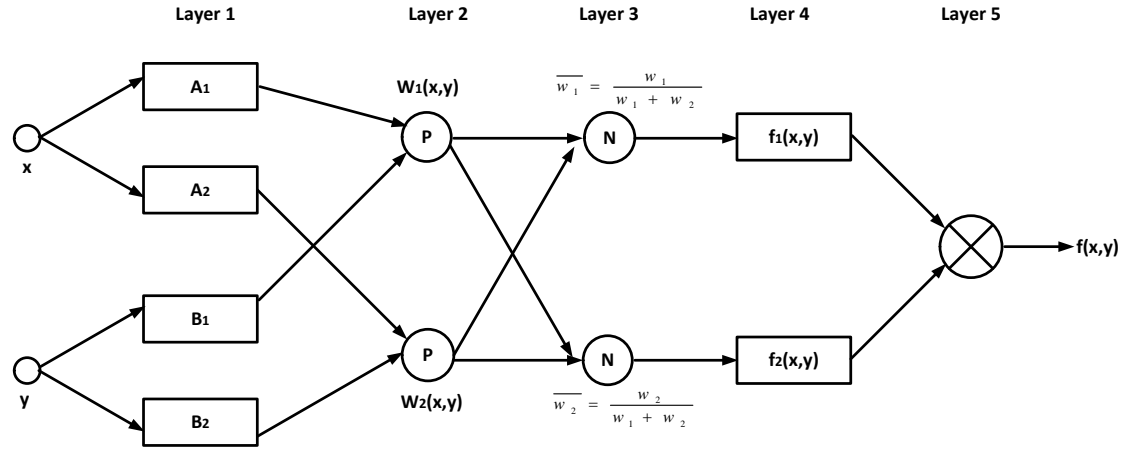


Figure 5.9: Typical equivalent ANFIS architecture

Figure 5.9 shows a simple configuration for a fuzzy inference system of Takagi-Sugeno’s type [142] , with one output variable f and two inputs x, y . Two fuzzy if-then rules constitute the knowledge base for this system as given below.

$$\text{if } x \text{ is } A_i \text{ and } y \text{ is } B_i \text{ then } f_i = p_i x + q_i y + r_i \text{ where } i = 1, 2 \quad (5.37)$$

The linguistic variables are denoted by A_i and B_i while the output is f_i and the parameters of i^{th} rule are p_i , q_i and r_i .

As shown in Figure 5.9, the ANFIS consists of five layers; where in the output from each node in every layer is represented by O_i^l . Here l denotes the layer number while the symbol i denotes the neuron number. The description of various layers in the ANFIS architecture is given in the following.

Layer-1: The purpose of this layer is to fuzzify the input parameters using a set of linguistic variables (small, medium, large etc.). Membership functions of these linguistic parameters determine the output of the layer.

$$O_i^1 = \mu_{A_i}(x) \quad (5.38)$$

$$O_i^1 = \mu_{B_i}(y) \quad (5.39)$$

Here $\mu_{A_i}(x)$ and $\mu_{B_i}(y)$ represent the membership functions that establish the degree to which the given inputs x and y satisfies the quantifier A_i and B_i . Variety of membership functions such as bell-shaped, trapezoidal, triangular, Gaussian, sigmoidal are often used in this layer.

The Gaussian membership function associated with the i th input and j th rule is given by

$$\mu_{A_i}(x) = \exp \left[\frac{-1}{2} \left(\frac{x - c_{ij}}{\sigma_{ij}} \right)^2 \right] \quad (5.40)$$

Where c_{ij} and σ_{ij} are the mean and variance of the j th function.

Layer-2: Firing strength for each rule quantifying the extent which any input data belongs to that rule, is computed in the second layer. The multiplication of all the incoming signals at a node named P yield the output for this layer.

$$O_1^2 = w_1 = \mu_{A_1}(x) * \mu_{B_1}(x) \quad (5.41)$$

$$O_2^2 = w_2 = \mu_{A_2}(x) * \mu_{B_2}(x) \quad (5.42)$$

Layer-3: The nodes present in the third layer perform the normalization operation and each node is represented as a circle labeled N , calculates the ratio of i^{th} rule's firing strength to the sum of all rule's firing strengths.

$$O_1^3 = \overline{w_1} = \frac{w_1}{w_1 + w_2} \quad (5.43)$$

$$O_2^3 = \overline{w_2} = \frac{w_2}{w_1 + w_2} \quad (5.44)$$

Layer-4: This layer has square shaped nodes with a node function as given below.

$$O_1^4 = \overline{w_1}f_1 = \overline{w_1}(p_1x + q_1y + r_1) \quad (5.45)$$

$$O_2^4 = \overline{w_2}f_2 = \overline{w_2}(p_2x + q_2y + r_2) \quad (5.46)$$

Layer-5: The summation of all incoming signals is taken as the overall output of the fifth layer. The single node in this layer is a circle node with node function as given below.

$$O_i^5 = \frac{\sum_{i=1}^2 w_i f_i}{\sum_{i=1}^2 w_i} \quad (5.47)$$

5.5.5 ANFIS training algorithm

A fuzzy IF-THEN rule is generally composed of two parts called premise and consequent. The parameters associated with premise part of the rule are the weights for input membership functions while the firing strength of output membership variables determines the consequent parameters. The firing strength of the input membership functions are usually known while the consequent parameters are to be tuned in order to achieve a desired output. The overall output from the ANFIS network can be expressed as linear combinations of consequent parameters.

$$f = \frac{w_1}{w_1 + w_2} f_1 + \frac{w_2}{w_1 + w_2} f_2 \quad (5.48)$$

$$f = \overline{w_1}f_1 + \overline{w_2}f_2$$

$$f = (\overline{w_1}x)p_1 + (\overline{w_1}y)q_1 + (\overline{w_1})r_1 + (\overline{w_2}x)p_2 + (\overline{w_2}y)q_2 + (\overline{w_2})r_2 \quad (5.49)$$

The consequent parameters in the above equation are p_1 q_1 r_1 and p_2 q_2 r_2 . The objective of a learning algorithm is to update the consequent and premise parameters in order to achieve least error between the input and the desired target output.

Hybrid training algorithm is normally applied to tune the parameters of an ANFIS network. Such a learning technique is composed of least square estimates and the gradient descend or back propagation algorithm. For a training data set with input X_i and target T , the sum of squares error function $E(W)$ is given as,

$$E(W) = \frac{1}{2} \sum_{q=1}^{N_L} [Z_L^q X_i - T_q X_i]^2 \quad (5.50)$$

In the first stage of the learning process the updating of consequent parameters is done through least square estimates by passing of function signals forward until layer 4. In the second stage, the errors rates are propagated backward which help in updating the premise parameters by gradient descent algorithm. The network training is carried out using the hybrid learning algorithm. Training process is stopped once the desired error tolerance is reached or the total number of epochs exceeds a pre-specified number.

Table 5.1: ANFIS hybrid learning rule

ANFIS Quantities	Forward pass	Backward pass
Premise parameters	Fixed	Gradient descent
Consequent parameters	Least squares estimate (LSE)	Fixed
Signals	Node outputs	Error rates

The essentials of training algorithm are shown in Table 5.1, while the flowchart showing the training procedure is given in Figure 5.10. The BBO algorithm generates the required training data required for ANFIS network. As shown in Figure 5.10, the algorithm starts with initialization of BBO parameters and generation of random operating scenario. This input vector is stored in externally in an array. The technique then computes the optimum decoupled controller parameters by applying migration, mutation and elitism operations. These PI gains constitute the target vector for ANFIS system and are stored in an external variable. After completing a loop of 100 iterations the training input-output data pair is obtained.

The next step in the algorithms involves training and validation of adaptive neuro-fuzzy network. The data set is imported into the ANFIS system and applying hybrid learning rule, with number of epochs as 500, the training process is completed. The network is saved for use in simulations requiring online computation of controller gains.

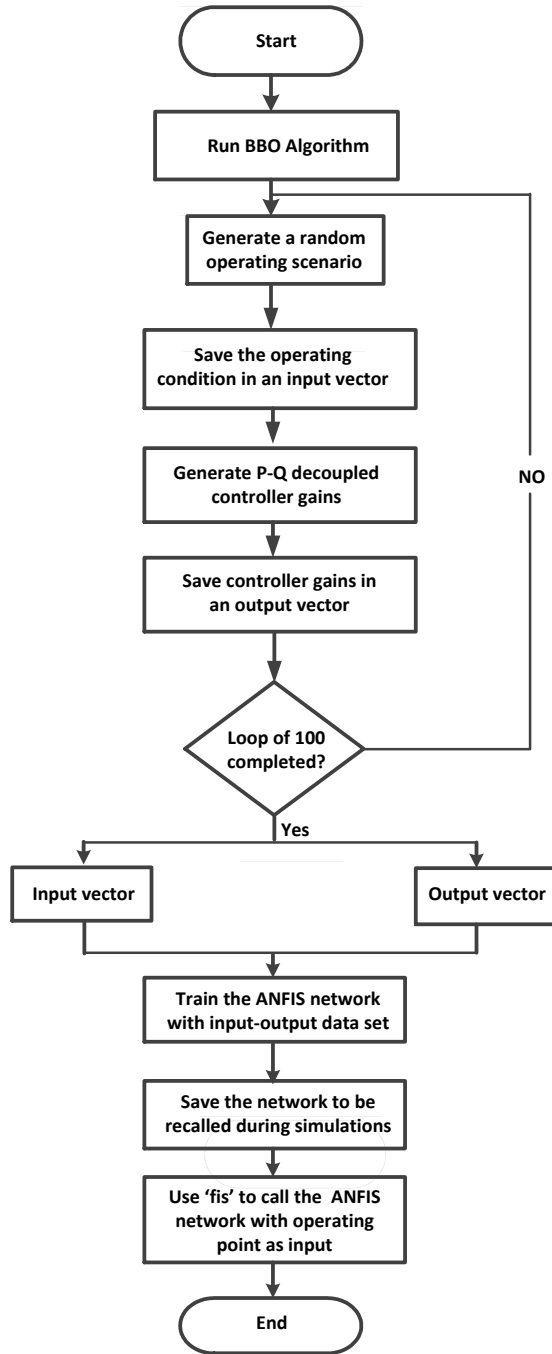


Figure 5.10: Flow chart of ANFIS network to be employed for P-Q decoupled controller

CHAPTER 6

TESTING THE ADAPTIVE NEURO-FUZZY ENERGY STORAGE CONTROLLER

The adaptive neuro-fuzzy P-Q decoupled controllers developed for battery and supercapacitor energy storage systems are tested for various contingencies and are evaluated for their performance. Adaptive control design is carried out for a range of operating points through optimal tuning of controller parameters using biogeography technique. A neuro-fuzzy network is trained on the optimal data samples obtained from the BBO search algorithm. The studies include,

- Simulation results of the BBO optimization procedure.
- Neuro-fuzzy based training and testing of the parameter.
- Determination of adaptive membership functions for the neuro-fuzzy system.

The performance evaluation of the proposed neuro-fuzzy controller for BESS and SCESS devices is carried out by simulating the following disturbances,

1. Input pulse of 0.15pu on the microgenerator
2. Torque step of 0.1pu on the microgenerator

Comparison among the two control strategies are presented for a 400 msec three-phase symmetrical fault at the grid.

6.1 Generation of Adaptive Controller Parameters

The evolutionary bio-geography based expert system computes the training data required for the adaptive neuro-fuzzy network. A bio-geography search program was used to generate the P-Q decoupled controller settings for various operating scenarios. The BBO uses a nonlinear fitness function, (5.34), to guide the search process. For a given initial conditions, the set of controller gains that achieve minimum objective value constitute the optimal parameters. The number of habitats was selected 50 and the number of iterations as 80. The other parameters of BBO technique are given in Table 6.1. The minimum and maximum values of control variables are specified in Table 6.2 and the algorithm tries to find the optimal control settings under given initial conditions.

Table 6.1: The BBO algorithm parameters

Parameter description	Value
Population size	50
Iterations	80
Elitism parameter	4
Number of SIV parameters	8
Habitat modification probability	1.0
Lower bound for immigration probability	0
Upper bound for immigration probability	1.0
Step size for numerical integration of probabilities	1.0
Maximum immigration rate I	1.0
Maximum emigration rate E	1.0
Stop iterations	75

Table 6.2: Range of decoupled control parameters

Control parameters	Minimum value	Maximum value
K_{p1}	0.0	1.0
K_{p2}	0.0	1.0
K_{p3}	1.0	500
K_{p4}	1.0	500
K_{i1}	0.0	1.0
K_{i2}	0.0	1.0
K_{i3}	0.0	1.0
K_{i4}	0.0	1.0

The algorithm begins with the microgenerator real power, terminal voltage, and power factor, PV output power, fuel cell power, and wind system power as input. It generates inhabitants of size 50 by taking random values for P-Q decoupled controller gains. Then the technique searches for optimal values of gains within the specified range.

Elitism, probabilistic based migration and mutation operations are performed on the initial population establishing optimal control settings. The system is assumed to be operating with microgenerator delivering 0.2 pu while the power from wind, PV and fuel cell was fixed at 0.9 pu, 0.8 pu, and 0.7 pu respectively. The load on the microgrid bus is considered to be $1.0+j0.15$ pu. For a torque pulse of 0.15 pu applied on the microgenerator for 300 msec, the BBO converged to the optimal fitness value in about 18 iterations as shown in Figure 6.1. From the cost function it can be seen that there are areas where the fitness value does not change. These areas are identified as local minima, which are avoided through application of migration and mutation procedure until the objective function report no further changes.

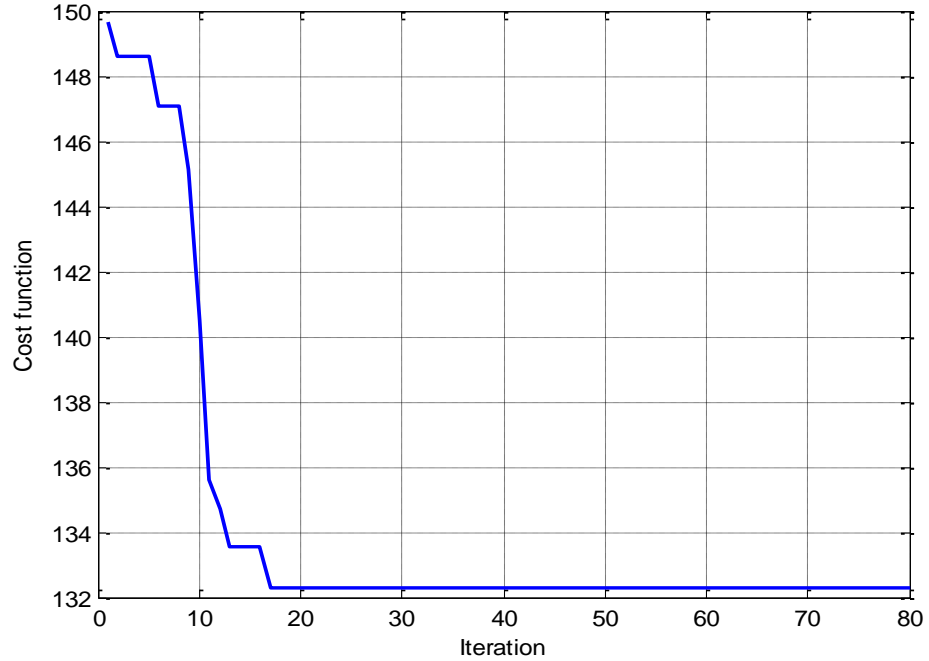


Figure 6.1: Variation of cost function against iterations for 0.15 pu input torque pulse applied at microgenerator for 300 msec

The convergence characteristics of PI gains of the controller gains are shown in Figure 6.2-Figure 6.9. It has been noticed that, similar to the fitness value of BBO, the controller gains do not change after 18 iterations. The converged values of the controller parameters are listed in Table 6.3.

Table 6.3: Optimum P-Q decoupled controller parameters for BESS when 0.15 pu torque pulse is applied at the microgenerator for 300 msec

Disturbance	Proportional gains			
	Torque pulse of 0.15 pu applied for 300 msec	$K_{p1} = 0.8948$	$K_{p2}=0.4181$	$K_{p3}=267.9043$
Integral gains				
$K_{i1}=0.5906$		$K_{i2} = 0.6473$	$K_{i3} = 0.1835$	$K_{i4} =0.1052$

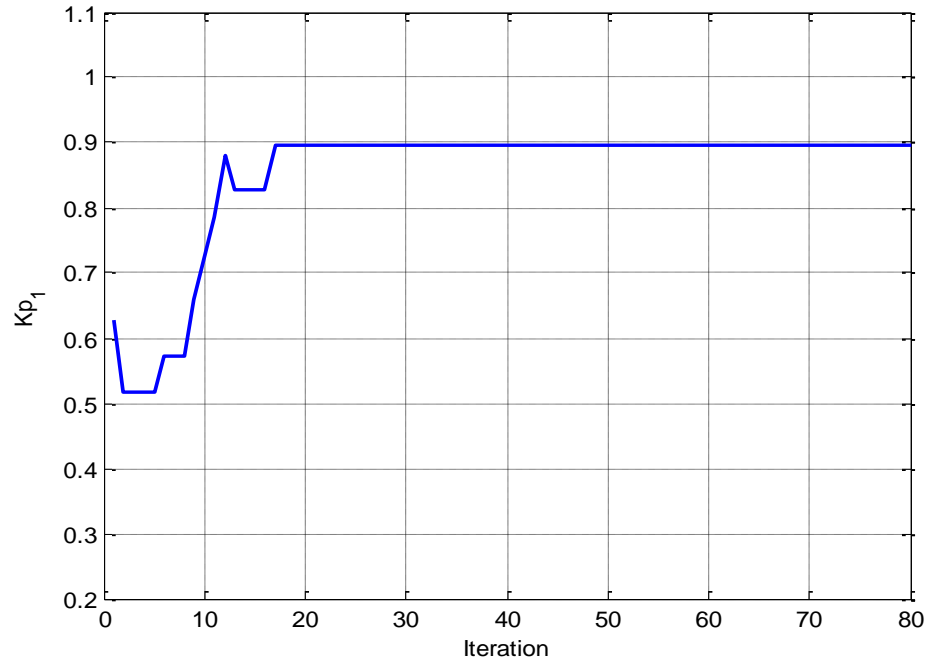


Figure 6.2: Convergence of Kp1 against iterations for optimization when 0.15 pu input torque pulse is applied at microgenerator for 300 msec

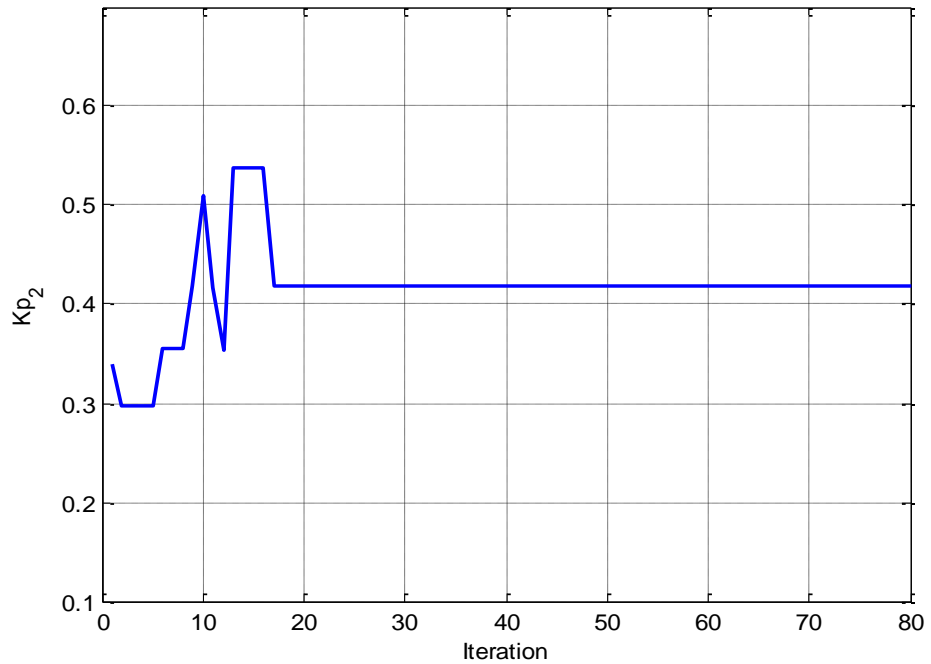


Figure 6.3: Convergence of Kp2 against iterations for optimization when 0.15 pu input torque pulse is applied at microgenerator for 300 msec

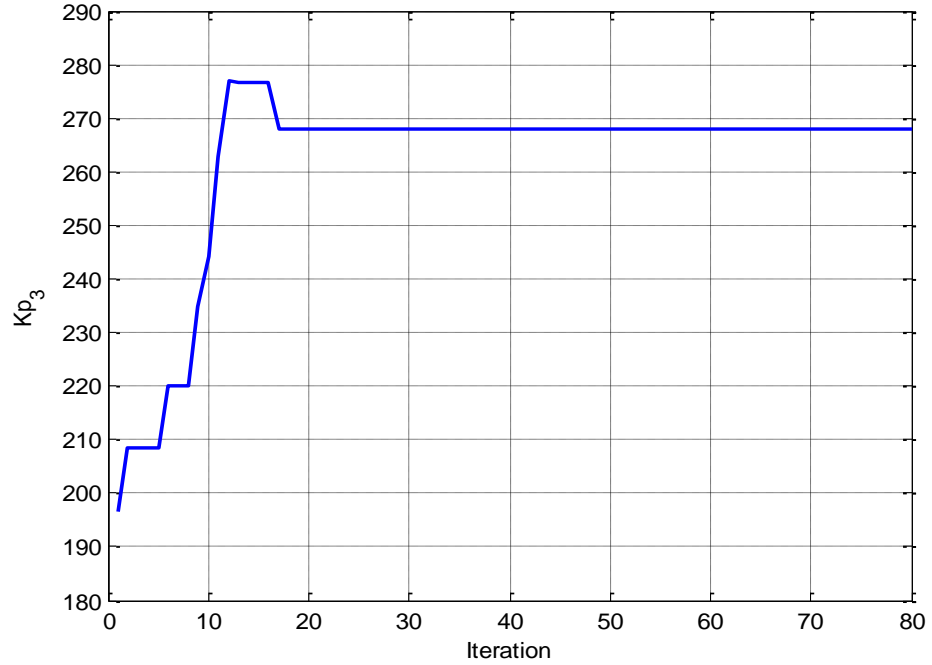


Figure 6.4: Convergence of Kp3 against iterations for optimization when 0.15 pu input torque pulse is applied at microgenerator for 300 msec

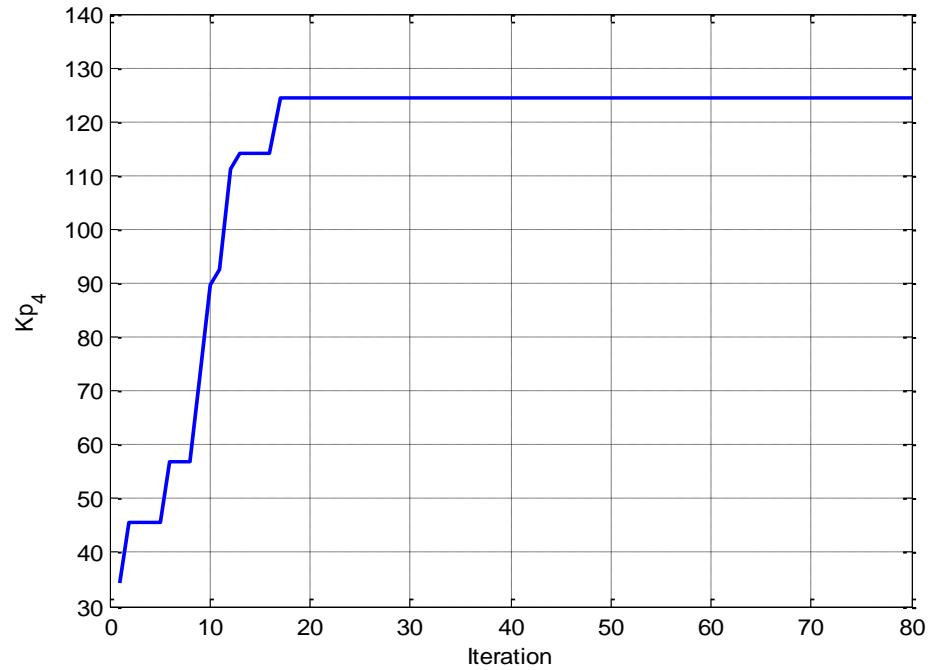


Figure 6.5: Convergence of Kp4 against iterations for optimization when 0.15 pu input torque pulse is applied at microgenerator for 300 msec

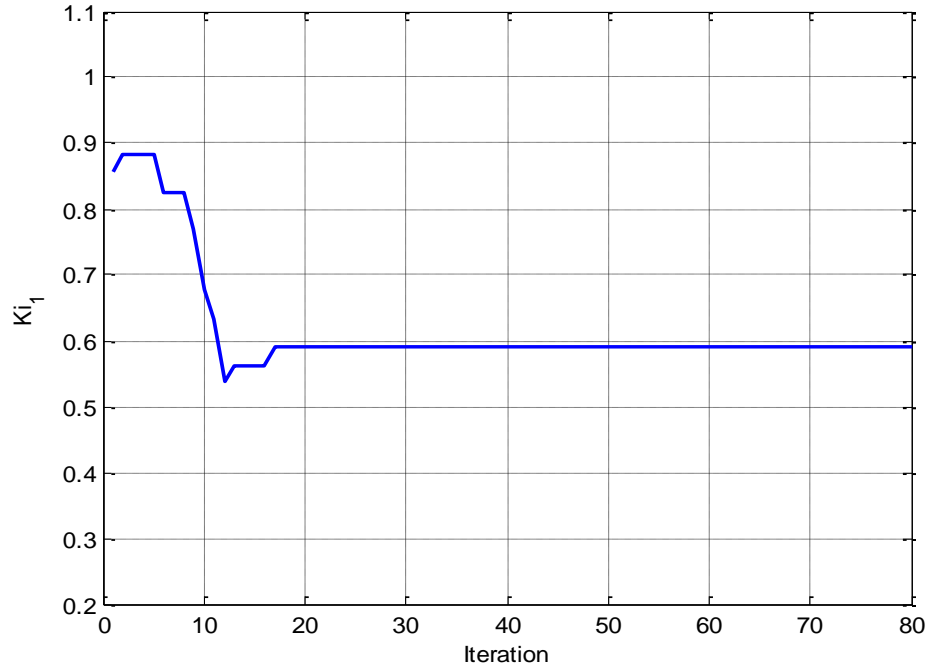


Figure 6.6: Convergence of K_{i1} against iterations for optimization when 0.15 pu input torque pulse is applied at microgenerator for 300 msec

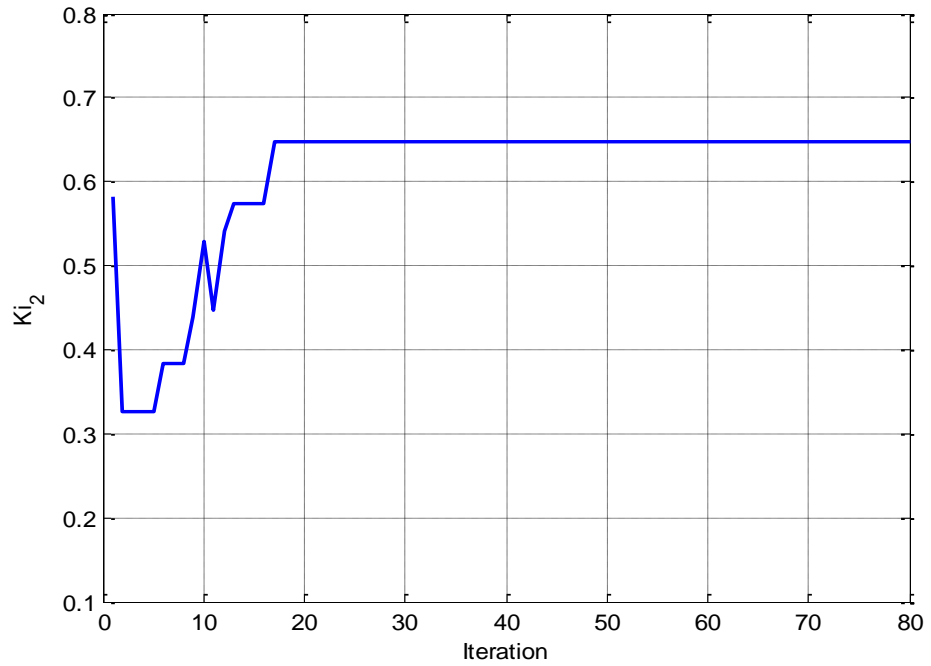


Figure 6.7: Convergence of K_{i2} against iterations for optimization when 0.15 pu input torque pulse is applied at microgenerator for 300 msec

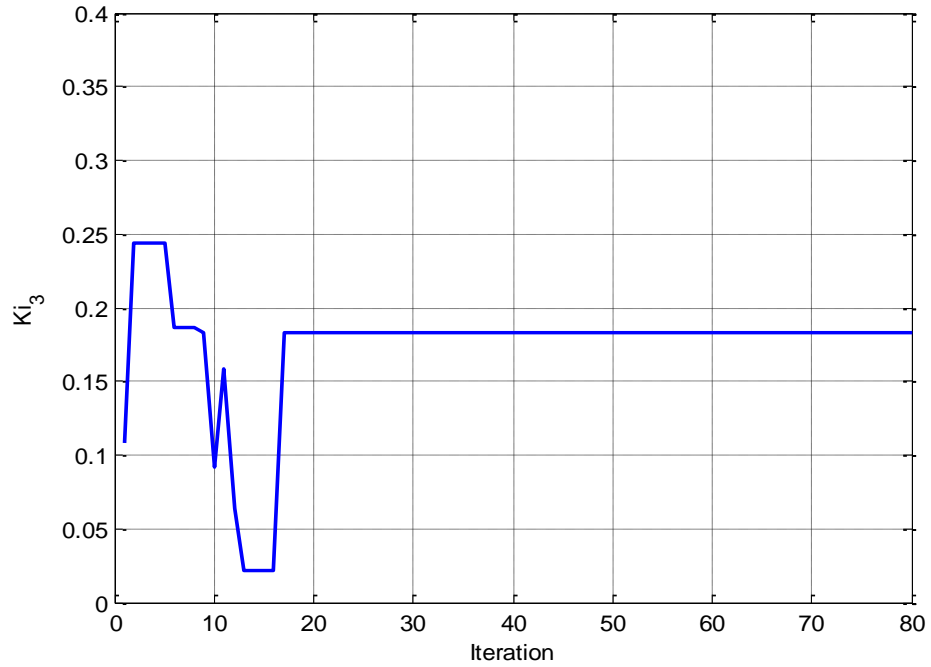


Figure 6.8: Convergence of K_{i3} against iterations for optimization when 0.15 pu input torque pulse is applied at microgenerator for 300 msec

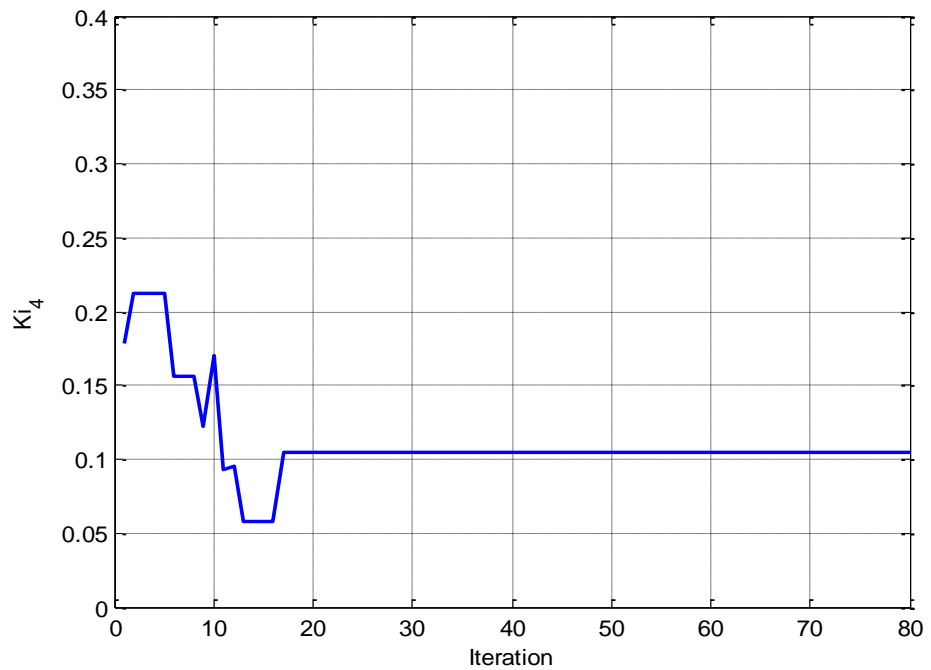


Figure 6.9: Convergence of K_{i4} against iterations for optimization when 0.15 pu input torque pulse is applied at microgenerator for 300 msec

An adaptive neuro-fuzzy system was trained using the data obtained from the BBO search algorithm for different initial conditions. The input vector consists of operating scenarios while the output vector is made up of optimized decoupled controller parameters. For learning phase 80 input-output data samples were taken and the remaining 20 were used for testing of the network. The ANFIS network updates the firing strengths of its membership functions depending on the data samples in order to derive a nonlinear relationship between the input-output pair. For each of the input, the number of membership functions was selected as 3. The fuzzy rules are optimized to accurately model the data set and an optimal fuzzy system is obtained which could be used for online applications.

6.2 BESS Energy Storage Controller

The composite microgrid system supported with battery energy storage device shown in Figure 5.1 was simulated to study the performance of the adaptive neuro-fuzzy based decoupled P-Q controller. The interfacing voltage source converter compensates the reactive power requirements of the system while the BESS device provides appropriate real power so as to damp the system transients. The transient performance of the system was investigated through different disturbance scenarios. The dynamic response of the BESS controller was evaluated with following two disturbances:

- a. Input torque pulse of 0.15 pu for 300 msec
- b. Step increase in input torque by 0.1 pu

The responses recorded are the variations of microgenerator speed deviations, , the PV array output current, PV filter capacitor voltage, the fuel cell dc-link voltage, fuel cell stack current, the wind turbine load angle, PMSG stator current, wind system dc-link voltage, the VSC current, dc-link voltage, the microgrid bus voltage, the terminal voltages of microgenerator and wind system, the real power delivered to the grid, and energy storage real and reactive powers.

6.2.1 Torque pulse disturbance

Small-signal and nonlinear analysis carried out in chapter 4 reveals that the microgenerator has significant influence on the performance of microgrid. In this study, unstable operating scenarios were simulated for input torque steps on the microgenerator. The microgenerator output is considered to be 0.2 pu, while the renewables such as wind system delivers 0.9 pu, PV assumed to supply 0.8 pu and fuel cell system provides 0.7 pu. This high loading operating scenario was selected as to study a worst case scenario.

For a 300 msec 0.15 pu torque pulse, Figure 6.10-Figure 6.11 shows the variation of microgenerator speed deviation and terminal voltage respectively. From the responses shown it is apparent that in the absence of any control the microgrid system gives rise to slowly growing transients. However, with the BESS control the growing oscillation is controlled very fast. This is achieved by real and reactive power injection by the BESS-VSC combination. Because of this support, the microgenerator terminal voltage and speed return to the pre-disturbance level after a brief oscillation.

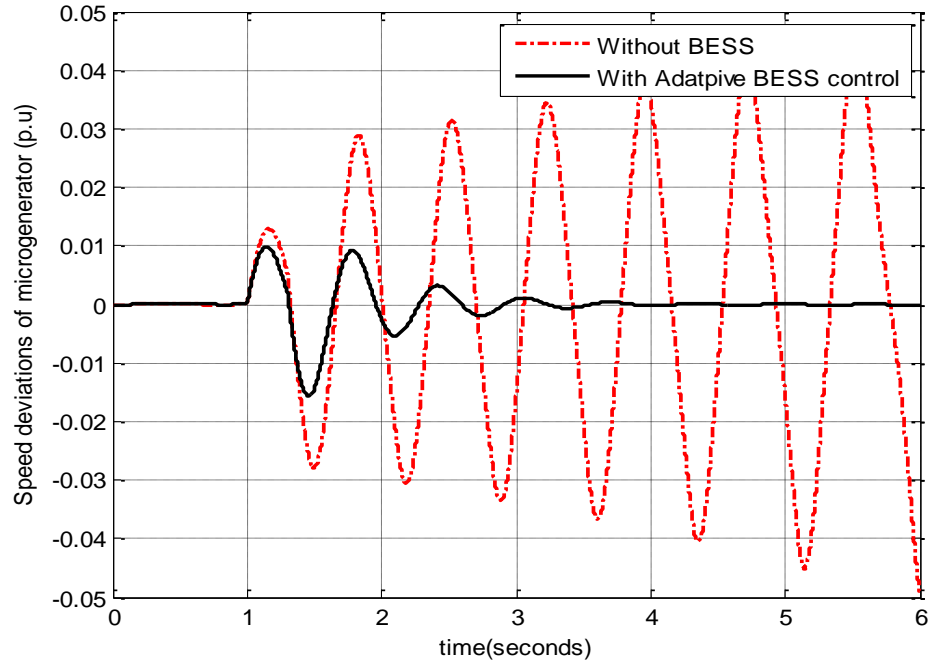


Figure 6.10: Microgenerator rotor speed deviation when a 15% torque pulse is applied for 300 msec, (a) Without BESS (b) With adaptive BESS control

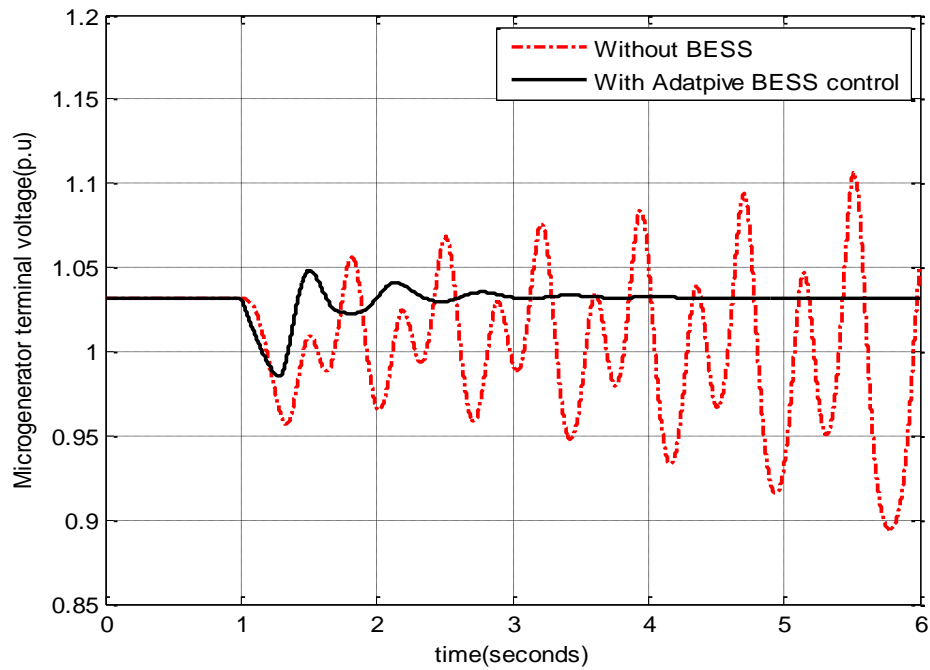


Figure 6.11: Microgenerator terminal voltage variation when a 15% torque pulse is applied for 300 msec, (a) Without BESS (b) With adaptive BESS control

The variations in PV array output current and PV filter capacitor voltage are shown in Figure 6.12-Figure 6.13. It can be seen from Figure 6.12 that in the absence of any control action the oscillations in array output current are growing. However, with the adaptive BESS controller the oscillations are damped quickly restoring steady state after 3 seconds. The transients arising in filter capacitor voltage also die out immediately as noticed from Figure 6.13.

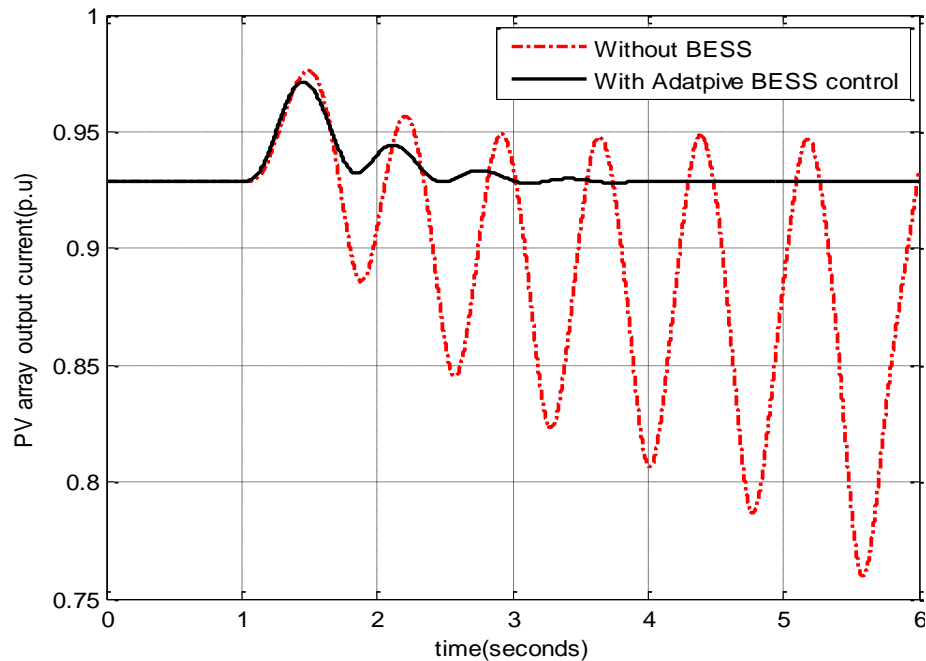


Figure 6.12: PV array current variation when a 15% torque pulse is applied for 300 msec, (a) Without BESS (b) With adaptive BESS control

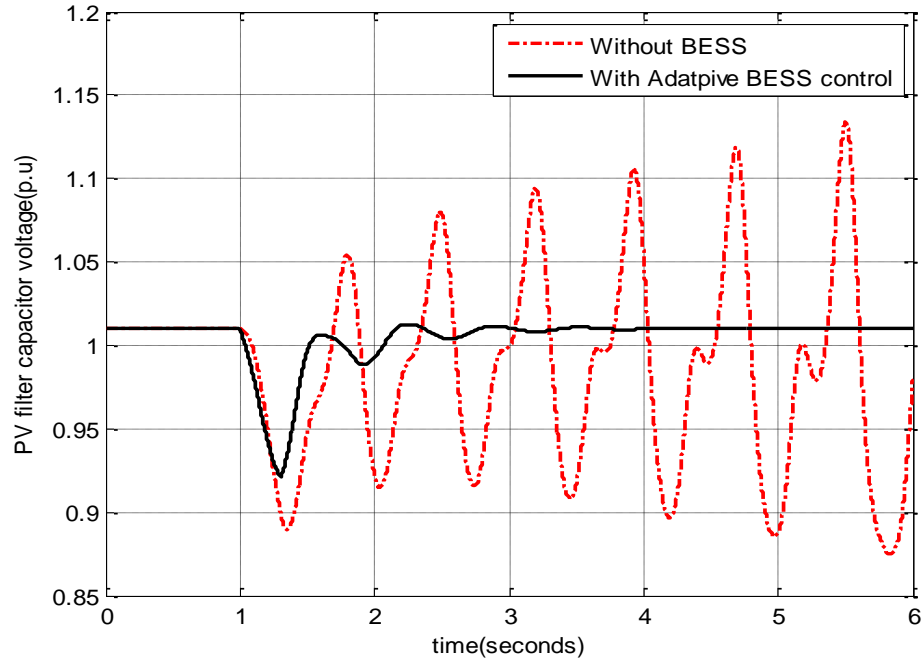


Figure 6.13: PV filter capacitor voltage variation when a 15% torque pulse is applied for 300 msec, (a) Without BESS (b) With adaptive BESS control

The transient responses of the wind system post contingency on the microgrid are shown in Figure 6.14-Figure 6.16. The variation in PMSG rotor speed and terminal voltage are recorded in Figure 6.14-Figure 6.15. Without BESS control, the oscillations in the rotor speed and terminal voltage dangerously increase leading to instability condition. However, with the adaptive BESS control the oscillations are damped quickly restoring steady state conditions. The PMSG stator current variations following contingency is shown in Figure 6.16.

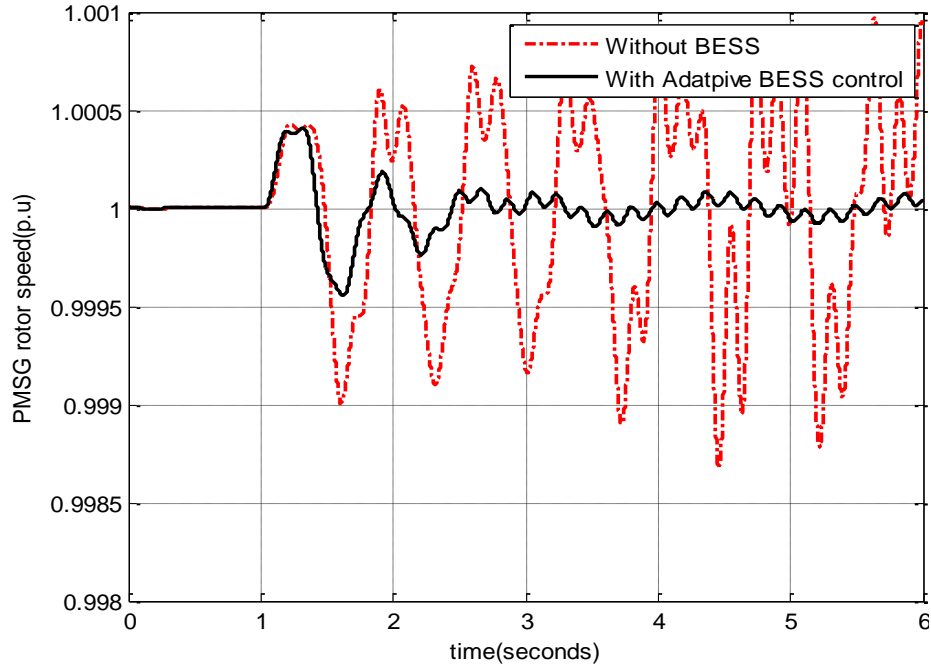


Figure 6.14: PMSG rotor speed variation when a 15% torque pulse is applied for 300 msec, (a) Without BESS (b) With adaptive BESS control

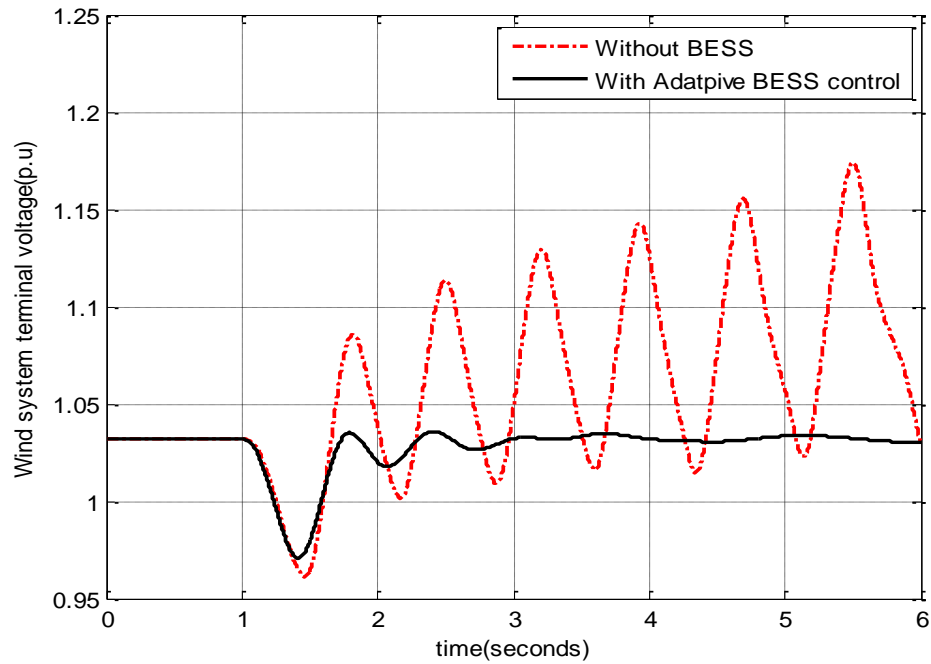


Figure 6.15: PMSG terminal voltage variation when a 15% torque pulse is applied for 300 msec, (a) Without BESS (b) With adaptive BESS control

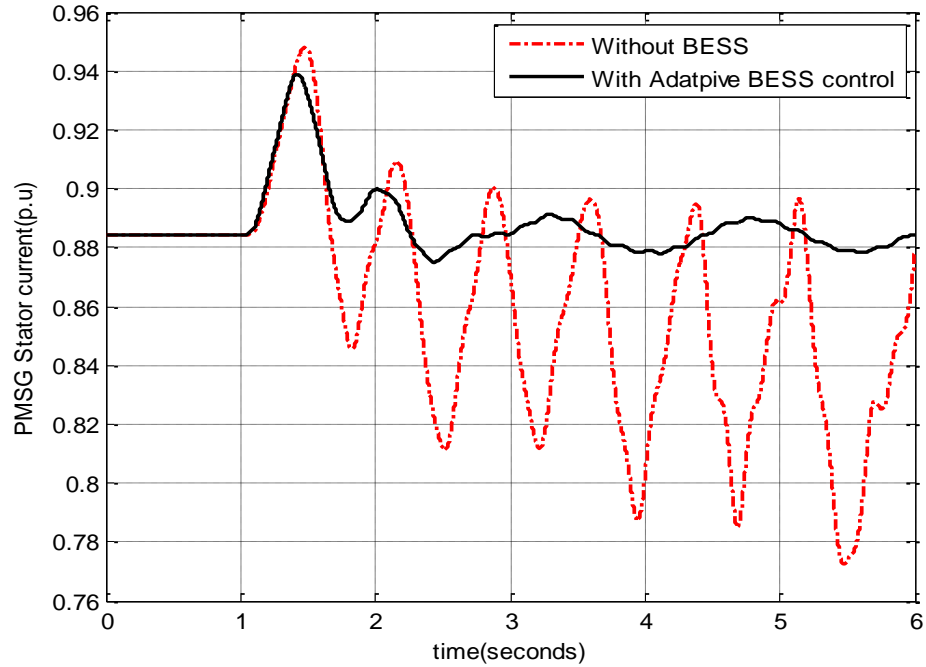


Figure 6.16: PMSG stator current variation when a 15% torque pulse is applied for 300 msec, (a) Without BESS (b) With adaptive BESS control

Figure 6.17 and Figure 6.18 show the response of VSC DC-link voltage and VSC current following a 15% torque pulse for 300 msec. It can be said from these figures that uncontrolled case leads to large amplitude oscillations which eventually takes the system into unstable region. However, with the adaptive BESS controller there is an improvement in the transient responses. The system normal operation conditions are restored in a few seconds post disturbance. The real power control provides good damping of system transients reestablishing the original conditions.

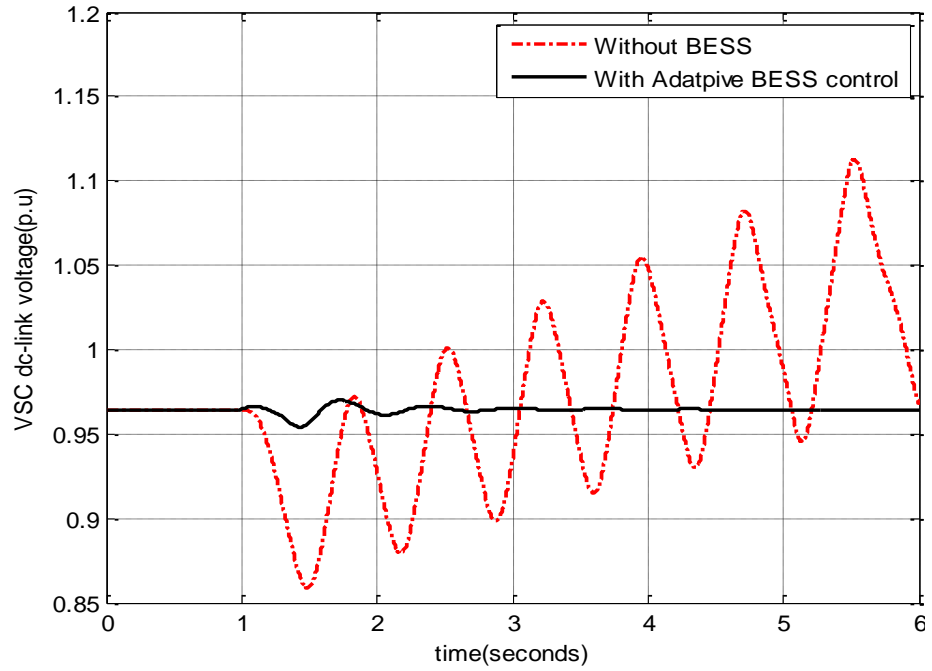


Figure 6.17: VSC DC-link voltage variation when a 15% torque pulse is applied for 300 msec, (a) Without BESS (b) With adaptive BESS control

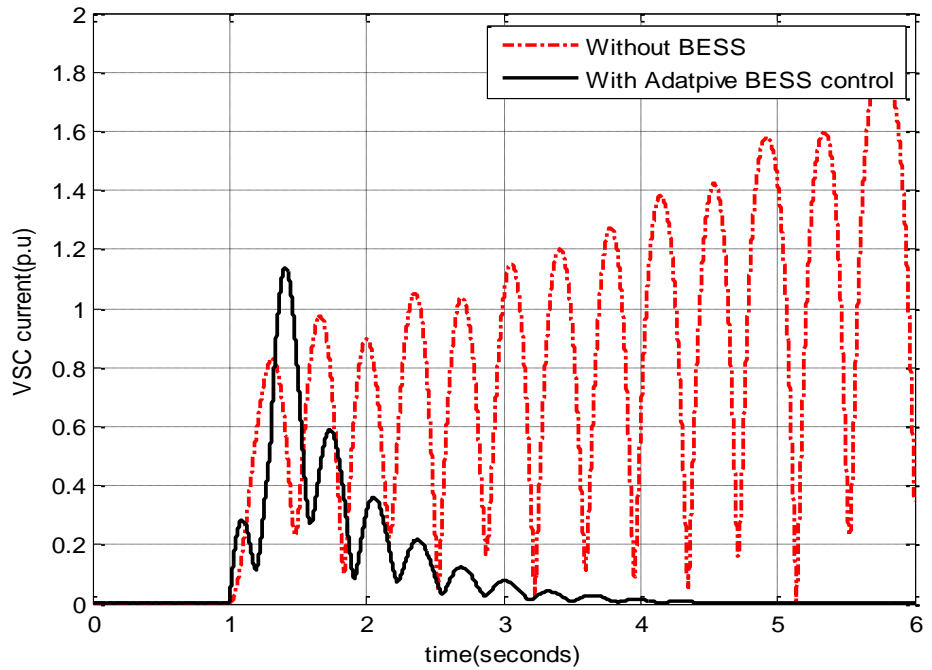


Figure 6.18: VSC current variation when a 15% torque pulse is applied for 300 msec, (a) Without BESS (b) With adaptive BESS control

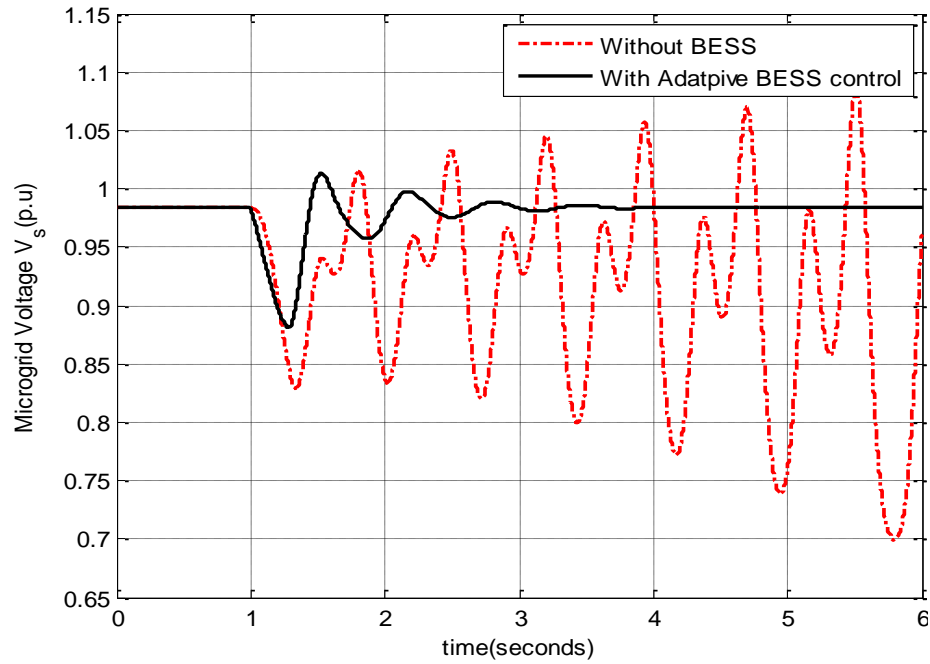


Figure 6.19: Microgrid bus voltage variation when a 15% torque pulse is applied for 300 msec, (a) Without BESS (b) With adaptive BESS control

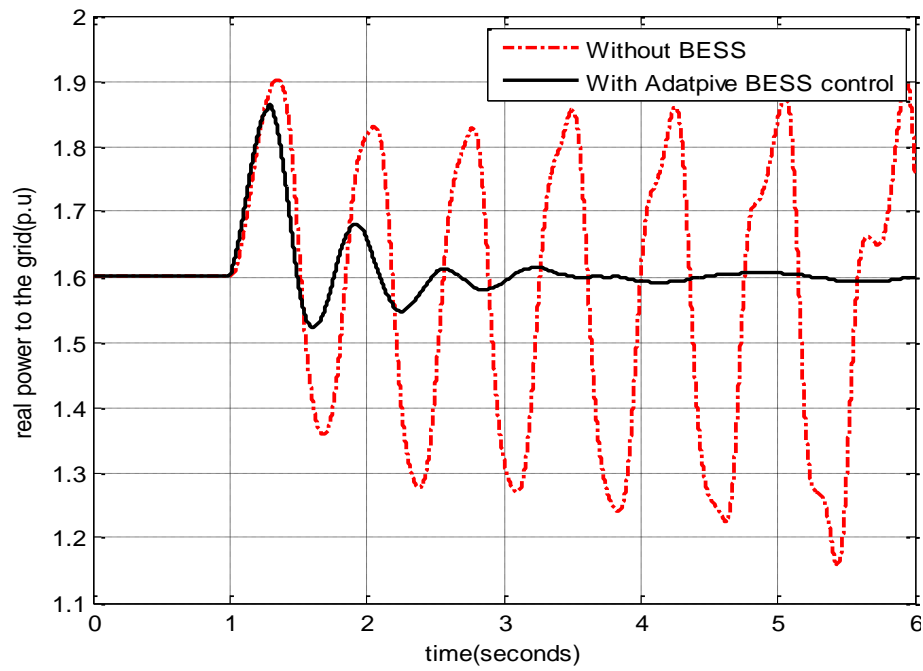


Figure 6.20: Microgrid delivered power to the grid variation when a 15% torque pulse is applied for 300 msec, (a) Without BESS (b) With adaptive BESS control

Variations in the microgrid bus voltage and the real power delivery to the grid are shown in Figure 6.19-Figure 6.20. The voltage instability condition seen without any control as depicted from Figure 6.19 is mitigated quickly by the BESS controller. The system reaches steady state in less than 3 seconds. From the Figure 6.20, it is seen that the BESS controller achieves smooth delivery of power to the grid.

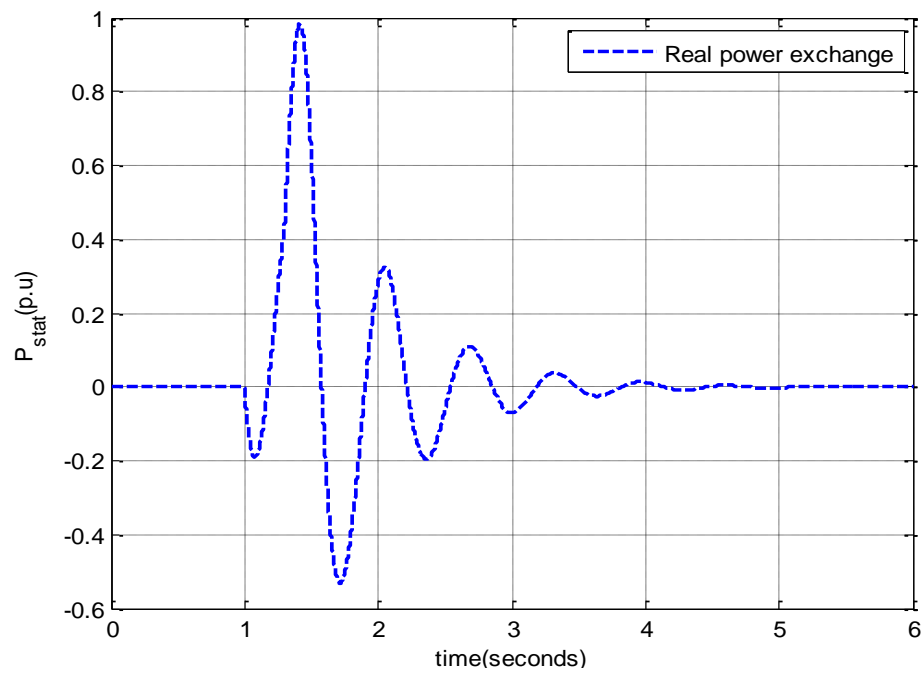


Figure 6.21: Injected real power by the BESS controller following a torque pulse of 15% for 300 msec duration

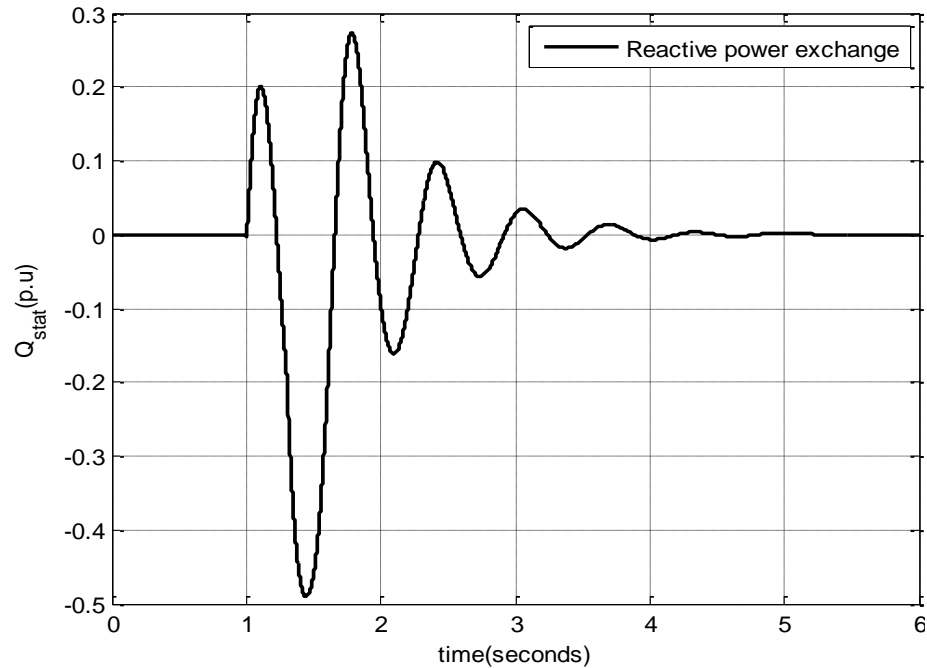


Figure 6.22: Injected reactive power by the BESS controller following a torque pulse of 15% for 300 msec duration

The real and reactive power injections by the BESS controller are shown in Figure 6.21-Figure 6.22. The sudden increase in mechanical torque input to the system is mitigated by the absorption of real power as seen in Figure 6.21. The real power absorption by the BESS controller reduces the amplitude of oscillations in various quantities. The decrease in the microgrid voltage during transient condition is overcome by appropriate reactive power injections from the VSC interfacing the BESS controller. As seen from Figure 6.22, the reactive power injection into the microgrid restores the voltage quickly with minimum transients and system operates in steady state after 3 seconds.

6.2.2 Torque step disturbance

The performance of the proposed adaptive neuro-fuzzy BESS controller is tested by applying a step change in input torque. Initially the microgenerator supplies 0.2 pu, while the wind system delivers 0.9 pu, PV 0.8 pu and fuel cell 0.7 pu. This represents a relatively large loading condition and is considered to study worst possible scenario. The variations in the microgenerator load angle and terminal voltage are shown in Figure 6.23-Figure 6.24 for a 0.1 pu step input change on the microgenerator.

As observed from Figure 6.23, with the step change in mechanical power input the microgenerator accelerates and its load angle increases. This will lead to eventual disconnection of the system when the rotor angle exceeds a certain limit. It is observed that, with the incorporation of adaptive BESS controller the oscillations are stabilized.

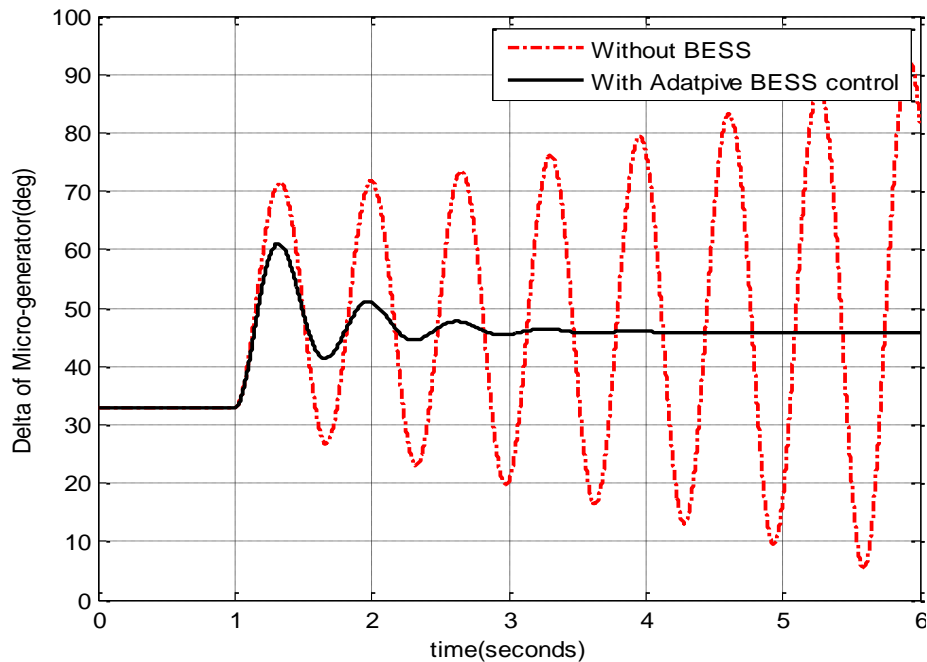


Figure 6.23: Microgenerator load angle variation following a 10% change in input torque, (a) Without BESS (b) With adaptive BESS control

It is noticed from Figure 6.24 that the microgenerator terminal voltage shows large oscillations growing up which would create voltage collapse if no proper control action were taken. However, with the adaptive BESS controller the voltage transients are controlled and new steady operation is restored in about 3 seconds.

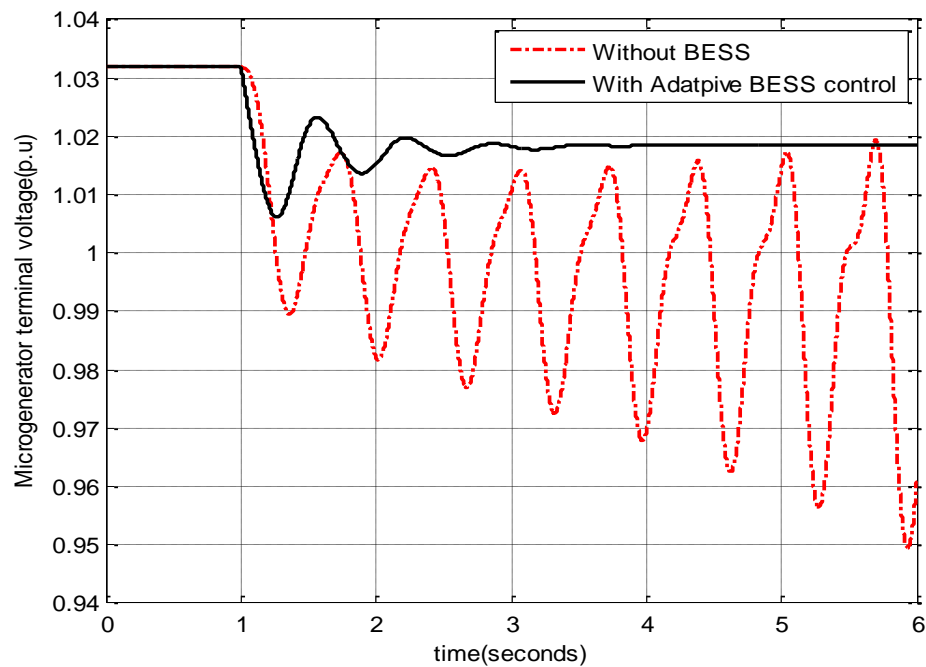


Figure 6.24: Microgenerator terminal voltage variation following a 10% change in input torque, (a) Without BESS (b) With adaptive BESS control

The variations in PV array output current and fuel cell DC-link voltage are shown in Figure 6.25-Figure 6.26. The application of BESS controller helps in stabilizing the undamped transients and shifts the system to new operating region quickly.

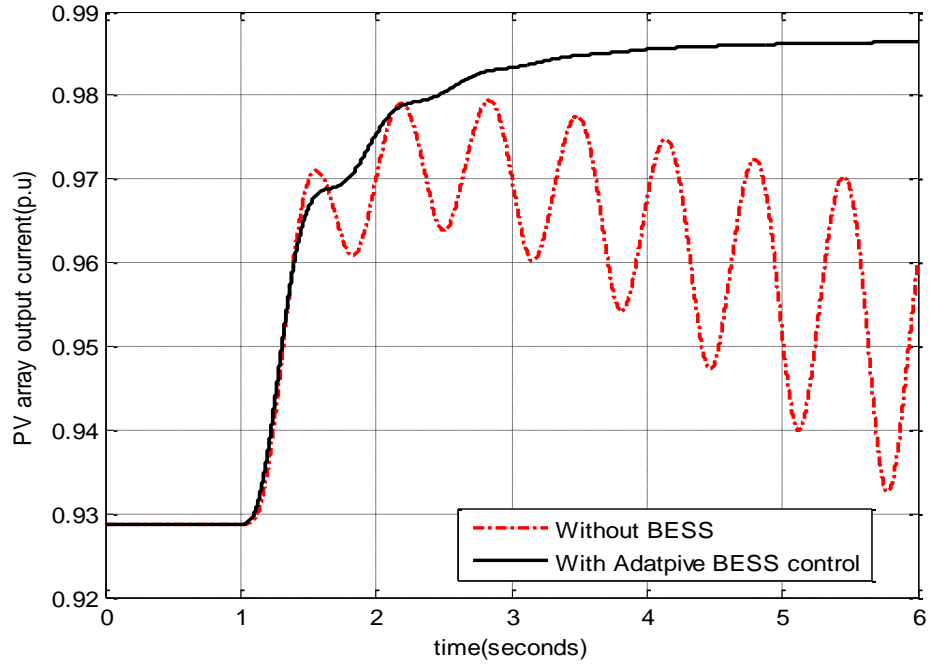


Figure 6.25: PV array output current variation following a 10% change in input torque, with (a) Without BESS (b) With adaptive BESS control

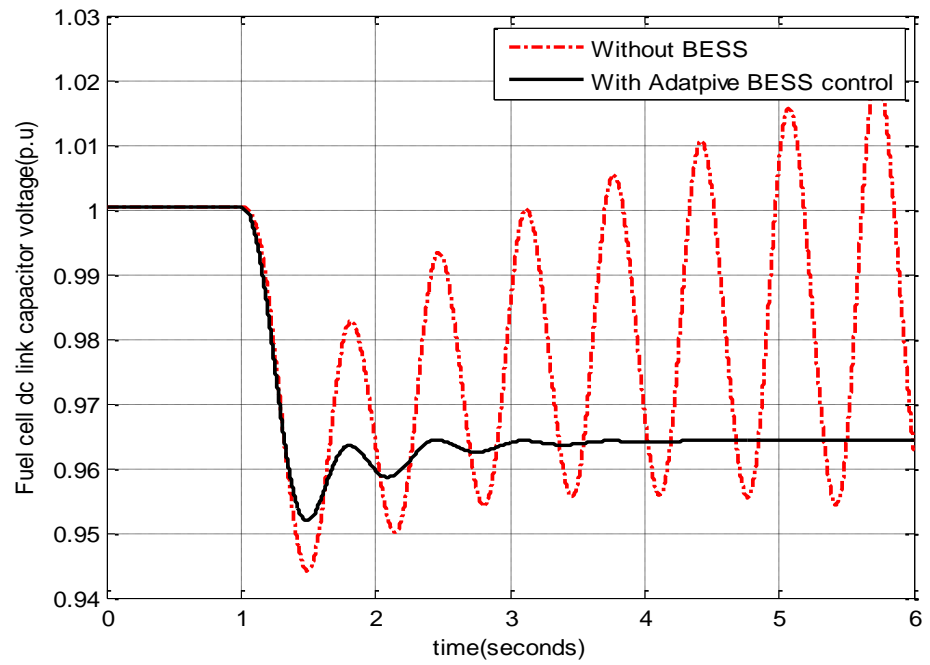


Figure 6.26: Fuel cell DC-link voltage variation following a 10% change in input torque, with (a) Without BESS (b) With adaptive BESS control

The wind system rotor speed and PMSG stator current following 10% step change in torque are recorded in Figure 6.27-Figure 6.28. The PMSG rotor speed oscillations arising due to sudden step increase in mechanical input are damped by the BESS controller. The speed variations are minimized and system stability is restored as shown in Figure 6.27.

The 10% step change in torque input to the microgenerator affects the PMSG stator current as given in Figure 6.28. The variations in the stator current lead to large amplitude oscillations which would eventually find a way to voltage collapse. With the adaptive BESS controller the arising current oscillations are mitigated very easily. The new steady state scenario is reached in about 3 seconds.

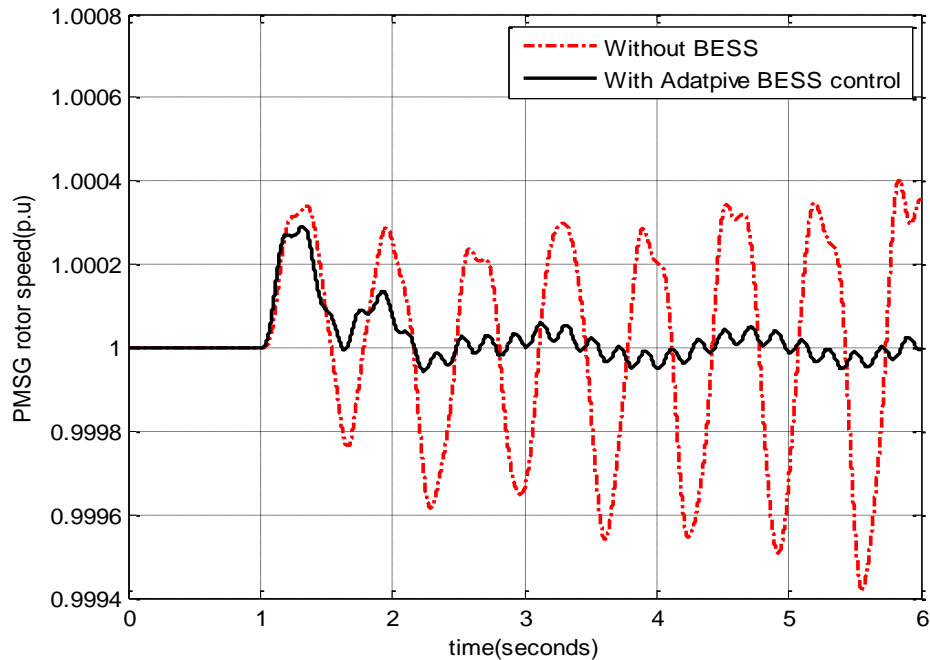


Figure 6.27: PMSG rotor speed variation following a 10% change in input torque, with (a) Without BESS (b) With adaptive BESS control

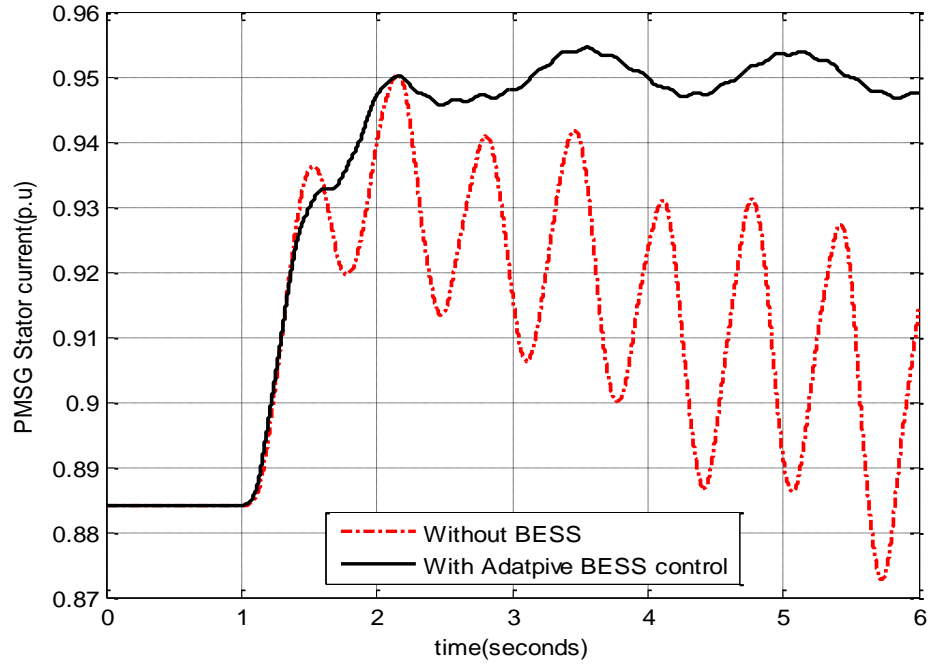


Figure 6.28: PMSG stator current variation following a 10% change in input torque, with (a) Without BESS (b) With adaptive BESS control

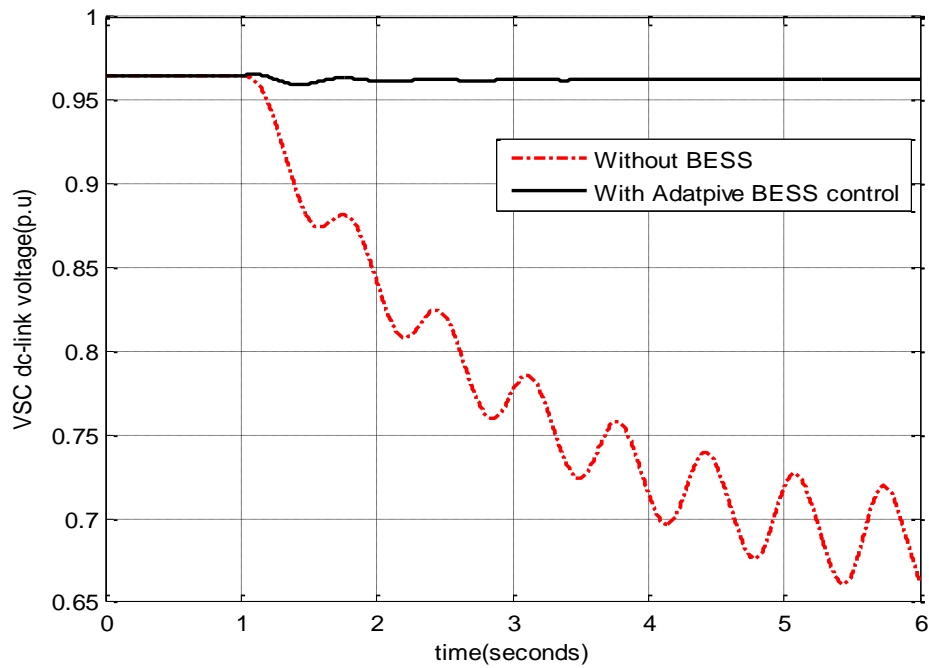


Figure 6.29: VSC DC-link voltage variation following a 10% change in input torque, with (a) Without BESS (b) With adaptive BESS control

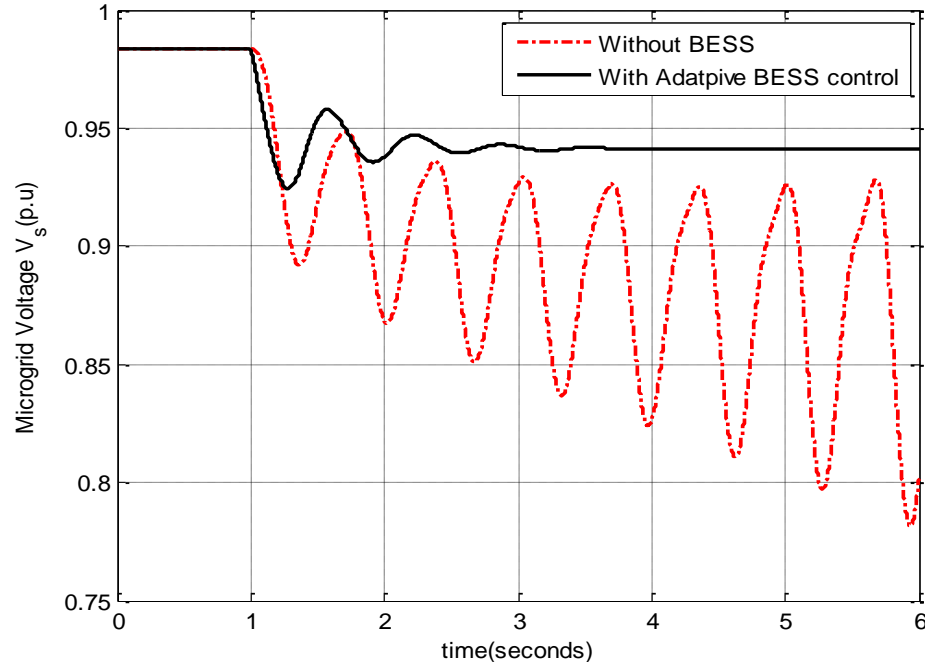


Figure 6.30: Microgrid voltage variation following a 10% change in input torque, with (a) Without BESS (b) With adaptive BESS control

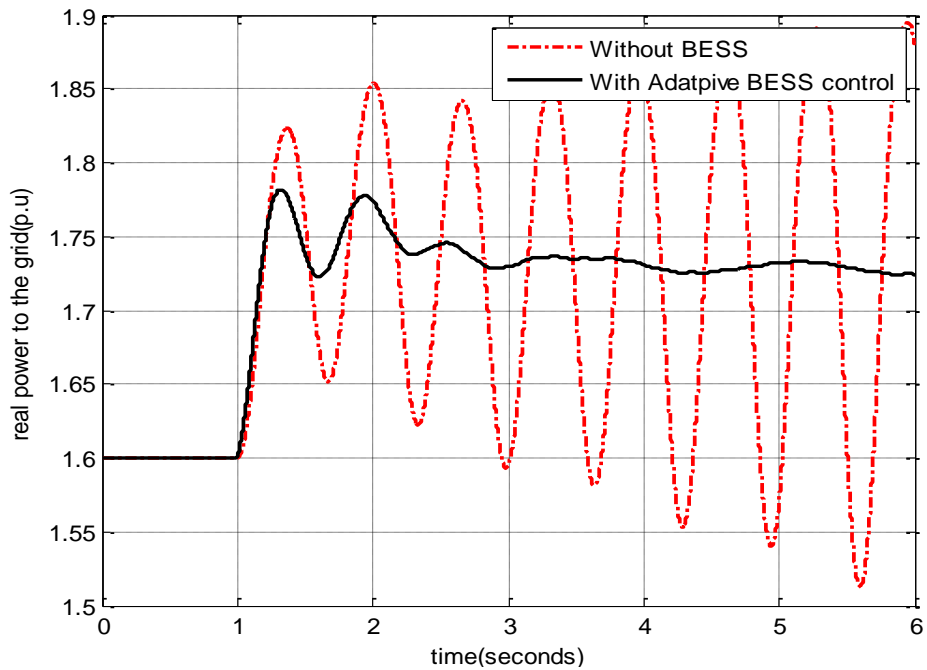


Figure 6.31: Real power delivered to the grid variation following a 10% change in input torque, with (a) Without BESS (b) With adaptive BESS control

The transient responses for VSC DC-link voltage, the microgrid voltage and real power delivered to the grid are shown in Figure 6.29-Figure 6.31. It can be said from these figures that uncontrolled case leads to large amplitude oscillations which eventually takes the system into unstable region. However, with the adaptive BESS controller there is an improvement in the transient responses. The system new operation conditions are restored in a few seconds post disturbance.

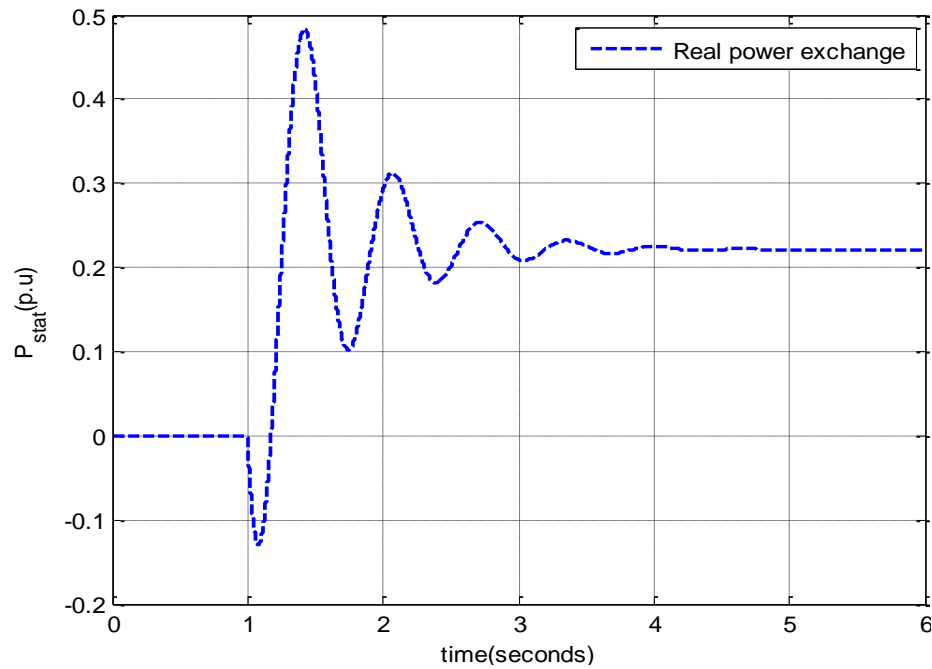


Figure 6.32: Injected real power by the BESS controller following a 10% change in input torque

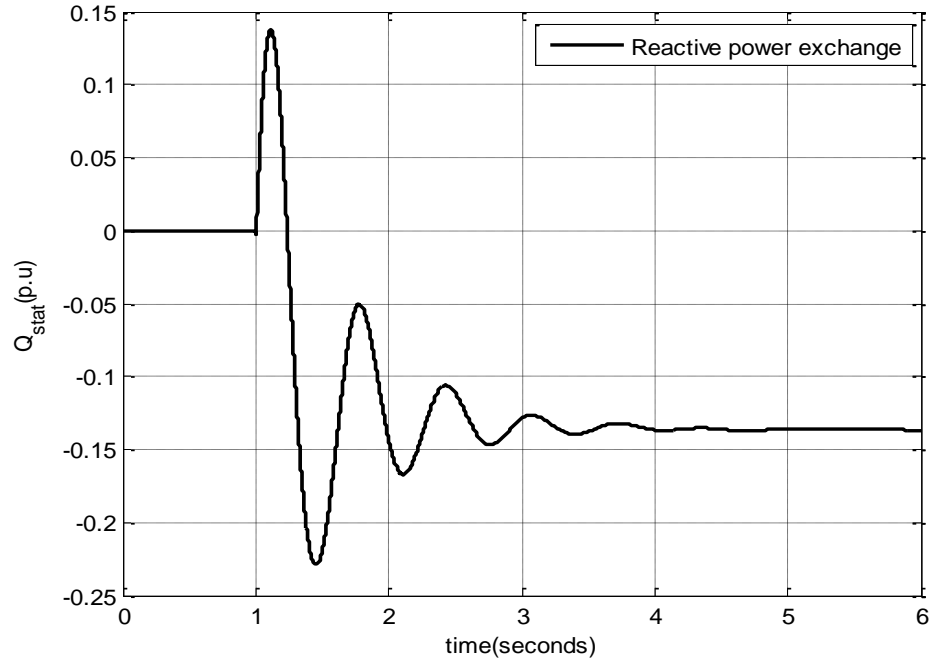


Figure 6.33: Injected reactive power by the BESS controller following a 10% change in input torque

The real and reactive power injections by the BESS controller are shown in Figure 6.32-Figure 6.33. The sudden increase in mechanical torque input to the system is mitigated by the absorption of real power as noticed in Figure 6.32. The real power absorption by the BESS controller reduces the amplitude of oscillations in various quantities. The system is maintained in the new operating region with continuous power injection from the BESS controller. The decrease in the microgrid voltage during transient condition is overcome by appropriate reactive power injection from the voltage source converter interfacing BESS device. As seen from Figure 6.33, the reactive power injection into the microgrid restores the voltage quickly with minimum transients and system operates in steady state after 3 seconds.

6.3 Supercapacitor (SCESS) Energy Storage Controller

The configuration of the microgrid system with a supercapacitor energy storage device is shown in Figure 5.4. The performance of the neuro-fuzzy based SCESS controller is investigated through different disturbance scenarios. The dynamic response of the SCESS controller is presented with following two disturbances:

- a. Input torque pulse of 0.15 pu for 300 msec
- b. Step increase in input torque by 0.1 pu

The responses recorded are for the variations of microgenerator speed deviations, the PV array output current, PV filter capacitor voltage, the fuel cell dc-link voltage, fuel cell stack current, the wind turbine load angle, PMSG stator current, wind system dc-link voltage, the VSC current, DC-link voltage, the microgrid bus voltage, the terminal voltages of microgenerator and wind system, the real power delivered to the grid, and energy storage real and reactive powers.

6.3.1 Torque pulse disturbance

Initially the DG loading considered in the analysis are: microgenerator 0.2 pu, wind system 0.9 pu, PV 0.8 pu, and fuel cell 0.7 pu. The load on the microgrid is considered to be held constant at $1+j0.15$ pu. For a 15 % input torque pulse on the microgenerator, its speed and terminal voltage variations are shown in Figure 6.34-Figure 6.35. It is observed from these figures that the uncontrolled system gives rise to growing oscillations, stable operating scenario has been established by the adaptive SCESS controller by damping out the oscillations in less than 1 second.

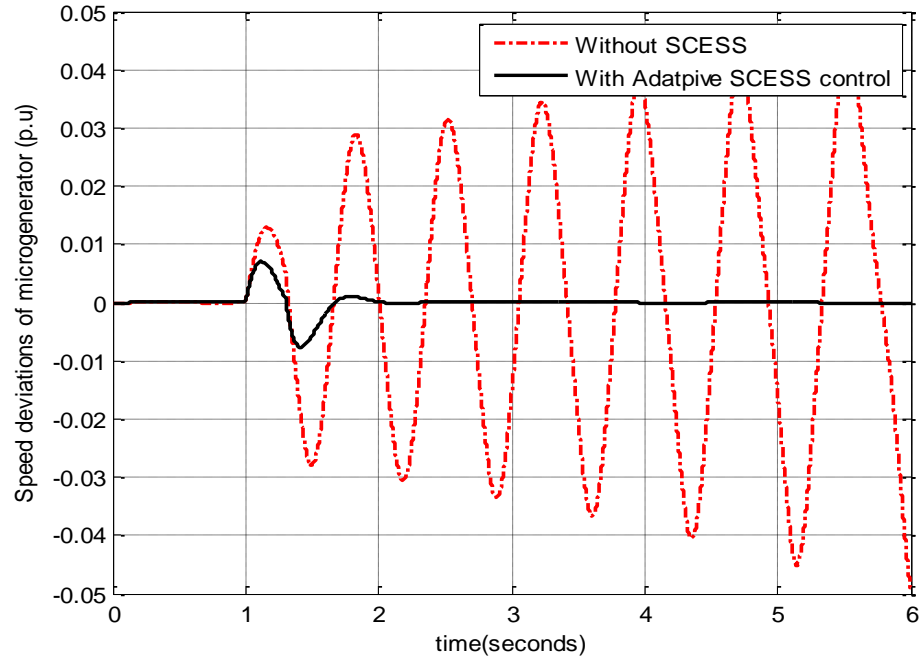


Figure 6.34: Microgenerator speed variation when a 15% torque pulse is applied for 300 msec, (a) Without SCESS (b) With adaptive SCESS control

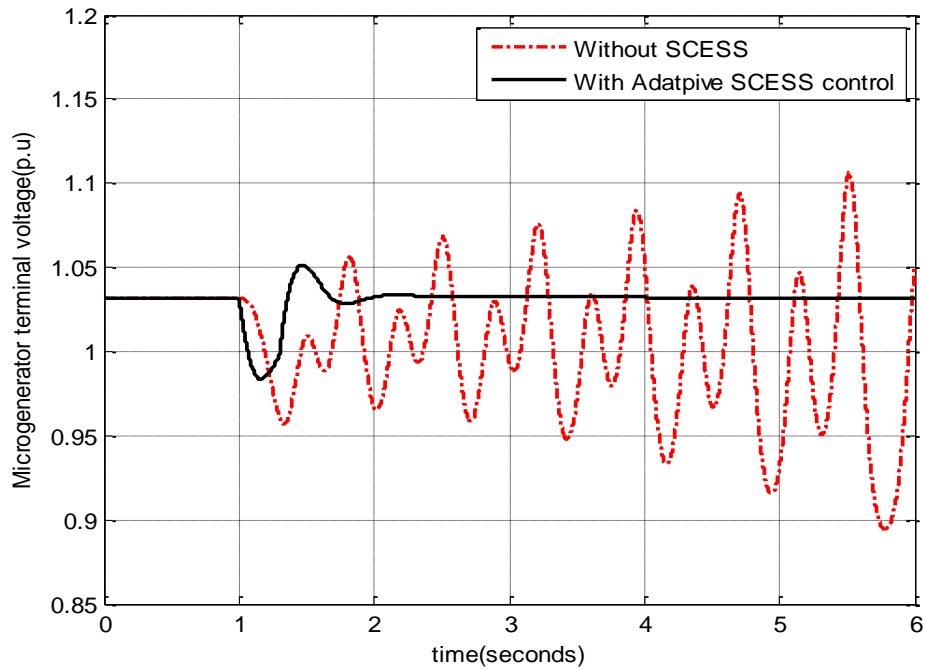


Figure 6.35: Microgenerator terminal voltage variation when a 15% torque pulse is applied for 300 msec, (a) Without SCESS (b) With adaptive SCESS control

The transient response of the PV array output current and DC-link capacitor voltage are recorded in Figure 6.36-Figure 6.37. Absence of control action introduces transients of large magnitude which eventually make the system unstable. On the other hand, effective control of active and reactive power through adaptive SCESS controller restores the system stability very quickly.

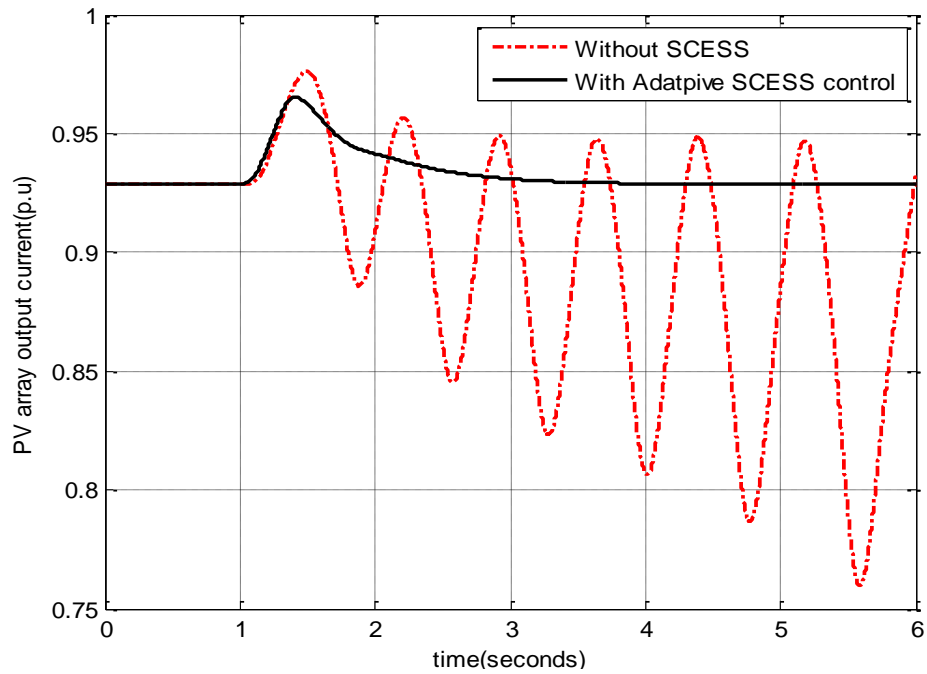


Figure 6.36: PV array current variation when a 15% torque pulse is applied for 300 msec, (a) Without SCESS (b) With adaptive SCESS control

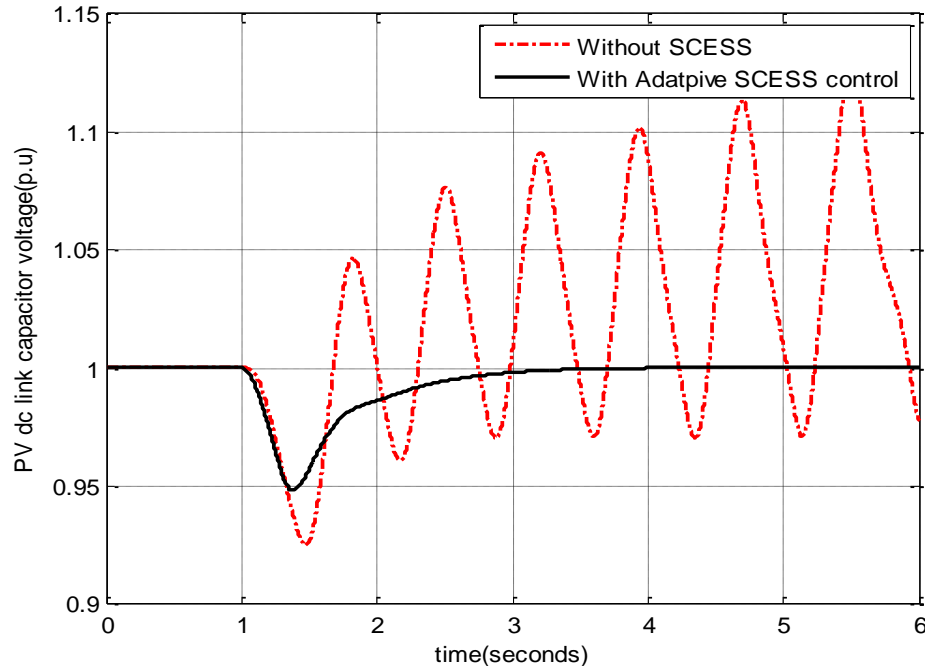


Figure 6.37: PV DC-link voltage variation when a 15% torque pulse is applied for 300 msec, (a) Without SCESS (b) With adaptive SCESS control

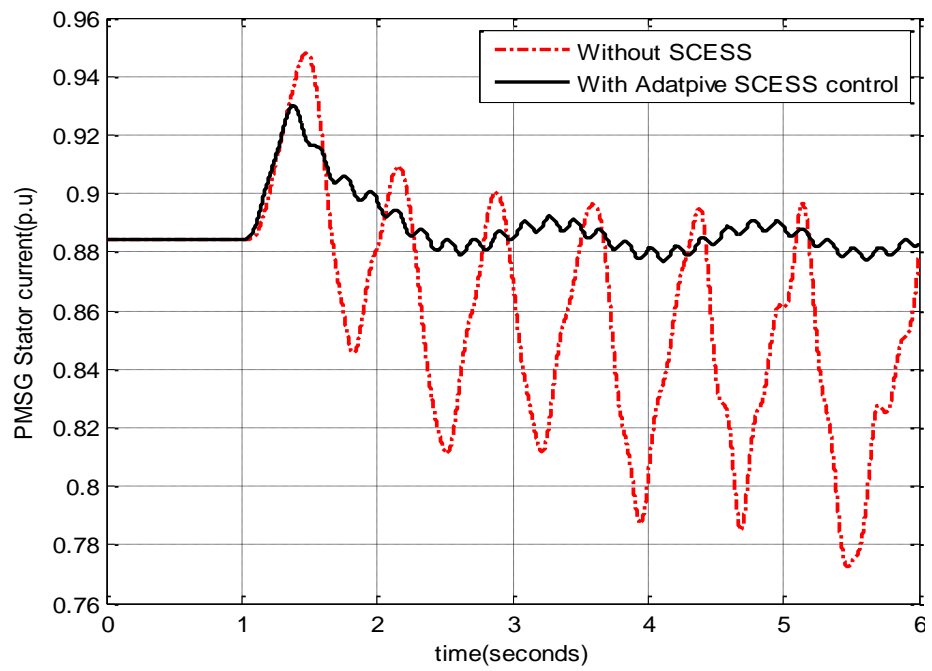


Figure 6.38: PMSG stator current variation when a 15% torque pulse is applied for 300 msec, (a) Without SCESS (b) With adaptive SCESS control

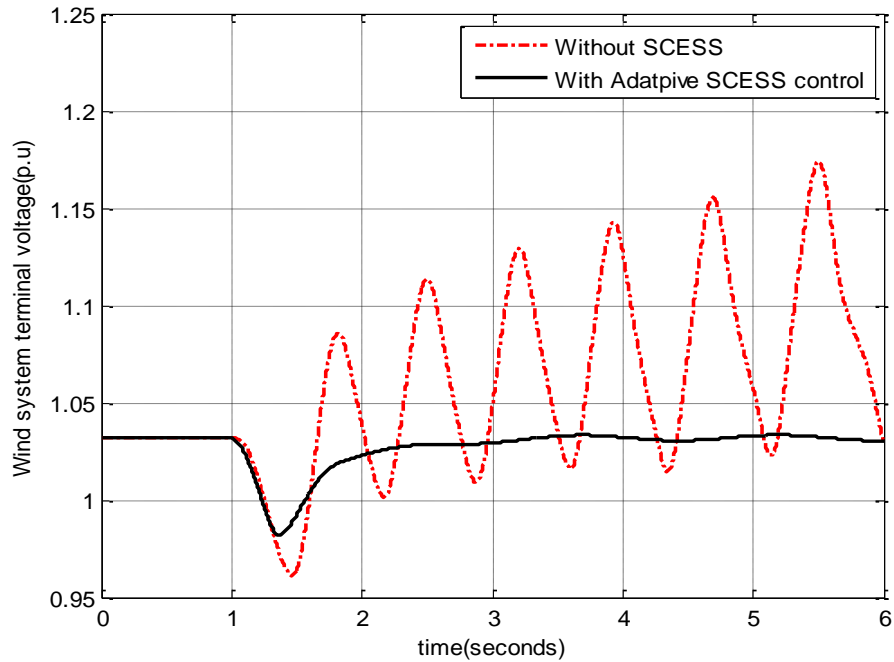


Figure 6.39: PMSG terminal voltage variation when a 15% torque pulse is applied for 300 msec, (a) Without SCESS (b) With adaptive SCESS control

The variations in the wind system stator current and terminal voltage are presented in Figure 6.38-Figure 6.39. The unstable operating condition arising out of transients is seen to be damped out by the SCESS controller in less than 1 second.

The variations in the microgrid bus voltage and real power delivery to the grid are recorded in Figure 6.40-Figure 6.41. Drop in the microgrid voltage during the transient is mitigated by appropriate reactive power injection by the SCESS controller into the system as shown in Figure 6.43. The real power delivery to the grid has less negligible transients thus ensuring smooth transfer of power. The corresponding real power injected by the SCESS controller is shown in Figure 6.42.

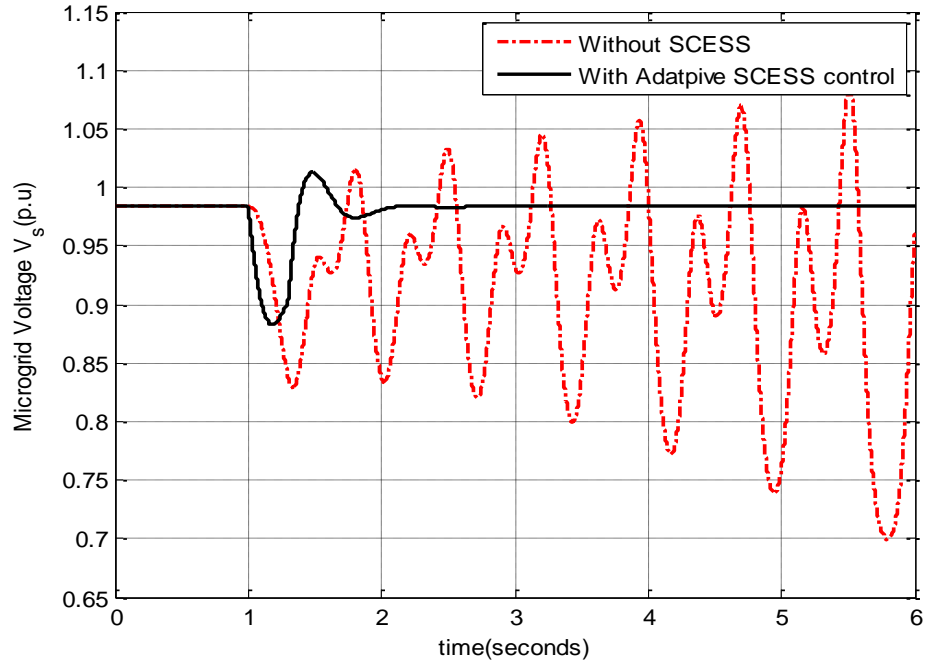


Figure 6.40: Microgrid bus voltage variation when a 15% torque pulse is applied for 300 msec, (a) Without SCESS (b) With adaptive SCESS control

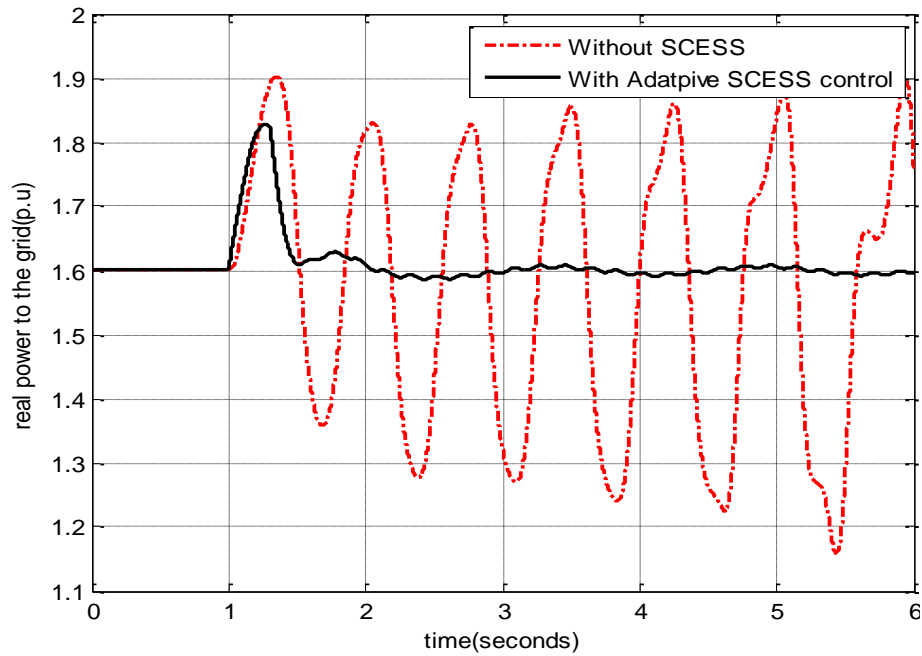


Figure 6.41: Real power delivered to the grid variation when a 15% torque pulse is applied for 300 msec, (a) Without SCESS (b) With adaptive SCESS control

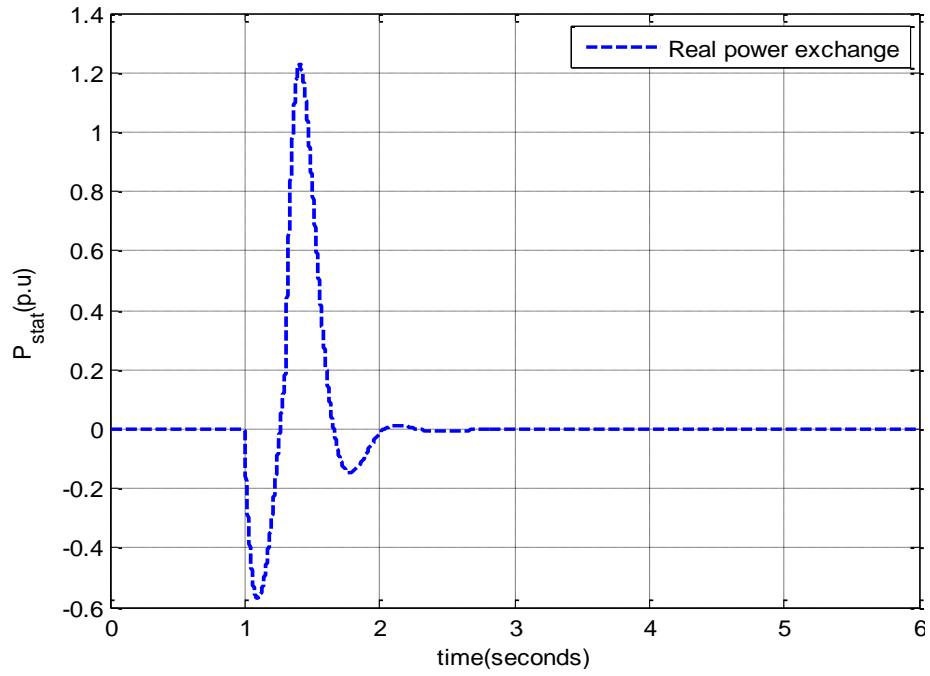


Figure 6.42: Injected real power by the SCESS controller following a 15% torque pulse for 300 msec

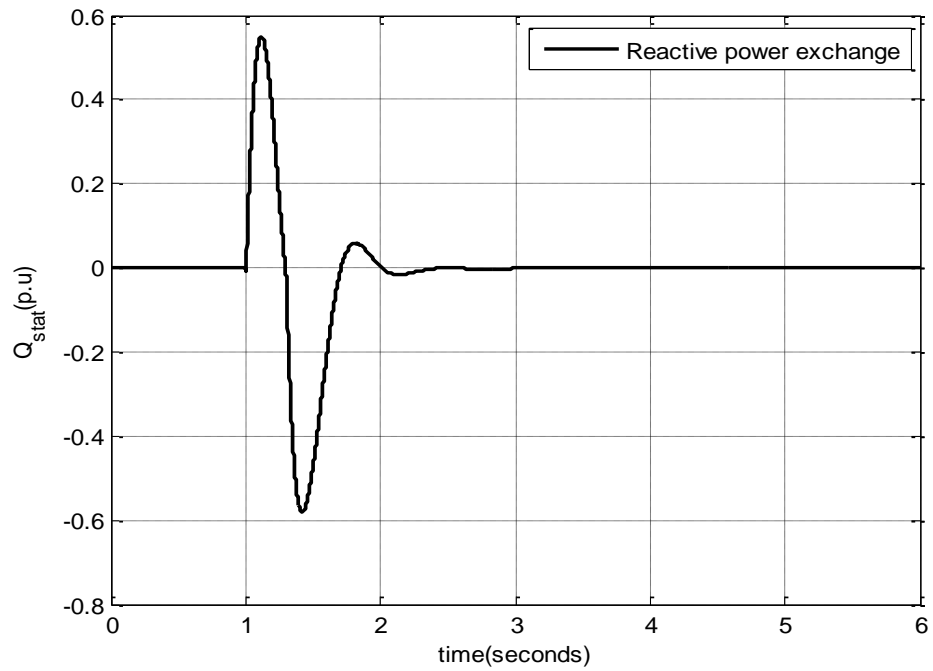


Figure 6.43: Injected reactive power by the SCESS controller following a 15% torque pulse for 300 msec

6.3.2 Torque step disturbance

For a step increase in input torque, the initial DG loadings are: microgenerator 0.2 pu, wind system 0.9 pu, PV 0.8 pu and fuel cell 0.7 pu. The load on the microgrid is considered to be held constant at $1+j0.15$ pu. The disturbance is applied at $t=1$ sec. A new mechanical power reference is set according to the step change in input torque. This sudden change in mechanical power reference introduces transients in the system. Without adequate damping in the system these oscillations would contribute towards voltage collapse or rotor angle instability.

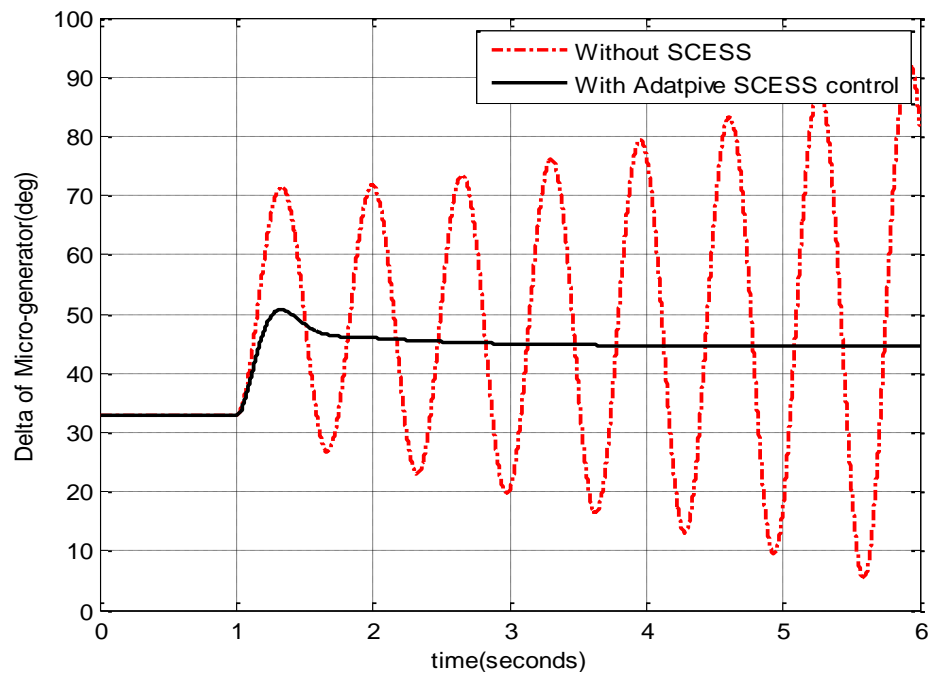


Figure 6.44: Microgenerator rotor angle variation following a 10% change in input torque, (a) Without SCESS (b) With adaptive SCESS control

The transient response recorded for the microgenerator load angle and terminal voltage following a 10% step change in input torque are shown in Figure 6.44- Figure 6.45. Absence of control action would amount to collapse of microgenerator

voltage as shown in Figure 6.45. The adaptive SCESS controller transfers the system to new operating point with negligible transients.

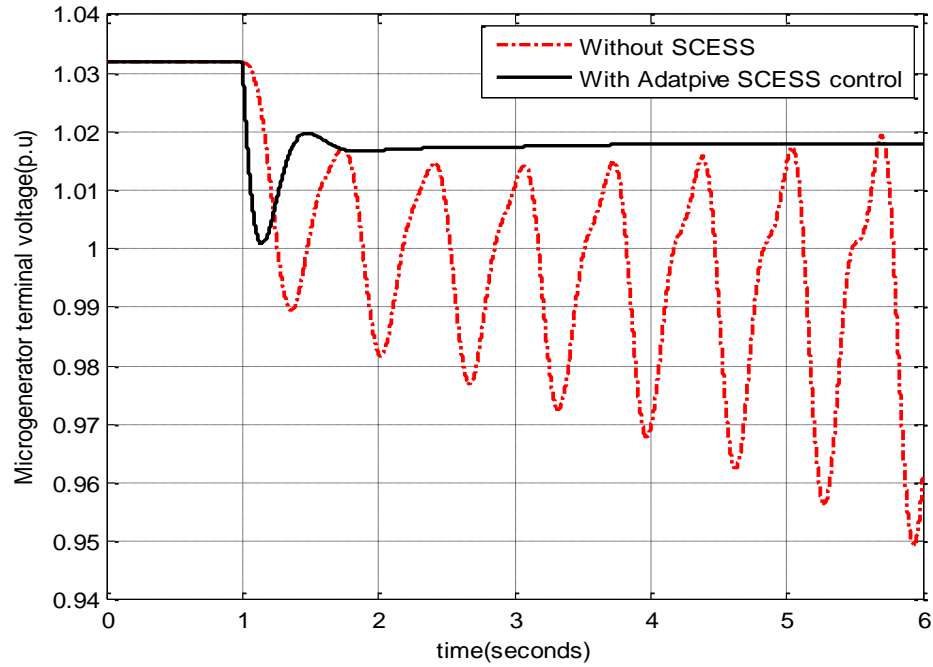


Figure 6.45: Microgenerator terminal voltage variation following a 10% change in input torque, (a) Without SCESS (b) With adaptive SCESS control

The fuel cell current and DC-link capacitor voltage variations are recorded in Figure 6.46-Figure 6.47. It can be observed from these figures that the proposed SCESS controller effectively damps out the system transients and makes the system settle at a new operating point.

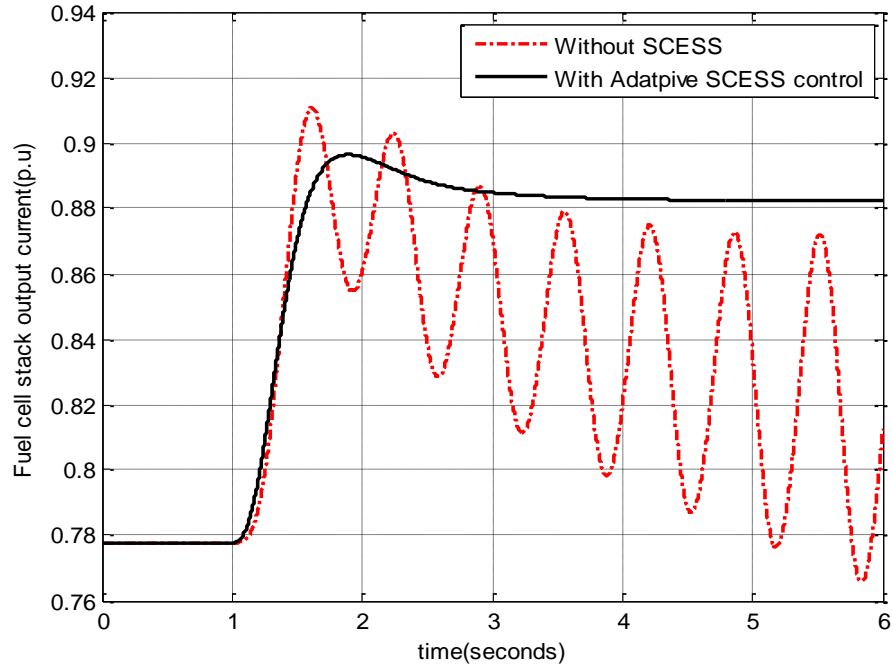


Figure 6.46: Fuel cell stack current variation following a 10% change in input torque, (a) Without SCESS (b) With adaptive SCESS control

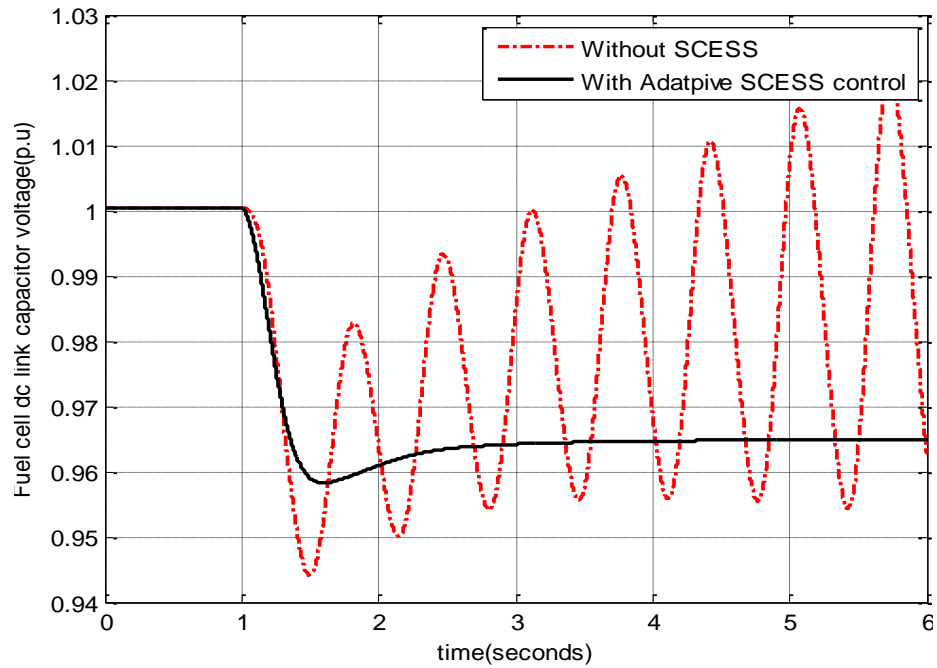


Figure 6.47: Fuel cell DC-link voltage variation following a 10% change in input torque, (a) Without SCESS (b) With adaptive SCESS control

Figure 6.48-Figure 6.49 shows the variation in wind system stator current and terminal voltage following a 10% step change in torque input. The VSC DC-link voltage and current variations are recorded in Figure 6.50-Figure 6.51. Uncontrolled case represents unstable operating scenario where as the presence of SCESS controller enhance the system transient stability.

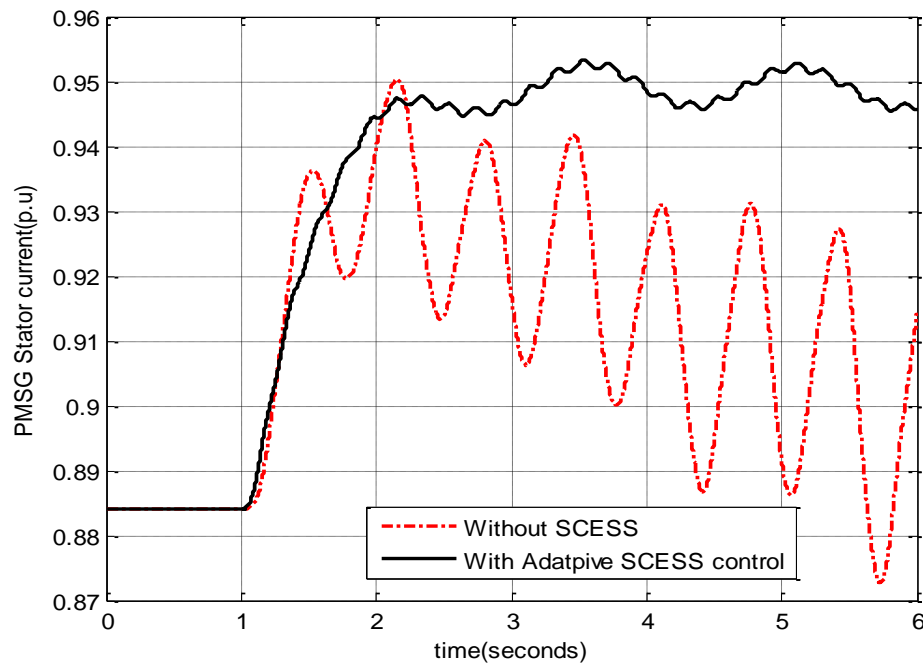


Figure 6.48: PMSG stator current variation following a 10% change in input torque, (a) Without SCESS (b) With adaptive SCESS control

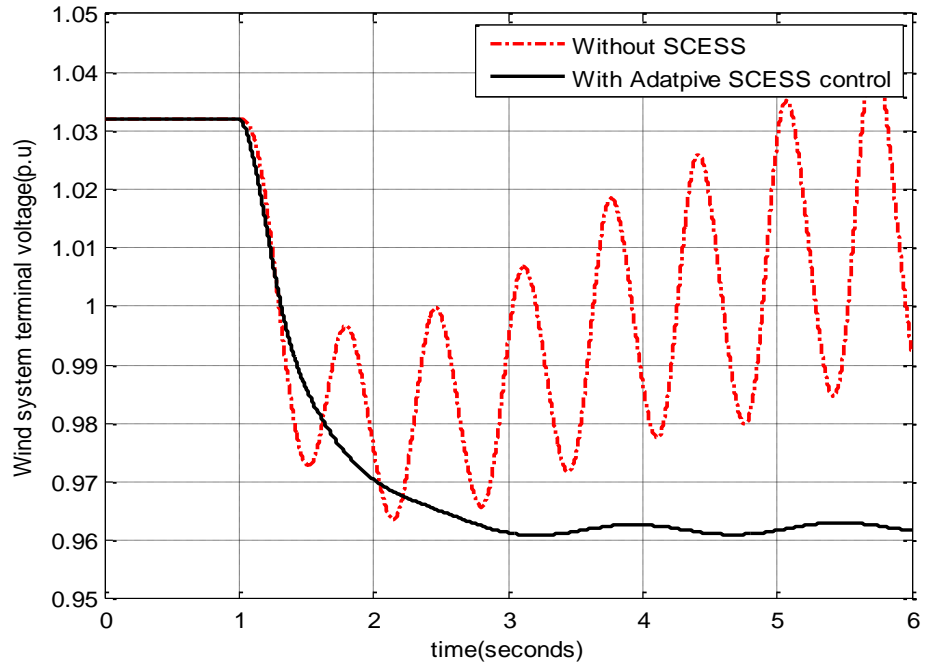


Figure 6.49: Wind system terminal voltage variation following a 10% change in input torque, (a) Without SCESS (b) With adaptive SCESS control

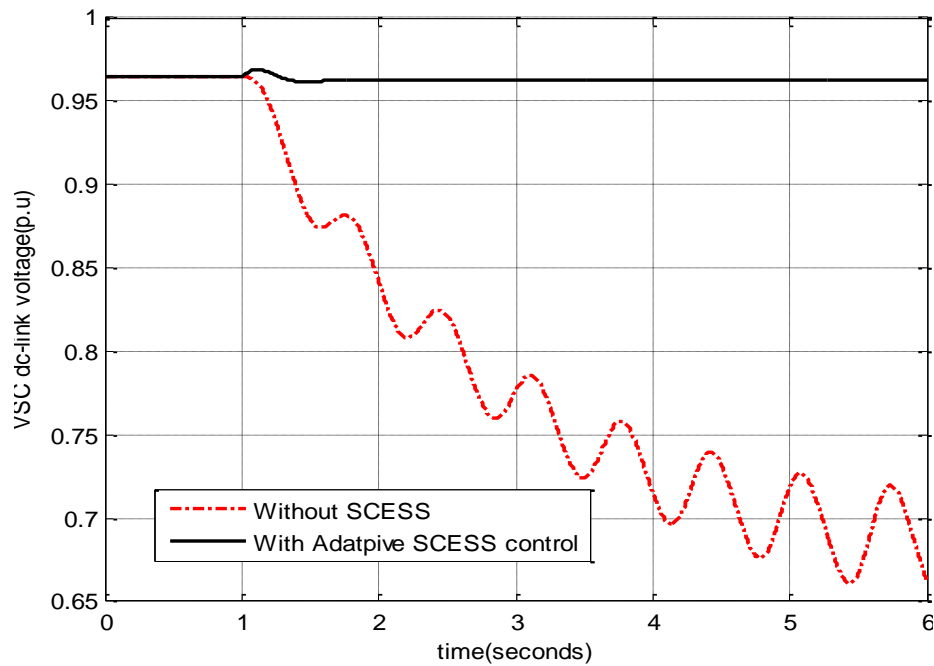


Figure 6.50: VSC DC-link voltage variation following a 10% change in input torque, (a) Without SCESS (b) With adaptive SCESS control

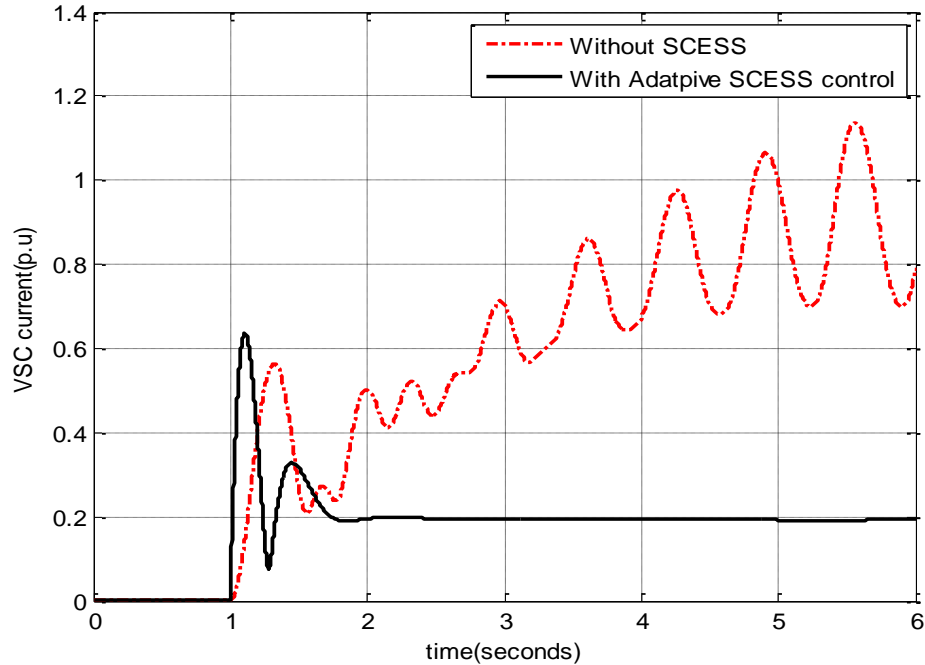


Figure 6.51: VSC current variation following a 10% change in input torque, (a) Without SCESS (b) With adaptive SCESS control

The microgrid bus voltage and real power delivery to the grid variations are shown in Figure 6.52-Figure 6.53. It can be seen that while the uncontrolled response is on the verge of instability, the adaptive SCESS controller is able to bring the system to stable manifold in less than 1 sec. The energy storage controller is shown to stabilize the system very quickly.

The corresponding real and reactive power injections by the SCESS controller are reported in Figure 6.54-Figure 6.55. It is seen that drop in the microgrid voltage is recovered through appropriate reactive power injection into the system and also the microgrid bus voltage is maintained at a new reference level.

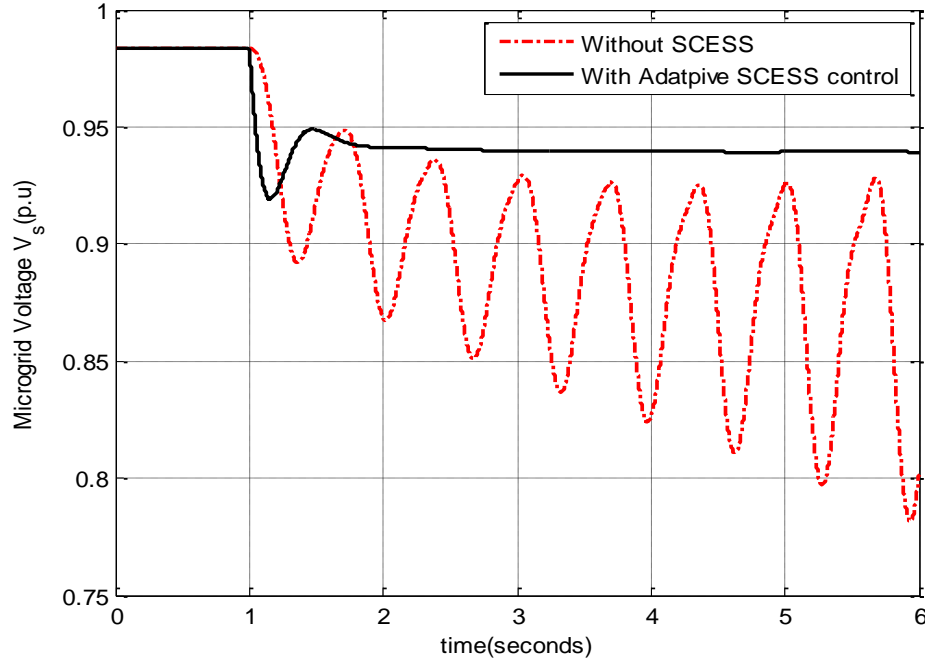


Figure 6.52: Microgrid voltage variation following a 10% change in input torque, (a) Without SCESS (b) With adaptive SCESS control

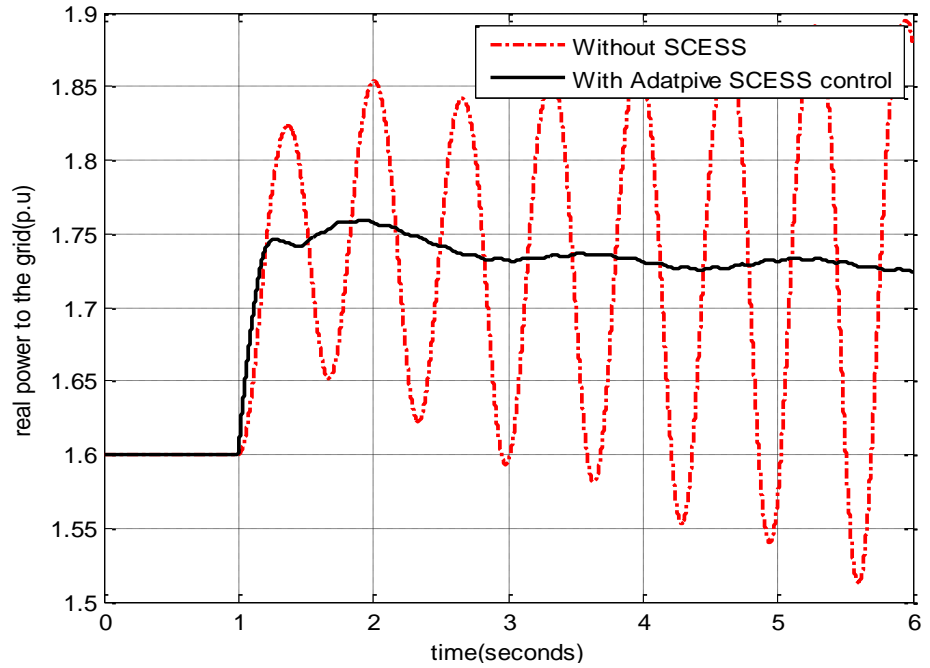


Figure 6.53: Real power delivered to the grid variation following a 10% change in input torque, (a) Without SCESS (b) With adaptive SCESS control

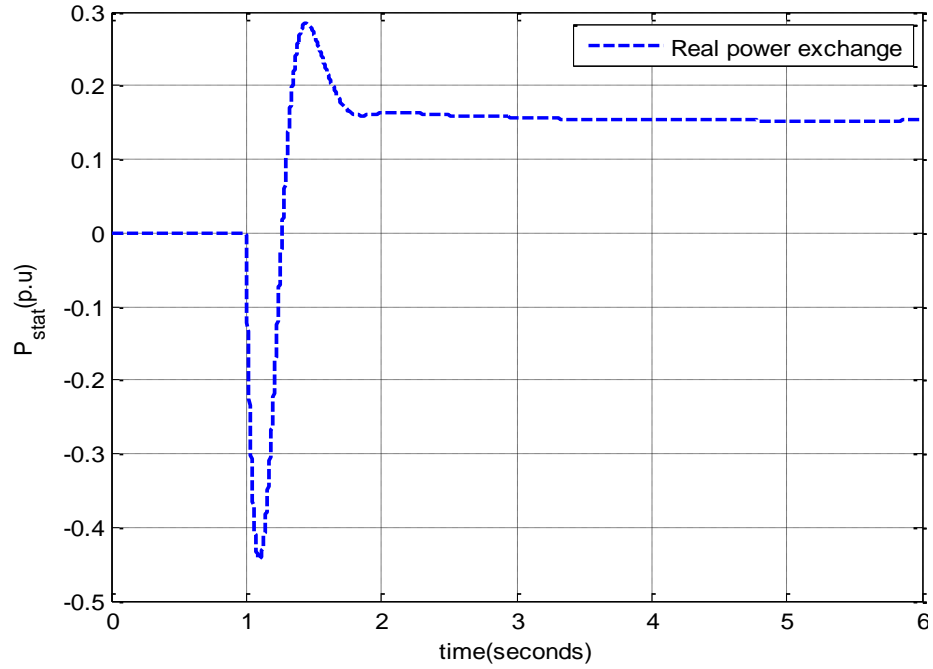


Figure 6.54: Real power injected by adaptive SCESS controller following a 10% change in input torque

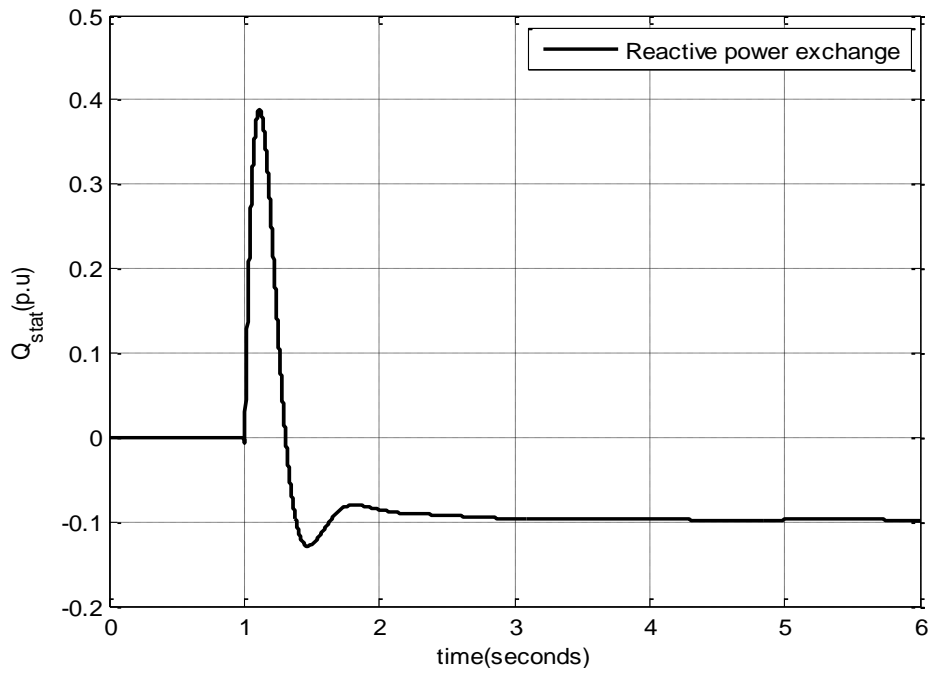


Figure 6.55: Reactive power injected by adaptive SCESS controller following a 10% change in input torque

6.4 Comparison of Adaptive BESS and SCESS Controllers

In the previous sections, it is demonstrated that both adaptive BESS and SCESS controls provide very good damping profiles when subjected to sudden power changes in the system. Another type of disturbance the microgrid system, particularly the renewables, is sensitive to is low voltage condition in the system. This section evaluates the performance of both the controllers when the grid is subjected to a 400 ms symmetrical short circuit. Also, a comparison of the performance of the BESS and SCESS controllers are made for this grid fault condition.

For the low voltage study, the DG loadings are: microgenerator 0.2 pu, wind 1.0 pu, PV 0.8 pu, and fuel cell 0.7 pu. The load on the microgrid is assumed to be lumped at one side with $1+j0.15$ pu. The responses recorded for the three-phase short circuit fault are microgenerator load angle and speed variations, microgrid voltage variations as shown in Figure 6.58-Figure 6.58. The real and reactive power injections by the corresponding storage controllers are recorded in Figure 6.59-Figure 6.60.

As seen from these figures, the sudden depression of microgrid voltage following a three phase grid fault is mitigated effectively by appropriate reactive power injection from the storage controllers. The supervisory controller backed up by an energy storage device allows enough time to redistribute the DG generation and load for safer operation of the system. Figure 6.56-Figure 6.57 show the load angle and speed deviations of the microgenerator. The acceleration of rotor speed and load angle is controlled through absorption of excess real power in the system by the storage controller. The system

stability is restored quickly by the SCESS controller in comparison to the BESS controller.

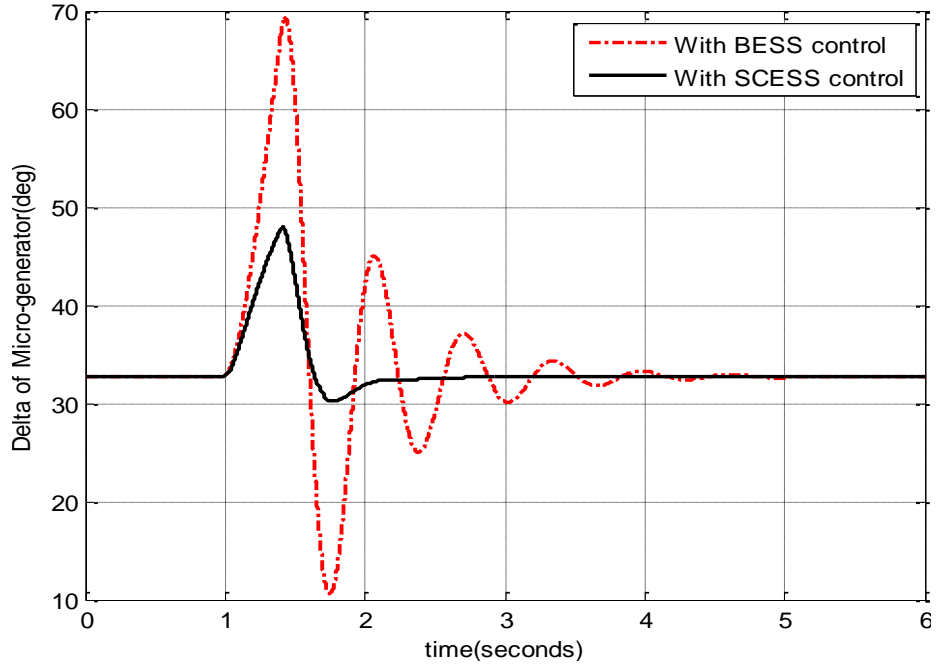


Figure 6.56: Microgenerator load angle variation when a three-phase grid fault is applied for 400 msec, (a) With BESS control (b) With SCESS control

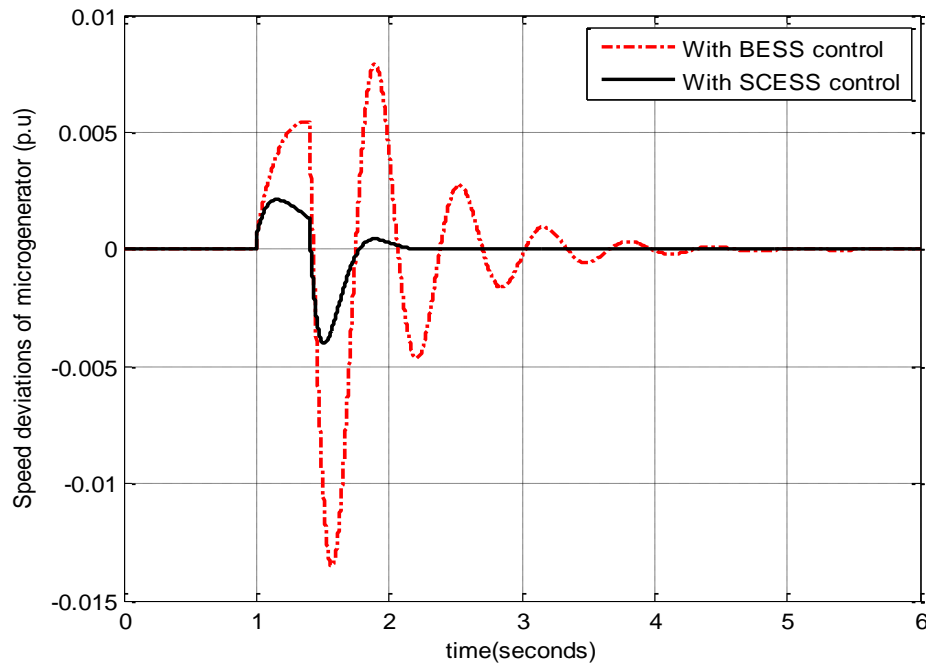


Figure 6.57: Microgenerator rotor speed deviation when a three-phase grid fault is applied for 400 msec, (a) With BESS control (b) With SCESS control

Responses recorded in Figure 6.58-Figure 6.60 indicate that the performance of SCESS based control strategy is superior to the BESS system. The supercapacitor operates faster through charging and discharging phenomena and damps the system oscillations in less than 1 second.

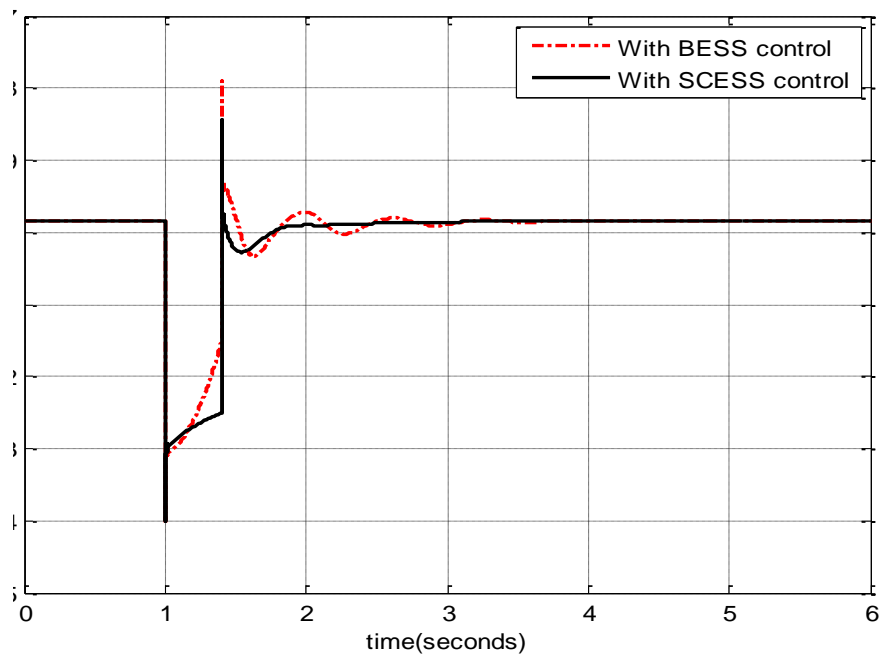


Figure 6.58: Microgrid voltage variation when a three-phase grid fault is applied for 400 msec, (a) With BESS control (b) With SCESS control

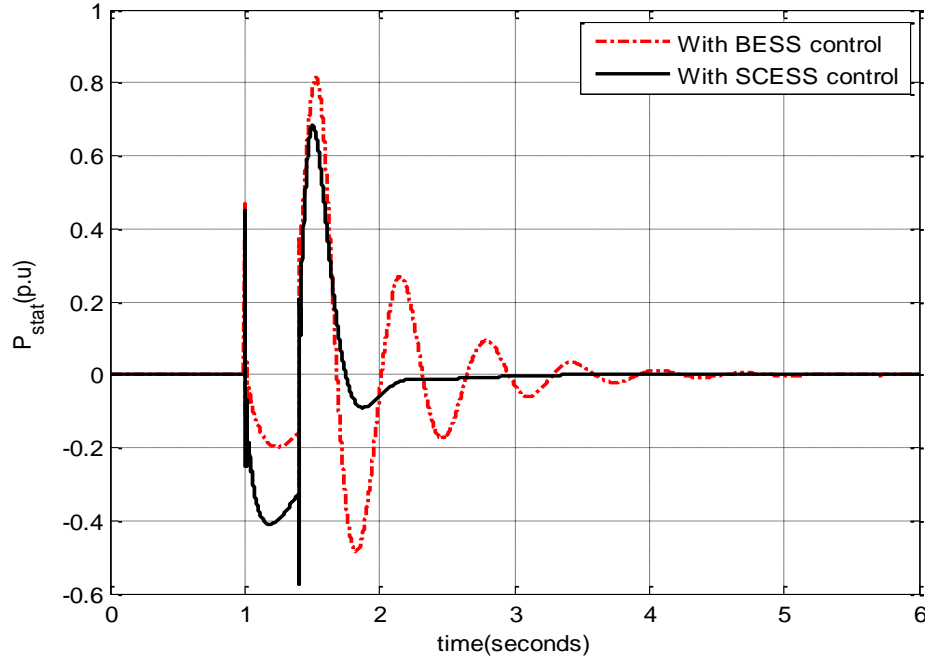


Figure 6.59: Injected real power variation when a three-phase grid fault is applied for 400 msec, (a) With BESS control (b) With SCESS control

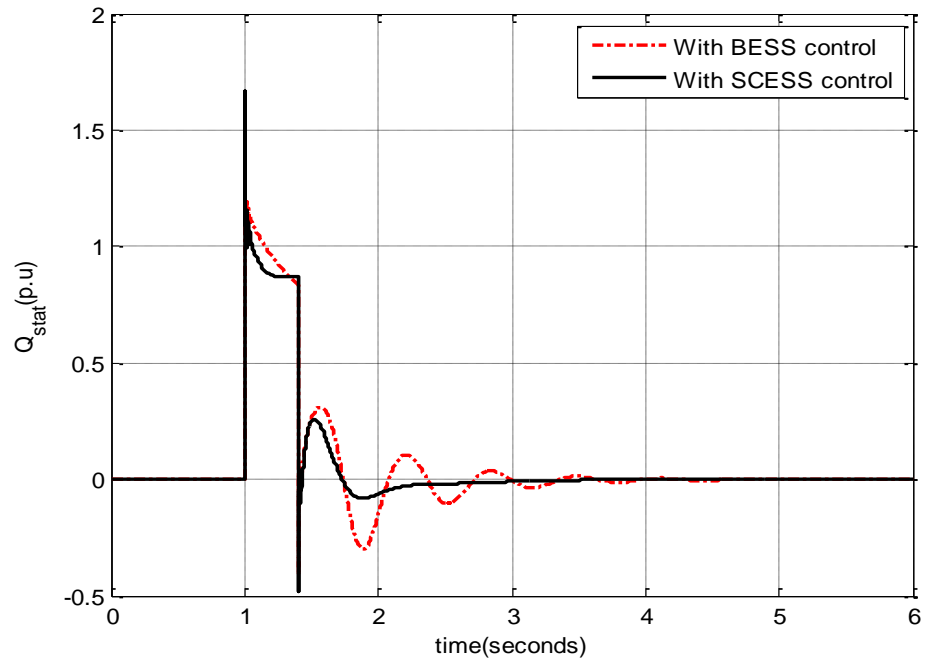


Figure 6.60: Injected reactive power variation when a three-phase grid fault is applied for 400 msec, (a) With BESS control (b) With SCESS control

CHAPTER 7

CONCLUSIONS AND FUTURE WORK

7.1 Conclusions

This study presents adaptive energy storage controller designs for a microgrid using neuro-fuzzy algorithm. Nonlinear and linear models of the individual components of the microgrid are developed. The behavior of DG interactions has been investigated through small-signal analysis. Nonlinear simulations are carried out to verify the results of linearized analysis.

From small signal analysis it is observed that for fixed amount of PV, wind, and fuel cell participation, the stability of the microgrid worsens as the amount of microgenerator power decreases. Decrease in system real load weakens the microgrid by reduced power factor operation. For a particular microalternator output and load, there exists a critical value of PV, wind, and fuel cell power above which the system performance degrades. It indicates that sudden large penetration of power from renewables can cause instability.

Use of battery and supercapacitor energy storage devices interfaced through voltage source converters have been proposed to mitigate the unstable operating scenario. The storage devices compensate for the real power need while the voltage source converter caters for the reactive power. The possibility of enhancing the stability

boundaries for critical cases of generation mixes is investigated. The optimum storage controller parameters are determined through an adaptive neuro-fuzzy approach trained on the data samples provided by evolutionary bio-geography based optimization technique.

The bio-geography based technique is favored over population based search procedures because of its robustness, ease of implementation, faster convergence, and lesser computational burden. It has been observed that the BBO can work with different fitness functions and is able to reach global optimum with minimum effort. The neuro-fuzzy method combines the advantages of both neural networks and fuzzy systems and has shown excellent adaptive learning ability. The adaptive neuro-fuzzy based storage controller generates the necessary control to keep the system stable with minimum transients.

For the simulation results it has been observed that both battery and supercapacitor provide excellent transient profile. Nonlinear system simulations with storage controllers prove that the supervisory control is capable of transferring the transiently unstable system to normal steady state operation. The storage controllers allows enough time for the operators to redistribute the generation and load mix transiting the system to safer range of operation.

While both the storage devices are observed to provide very good transient response, a comparison of the two energy storage system shows that the adaptive neuro-fuzzy SCESS control can provide superior performance over the battery system. This is

primarily attributed to the quick charging and discharging of supercapacitor module compared to the battery storage.

7.2 Future Work

Future research in the area of microgrids includes:

1. Operation of the microgrid with storage controllers in autonomous mode.
2. Investigations of the other storage devices like superconducting magnetic energy storage systems (SMES).
3. Mechanical energy storage systems such as the flywheels, compressed air energy storage (CAES) may also be considered
4. Efficient maximum power point tracking (MPPT) methods of the renewables involve in the microgrid.
5. Consideration of other type of wind generators, like Doubly-fed induction generator (DFIG), Induction generator etc.
6. Implementation of the controllers in real time using Real Time Digital Simulation (RTDS).
7. Unbalanced operation of the microgrid and impact of storage devices.
8. Other controls on the DGs, like pitch control, optimum relationship based control on the wind system.

References

- [1] P. P. Barker and R. W. De Mello, "Determining the impact of distributed generation on power systems. I. Radial distribution systems," in *2000 Power Engineering Society Summer Meeting (Cat. No.00CH37134)*, 2010, vol. 3, no. c, pp. 1645–1656.
- [2] W. El-Khattam and M. M. . Salama, "Distributed generation technologies, definitions and benefits," *Electric Power Systems Research*, vol. 71, no. 2, pp. 119–128, Oct. 2004.
- [3] J. M. Carrasco, L. G. Franquelo, J. T. Bialasiewicz, E. Galvan, R. C. P. Guisado, M. A. M. Prats, J. I. Leon, and N. Moreno-Alfonso, *Power-Electronic Systems for the Grid Integration of Renewable Energy Sources: A Survey*, vol. 53, no. 4. IEEE, 2006, pp. 1002–1016.
- [4] F. Blaabjerg, Z. Chen, and S. Kjaer, "Power electronics as efficient interface in dispersed power generation systems," *Power Electronics, IEEE ...*, vol. 19, no. 5, pp. 1184–1194, 2004.
- [5] M. Marwali, J. Jung, and A. Keyhani, "Control of distributed generation systems-Part II: Load sharing control," *Power Electronics, IEEE ...*, vol. 19, no. 6, pp. 1551–1561, 2004.
- [6] I. Vechiu, O. Curea, A. Llaria, and H. Camblong, "Control of power converters for microgrids," *COMPEL: The International Journal for Computation and Mathematics in Electrical and Electronic Engineering*, vol. 30, no. 1, pp. 300–309, 2011.
- [7] Z. Chen and Y. Hu, "Control of power electronic converters for distributed generation units," *31st Annual Conference of IEEE Industrial Electronics Society, 2005. IECON 2005.*, p. 6 pp., 2005.
- [8] Y. Liu, J. Bebic, B. Kroposki, J. de Bedout, and W. Ren, "Distribution System Voltage Performance Analysis for High-Penetration PV," in *2008 IEEE Energy 2030 Conference*, 2008, no. November, pp. 1–8.
- [9] F. Katiraei, M. R. Iravani, and P. W. Lehn, "Micro-Grid Autonomous Operation During and Subsequent to Islanding Process," *IEEE Transactions on Power Delivery*, vol. 20, no. 1, pp. 248–257, Jan. 2005.
- [10] Y. Mohamed, "New control algorithms for the distributed generation interface in grid-connected and micro-grid systems," 2008.

- [11] J. Liang and C. Feng, "Stability Improvement of Micro-grids with Coordinate Control of Fuel Cell and Ultracapacitor," *Power Electronics Specialists Conference*, ..., pp. 2472–2477, 2007.
- [12] T. C. Green and M. Prodanović, "Control of inverter-based micro-grids," *Electric Power Systems Research*, vol. 77, no. 9, pp. 1204–1213, Jul. 2007.
- [13] D. Jayaweera, S. Galloway, G. Burt, and J. R. McDonald, "A Sampling Approach for Intentional Islanding of Distributed Generation," *IEEE Transactions on Power Systems*, vol. 22, no. 2, pp. 514–521, May 2007.
- [14] A. G. Tsikalakis and N. D. Hatziargyriou, "Centralized control for optimizing microgrids operation," in *2011 IEEE Power and Energy Society General Meeting*, 2011, pp. 1–8.
- [15] P. F. Ribeiro, B. K. Johnson, M. L. Crow, A. Arsoy, and Y. Liu, "Energy storage systems for advanced power applications," in *Proceedings of the IEEE*, 2001, vol. 89, no. 12, pp. 1744–1756.
- [16] F. D. Kanellos, A. I. Tsouchnikas, N. D. Hatziargyriou, and S. Member, "Micro-Grid Simulation during Grid-Connected and Islanded Modes of Operation."
- [17] F. Katiraei, S. Member, and M. R. Iravani, "Transients of a Micro-Grid System with Multiple Distributed Energy Resources," pp. 1–6.
- [18] F. Katiraei and M. R. Iravani, "Power Management Strategies for a Microgrid With Multiple Distributed Generation Units," *IEEE Transactions on Power Systems*, vol. 21, no. 4, pp. 1821–1831, Nov. 2006.
- [19] G. Davis, "Integration of Distributed Energy," no. October, 2003.
- [20] H. Geng and G. Yang, "Robust pitch controller for output power levelling of variable-speed variable-pitch wind turbine generator systems," *IET Renewable Power Generation*, vol. 3, no. 2, p. 168, 2009.
- [21] H. Yokoyama, "Tip speed ratio control of wind turbine generating system connected in series," *Electrical Machines and ...*, 2011.
- [22] X. Yao, C. Guo, Z. Xing, and Y. Li, "Pitch regulated LQG controller design for variable speed wind turbine," ... *and Automation*, 2009. ..., pp. 845–849, 2009.
- [23] J. Hui, "An adaptive control algorithm for maximum power point tracking for wind energy conversion systems," no. December, 2008.

- [24] E. Power, "Maximum power point tracking for wind energy conversion systems based on fuzzy modelling and control Ayman Francees * Abdel-Latif Elshafei," vol. 3, no. 1, pp. 36–57, 2012.
- [25] U. States, M. R. Rad, M. R. Rad, S. Akbari, and S. A. Taher, "Using ANFIS , PSO , FCN in Cooperation with Fuzzy Controller for MPPT of Photovoltaic Arrays," vol. 1, no. 1, pp. 37–45, 2012.
- [26] a. Bati and S. Leabi, "NN Self-Tuning Pitch Angle Controller of Wind Power Generation Unit," in *2006 IEEE PES Power Systems Conference and Exposition*, 2006, pp. 2019–2029.
- [27] M. Narayana and G. Putrus, "Optimal control of wind turbine using neural networks," *Universities Power Engineering ...*, pp. 8–12, 2010.
- [28] L. A. Zadeh, "Fuzzy logic: issues, contentions and perspectives," in *Proceedings of ICASSP '94. IEEE International Conference on Acoustics, Speech and Signal Processing*, 1994, vol. vi, p. VI/183.
- [29] S. Dick, "Toward complex fuzzy logic," *IEEE Transactions on Fuzzy Systems*, vol. 13, no. 3, pp. 405–414, Jun. 2005.
- [30] E. R. Fowler, "Rule based fuzzy logic inferencing," in *Proceedings of IEEE International Conference on Systems, Man and Cybernetics*, 1994, vol. 1, pp. 465–470.
- [31] P. P. Bonissone, "Adaptive Neural Fuzzy Inference Systems (ANFIS): Analysis and Applications," pp. 1–41, 2002.
- [32] A. Cruz, "ANFIS : Adaptive Neuro-Fuzzy Inference Systems ANFIS Architecture Hybrid Learning Algorithm ANFIS as a Universal Approximator Simulation Examples," pp. 1–33.
- [33] M. a. Abido, "Design of PSS and STATCOM-based damping stabilizers using genetic algorithms," *2006 IEEE Power Engineering Society General Meeting*, p. 8 pp., 2006.
- [34] S. Raza and A. Rahim, "Smart Pitch Control Strategy of Wind Generation System Using Differential Evolution and Neural Network," *ier-institute.org*, vol. 13, pp. 202–207, 2012.
- [35] M. a. Hassan and M. a. Abido, "Optimal Design of Microgrids in Autonomous and Grid-Connected Modes Using Particle Swarm Optimization," *IEEE Transactions on Power Electronics*, vol. 26, no. 3, pp. 755–769, Mar. 2011.

- [36] W. Deng, X. Tang, and Z. Qi, "Research on Dynamic Stability of Hybrid Wind / PV System Based on Micro-Grid," pp. 2627–2632, 2008.
- [37] T. M. Hussain, "Modeling and Control of a Microgrid including Photovoltaic and Wind generation," King Fahd University of Petroleum and Minerals, 2012.
- [38] M. G. Villalva, J. R. Gazoli, and E. R. Filho, "Comprehensive Approach to Modeling and Simulation of Photovoltaic Arrays," *IEEE Transactions on Power Electronics*, vol. 24, no. 5, pp. 1198–1208, May 2009.
- [39] M. Shahed Ali, "Photovoltaic Systems Modeling and Analysis," King Fahd University of Petroleum and Minerals, 2010.
- [40] M. Sheraz and M. Abido, "An efficient MPPT controller using differential evolution and neural network," *Power and Energy (PECon), 2012 IEEE ...*, no. December, pp. 2–5, 2012.
- [41] D. F. Menicucci and J. P. Fernandez, "User ' s Manual for PVFORM: A Photovoltaic System Shulation Program For Stand-Alone and Grid-interactive Applications," 1989.
- [42] Y. Tsuno, "Translation Equations for Temperature and Irradiance of the IV curves of Various PV Cells and Modules," *Photovoltaic Energy ...*, no. 1, pp. 2246–2249, 2006.
- [43] D. King, J. Kratochvil, and W. Boyson, *Photovoltaic array performance model*, no. December. 2004.
- [44] A. H. ALQahtani, M. S. Abuhamdeh, and Y. M. Alsmadi, "A simplified and comprehensive approach to characterize photovoltaic system performance," in *2012 IEEE Energytech*, 2012, no. 1, pp. 1–6.
- [45] B. P. Sx, "Bp sx 150," pp. 1–4, 2001.
- [46] R. Yan and T. K. Saha, "Development of Simplified Models for a Single Phase Grid Connected Photovoltaic System," 2004.
- [47] R. Wai, S. Member, and W. Wang, "Grid-Connected Photovoltaic Generation System," *IEEE Transactions on Circuits and Systems I: Regular Papers*, vol. 55, no. 3, pp. 953–964, Apr. 2008.
- [48] M. E. Ropp and S. Gonzalez, "Development of a MATLAB/Simulink Model of a Single-Phase Grid-Connected Photovoltaic System," *IEEE Transactions on Energy Conversion*, vol. 24, no. 1, pp. 195–202, Mar. 2009.

- [49] A. I. Technology, "MODELING AND SIMULATION OF GRID-CONNECTED PHOTOVOLTAIC DISTRIBUTED GENERATION SYSTEM," vol. 45, no. 2, 2012.
- [50] A. Canova, L. Giaccone, F. Spertino, and M. Tartaglia, "Electrical Impact of Photovoltaic Plant in Distributed Network," *IEEE Transactions on Industry Applications*, vol. 45, no. 1, pp. 341–347, 2009.
- [51] Q. Sun, Z. Li, and H. Zhang, "Impact of Distributed Generation on Voltage Profile in Distribution System," *2009 International Joint Conference on Computational Sciences and Optimization*, pp. 249–252, Apr. 2009.
- [52] Y. T. Tan, D. S. Kirschen, and N. Jenkins, "A Model of PV Generation Suitable for Stability Analysis," *IEEE Transactions on Energy Conversion*, vol. 19, no. 4, pp. 748–755, Dec. 2004.
- [53] S. Achilles, S. Schramm, and J. Bebic, "Transmission System Performance Analysis for High-Penetration Photovoltaics Transmission System Performance Analysis for High-Penetration Photovoltaics," no. February, 2008.
- [54] G. Li, "Design of a Photo-Voltaic System to Enhance Network Dynamic Stability," *Smart Grid and Renewable Energy*, vol. 01, no. 01, pp. 1–6, 2010.
- [55] R. Shah, N. Mithulananthan, A. Sode-Yome, and K. Y. Lee, "Impact of large-scale PV penetration on power system oscillatory stability," in *IEEE PES General Meeting*, 2010, pp. 1–7.
- [56] S. Shrivastava, S. Jain, and R. Nema, "Distributed generation: technical aspects of interconnection," *researchtrend.net*, vol. 1, no. 1, pp. 37–40, 2010.
- [57] B. Kroposki and R. DeBlasio, "Technologies for the new millennium: photovoltaics as a distributed resource," *Power Engineering Society Summer ...*, vol. 00, no. c, pp. 1798–1801, 2000.
- [58] J. H. R. Enslin and P. J. M. Heskes, "Harmonic Interaction Between a Large Number of Distributed Power Inverters and the Distribution Network," *IEEE Transactions on Power Electronics*, vol. 19, no. 6, pp. 1586–1593, Nov. 2004.
- [59] F. Wang and J. Duarte, "Modeling and analysis of grid harmonic distortion impact of aggregated DG inverters," ... , *IEEE Transactions on*, vol. 26, no. 3, pp. 786–797, 2011.
- [60] B. B. . Heindenreich, "Impact of Large Photovoltaic Penetration on the Quality of the Supply: A Case Study at the Photovoltaic Noise Barrier in Austria," in *19th European Photovoltaic Solar Energy Conference Exhibition*, 2005.

- [61] A. Girgis and S. Brahma, “Effect of distributed generation on protective device coordination in distribution system,” ... *'01. 2001 Large Engineering Systems ...*, 2001.
- [62] Y. Ueda and K. Kurokawa, “Analysis results of output power loss due to the grid voltage rise in grid-connected photovoltaic power generation systems,” *Industrial Electronics ...*, vol. 55, no. 7, pp. 2744–2751, Jul. 2008.
- [63] G. Bucci, F. Ciancetta, E. Fiorucci, E. Rotondale, and F. Veglio, “Experimental validation of a PEM fuel cell dynamic model,” in *International Symposium on Power Electronics, Electrical Drives, Automation and Motion, 2006. SPEEDAM 2006.*, 2006, pp. 546–551.
- [64] M. T. Gencoglu and Z. Ural, “Design of a PEM fuel cell system for residential application,” *International Journal of Hydrogen Energy*, vol. 34, no. 12, pp. 5242–5248, Jun. 2009.
- [65] C. Spiegel, *Modeling Fuel Cell Stacks 12.1*. Elsevier Ltd, 2008.
- [66] Z. Lemeš, A. Vath, T. Hartkopf, and H. Mäncher, “Dynamic fuel cell models and their application in hardware in the loop simulation,” *Journal of Power Sources*, vol. 154, no. 2, pp. 386–393, Mar. 2006.
- [67] J. Pukrushpan, “Modeling and control for PEM fuel cell stack system,” *American Control ...*, vol. 4, pp. 3117–3122, 2002.
- [68] P. J. H. Wingelaar, J. L. Duarte, and M. a. M. Hendrix, “PEM fuel cell model representing steady-state, small-signal and large-signal characteristics,” *Journal of Power Sources*, vol. 171, no. 2, pp. 754–762, Sep. 2007.
- [69] P. J. H. Wingelaar, J. L. Duarte, and M. A. M. Hendrix, “Dynamic Characteristics of PEM Fuel Cells,” in *IEEE 36th Conference on Power Electronics Specialists, 2005.*, 2005, pp. 1635–1641.
- [70] P. J. H. Wingelaar, J. L. Duarte, and M. A. M. Hendrix, “Dynamic and static simulation tool for PEM fuel cells,” in *2006 IEEE International Symposium on Industrial Electronics*, 2006, no. 2, pp. 1700–1705.
- [71] A. D. Le and B. Zhou, “A general model of proton exchange membrane fuel cell,” *Journal of Power Sources*, vol. 182, no. 1, pp. 197–222, Jul. 2008.
- [72] S. M. Njoya, O. Tremblay, and L. -a. Dessaint, “A generic fuel cell model for the simulation of fuel cell vehicles,” *2009 IEEE Vehicle Power and Propulsion Conference*, pp. 1722–1729, Sep. 2009.

- [73] S. J. Watson, "Application of wind speed forecasting to the integration of wind energy into a large scale power system," *IEE Proceedings - Generation, Transmission and Distribution*, vol. 141, no. 4, p. 357, 1994.
- [74] T. Ackermann, *Wind Power in Power Systems Edited by. .*
- [75] F. M. Gonzalez-longatt, O. Amaya, M. Cooz, and L. Duran, "Dynamic Behavior of Constant Speed WT based on Induction Generator Directly connect to Grid."
- [76] P. Ledesma, J. Usaola, and J. L. Rodríguez, "Transient stability of a fixed speed wind farm," *Renewable Energy*, vol. 28, no. 9, pp. 1341–1355, Jul. 2003.
- [77] L. Dusonchet and E. Telaretti, "Effects of electrical and mechanical parameters on the transient voltage stability of a fixed speed wind turbine," *Electric Power Systems Research*, vol. 81, no. 7, pp. 1308–1316, Jul. 2011.
- [78] L. M. Fernández, J. R. Saenz, and F. Jurado, "Dynamic models of wind farms with fixed speed wind turbines," *Renewable Energy*, vol. 31, no. 8, pp. 1203–1230, Jul. 2006.
- [79] W. Qiao, R. G. Harley, and G. K. Venayagamoorthy, "Dynamic Modeling of Wind Farms with Fixed-Speed Wind Turbine Generators," in *2007 IEEE Power Engineering Society General Meeting, 2007*, pp. 1–8.
- [80] O. Noureldeen, M. Rihan, and B. Hasanin, "Stability improvement of fixed speed induction generator wind farm using STATCOM during different fault locations and durations," *Ain Shams Engineering Journal*, vol. 2, no. 1, pp. 1–10, Mar. 2011.
- [81] M. Mansour, M. N. Mansouri, and M. F. Mimouni, "Comparative study of fixed speed and variable speed wind generator with pitch angle control," in *2011 International Conference on Communications, Computing and Control Applications (CCCA), 2011*, no. 2, pp. 1–7.
- [82] K. Tan and S. Islam, "Optimum Control Strategies in Energy Conversion of PMSG Wind Turbine System Without Mechanical Sensors," *IEEE Transactions on Energy Conversion*, vol. 19, no. 2, pp. 392–399, Jun. 2004.
- [83] I. Erlich, J. Kretschmann, S. Mueller-Engelhardt, F. Koch, and J. Fortmann, "Modeling of wind turbines based on doubly-fed induction generators for power system stability studies," in *2008 IEEE Power and Energy Society General Meeting - Conversion and Delivery of Electrical Energy in the 21st Century, 2008*, pp. 1–8.
- [84] H. E. Farag, E. F. El-Saadany, R. El Shatshat, and A. Zidan, "A generalized power flow analysis for distribution systems with high penetration of distributed

- generation,” *Electric Power Systems Research*, vol. 81, no. 7, pp. 1499–1506, Jul. 2011.
- [85] B. Renders, L. Vandeveldel, L. Degroote, K. Stockman, and M. H. J. Bollen, “Distributed generation and the voltage profile on distribution feeders during voltage dips,” *Electric Power Systems Research*, vol. 80, no. 12, pp. 1452–1458, Dec. 2010.
- [86] D. Menniti, A. Pinnarelli, and N. Sorrentino, “A METHOD TO IMPROVE MICROGRID RELIABILITY BY OPTIMAL SIZING PV / WIND PLANTS AND STORAGE SYSTEMS.”
- [87] S. J. Park, B. B. Kang, J. P. Yoon, I. S. Cha, and J. Y. Lim, “A study on the stand-alone operating or photovoltaic/wind power hybrid generation system,” in *2004 IEEE 35th Annual Power Electronics Specialists Conference (IEEE Cat. No.04CH37551)*, 2004, no. 3, pp. 2095–2099.
- [88] T. Tadokoro, K. Taira, and M. Asaoka, “A photovoltaic-diesel hybrid generation system for small islands,” in *Proceedings of 1994 IEEE 1st World Conference on Photovoltaic Energy Conversion - WCPEC (A Joint Conference of PVSC, PVSEC and PSEC)*, 1994, vol. 1, pp. 708–715.
- [89] J. Suh, “An analysis of PEMFC & photovoltaic 500W hybrid system,” in *2007 7th International Conference on Power Electronics*, 2007, pp. 522–524.
- [90] F. Valenciaga, P. F. Puleston, and P. E. Battaiotto, “Power control of a solar/wind generation system without wind measurement: a passivity/sliding mode approach,” *IEEE Transactions on Energy Conversion*, vol. 18, no. 4, pp. 501–507, Dec. 2003.
- [91] F. Katiraei, M. R. Iravani, and P. W. Lehn, “Small-signal dynamic model of a micro-grid including conventional and electronically interfaced distributed resources,” *IET Generation, Transmission & Distribution*, vol. 1, no. 3, p. 369, 2007.
- [92] J. M. Guerrero, J. C. Vasquez, J. Matas, L. G. de Vicuna, and M. Castilla, “Hierarchical Control of Droop-Controlled AC and DC Microgrids—A General Approach Toward Standardization,” *IEEE Transactions on Industrial Electronics*, vol. 58, no. 1, pp. 158–172, Jan. 2011.
- [93] Y. Mohamed and E. F. El-Saadany, “Adaptive Decentralized Droop Controller to Preserve Power Sharing Stability of Paralleled Inverters in Distributed Generation Microgrids,” *IEEE Transactions on Power Electronics*, vol. 23, no. 6, pp. 2806–2816, Nov. 2008.

- [94] M. Prodanovic and T. C. Green, "Control and filter design of three-phase inverters for high power quality grid connection," *IEEE Transactions on Power Electronics*, vol. 18, no. 1, pp. 373–380, Jan. 2003.
- [95] J. H. R. Enslin and P. J. M. Heskes, "Harmonic interaction between a large number of distributed power inverters and the distribution network," in *IEEE 34th Annual Conference on Power Electronics Specialist, 2003. PESC '03.*, vol. 4, pp. 1742–1747.
- [96] D. P. Ariyasinghe and D. M. Vilathgamuwa, "Stability analysis of microgrids with constant power loads," in *2008 IEEE International Conference on Sustainable Energy Technologies*, 2008, pp. 279–284.
- [97] X. Xu, T. Lin, and X. Zha, "Probabilistic analysis of small signal stability of microgrid using point estimate method," in *2009 International Conference on Sustainable Power Generation and Supply*, 2009, pp. 1–6.
- [98] Z. Chen, F. Blaabjerg, and Y. Hu, "Stability Improvement of Wind Turbine Systems by STATCOM," *IECON 2006 - 32nd Annual Conference on IEEE Industrial Electronics*, pp. 4213–4218, Nov. 2006.
- [99] Z. Saad-Saoud, M. L. Lisboa, J. B. Ekanayake, N. Jenkins, and G. Strbac, "Application of STATCOMs to wind farms," *IEE Proceedings - Generation, Transmission and Distribution*, vol. 145, no. 5, p. 511, 1998.
- [100] A. Sattar, A. Al-Durra, and S. M. Mueeen, "Real time implementation of STATCOM to analyze transient and dynamic characteristics of wind farm," in *IECON 2011 - 37th Annual Conference of the IEEE Industrial Electronics Society*, 2011, pp. 3742–3747.
- [101] L. Xu, L. Yao, and C. Sasse, "Comparison of Using SVC and STATCOM for Wind Farm Integration," in *2006 International Conference on Power System Technology*, 2006, pp. 1–7.
- [102] J. Fraile-Ardanuy and P. J. Zufiria, "Design and comparison of adaptive power system stabilizers based on neural fuzzy networks and genetic algorithms," *Neurocomputing*, vol. 70, no. 16–18, pp. 2902–2912, Oct. 2007.
- [103] C. Jauch, S. M. Islam, P. Sørensen, and B. Bak Jensen, "Design of a wind turbine pitch angle controller for power system stabilisation," *Renewable Energy*, vol. 32, no. 14, pp. 2334–2349, Nov. 2007.
- [104] J. Wang, N. Tse, and Z. Gao, "Synthesis on PI-based pitch controller of large wind turbines generator," *Energy Conversion and Management*, vol. 52, no. 2, pp. 1288–1294, Feb. 2011.

- [105] C. Jauch, T. Cronin, P. Sørensen, and B. Jensen, “A fuzzy logic pitch angle controller for power system stabilization,” *Wind Energy*, no. July 2006, pp. 19–30, 2007.
- [106] T. Senjyu, R. Sakamoto, N. Urasaki, H. Higa, K. Uezato, and T. Funabashi, “Output power control of wind turbine generator by pitch angle control using minimum variance control,” *Electrical Engineering in Japan*, vol. 154, no. 2, pp. 10–18, Jan. 2006.
- [107] J. F. Hall and D. Chen, “Performance of a 100 kW wind turbine with a Variable Ratio Gearbox,” *Renewable Energy*, vol. 44, pp. 261–266, Aug. 2012.
- [108] A. Causebrook, D. J. Atkinson, and A. G. Jack, “Fault Ride-Through of Large Wind Farms Using Series Dynamic Braking Resistors (March 2007),” *IEEE Transactions on Power Systems*, vol. 22, no. 3, pp. 966–975, Aug. 2007.
- [109] K. N. Rashad M. Kamel, “Maintaining Stability of Standalone Micro-Grid by Employing Electrical and Mechanical Fault Ride Through Techniques upon Fixed Speed Wind Generation Systems,” *Energy Conversion and Management*, 2013.
- [110] Z. Chen, Y. Hu, and F. Blaabjerg, “Stability improvement of induction generator-based wind turbine systems,” *Renewable Power Generation, IET*, pp. 81–93, 2007.
- [111] Z. Yang, C. Shen, and L. Zhang, “Integration of a StatCom and battery energy storage,” *Power Systems, IEEE ...*, vol. 16, no. 2, pp. 254–260, 2001.
- [112] C. Abbey and G. Joos, “Supercapacitor Energy Storage for Wind Energy Applications,” *IEEE Transactions on Industry Applications*, vol. 43, no. 3, pp. 769–776, 2007.
- [113] K. Dinh and Y. Hayashi, “Centralized BESS control to minimize demand of PV-supplied micro-grid under voltage constraints,” *Power and Energy (PECon), 2012 IEEE ...*, no. December, pp. 864–869, Dec. 2012.
- [114] A. Arulampalam and M. Barnes, “Power quality and stability improvement of a wind farm using STATCOM supported with hybrid battery energy storage,” ... *and Distribution, IEE ...*, pp. 701–710, 2006.
- [115] X. Wu, A. Arulampalam, C. Zhan, and N. Jenkins, “Application of a static reactive power compensator (STATCOM) and a dynamic braking resistor (DBR) for the stability enhancement of a large wind farm,” *Wind Engineering*, 2003.
- [116] S. Muyeen and R. Takahashi, “Transient stability augmentation of power system including wind farms by using ECS,” *Power Systems, ...*, vol. 23, no. 3, pp. 1179–1187, 2008.

- [117] H. Wei, W. Xin, G. Jiahuan, Z. Jianhua, and Y. Jingyan, "Discussion on application of super capacitor energy storage system in microgrid," in *2009 International Conference on Sustainable Power Generation and Supply*, 2009, pp. 1–4.
- [118] P. Soori, S. Shetty, and S. Chacko, "Application of super capacitor energy storage in microgrid system," *GCC Conference and ...*, pp. 581–584, 2011.
- [119] M. Ahsanul Alam, A. H. M. a. Rahim, and M. a. Abido, "Supercapacitor based energy storage system for effective fault ride through of wind generation system," in *2010 IEEE International Symposium on Industrial Electronics*, 2010, pp. 2481–2486.
- [120] A. H. M. A. Rahim and M. A. Alam, "Fast low voltage ride-through of wind generation systems using supercapacitor based energy storage systems," *2011 Fourth International Conference on Modeling, Simulation and Applied Optimization*, pp. 1–6, Apr. 2011.
- [121] G. Zhang, X. Tang, and Z. Qi, "Research on Battery Supercapacitor Hybrid Storage and its application in MicroGrid," in *2010 Asia-Pacific Power and Energy Engineering Conference*, 2010, pp. 1–4.
- [122] D. Simon, "Biogeography-based optimization," *Evolutionary Computation, IEEE Transactions on*, vol. 12, no. 6, pp. 702–713, 2008.
- [123] R. MacArthur and E. Wilson, *The Theory of Biogeography*. Princeton, NJ: Princeton Univ. Press, 1967.
- [124] A. K. Bansal, R. Kumar, and R. A. Gupta, "Economic Analysis and Power Management of a Small Autonomous Hybrid Power System (SAHPS) Using Biogeography Based Optimization (BBO) Algorithm," *IEEE Transactions on Smart Grid*, vol. 4, no. 1, pp. 638–648, Mar. 2013.
- [125] S. Rajasomashekar and P. Aravindhababu, "Biogeography based optimization technique for best compromise solution of economic emission dispatch," *Swarm and Evolutionary Computation*, vol. 7, pp. 47–57, Dec. 2012.
- [126] Y. Yu, *Electric Power System Dynamics*. Academic Press Inc, 1983, p. 256.
- [127] H. Tsai, C. Tu, and Y. Su, "Development of Generalized Photovoltaic Model Using MATLAB / SIMULINK," *Proceedings of the World Congress on Engineering and Computer Science 2008*, pp. 0–5, 2008.
- [128] V. J. Fesharaki, M. Dehghani, and J. J. Fesharaki, "The Effect of Temperature on Photovoltaic Cell Efficiency," no. November, pp. 20–21, 2011.

- [129] M. Petkov, D. Markova, and S. Platikanov, "MODELLING OF ELECTRICAL CHARACTERISTICS OF PHOTOVOLTAIC POWER SUPPLY SOURCES," *Contemporary Materials*, vol. 2, no. 2, pp. 171–177, Dec. 2011.
- [130] V. Quaschnig and R. Hanitsch, "NUMERICAL SIMULATION OF PHOTOVOLTAIC GENERATORS WITH SHADED CELLS," no. 0, pp. 583–586, 1995.
- [131] F. C. Lee, "High-efficiency, high step-up DC-DC converters," *IEEE Transactions on Power Electronics*, vol. 18, no. 1, pp. 65–73, Jan. 2003.
- [132] B. Gu and K. Nam, "A DC link capacitor minimization method through direct capacitor current control," *Conference Record of the 2002 IEEE Industry Applications Conference. 37th IAS Annual Meeting (Cat. No.02CH37344)*, vol. 2, pp. 811–817, 2002.
- [133] N. Mahamad, C. M. Hadzer, and S. Masri, "Application of LC filter in harmonics reduction," *PECon 2004. Proceedings. National Power and Energy Conference, 2004.*, pp. 268–271, 2004.
- [134] M. Mansour, M. N. Mansouri, and M. F. Mimouni, "Study of performance of a variable-speed wind turbine with pitch control based on a Permanent Magnet Synchronous Generator," in *Eighth International Multi-Conference on Systems, Signals & Devices*, 2011, no. 1, pp. 1–6.
- [135] Y. Kazachkov and R. Voelzke, "Modeling wind farms for power system load flow and stability studies," in *2005 IEEE Russia Power Tech*, 2005, pp. 1–8.
- [136] M. S. (KFUPM) Ali, "Evaluation of damping controls of a permanent magnet synchronous generator wind system with STATCOM," KFUPM, 2012.
- [137] H. F. Wang, "Phillips–Heffron model of power systems installed with STATCOM and applications," *IEE Proceedings - Generation, Transmission and Distribution*, vol. 146, no. 5, p. 521, 1999.
- [138] A. H. M. A. Rahim and E. P. Nowicki, "Supercapacitor energy storage system for fault ride-through of a DFIG wind generation system," *Energy Conversion and Management*, vol. 59, pp. 96–102, Jul. 2012.
- [139] M. E. a. Farrag and G. a. Putrus, "Design of an Adaptive Neurofuzzy Inference Control System for the Unified Power-Flow Controller," *IEEE Transactions on Power Delivery*, vol. 27, no. 1, pp. 53–61, Jan. 2012.
- [140] S. R. Khuntia and S. Panda, "ANFIS approach for SSSC controller design for the improvement of transient stability performance," *Mathematical and Computer Modelling*, vol. 57, no. 1–2, pp. 289–300, Jan. 2013.

- [141] a. Meharrar, M. Tioursi, M. Hatti, and A. Boudghène Stambouli, “A variable speed wind generator maximum power tracking based on adaptative neuro-fuzzy inference system,” *Expert Systems with Applications*, vol. 38, no. 6, pp. 7659–7664, Jun. 2011.
- [142] J.-S. R. Jang, “ANFIS: adaptive-network-based fuzzy inference system,” *IEEE Transactions on Systems, Man, and Cybernetics*, vol. 23, no. 3, pp. 665–685, 1993.

VITAE

Name: Mohammed Ashraf Ali

Date of birth: 12 May, 1988

Nationality: Indian

Present Address: KFUPM P.O. Box # 8617, King Fahd University of
Petroleum and Minerals, Dhahran - 31261, Saudi Arabia
Phone:+966-507246575

Permanent Address: P.O. Box # 5-1-56/1, Tandur - 501141, India

Email Address: ashraf8812@gmail.com

Educational Qualification: **M.S (Electrical Power Engineering)**

May, 2013

King Fahd University of Petroleum and Minerals,

Dhahran, Saudi Arabia.

B.E. (Electrical and Electronics Engineering)

June, 2009

Osmania University, Hyderabad, India.